A Technical and Economic Assessment of Molten Salt Parabolic Trough Power Plants and Operating Strategies in Southern Africa

by

Christoph Adrian Pan

Dissertation presented for the degree of
Doctor of Philosopy in the
Faculty of Engineering at
Stellenbosch University

Supervisor:	Prof. F. Dinter
Co-supervisors:	Prof. T.M. Harms
	Prof. S.J. van der Spuy

December 2020

Declaration

By submitting this dissertation electronically, I declare that the entirety of the work contained therein is my own, original work, that I am the sole author thereof (save to the extent explicitly otherwise stated), that reproduction and publication thereof by Stellenbosch University will not infringe any third party rights and that I have not previously in its entirety or in part submitted it for obtaining any qualification.

Date: December 2020 .....

Abstract

A Technical and Economic Assessment of Molten Salt Parabolic Trough Power Plants and Operating Strategies in Southern Africa

C.A. Pan

Department of Mechanical and Mechatronic Engineering,
Stellenbosch University,
Private Bag X1, Matieland 7602, South Africa.

Dissertation: PhD (Eng)

December 2020

Parabolic trough power plants (PTPP) using thermal oils as heat transfer fluid (HTF) are currently still state-of-the-art. Using molten salts as HTF instead enables higher operating temperature differences and therefore higher cycle efficiencies. Nevertheless, the use of molten salts is linked to several engineering and operational challenges that require special consideration to be placed on improved operating strategies and power plant configurations. This can, for example, be achieved through a technical and economic assessment, where design variables and operational parameters can be determined that lead to an optimised financial feasibility of molten salt PTPPs for various operating objectives.

For this purpose, a two-dimensional dynamic parabolic trough solar collector model using molten as HTF was developed and validated with measurement data obtained from the Archimede Solar Energy demonstration plant for molten salt receiver tubes in Massa Martana, Italy. An empirical heat loss equation based on the outer surface temperature of the absorber tube was introduced to the model in order to improve simulation efficiency. The finite volume method was applied to discretise the receiver into control volumes, whereby the effect of decreasing levels of discretisation on the model accuracy is analysed. The relative error of the loop outlet temperature is 0.69 % for the most detailed model and 0.99 % when one control volume per solar collector array is used. A division into five control volumes is recommended as a trade-off between model accuracy and simulation time.

A location-tailored economic model for South Africa and Namibia was implemented and validated with financial data of two existing concentrating solar power plants in South Africa, leading to a maximum error of −5 % for the levelised cost of electricity (LCOE). A sensitivity analysis was carried out to identify the key technical and financial design parameters that lead to the best potential improvements in terms of power plant efficiency and profitability. In order to combine the cost reduction potentials of all key design parameters identified in the sensitivity analysis, a multi-objective optimisation was carried out, simultaneously minimising the investment costs and maximising the internal rate of return. The results show that Solar Salt offers the lowest LCOE out of three investigated HTFs and a freeze protection system using thermal energy from the hot tank enables a significant reduction of the LCOE in comparison to the baseline approach of relying on electric freeze protection only.

Based on the optimisation results, a range of power plant configurations and operational parameter set points are recommended for baseload and two-tier tariff structures. For baseload power plants, the minimum required bidding tariff is 119.4 $/MWh in South Africa and 115.8 $/MWh in Namibia under current financial boundary conditions. A projection of the LCOE until 2050 shows that an LCOE of 49.6 $/MWh is expected for South Africa and 49.3 $/MWh for Namibia with a technology learning rate of 20 %. However, assuming reduced financing costs, tariffs as low as 50.4 $/MWh can already be financially feasible today and a spot market participation of molten salt PTPPs is possible with LCOEs between 58.9 $/MWh and 65.6 $/MWh.

Uittreksel

'n Tegniese en Ekonomiese Assessering van Gesmeltesout Paraboliese-trog Kragsentrales en hul Bestuursstrategieë in Suidelike Afrika

(A Technical and Economic Assessment of Molten Salt Parabolic Trough Power Plants and Operating Strategies in Southern Africa)

C.A. Pan

Departement Meganiese en Megatroniese Ingenieurswese,
Universiteit van Stellenbosch,
Privaatsak X1, Matieland 7602, Suid Afrika.

Proefskrif: PhD (Ing)

Desember 2020

Die gebruik van termiese olies as hitte-oordrag vloeistof (HOV) in paraboliese-trog krag sentrales (PTKS) is tans nog die mees gevorderde in die tegnologie. Gesmelte sout (GS) kan wel in pleks van termiese olies as HOF gebruik word en daardeur hoër bedryf temperature handhaaf en sodoende hoër effketiwiteit. Nietemin, bied die gebruik van GS as HOF verskeie ingenieurs en bedryfs-uitdagings wat spesiale oorweging verg vir dit om saam met verbeterde bedryfs-strategieë en kragstasie konfigurasies gebruik te word. Hierdie kan aangespreek word deur tegniese en ekonomiese analises waar die ontwerp en bedryfs-veranderlikes bepaal kan word wat sal lei tot die optimale finansiële lewensvatbaarheid van GS in PTKS vir verskeie bedryfs-doelwitte.

Vir hierdie doel is 'n dinamiese, twee-dimensionele paraboliese trog sonkollektor-model, wat GS as HOV gebruik, ontwikkel en gevalideer met gemete data verkry vanaf die Archimede Son-energie demonstrasie-aanleg vir GS-ontvangerbuise in Massa Martana, Italië. 'n Empiriese hitteverlies vergelyking, gebaseer op die buite-oppervlaktemperatuur van die absorbeerder-buis, is in die model gebruik om simulasie-doeltreffendheid te verbeter. Die eindige volume-metode is toegepas om die ontvanger in diskrete beheervolumes te verdeel en die effek van dalende vlakke van diskretisasie op die akkuraatheid van die model is gevolglik geanaliseer. Die relatiewe fout van die lusuitlaat temperatuur is 0.69 % vir die mees gedetailleerde model en 0.99 % wanneer een

beheervolume per son-kollektor stel gebruik word. 'n Verdeling in vyf beheervolumes word aanbeveel as 'n kompromie tussen akkuraatheid en simulasietydsduur.

'n Ekonomiese model is gebou vir Suid-Afrikaanse en Namibiese omstandighede en is gemodelleer en gevalideer met finansiële gegewens van twee bestaande gekonsentreerde sonkragsentrales in Suid-Afrika. Dit lei tot resultate met 'n maksimum fout van $-5\,\%$ vir die lewensikluskoste van elektrisiteit (LKVE) teenoor die gemete resultate van die Suid-Afrikaanse gevalle. 'n Sensitiwiteitsanalise is uitgevoer om die belangrikste tegniese en finansiële ontwerpparameters te identifiseer wat tot die beste moontlike verbeterings in terme van doeltreffendheid en winsgewendheid in die kragsentrale kan lei. Ten einde die koste-verminderingsvermoë van alle sleutelontwerp-parameters wat in die sensitiwiteitsanalise geïdentifiseer is, te kombineer, is 'n multi-doelstelling optimering uitgevoer, wat ten doel het om gelyktydig die investeringskoste te minimeer sowel as die interne opbrengskoers te maksimeer. Die resultate toon dat GS die laagste LKVE bied uit drie HOV's wat aan die ondersoek onderwerp was. 'n Vries-beskermingstelsel wat termiese energie uit die warm tenk gebruik maak 'n aansienlike vermindering van die LKVE moontlik, teenoor die basislynbenadering wat slegs elektriese vriesbeskerming gebruik.

Op grond van die resultate van die optimering word 'n reeks kragaanlegkonfigurasies en operasionele bedryfsparameters aanbeveel vir basis-las en dubbel-vlak tariefstrukture. Vir basis-las kragsentrales is die minimum tariewe $119.4\,\$/\text{MWh}$ in Suid-Afrika en $115.8\,\$/\text{MWh}$ in Namibië onder huidige finansiële omstandighede. 'n Vooruitskatting van die LKVE tot 2050 wys dat 'n LKVE van $49.6\,\$/\text{MWh}$ vir Suid-Afrika en $49.3\,\$/\text{MWh}$ vir Namibië verwag word met 'n tegnologie-leer-tempo van $20\,\%$. Met die veronderstelling van laer finansieringskostes, kan tariewe so laag as $50.4\,\$/\text{MWh}$ vandag egter reeds haalbaar wees, en die plekmark-deelname van GS-PTKSs is moontlik met LKVE's tussen $58.9\,\$/\text{MWh}$ en $65.6\,\$/\text{MWh}$.

Acknowledgements

I would like to express my sincere gratitude to the following people and organisations:

My supervisor, Prof. Frank Dinter, for his valuable guidance throughout this project and for his positive attitude that kept me motivated.

My co-supervisor, Prof. Thomas M. Harms, for his continuous support and feedback, as well as for providing funding to attend the SolarPACES conference in 2017 in Santiago, Chile, and the SolarPACES conference in 2018 in Casablanca, Morocco.

My co-supervisor, Prof. Johan van der Spuy, for his ideas and expert knowledge in turbo machinery.

Dr. Rafael Guédez from the KTH Royal Institute of Technology for providing the optimisation software DYESOPT and for his continuous feedback and suggestions for my work.

Dr. Davide Ferruzza from the DTU Technical University of Denmark for sharing his thermal oil parabolic trough model and for his patience in showing me how to effectively de-bug errors in TRNSYS.

The Autonomous Province of Bolzano-Alto Adige, Italy, for providing a four-year study grant for my doctoral programme. Opinions expressed and conclusions arrived at, are those of the author and are not necessarily to be attributed to the Autonomous Province of Bolzano-Alto Adige.

The Solar Thermal Energy Research Group (STERG) at Stellenbosch University for providing funding to attend the SolarPACES conference in 2017 in Santiago, Chile, and the SolarPACES conference in 2018 in Casablanca, Morocco.

The Centre for Renewable and Sustainable Energy Studies (CRSES) at Stellenbosch University for providing funding to attend the Southern African Solar Energy Conference (SASEC) 2018 in Durban, South Africa, and the STERG Technical Tour to Upington, South Africa.

Mr. Augusto Maccari for providing the measurement data of the solar collector demonstration plant at Archimede Solar Energy in Massa Martana, Italy.

My wife, Dr. Francine Simon, in her professional role as editor for editing all my papers.

Dr. Dries Frank Duvenhage and Mr. Ernest Dall for translating the abstract into Afrikaans.

My fellow students and colleagues at STERG, especially Dr. Matti Lubkoll, Dr. Dries Frank Duvenhage and Dr. Stephen Richard Clark for countless discussions, coffee breaks, braais, wine tastings and all their wisdom they provided in the process.

My friends, Luca Cosenza and Markus Stufferin, who I list in alphabetical order so they can keep arguing about who is my best friend, for providing occasionally much needed distractions from the project and without whom I would have finished a year earlier.

Last but not least, my family, whose love and support is unmatched.

Dedication

To my wonderful wife Francine
For her endless love, support and patience

Contents

List of Figures

List of Tables

Nomenclature

Constants

C_1	constant of integration	
$R_{air} =$	$287\,\mathrm{J/(kg\,K)}$	

Variables[1]

a	incidence angle modifier coefficient	$[-]$
A	area	$[\mathrm{m^2}]$
Bi	Biot number	$[-]$
c	specific investment costs	[$/unit]
C	capital costs	[$]
C	Coefficient	$[-]$
C	Courant number	$[-]$
c_1	convective receiver heat loss coefficient	$[\mathrm{W/(m\,°C)}]$
c_4	radiative receiver heat loss coefficient	$[\mathrm{W/(m\,°C^4)}]$
$CAPEX$	capital expenditure	[$]
cf	cleanliness factor	[%]
c_p	specific heat at constant pressure	$[\mathrm{J/(kg\,K)}]$
d	diameter; characteristic length	[m]
d	discount rate	[%/a]
D	daylight saving time	$[-]$
$DISP$	dispatch hour	$[-]$
$DSCR$	debt service coverage ratio	$[-]$
e	specific energy	$[\mathrm{W\,h/W}]$
E	energy	$[\mathrm{J; W\,h}]$
err	error	$[-]$
f	factor	$[-]$
f	Darcy friction factor	$[-]$
f	focal length	[m]

[1] All values reported in $ refer to United States Dollar (USD).

f	financial factor/rate	[%]
F	force	[kg m/s^2; N]
h	enthalpy	[J/kg]
h	heat transfer coefficient	[W/(m^2 K)]
i	node number	[−]
i	interest rate	[%]
I	irradiance	[W/m^2]
I	irradiation	[Wh/m^2]
IRR	internal rate of return	[%]
k	thermal conductivity	[W/(m K)]
k	cost of debt/equity	[%]
K	resistance coefficient	[−]
L	length	[m]
LC	longitude correction	[min]
LR	learning rate	[%]
m	mass	[kg]
$\dot{m}$	mass flow rate	[kg/s]
n	financial lifetime	[a]
n	loan period	[a]
n	number of days	[−]
n	number of discretisation segments	[−]
N	number; amount	[−]
NPV	net present value	[$]
Nu	Nusselt number	[−]
$OPEX$	operational expenditure	[$]
p	price	[$/MWh]
P	pressure; pressure drop	[kg/(m s^2); bar]
pr	progress ratio	[−]
Pr	Prandtl number	[−]
q	thermal energy	[J]
$\dot{q}$	heat transfer rate	[W]
$\dot{q}'$	heat transfer rate per unit length	[W/m]
$\dot{q}''$	heat transfer rate per unit area	[W/m^2]
Q	sum of thermal energy	[J]
$\dot{Q}$	sum of heat transfer rate	[W]
r	radius	[m]

r	rate	[%]
R	gas constant	[J/(kg K)]
R	revenue	[$]
Re	Reynolds number	[−]
s	share of equity	[%]
s	scaling factor	[−]
S	surface	[m^2]
SM	solar multiple	[−]
t	time	[s]
T	temperature	[°C]
TI	taxable income	[$]
TOH	total operating hours per day	[−]
TZ	time zone	[−]
u	substitution variable	[−]
u	tank heat loss coefficient	[W/(m^2 K)]
U	internal energy	[J]
UA	overall heat transfer coefficient	[W/K]
v	bulk flow velocity	[m/s]
$\bar{v}$	average flow velocity	[m/s]
V	cumulative average water demand	[m^3/a]
V	volume	[m^3]
$\dot{V}$	volume flow rate	[m^3/s]
w	aperture width of solar collector	[m]
w	weighted share of debt to equity	[%]
$\dot{W}$	rate of doing work	[W]
x	discretised length	[m]
X	component design size	[m^2; W; W h]

Greek Symbols

α	absorptance	[%]
β	sales tax basis	[%]
γ	solar azimuth angle	[°]
γ	intercept factor	[%]
δ	declination angle	[°]
Δ	finite increment	[−]
Δ	difference	[−]
ϵ	effectiveness	[%]

ϵ	error tolerance	$[-]$
η	efficiency	$[\%]$
θ	incidence angle	$[^\circ]$
θ_e	solar elevation angle	$[^\circ]$
θ_z	solar zenith angle	$[^\circ]$
κ	incidence angle modifier	$[\%]$
μ	dynamic viscosity	$[\mathrm{Pa\,s}]$
μ	integrating factor	$[-]$
ρ	density	$[\mathrm{kg/m^3}]$
ρ	mirror reflectance	$[\%]$
ρ	electrical resistivity	$[\Omega\,\mathrm{m}]$
τ	shear stress	$[-]$
τ	time constant	$[-]$
τ	transmittance	$[\%]$
ϕ	latitude	$[^\circ]$
χ	vapour quality	$[\%]$
ψ	longitude	$[^\circ]$
Ψ	solar field efficiency	$[\%]$
ω	hour angle	$[^\circ]$
Ω	control volume	$[-]$
∇	vector of partial derivative operators	$[-]$

Subscripts

abs	absorber; absorbed
air	air
amb	ambient
ann	annuity
avail	availability
avg	average
b	beam
base	base
bellow	bellow
BOP	balance of plant
brac	bracket
c	cold; characteristic
cap	capacity
CND	condenser; condensate

coll	collector
comp	component
con	construction
cond	conduction
cont	contingency
cont	contraction
conv	convection
cool	cool-down
COP	cross-over piping
cycle	steam cycle
DAM	day-ahead market
debt	debt
dec	decommissioning
depr	depreciation
des	design
dev	developer
dir	direct
div	division
dp	debt payment
e	electrical
EC	economiser
eff	effective
el	electricity
elb	elbow
end	end
EPC	owner's engineering, procurement & construction
eq	equity
eval	evaluation
exp	expansion; exponent
f	friction
fan	fan
fin	financial
fit	fitting
fix	fixed
fp	freeze protection
FW	feed water

g	gravitational
gain	gain
gap	gap between solar collectors
gen	generator
glass	glass
grid	electric grid
gross	gross
grp	group
guess	guess value
h	hour
h	hot
h	hourly index for financial analysis from 1 to 8760
hdr	header
hl	heat loss
HCE	heat collection element
HPT	high pressure turbine
HTF	heat transfer fluid
i	day of year index from 1 to 365
i	control volume index from 1 to n
i	header section index from 1 to $N_{\text{div},j}$
i	solar collector array component index
in	inlet
inc	incident; income
indir	indirect
infl	inflation
initial	initial approximation
ins	insurance
int	interest
ITD	inlet temperature difference
j	hour of day index from 1 to 24
j	header group index from 1 to N_{grp}
j	solar collector array index in a loop from 1 to N_{SCA}
k	fitting component index from 1 to $N_{\text{fit,comp}}$
land	land
lev	levelised
load	turbine loading

loc	local; location
loss	loss
loop	loop
LPT	low pressure turbine
m	measured
max	maximal; maximum
mech	mechanical
min	minimal; minimum
mirr	mirror washing
misc	miscellaneous
net	net
nom	nominal
op	operation
OPEX	operational expenditure
opt	optical
out	outlet
p	pressure
paras	parasitic
PB	power block
peak	peak
PH	preheater
piping	interconnecting piping
pp	principal payment
PPA	power purchase agreement
proj	project
pump	pump
rad	radiation
rampdown	turbine ramp-down
real	real
refl	reflective aperture
req	required
RH	reheater
run	runner
s	simulated
s	stage
s	isentropic

S	surface
S2E	solar-to-electric
sales	sales
sat	saturation
SCA	solar collector array
sec	section
SF	solar field
SH	superheater
shadow	shadowing
sim	simulation
simple	simplified
site	site preparation
sky	sky
spacing	collector row spacing
split	split
sol	solar
st	standard
steam	steam
sync	synchronous speed
sys	system
targ	target
t	time
t	yearly index for financial analysis
T	temperature
tank	tank
tax	tax
TES	thermal energy storage
th	thermal
track	tracking
trans	transmission line
TTD	terminal temperature difference
tube	absorber tube
upfront	up-front fee
v	volume
V	volume
var	variable

$_{w}$	wall
$_{water}$	water

Superscripts

$'$	per unit length; first derivative of function $f(x)$
$''$	per unit area
^{ref}	reference value

Overscores

$\bar{}$	average value
$\dot{}$	per unit time

Abbreviations

ACC	air-cooled condenser
AISI	American Iron and Steel Institute
BOP	balance of plant
BW	bid window
CAPEX	capital expenditure
CEPCI	Chemical Engineering Plant Cost Index
CIEMAT	Centro de Investigaciones Energéticas, Medioambientales y Tecnológicas
CNDT	condensate tank
CPI	consumer price index
CR	central receiver
CRSES	Centre for Renewable and Sustainable Energy Studies
CSP	concentrating solar power
CT	cold tank
CV	control volume
D	deaerator
DAM	day-ahead market
DEWA	Dubai Electricity & Water Authority
DLR	German Aerospace Centre
DNI	direct normal irradiance
DSCR	debt service coverage ratio
DSG	direct steam generation
DYESOPT	Dynamic Energy Systems Optimizer
EC	economiser
EV	evaporator

FIT	feed-in tariff
FP	freeze protection
FPS	freeze protection strategy
FVM	finite volume method
G	generator
HCE	heat collection element
HCEMS	Heat Collection Element for Molten Salt
HPT	high pressure turbine
HT	hot tank
HTF	heat transfer fluid
IEA	international Energy Agency
IPP	independent power producer
IRP	Integrated Resource Plan
IRR	internal rate of return
ITD	initial temperature difference
LCOE	levelised cost of electricity
LF	linear Fresnel
LPT	low pressure turbine
LR	learning rate
MSPTPP	molten salt parabolic trough power plant
NREL	National Renewable Energy Laboratory
OECD	Organisation for Economic Co-operation and Development
ODE	ordinary differential equation
OM	operation mode
OPEX	operation and maintenance costs (operational expenditure)
PB	power block
PDE	partial differential equation
PDS	pre-defined dispatch strategy
PH	preheater
PPA	power purchase agreement
PPI	Producer Price Index
PT	parabolic trough
PTPP	parabolic trough power plant
PV	photovoltaic
REIPPPP	Renewable Energy Independent Power Producer Procurement Program
RH	reheater
S2E	solar-to-electric

SAM	System Advisor Model
SAPP	Southern African Power Pool
SASEC	Southern African Solar Energy Conference
SCA	solar collector array
SEGS	Solar Electric Generating System
SF	solar field
SH	superheater
SM	solar multiple
STERG	Solar Thermal Energy Research Group
TES	thermal energy storage
TMY	typical meteorological year
TRNSYS	Transient System Simulation Tool
TTD	terminal temperature difference
USD	United States Dollar
UTC	Coordinated Universal Time
WACC	weighted average capital cost
ZAR	South African Rand

Chapter 1

Introduction[1]

Concentrating solar power (CSP) plants are widely considered to play a key role in the de-carbonisation of commercial power generation, especially in solar-rich areas. Although *photovoltaic* (PV) power plants currently offer the lowest *levelised cost of electricity* (LCOE) with a recent bid of 16 \$/MWh in Portugal (PV Magazine, 2019), the value of CSP lies in its characteristic cost-effective energy storage and thus, dispatchability. High temperature *thermal energy storage* (TES) is used to extend the power production period, which can reduce the LCOE, or to shift power generation to peak hours during which tariffs are typically higher, thus, increasing the profitability of CSP plants. Nevertheless, CSP technologies are currently still not considered to be cost-competitive with other renewable or non-renewable technologies such as PV, wind or coal. The global weighted average LCOE of PV in 2018 is 85 \$/MWh, whereas the average for CSP plants is 185 \$/MWh (IRENA, 2019). Compared to the 2018 cost of new build coal-fired power stations in South Africa, which is estimated to be 1.01 ZAR/kWh, or 76 \$/MWh[2] (Department of Energy, 2019*a*), CSP is still considerably more expensive. However, the increasing need for dispatchable power generation makes CSP an invaluable player in a rapidly changing energy sector with high renewable energy market penetration (Lubkoll, 2017).

1.1 Background

The first CSP plants, the *Solar Electric Generating Stations* (SEGS) I to IX, were built in the 1980s but did not have TES. Nearly twenty years would go by until the first CSP plant with a significantly large TES capacity of 7.5 h was built in Spain in 2008: Andasol 1. Over the next 5 years, another 47 commercial power plants were built in Spain, nearly half with TES in order to shift the power production to hours with higher market prices or when required to do so by the grid operator. As more and more countries started

[1] Parts of this chapter have been submitted for publication (see Pan *et al.*, 2021).
[2] Yearly average exchange rate of 13.242 ZAR/\$ in 2018 (X-Rates, 2019*c*).

to recognise the value of dispatchability, the global deployment of CSP gained momentum and reached a cumulative installed gross capacity of 6.5 GW in 2019 (NREL, 2020). Figure 1.1a shows the cumulative installed gross CSP capacity between 2005 and 2019 (solid line). An additional 0.7 GW is due to come online in 2020 and 2.6 GW is expected to be completed by 2023 (dashed line).

With nearly 80 out of 100 commercial CSP plants currently in operation worldwide (NREL, 2020), *parabolic trough* (PT) power plants make up the lion's share of the CSP market. They have proven to be the most mature solar thermal technology up to date and, at the present time, are still considered to be the most bankable CSP technology for large scale power production. Figure 1.1b reflects this trend with 5 GW gross capacity of *parabolic trough power plants* (PTPP) installed worldwide. In comparison, *central receiver* (CR) plants only amount to 1.2 GW installed gross capacity. An additional 1 GW of PTPP gross capacity is currently under construction or development. However, central receiver plants are catching up quickly with nearly 2 GW in the pipeline. Last but not least, 0.2 GW of *linear Fresnel* (LF) is currently in operation and 0.16 GW under construction or development (NREL, 2020).

At the time of writing, the majority of commercial PTPPs are installed in Spain (45) and the US (13), followed by 5 plants in South Africa (NREL, 2020). In contrast, only 17 CR and four LF plants are in operation. According to NREL (2020), most of the 25 projects presently under construction or development are located in China (13) and Chile (four). In September 2016, China released its "Chinese 1 GW Demonstration Project Short List", where it awarded the first round of 20 demonstration projects a *feed-in tariff* (FIT)

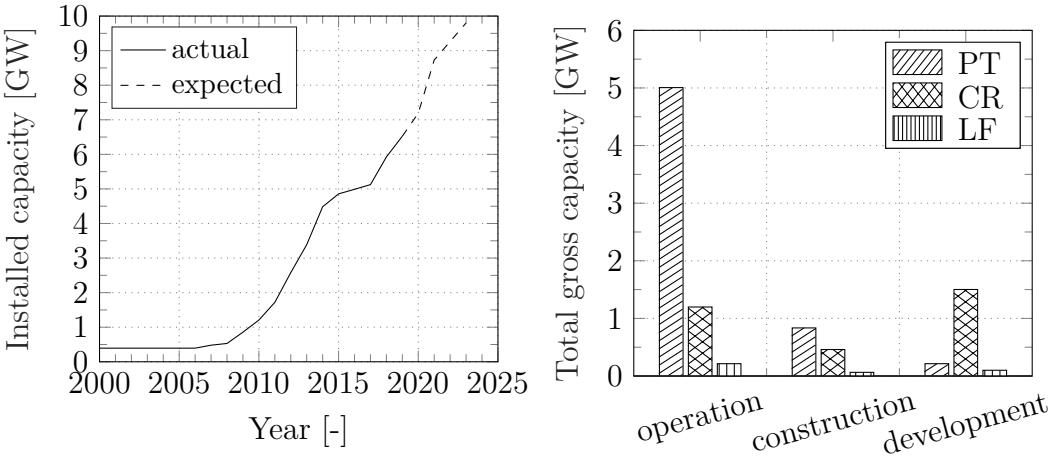

(a) Globally installed CSP capacity. **(b)** CSP technologies by project status.

Figure 1.1: CSP trends for (a) the globally installed gross capacity and (b) the technologies of commercial projects worldwide by project status (NREL, 2020).

of 1.15 CNY/kWh, or 0.174 $/kWh (CSP Plaza, 2016)[3]. Among these projects are seven PTPPs, two of which will use molten salt as a *heat transfer fluid* (HTF).

Although CR systems offer a higher plant performance and thus also a lower LCOE (Lubkoll, 2017), PTPPs offer a moderate technology risk due to many years of experience in construction and operation (IFC, 2012). To date, thermal oil as HTF in PTPPs is still state-of-the-art due to the proven technology and extensive track record. However, the drawback of thermal oil, a mixture of biphenyl and diphenyl oxide, is its relatively low thermal stability limit of 400 °C (Eastman, 2019). To further increase the competitiveness of PTPPs, the main challenge is to reduce the LCOE which can, for instance, be achieved by increasing the cycle efficiency. For that purpose, alternative fluids with higher maximum operating temperatures have been proposed, enabling a larger temperature difference between the steam turbine inlet and condenser outlet. These include molten salts, such as nitrate salts, carbonate salts, chloride salts and alkali-fluorides; liquid metals, like e.g. sodium and a sodium-potassium mixture; or gases, such as pressurised air, pressurised CO_2, helium, hydrogen and steam through *direct steam generation* (DSG). A comprehensive review of proposed HTFs can be found in the works of Serrano-López *et al.* (2013), Vignarooban *et al.* (2015) and Benoit *et al.* (2016). Besides DSG and pressurised air, only molten salts such as *Solar Salt*, *Hitec* and *Hitec XL* are at present commercially available or have been demonstrated in commercial CSP applications. Hence, this study will focus on these salt mixtures, which have already been successfully used as HTF in CR plants and in the majority of commercial solar thermal power plants as TES medium.

The most commonly used molten salt in PTPPs is Solar Salt, a binary salt mixture of 60 % $NaNO_3$ and 40 % KNO_3 by weight. It has a thermal stability limit of 600 °C (SQM, 2017) due to the chemical decomposition and increased corrosion rates at high temperatures (Bradshaw and Siegel, 2008). The freezing temperature of Solar Salt is 220 °C as compared to only 12 °C of thermal oil (Vignarooban *et al.*, 2015). This relatively elevated operating temperature range is linked to a series of engineering and operational challenges, which have been thoroughly evaluated by Kearney *et al.* (2003). These include, amongst others, high heat losses in the *solar field* (SF), a lower HTF flow rate detrimental to thermal mixing, the need for more expensive materials due to higher corrosion rates and the need for a reliable *freeze protection* (FP) system with rapid response times. For the latter, a suitable alternative to gas-fired backup heaters commonly used in conventional PTPPs is *impedance heating*, where the absorber tubes are used as resistors by letting an electric current flow directly through the pipes (Pacheco and Kolb, 1997). Through this so-called *Joule-effect*, heat is generated in the absorber tubes, keeping the fluid flowing through them above the desired temperature. In contrast,

[3] Yearly average exchange rate of 6.613 CNY/$ in 2018 (X-Rates, 2019*b*).

more commonly used ohmic *resistance heating* uses heating cables along the length of interconnecting piping. Other approaches include the recirculation of the fluid from the hot storage tank with a low flow rate to reduce heat losses or a passive or forced drainage of the solar field at night or in the event of emergencies (Eickhoff *et al.*, 2016; Dinter and Tolksdorf, 2018). Thus, the increased energy consumption needed for maintaining the fluid temperature above its freezing point through impedance heating, as well as the resulting heat losses due to higher absorber tube temperatures, can be reduced. On the other hand, the upper operating temperature of up to 600 °C in the case of Solar Salt also significantly increases the heat losses in the solar field during normal operation. However, the same high upper operating temperature has the reverse effect on the mass flow rate, which is consequently lower than in thermal oil PTPPs. This, in turn, results in a lower pressure drop in the solar field and hence also reduces pumping parasitics.

Considering all the challenges linked to the usage of molten salts as HTF, advanced operating strategies are required to maximise the annual energy yield and reduce fossil fuel consumption. A technical and economic assessment is thus necessary to propose a range of plant component designs and operating strategies that lead to an optimised financial feasibility for various objectives (e.g. maximisation of energy production and profits or reduction of turbine stops). The research work at hand aims to answer questions related to the component level up to the system level and the operation of PTPPs within a Southern African context. This study is intended as an applied research work rather than fundamental. It aims at understanding the complex processes in a *molten salt parabolic trough power plant* (MSPTPP) and what effect an HTF with a high freezing point has on the plant operation and performance to increase the competitiveness of CSP. Using molten salt as HTF in PTPPs opens up new opportunities for CSP in Southern Africa (and similar climatic locations worldwide), in both research and industry, due to its cost reduction potentials and high efficiency in conjunction with high *direct normal irradiance* (DNI) values.

1.2 Literature Review

A literature review has been carried out to identify the state-of-the-art and the current knowledge gap linked to the main challenges of MSPTPP technology. A review of existing solar collector models is provided to acknowledge the work that has already been done by other authors in CSP research. A short introduction to the specific Southern African context is provided at the end of the review.

1.2.1 Heat transfer fluids

HTFs play a key role in the development of CSP plants as they have to meet specific thermo-physical, safety and cost requirements. Among these requirements are a low lower temperature limitation to avoid freezing and a high upper temperature limit without the risk of thermal degradation. Others include high thermal conductivity, low viscosity and low corrosiveness. A high density and heat capacity enables use as a thermal storage medium (Heller, 2013). Low toxicity, flammability, explosiveness and environmental hazard allow safer operation. Lastly, high availability can be reflected in a low price.

The state-of-the-art HTFs in commercial PTPPs across the world are thermal oils such as *Therminol® VP-1* or *Dowtherm™A*, which are used in almost all commercial PTPPs (NREL, 2020). These oils are a eutectic mixture of biphenyl and diphenyl oxide (Vignarooban *et al.*, 2015). However, their maximum operating temperature is limited to approximately 400 °C due to thermal degradation (Eastman, 2019). Other disadvantages include high costs of 5.15 $/kg (Kurup and Turchi, 2015), flammability and a high vapour pressure of approximately 10 bar at 390 °C (Raade and Padowitz, 2011). This makes it technically infeasible to use them as a TES medium, hence indirect storage with a thermal energy transfer to a second HTF is necessary (linked to additional costs for an extra heat exchanger). Some power plants also use water for direct steam generation but the high operating pressure is a limiting factor especially in the receiver equipment, particularly the couplings. Furthermore, TES is only possible for a short period of time when using live steam (~30 min).

Molten salts, on the other hand, are a suitable alternative HTF due to their good heat transfer qualities at high temperatures and the absence of phase-change within the typical operating temperature range. Vignarooban *et al.* (2015) reviewed the current status of HTFs and concluded that molten salts are the most favourable ones due to their relatively low melting point and high thermal stability limit (Figure 1.2). The most commonly used salt mixtures for CSP plant simulations used in literature are a binary nitrate salt, commonly known as *Solar Salt*, and a ternary nitrite salt, *Hitec® Heat Transfer Salt*, commonly known as *Hitec*. However, the overwhelming majority of commercial CSP plants relies on Solar Salt as HTF. Solar Salt and Hitec were also the HTFs and TES media used in the first CSP pilot CR plants Molten-Salt Electric Experiment (1 MW; Solar Salt), THEMIS (2.5 MW; Hitec) and Solar Two (10 MW; Solar Salt) (Reilly and Kolb, 2001). Solar Salt is also used as HTF at the Archimede combined cycle power plant in Priolo Gargallo, Italy. The solar field is used to produce steam (at an electric equivalent of 5 MW) for a combined cycle steam turbine[4] (Consoli, 2012). It was the first parabolic trough solar field using molten salt as HTF entering commercial operation. It uses *Archimede Solar Energy*'s receiver tube, named *Heat Collection Element for Molten Salt-11* (HCEMS-11), which was specifically developed for high

[4] In addition to two closed cycle gas turbines with 380 MW each (Consoli, 2012).

temperature applications using molten salt (Archimede Solar Energy, 2017). Solar Salt is non-toxic, non-flammable and has a low vapour pressure. It has a melting point of 220 °C and a thermal stability limit of 600 °C.

Hitec is mainly used for lower temperature applications and has a melting point of 142 °C. However, it has not yet been used in commercial power plants (Xu *et al.*, 2016). Although the maximum recommended operating temperature of Hitec is 538 °C, the manufacturer, Coastal Chemical Co. (n.d.), recommends a maximum temperature of 454 °C for long period operation to avoid thermal breakdown of the nitrite to nitrate. Thus, the maximum practical operating temperature of Hitec is assumed to be 450 °C. Additionally, the salt can react with oxygen in the storage tanks, leading to a conversion from nitrite to nitrate, which causes its freezing point to rise (Kearney *et al.*, 2003). A nitrogen (N_2) cover gas is therefore needed to avoid this reaction.

Another molten salt commonly used in literature is *Hitec® XL*, a ternary calcium nitrate salt with a low melting point of 120 °C, which can be used up to 500 °C. However, Hitec XL has been discarded as a candidate for commercial use in high-temperature applications due to NO_x off-gassing in a temperature range of 450 °C to 465 °C (Grogan, 2013). Hence, the maximum operating temperature for Hitec XL has been limited to 450 °C in this study. More detailed information on the composition and thermo-physical properties of the above mentioned salt mixtures is provided in section 2.3.8.

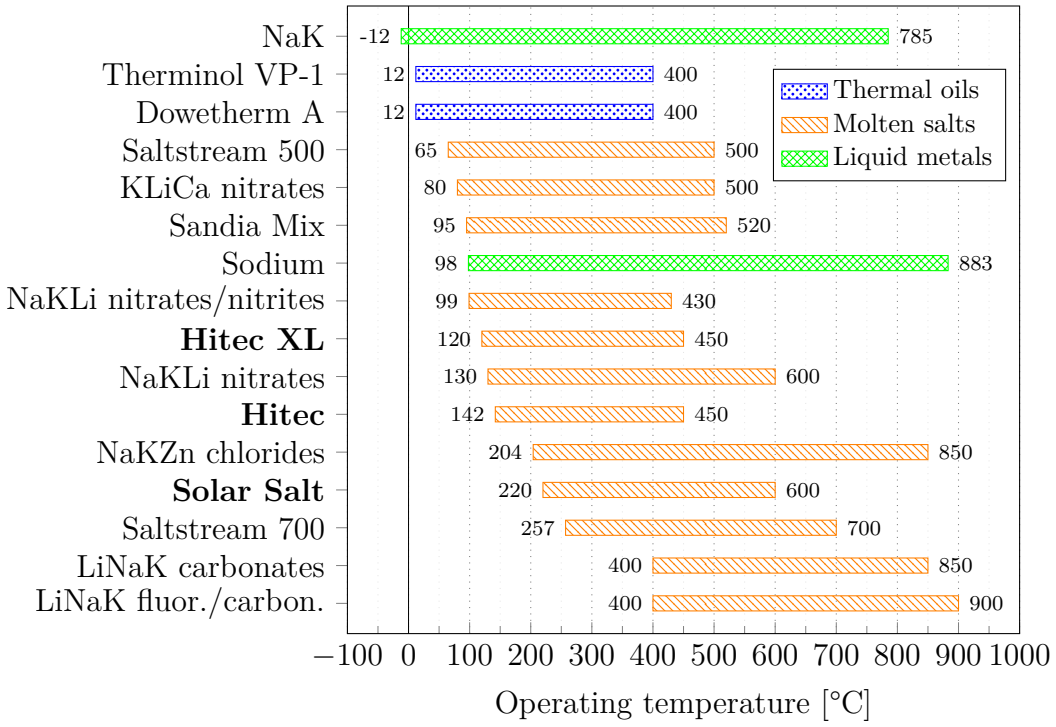

Figure 1.2: Operating temperature ranges of commonly used HTFs (Eastman, 2019; Vignarooban *et al.*, 2015; Dow, 2001; Bradshaw and Siegel, 2008; SQM, 2017).

Bradshaw and Brosseau (2008) developed a molten salt mixture, known as *Sandia Mix*, with a freezing point below 95 °C and a thermal stability limit of ~520 °C. One of its constituents, lithium nitrate, can be converted from lithium carbonate with nitric acid (Bradshaw and Siegel, 2008). The price of lithium carbonate, however, has doubled since 2006 (OilPrice.com, 2016) due to high demand for lithium batteries and is now 6.5 $/kg (Mehos *et al.*, 2017).

Other molten salt candidates include NaKLi nitrate/nitrites, KLiCa nitrates and NaKLi nitrates/nitrites, LiNaK carbonates, LiNaK fluorides/carbonates and NaKZn chlorides. These salts generally offer a wider operating temperature range and maximum temperature limits of up to 900 °C (Figure 1.2). However, they are still under development so further tests and material analyses are needed to determine their suitability as a HTF in PTPPs. Hence, this study will focus on commercial salts with available operational experience and cost data, such as Solar Salt, Hitec and Hitec XL.

Advantages of molten salts as heat transfer fluid

The stability limit of the most commonly used molten salt, Solar Salt, is 600 °C. The higher operating temperature of up to 570 °C and live steam pressures from 82 bar to 290 bar with Solar Salt increase the Rankine cycle efficiency (wet-cooled) well above the 40 % range (Richert *et al.*, 2015) compared to 393 °C and 66 bar with synthetic oils with a cycle efficiency of 37.6 % (Kearney *et al.*, 2003). According to Lenzen (2014), a cycle efficiency of 45 % is possible at 550 °C and 150 bar (wet-cooled).

Raade and Padowitz (2011) state that the low viscosity of molten salts makes them suitable for pumping at high temperatures and the corrosiveness of some salts (e.g. Solar Salt, Hitec and Hitec XL) can be accommodated to some extend with common stainless steels. The high density and heat capacity of molten salts enables direct TES at relatively low costs. i.e. 0.8 $/kg in the case of Solar Salt (Turchi *et al.*, 2019). The overall TES costs also drop when compared to power plants with oil as HTF due to the omission of the additional oil-to-salt heat exchanger. Furthermore, Kearney *et al.* (2003) state that the necessary physical TES size is reduced by using molten salt as HTF due to the higher temperature difference that allows storing two to three times the energy in the same amount of salt as compared to an indirect system. Thus, TES costs drop by up to 65 % compared to, for example, PTPPs using Therminol VP-1 as HTF in combination with a molten salt TES.

Reilly and Kolb (2001) summarised the results of the Solar Two project (central receiver) where molten salt was used as HTF and storage medium. Solar Two was a 10 MW test and demonstration facility, which successfully demonstrated that molten salt can be efficiently used as a low-cost TES as opposed to more expensive thermal oil that is furthermore constrained by its lower maximum operating temperature. Further operational experience with

molten salt as HTF and storage medium has been gained at the well-known Gemasolar CR plant in Seville, Spain.

The first stand-alone MSPTPP has been built by Archimede Solar Energy in Massa Martana, Italy, as a demonstration plant for their molten salt receivers (HCEMS-11). Maccari *et al.* (2016) reviewed the first two years of operation and concluded that MSPTPP technology is a viable option for utility scale CSP plants if the peculiarities of molten salts are taken into account.

Challenges of molten salts as HTF

The biggest drawback of molten salts, however, is their relatively high freezing point of e.g. 120 °C and 220 °C for Hitec and Solar Salt, respectively. This imposes new challenges to the safe operation of the solar field and leads to significant operation and maintenance challenges. Additional equipment like insulation and heat tracing is necessary to prevent freezing of the salt in the pipes and innovative FP concepts are required (see section 1.2.2). Furthermore, the high operating temperatures enabled by molten salts lead to increased corrosiveness of the HTF which requires a re-design of the solar field piping and especially of the rotary joints (and its seals). The increased temperatures during operation also affect the thermal expansion of the pipes, requiring more expansion loops in the hot runner and header piping. The thermal expansion of the receiver tubes can be managed by using flexible hoses in combination with rotary joints instead of the typically used ball joint assemblies in PTPPs using thermal oil. According to Abengoa Solar (2013), the ball joint seals are not compatible with molten salts at temperatures above 500 °C due to leaking and oxidation of the graphite seal. Caution is also necessary during preheating of the piping before filling it with salt (i.e. for the first filling or during maintenance work on individual loops) in order to avoid thermal stresses.

Kearney *et al.* (2003) note that more expensive equipment is required in the HTF system due to higher operating temperatures, e.g. using high-temperature resistant materials for piping and fittings. The high operating temperatures also lead to high heat losses in the solar field. A 55 MW plant for example can have heat losses of 10.7 MW_{th} overnight (assuming heat losses of 25 W/m^2). The heat loss has to be recovered by putting energy back into the system, which can be done through a gas-fired heater (linked to additional operating costs and CO_2 emissions), electric heat tracing or recirculating HTF from the *cold tank* (CT).

The current most commonly used salt mixtures are based on sodium and potassium nitrates and nitrites. However, the worldwide nitrate salt production is limited. In order to meet the *International Energy Agency*'s (IEA) target of 630 GW of CSP by 2050, the required amount of nitrate salts would represent 30 times the Chilean mine production capacity (Guillot *et al.*, 2012). The limited resources of some salt components are crucial for an economic molten salt candidate (e.g. conflict of interest with the growing battery indus-

try) and HTFs made from cheaper and earth abundant materials are being investigated (Xu *et al.*, 2016). In order to reduce the extraction of nitrate and nitrite salts from the earth's crust, the German company BASF produces their sodium nitrate and nitrite synthetically (BASF, 2020). This process also increases the salts purity, resulting in a low chloride content and therefore lower corrosiveness.

1.2.2 Freeze protection and draining systems

Due to the high melting point of molten salt, it is necessary to prevent the fluid from freezing in the receiver to avoid damage of the glass envelope (loss of vacuum). Several concepts for FP were identified in literature and are discussed here. Kearney *et al.* (2003) and Poole (2017) investigated the feasibility of molten salt as HTF and storage medium in a parabolic trough solar field. The fluid is pumped into the *hot tank* (HT) during normal operation as long as its temperature is above a certain set point (e.g. 525 °C). Once the solar field outlet temperature drops below this value, the HTF is redirected into the cold tank, resulting in an increase of the average fluid temperature in the tank to approximately 300 °C to 320 °C. At night, the fluid is pumped from the cold tank through the solar field and recirculated back to the cold tank at a flow rate of 4 kg/s for routine FP. This relatively high flow rate ensures that the piping and valves are kept warm throughout the night. The return temperature of the fluid then drops to approximately 285 °C by the time the sun rises again and the initially low solar flux can be used to heat the now cooler fluid in the cold tank back up to its design temperature of 290 °C. According to Kearney *et al.* (2003), a 6 h TES capacity is sufficient for 4.6 days of FP of a 55 MW plant. An auxiliary heater is used if the HTF temperature falls below a certain set point. In this case, it was 150 °C for Hitec XL. Electric heat tracing of the *heat collection elements* (HCE) for solar field preheating is necessary to avoid transient thermal stresses before filling or for thawing the frozen salt in case of a failure. For collector loop maintenance, the researchers suggest draining the entire loop to a heated service truck while trace heating the HCE.

Seubert *et al.* (2015) analysed various operation options for FP by using residual heat from a thermocline storage. Depending on the configuration, the charge or discharge pump of the storage can be used. The researchers found that annual fossil energy savings of up to 48 % are possible compared to a FP system operated purely by a backup heater.

BASF follows a different approach by using the drainage tank of the solar field for mixing and recirculation (Hinrichs *et al.*, 2016). This allows the solar field outlet temperature to fall below the cold storage temperature and reduces the discharging of the storage tanks. The result is an LCOE reduction of 1.8 % compared to the reference scenario with circulation of HTF from the cold tank (Hinrichs *et al.*, 2016).

Morin *et al.* (2015) demonstrated night circulation without impedance heating in a 550 m long linear Fresnel demonstration test loop built by Novatec and BASF by successfully circulating molten salt (Hitec) for over 24 hours. They also performed six freeze-thaw tests without encountering problems or failures. Draining tests were successful as well and showed little influence of the impedance heating current on the draining duration. The receivers were drained by gravity and residual molten salt was removed by pressurised N_2.

Total draining of the solar field for maintenance or following a major fault without heat tracing can be critical in order to avoid freezing of the salt. Falchetta and Rossi (2014) suggest draining the molten salt by closing the inlet and outlet valves of each loop and then open two draining valves at the header lines. Vent valves in the middle of every loop will open automatically when the internal pressure drops below ambient pressure, allowing the HTF to drain by gravity. A total drain of the whole solar field lasts one hour. However, the freeze limit of the HTF would be reached within a few minutes in some collectors, making heat trace equipment still necessary in the case of unfavourable conditions.

In order to completely avoid the trace heating requirement in the solar field, Eickhoff *et al.* (2016) propose an operating strategy of daily drainage in the evening. The HTF is drained into an underground drainage tank by gravity and supported by compressed air (within 15-20 min). The header and connection lines are kept hot through a heat tracing system using heat from the TES. The heat in these lines is used before sunrise to preheat the collector inlet and outlet lines by an air blower. The absorber tubes are then preheated using the morning sun and the molten salt can be filled from the storage tank. The main advantage of this concept is that even in a blackout situation when all backup measures fail, the field can still be drained by gravity. This operating strategy results in 12 % more thermal energy production in the solar field and about 5 % cost reduction.

Lastly, Kolb *et al.* (2010) conducted a series of freeze and thaw tests of molten salt in HCEs and showed that thawing after a freeze-accident does not lead to damage if the HCEs are not completely filled. Iverson *et al.* (2011), Maccari *et al.* (2015) and Morin *et al.* (2015) performed similar tests and concluded that recovery of the solar field without any damage is possible after a freezing accident.

1.2.3 MSPTPP modelling and simulation

A detailed literature review on simulation of PTPPs using molten salt as HTF showed that several models have been developed to estimate the energy yield and efficiencies as well as financial performance of such systems (mostly compared to PTPPs with oil as HTF). However, most of the studies employ pseudo-steady-state models and do not take transient and continuous

changes in operational conditions into account. Nevertheless, these transient effects have to be accounted for in detailed simulations due to their impact on the power plant efficiency.

The main goal of most studies is to show the reduction in LCOE by using molten salts as HTF compared to thermal oil or the difference between various molten salt mixtures. Dersch *et al.* (2014) calculated LCOE reductions of approximately 12 % for a solar-only MSPTPP with storage in comparison to a hybrid thermal oil plant without storage but comprising of a gas-fired booster. This can mainly be attributed to the higher *power block* (PB) efficiency and the addition of a TES system, as well as the solar-only operating strategy without any fossil fuel consumption. Ruegamer *et al.* (2014) estimate that switching from thermal oil to molten salt as HTF results in an LCOE reduction of 20 %. They found that a further reduction by 10 % is possible when doubling the installed capacity. Different salt mixtures only account for 3 % to 5 % in LCOE reduction which, however, is still considered significant.

Sau *et al.* (2016) compared a binary salt mixture with a ternary salt mixture. Both plants used the binary mixture as storage medium. They concluded that the ternary mixture reduces heat losses because of the lower average temperature in the solar field. However, the financial benefit under their assumptions are practically the same, which would prefer the binary mixture in reality due to the lower costs of the HTF and omission of an additional heat exchanger, allowing for better manageability in the case of the binary mixture.

Boukelia *et al.* (2015*c*) compared a 50 MW PTPP with 7.5 hours TES using Solar Salt to one using Therminol VP-1. The results showed an LCOE reduction of 16.4 % and a thermal efficiency increase of the power block of 10.3 %. The effect of TES and fuel backup heater on the energy and exergy efficiency in a PTPP using molten salt as HTF compared to oil has been studied in Boukelia *et al.* (2015*a*). The annual solar-to-electric efficiency of a plant using thermal oil as HTF is 17.52 % compared to 18.28 % with molten salt (both plants without TES and fuel backup). If the plants have an integrated TES and fuel backup, the efficiency increases to 17.69 % and 18.48 %, respectively. The researchers concluded that the energy and exergy efficiency is higher and the LCOE lower for molten salt plants with both TES and fuel backup. However, their environmental impact is larger than that of the other configurations without TES or fuel backup due to the higher CO_2 emissions of the gas burner.

Wagner (2012) developed a quasi-steady parabolic trough model with molten salt as HTF with a 10 hour TES in *EBSILON® Professional*. He compared the transient solar field start-up behaviour to a stationary model and concluded that the more detailed transient model has a higher thermal storage mass that affects the solar field temperature, power block efficiency, solar field parasitics and auxiliary heater energy input. This underlines the importance of modelling transient system effects in order to accurately predict the power plant's performance and their impact on different operating strategies. However, a validation of the model with measurement data from test facilities is

necessary.

Some researchers also focus on the hybridisation of thermal oil and molten salt as HTF by having a dual solar field with a low temperature field and a high temperature field. Vogel *et al.* (2015) propose to add a molten salt solar field to a thermal oil field as a live steam temperature booster (super-heating and reheating). Giostri *et al.* (2012) analysed a DSG solar field for steam evaporation combined with a second field with thermal oil or molten salt for steam super-heating and reheating. However, the benefits of a TES integration in a direct MSPTPP have not been accounted for and could improve the annual overall efficiency as suggested by Boukelia *et al.* (2015*a*).

It has to be noted that in addition to the aforementioned studies that specifically deal with the possible reduction of LCOE and increase of power plant efficiency, numerous other studies can be found in literature that use models of parabolic trough collectors for, amongst others, control design studies, performance yield analyses, component design applications or comparative analyses of different technologies.

In terms of parabolic trough collector modelling specifically, numerous models have been proposed for different purposes, which will be presented hereinafter. Firstly, zero and one-dimensional steady-state models have been developed for use in quasi-stationary performance analyses of PTPPs. Edenburn (1976) presented a one-dimensional model with a division of the absorber tube into segments using the finite difference method. The energy balance in each absorber tube section has been modelled through detailed heat transfer equations but neglecting the heat capacity of the absorber tube and glass envelope.

A zero-dimensional solar collector model has been developed by Lippke (1995) to analyse the part-load behaviour of a 30 MW SEGS plant in Kramer Junction, California, using empirical performance equations derived from performance tests conducted by Sandia National Laboratories (Dudley *et al.*, 1994). The same steady-state model has been used as the basis for the parabolic trough model in the *Transient System Simulation Tool* (TRNSYS) as part of the *Solar Thermal Electric Components* (STEC) library developed by Pitz-Paal and Jones (1998). This model has been used by Jones *et al.* (2001) to simulate the transient behaviour of the SEGS plants with a 5 minute time step leading to errors of less than 10 %. The collector performance equations of the SEGS plants, derived by Dudley *et al.* (1994) with thermal oil as the working fluid, have been used by Odeh *et al.* (1998) to formulate a heat loss model based on the absorber tube outer surface temperature instead of the fluid's bulk temperature. By doing so, the collector's performance can be estimated for any HTF, in this case water/steam for DSG.

Forristall (2003) developed and validated a detailed one-dimensional steady-sate solar receiver model using a thermal resistance model and considering the conductive, convective and radiative heat transfer of the fluid, the absorber tube and the glass envelope. In order to also incorporate the non-linear

temperature distribution along a HCE, Forristall discretised the receiver into finite segments and applied the previously presented one-dimensional energy balance to each segment assuming a linear temperature distribution across each division, thus obtaining a two-dimensional model. In order to reduce the computational effort associated with solving the receiver's system of equations at each time step, Patnode (2006) developed a zero-dimensional parabolic trough collector model, where the heat losses are modelled through linear regression based on Forristall's detailed heat transfer analysis. The model estimates the receiver heat loss as a function of bulk fluid temperature and DNI. The longitudinal discretisation approach presented by Forristall (2003) has also been used by Larraín *et al.* (2010) to model a DSG PTPP in northern Chile, using the heat loss correlation developed by Odeh *et al.* (1998). A one-dimensional steady-state parabolic trough collector model has been developed by Manzolini *et al.* (2011) for performance predictions and preliminary plant sizing under nominal operating conditions, using the HCE energy balance developed by Forristall (2003).

Secondly, dynamic lumped one-dimensional models or two-dimensional models using a longitudinal discretisation of the receiver tube are mainly used for transient performance simulations and control design studies. Llorente García *et al.* (2011) developed a transient parabolic trough collector model in Modelica, using an empirical heat loss correlation for the receiver tubes and applying a discretisation of the collector loop into four sections. A linear and discrete approximation of the energy balance has been assumed to simplify the governing differential equations. For this iterative modelling approach, a time step of 10 s was necessary for the model to be valid. In contrast, Spelling *et al.* (2012) presented a parabolic trough collector model with a discretisation into 40 nodes using the finite difference method. This implicit modelling approach allows numerical stability for time steps greater than 5 min. The receiver model was based on the approach presented by Stuetzle *et al.* (2004) using a series of coupled differential equations, i.e. for the fluid, the absorber tube and the glass envelope.

Wagner (2012) used the parabolic trough collector model from the EBSILON® Professional solar library, which was developed in collaboration with the *German Aerospace Centre* (DLR), in order to perform an annual performance evaluation of a MSPTPP (see above). The transient model uses a longitudinal discretisation of the receiver tube and an empirical heat loss correlation of the HCE based on the absorber tube surface temperature, which was derived by Burkholder and Kutscher (2009) based on tests performed at the *National Renewable Energy Laboratory* (NREL). Although the absorber tube wall thickness has been neglected for the heat transfer into the HTF, the transient behaviour of the solar field has been modelled through a two-dimensional Fourier differential equation assuming circumferential symmetry of the pipe.

The same two-dimensional modelling approach presented by Forristall

(2003) has also been used by Zaversky *et al.* (2013), implemented in Modelica, for the transient performance simulation of parabolic trough collectors using molten salt as HTF. The model has been validated with measurement data from the SOLTERM molten salt test loop in Casaccia, Italy, and an analysis of different levels of discretisation has been performed in order to propose a suitable spatial resolution for performance simulations and control design studies. In order to simplify the heat loss calculation from the receiver tube, Zaversky *et al.* recommend the usage of an empirically derived equation to estimate the heat losses "based on the temperature difference between the outer absorber tube surface temperature and the ambient air and the sky temperature" (Zaversky *et al.*, 2013).

Similarly to the model developed by Zaversky *et al.*, a transient one-dimensional parabolic trough receiver model using the staggered grid approach for the finite volume method has also been presented by Xu *et al.* (2019). This model has been used to evaluate the response delay of the HTF outlet temperature to a step change of the DNI through a comparison of thermal oil with molten salt as HTF. An exponential correlation of the response delay for both fluids had then been derived as a function of mass flow rate and DNI.

Yang *et al.* (2019) presented a hybrid DSG and molten salt solar field by discretising the loop into 6000 control volumes. The receiver model considers conductive and convective heat transfer phenomena for the absorption of the solar energy into the HTF and uses an empirical correlation for the heat loss based on the absorber tube surface temperature and neglecting ambient conditions.

Lastly, three-dimensional collector models can be used for component design and optimisation using a high spatial resolution that enables an extensive heat transfer analysis. Detailed three-dimensional models can, for example, be found in the works of Cheng *et al.* (2010), Wu *et al.* (2014) and Chang *et al.* (2018). These models are mainly used to obtain a better understanding of the temperature profile in the radial and axial direction of the receiver tube depending on the DNI and flow rate or for the design and optimisation of parabolic trough receivers by improving the heat transfer, e.g. through the insertion of rods into the absorber tube (see for example Chang *et al.*, 2018). However, these models lie beyond the scope of this study and will therefore not further be discussed.

1.2.4 Operating strategies of CSP plants

Several studies were conducted to analyse different operating strategies in order to improve the power plant efficiency as well as to fulfil a certain operational objective. The most basic strategy is the so-called solar-driven strategy. It is used to generate electricity whenever the solar irradiation and TES allow operation of the power block. Weather forecasts can help to predict if the

start or stop of the steam turbine is reasonable and to manage the times of operation.

The first research on the influence of different operating strategies on a CSP plant was conducted by Lippke (1997), who optimised the solar field operating temperature for part-load operation of the SEGS plants. Cerni and Price (1997) added weather forecasts to set up daily operating schedules. Wittmann *et al.* (2008) analysed optimised operating strategies based on irradiance forecasts during a clear and overcast day as well as in an aerosol-charged situation. In order to increase the revenue of CSP plants with TES in the Spanish electricity market, Wittmann *et al.* (2011) proposed an optimisation methodology based on meteorological forecasts for a day-ahead market. Wagner and Wittmann (2014) analysed the influence of a solar-driven, fixed and dynamic operating strategy with an integrated daily weather forecast on the annual electricity production by varying the hot tank fill level and power block start-up threshold. The influence of different operating objectives on the annual gas consumption of the auxiliary heater was studied by García-Barberena *et al.* (2012). Depending on the operating objective, the electricity production differs by more than 10 %, whereby the difference in gas consumption is up to 15 %.

García-Barberena and Erdocia (2016) showed the potential of well-designed operating strategies by reducing turbine stops by 67 % compared to a solar-driven strategy. At the same time, the power block operating hours increased by 57 %. However, the operating strategy was not optimised, leaving space for improvement. Biencinto *et al.* (2014) focused on the value of TES in order to improve the power plant performance and assessed charging and discharging strategies of a thermocline storage. Although the various strategies result in differences in annual yield, fossil fuel consumption and start-up time of the power block, the annual electricity yield is higher with a two-tank storage system. The value of TES in a solar thermal power plant and its impact on the operating strategy has also been investigated by Guédez *et al.* (2014*b*) and Guédez *et al.* (2015). They optimised the *internal rate of return* (IRR) and LCOE by varying the solar field and TES size for baseload and peaking strategies. The same strategies were also used to analyse the influence of different remuneration structures (e.g. fixed tariff, two-tier tariff or pool price tariff) on the IRR of a project.

Lastly, Dinter and Möller (2016) suggest that a reduction in maintenance time and an improved start-up procedure offer potential for optimisation after reviewing operational data from Andasol 3. This emphasises the need for a transient power plant model that reproduces the start-up procedure more accurately and allows a more detailed investigation.

1.2.5 Southern African context

Southern Africa has an exceptionally high solar resource, being the second highest in the world (after Chile). The annual DNI in South Africa and Namibia can reach peak values well above 3200 kWh/m^2 (Solargis, 2019). The highest yearly solar irradiation can be found in the southwest of Namibia and the Northern Cape Province of South Africa. All current operational and planned CSP projects under the *Renewable Energy Independent Power Producer Procurement Program* (REIPPPP) are located in the latter.

South Africa

South Africa's renewable energy capacities targeted in the *Integrated Resource Plan* (IRP) for 2010 to 2030 are allocated through the REIPPPP (Department of Energy, 2013). This program foresees the allocation of renewable energy capacities through five bidding rounds, where *independent power producers* (IPP) can offer their bid tariff for a proposed CSP plant. So far, 6422 MW have been allocated, of which 600 MW were CSP projects (Department of Energy, 2019*b*). The REIPPPP also defines the tariff structure under which the power plants are remunerated. The first two *bid windows* (BW) received an average fixed tariff of 3930 ZAR/MWh and 3680 ZAR/MWh (Department of Energy, 2018), which corresponds to 296.8 $/MWh and 277.9 $/MWh, respectively[5]. The tariff for the last two bid windows was changed to a two-tier tariff structure where in BW3.5, a base tariff of 1990 ZAR/MWh (150.3 $/MWh) is paid for electricity generation from 5:00 to 16:30 and 21:30 to 22:00. During peak hours from 16:30 to 21:30, the tariff is inflated by 270 % to 5373 ZAR/MWh (405.8 $/MWh). During low demand hours between 22:00 and 5:00, the tariff is zero. The average CSP tariffs per bid window are shown in Figure 1.3 in comparison with the average tariffs for wind and PV. These different tariff

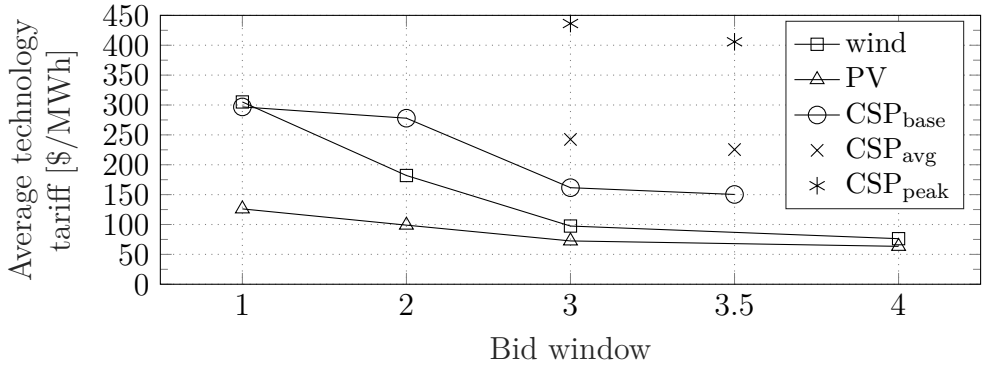

Figure 1.3: Average technology tariffs of REIPPPP bid windows as of December 2018 (Department of Energy, 2019*a*).

[5] Yearly average exchange rate of 13.242 ZAR/$ in 2018 (X-Rates, 2019*c*).

structures make it difficult to develop a CSP project and limit technological options and operating strategies. A fixed tariff for example encourages the project developer to implement TES to maximise revenue. The plant operator will then seek to keep the steam turbine running, hence acting as a baseload power plant. With a tariff structure that penalises night-time electricity generation, the plant operator will stop the steam turbine during those hours to save money and energy in the TES. This affects the governing operating strategy significantly and has to be taken into account when optimising the power plant for different operating objectives.

The latest IRP of 2019, however, does not foresee any allocation of CSP capacity in the last bid window (Department of Energy, 2019*b*), although several comments regarding the inclusion of CSP in the IRP have been submitted to the draft report by industry stakeholders and researchers. One of the main arguments of the comments in favour of CSP were that the cost assumptions for CSP used in the IRP were too high and that learning curves from international and domestic projects should be considered. Furthermore, unlike other renewable energy technologies, CSP is able to provide ancillary services and should also be allowed in the baseload, mid merit or peaking procurement programme in order to procure a solution and not a technology (Department of Energy, 2019*b*). The Department of Energy has noted the proposal for a technology agnostic bid window but did not yet release any plans in this regard.

Namibia

At the time of writing, Namibia does not have any CSP plants in operation or under construction, nor did it announce any official plans for their deployment. However, a pre-feasibility study to identify potential sites and suitable CSP technologies has been carried out by REEEI (2012). After conducting a nation-wide solar resource assessment, it was found that Namibia has a total potential for the development of 250 GW of CSP capacity. However, five sites have been identified that offer the highest short-term potential for CSP development, where parabolic trough and central receiver plants with storage capacities between 6 h and 8 h were proposed as the most feasible CSP technology options.

1.3 Motivation

PTPPs are the most mature CSP technology with low technical and financial risks. The next logical step would be to use the advantage of a long track record of operating experience of this technology and combine it with an HTF that has proven itself in several projects, i.e. molten salt. However, some of the operational issues linked to molten salts, like a high freezing point and heat losses in the solar field, remain a challenge and need further investigation. The

need for an energy-consuming FP system diminishes the advantages enabled by molten salts, such as a high power cycle temperature and thus efficiency and direct TES (two-tank or thermocline). These effects on the annual electricity yield have to be quantified in order to propose an optimal power plant configuration and operating strategy. The plant operator has a certain degree of freedom when operating a solar thermal power plant in order to fulfil a specific objective set by project stakeholders or legal requirements (maximise profits, avoid turbine stops, provide capacity when required by the grid, minimise CO_2 emissions). Depending on the remuneration conditions set by *power purchase agreements* (PPAs), the flexible use of TES is one of the most important options. Further options include the use of a fossil burner (for hybridisation or backup) or adjusting inlet and outlet temperatures of the solar field. Hence, models that allow flexibility in terms of plant configurations and cost models are needed for plant designers (developers) to assess the viability of a planned investment. A range of proposed power plant configurations and operational parameter set points for different operating objectives and financial framework conditions will shed light on their effect on technical and economic performance indicators.

For this reason, studies dealing with the analysis of various operational objectives and the effect of component designs and operational parameter set points on the technical and economic power plant performance are needed in order to provide a tool that allows the recommendation of optimal power plant configurations under location-tailored economic boundary conditions. As such, in order to further reduce the LCOE of MSPTPPs, one possibility is through a multi-objective optimisation, where design variables and operational parameters can be determined that lead to an optimised financial feasibility of molten salt PTPPs for various operating objectives.

Furthermore, the reported values for the LCOE in the studies mentioned above vary greatly between 15.9 \$/MWh and approximately 236 \$/MWh depending on the location and assumptions of system and component size. The proposed study will focus on a Southern African context, which has not yet been investigated in literature, by presenting optimised LCOEs for a range of system sizes and configurations based on various operating objectives. Therefore, a project developer or plant operator can easily identify the optimal solution for an anticipated power plant based on the intended objective, e.g. produce cheap electricity, maximise IRR, minimise investment costs, etc.

This dissertation aims to better understand the technical and economic feasibility of MSPTPPs in Southern Africa and to provide support in the decision making process of plant operators, project developers and policy makers, as well as to promote research in the field. A technical and economic assessment of key design parameters will derive a range of component sizes and operational parameter set points that lead to an optimised financial feasibility of MSPTPPs. Furthermore, the potential of using molten salts in PTPPs will highlight possible development opportunities and research paths, overall

increasing the competitiveness of CSP. Presuming that this is in fact the case, the ultimate goal of the study is to promote the feasibility of MSPTPPs and encourage research and development specifically in Southern Africa.

1.4 Objectives

This study aims to answer two major research questions:

i. What impact does the type of HTF, operating strategy and freeze protection strategy have on the energetic performance and financial indicators of MSPTPPs within a Southern African context?

ii. What power plant configurations, operating strategies and tariff structures lead to an optimised financial viability of MSPTPPs within a Southern African context?

The original contribution of this research is to supply the CSP industry, policy makers and researchers with insight into the technological advantages and potential cost reductions of MSPTPPs. This insight will be in the form of a review of the influence of different HTFs and operating strategies on power plant performance and economics. Component sizes and operational parameters that maximise the economic feasibility if MSPTPPs for different operating objectives are proposed. The insights gained in this study can be used by developers along the value chain of CSP projects for technical developments, pre-feasibility studies, planning and engineering, as well as by power plant operators to make plant-specific operational decisions. Policy makers and researchers can use the results to propose and develop new tariff structures, infrastructure expansions and innovative power plant concepts. This study also serves as a stepping-stone for further technological improvements and advanced operating strategies. The key objectives leading to results used to answer the research questions are:

- To develop a dynamic model of a MSPTPP and implement the possibility to select different HTFs, operating strategies and freeze protection strategies.
- To formulate an economic model with financial data specific to Southern Africa (South Africa and Namibia).
- To validate the model against real measurement data.
- To conduct a sensitivity analysis to assess the impact of key design variables on the technical and economic performance of MSPTPPs.
- To investigate different freeze protection strategies and to find their optimal parameters to maximise power plant performance.
- To analyse the influence of different HTFs, operating strategies and tariff structures on power plant performance.

- To propose power plant configurations and operating strategies that lead to a maximisation of financial feasibility through a multi-objective optimisation for different tariff structures.
- To propose a minimum required PPA tariff that allows a financially feasible operation of MSPTPPs in Southern Africa.
- To propose the lowest possible PPA tariff for baseload operation in South Africa assuming reduced financing costs.
- To investigate the feasibility of CSP plants to participate in the spot market in Southern Africa under the premise of reduced financing costs.
- To provide an outlook for the projected LCOE evolution of MSPTPPs in Southern Africa until 2050.

1.5 Methodology

The main work in this study is the development of a dynamic MSPTPP model that uses an empirical heat loss model for Archimede Solar Energy's HCEMS-11 receiver. Two different FP systems are implemented as well as the possibility to operate the power plant as a baseload or peaking plant under the consideration of different tariff structures. In order to validate the model, measurement data from a molten salt parabolic trough demonstration plant using the same receiver tubes is used. The model is validated by comparing the measured loop outlet temperature to the simulated loop outlet temperature for decreasing levels of discretisation and the induced error is calculated.

The power plant model is extended by an economic model that is tailored specifically to the financial boundary conditions in Southern Africa (with focus on South Africa and Namibia). A validation of the economic model is carried out by comparing the financial performance metrics of two existing power plants in South Africa with the results from the simulations.

A sensitivity analysis is carried out to assess the impact of key design variables on the technical and economic performance of the power plant. The model is then used to predict the annual power generation and technical and economic performance of power plants using various HTFs, operating strategies and freeze protection strategies as part of a multi-objective optimisation study. Based on the results, recommendations for power plant configurations, HTFs and parameter set points that lead to the best trade-off between costs and efficiency are deduced. Next, the minimum required PPA tariff of MSPTPPs in Southern Africa is calculated once under current financial boundary conditions and once assuming reduced financing costs. The feasibility of a participation on the spot market is then analysed, assuming reduced financing costs.

Finally, an outlook for the evolution of the LCOE in South Africa and Namibia until 2050 is made based on the results from the optimisation study using the learning curve approach.

Chapter 2

Molten Salt Parabolic Trough Power Plant Model[1]

In this chapter, a detailed MSPTPP model is developed. The following sections present the modelling approach and the tools used for the model implementation as well as the individual component models and their respective control logics. This study investigates the feasibility of CSP plants at two sites, namely, Upington in South Africa and Kokerboom in Namibia. These locations were selected due to their high solar resource with an annual direct normal irradiation in the range of 2800 to 2900 kWh/m^2. Furthermore, six CSP plants have already been built in the greater area near the town of Upington (within a radius of approximately 230 km), making it the CSP hub of South Africa. This area — and the Northern Cape in general — has been found to offer the highest technical potential for CSP plant development in South Africa due to the high solar irradiance, proximity to existing or planned transmission lines and water availability (Duvenhage, 2019). In the case of Kokerboom, this site has been identified as one of five potential locations for the construction of CSP plants in Namibia through a pre-feasibility study (REEEI, 2012). Although there are currently no CSP plants in Namibia, this location is suitable due to its proximity to the Kokerboom substation (400 kV/220 kV/132 kV/66 kV), which provides the possibility of a grid connection of potential power plants. An overview of the meteorological data for both locations is provided in Appendix A.

2.1 Modelling Tools

The MSPTPP model has been developed in the *Transient System Simulation Tool*, or TRNSYS (Klein *et al.*, 2017), which is a commercial software package for transient renewable energy system and building simulations that allows the

[1] Parts of this chapter have previously been published in Pan *et al.* (2018*a*) or submitted for publication (see Pan *et al.*, 2021).

user to create their own models, or so-called Types, written in *Fortran*. It has been developed at the Solar Energy Laboratory at the University of Wisconsin-Madison and features a dedicated model library for CSP, i.e. the STEC library (Schwarzbözl, 2006). TRNSYS used to be the basis for NREL's open-source simulation software *System Advisor Model* (SAM) (NREL, 2018) until 2013 and has been used extensively for performance simulations in the field of CSP as, for example, in the works of Jones *et al.* (2001), Guédez *et al.* (2014*b*), Biencinto *et al.* (2016) and Pan *et al.* (2018*b*). The schematic power plant layout modelled in TRNSYS is depicted in Figure 2.1 and each component is discussed in detail in the respective sections within this chapter.

The transient annual performance simulation and plant control are implemented in TRNSYS, whereas the power plant design, component sizing and optimisation is carried out using the *Dynamic Energy Systems Optimizer*

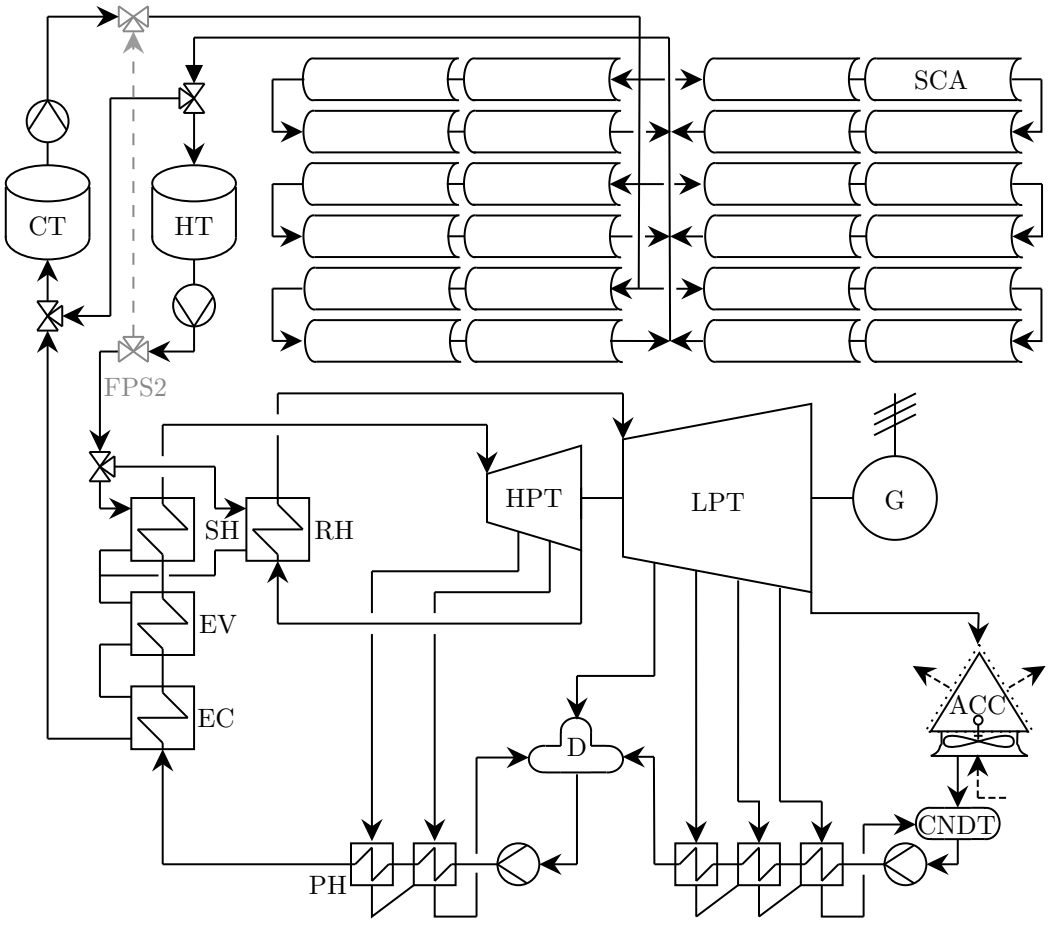

Figure 2.1: MSPTPP schematic layout[2].

[2] Legend: CT - cold tank; HT - hot tank; SCA - solar collector array; EC - economiser; EV - evaporator; SH - superheater; RH - reheater; HPT - high pressure turbine; LPT - low pressure turbine; G - generator; ACC - air-cooled condenser; CNDT - condenser tank; D - deaerator; PH - preheater; FPS2 - freeze protection strategy 2.

(DYESOPT). DYESOPT is a numerical tool developed at the Department of Energy Technology at KTH Royal Institute of Technology[3], which incorporates the location-tailored design and technical and economic performance evaluation of power plants. DYESOPT is implemented in *MATLAB* (The MathWorks Inc., 2017) and is coupled with a multi-objective optimisation algorithm, which allows the optimisation of multiple objective functions at the same time. This optimisation procedure will be presented in section 5.3.

Figure 2.2 shows the simplified schematic workflow of DYESOPT. The op-

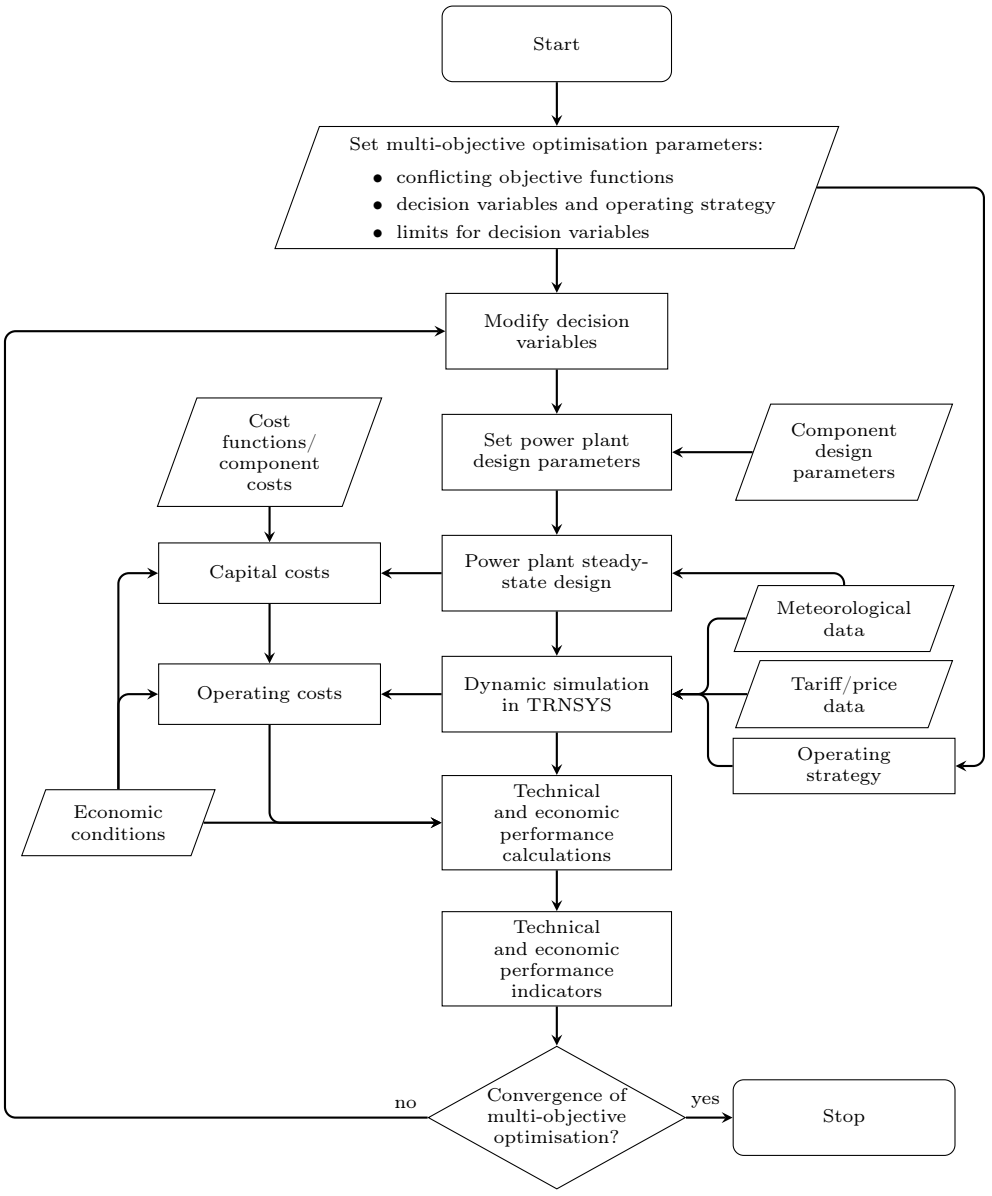

Figure 2.2: Simplified schematic of the DYESOPT workflow (adapted from Guédez *et al.*, 2016).

[3] See for example Spelling (2013), Guédez (2016) and Topel (2017).

timisation starts with setting the parameters for the multi-objective optimiser, i.e. defining the conflicting objective functions, decision variables and their limits as well as the operating strategy. These parameters will be discussed in detail in section 5.3. The optimiser sets the user-specified decision variables and modifies the relevant power plant design parameters. Using the component design parameters and meteorological data, the power plant steady-state design is carried out to size the power plant. Following the initial design process, the resulting component design parameters, meteorological data, tariff data, operating strategies and simulation-relevant boundary conditions are inputs for the technical model in TRNSYS, where an hourly or sub-hourly annual performance simulation is carried out. The results of this transient simulation are then sent back to DYESOPT for post-processing, which includes the computation of technical and economic performance indicators based on location-specific economic boundary conditions where the user can define cost functions and component costs for the economic model. Finally, DYESOPT generates new power plant designs based on the objective functions by modifying the decision variables and repeats the simulation process until the solution of the multi-objective optimisation converges. This process will be described in more detail in section 5.3. DYESOPT is also used for the sensitivity analysis in this study, which will be introduced in section 5.2.

2.2 Solar Collector

The following section describes the modelling of the parabolic trough collectors, which allows single-axis tracking of the sun and concentrates the incident DNI on the receiver tubes located at the focal point of the mirrors. This study uses the *Ultimate Trough*® collector (developed by *FLABEG GmbH*), which is one of the largest and most advanced collectors currently available on the market. Furthermore, this collector has been the subject of extensive research and cost analyses (e.g. by Riffelmann *et al.*, 2014; Richert *et al.*, 2015; Kurup and Turchi, 2015; Dieckmann *et al.*, 2017; Turchi *et al.*, 2019), which ensures the availability of reliable technical data and costs in literature. The Ultimate Trough collector is 245.3 m long and has an aperture width of 7.51 m (Riffelmann *et al.*, 2014). The net aperture area of the mirrors is 1715.92 m^2. The collector's geometry and optical parameters are provided in Table 2.1. In the case of the Ultimate Trough collector, four so-called *solar collector arrays* (SCA) are connected in series to form a loop. For simplicity, it is assumed that the modelling of only one loop is representative of the entire solar field by subsequently scaling it up to account for the actual number of installed loops in terms of mass flow rate and thermal power. Therefore, the outlet temperature is assumed to be equal for all loops in the solar field. The solar collector model requires the calculation of the incidence angle θ at any given location. This angle is calculated through the solar time based on a location's coordinates and time zone, which is then

Table 2.1: Ultimate Trough collector geometry and optical parameters (Riffelmann *et al.*, 2014).

Parameter	Variable	Unit	Value
Collector geometry			
SCA length	L_{coll}	[m]	245.3
Collector aperture width	w	[m]	7.51
Loop net aperture area	A_{coll}	[m^2]	1715.92
Average focal length	f_{avg}	[m]	2.51
Piping distance between assemblies	$L_{\text{SCA,gap}}$	[m]	1.5
Number of SCAs in a loop	N_{SCA}	[-]	4
Optical parameters			
Mirror reflectance	ρ_{coll}	[%]	94.0
Intercept factor (geometry defects)	γ_{coll}	[%]	99.2
Tracking efficiency	η_{track}	[%]	99.4
Cleanliness factor	cf_{coll}	[%]	97.0
Collector optical efficiency	$\eta_{\text{opt,0}}$	[%]	89.9

used to compute the solar angles at any given time (depending on the time step size). This calculation method is described in detail in Appendix B. The incidence angle can then be used to calculate the incident solar flux on the receiver tubes, which will be discussed in the following section.

2.2.1 Solar collector efficiency

The direct normal irradiance, or beam irradiance I_{b}, is concentrated by the mirrors of each SCA of aperture area (rectangular projected surface area of the reflective parabola) A_{coll} to the incident solar flux $\dot{q}_{\text{inc}}$ on the receivers with

$$\dot{q}_{\text{inc}} = I_{\text{b}} \cos(\theta) A_{\text{coll}} \eta_{\text{opt,coll}}, \tag{2.1}$$

where $\cos(\theta)$ accounts for the cosine effect losses of the incidence angle θ. The collector optical efficiency $\eta_{\text{opt,coll}}$ is calculated with Eq. (2.2) and includes the collector optical peak efficiency $\eta_{\text{opt,0}}$, shadowing losses η_{shadow}, end losses $\eta_{\text{end,loss}}$ and an empirical correlation for the *incidence angle modifier* (IAM) κ of the SCA, which is a function of the incidence angle θ. The incident solar flux on the collector is assumed to be equal for each SCA. The subsequent absorption of the reflected solar flux in the absorber tube will be discussed in section 2.3.3.

$$\eta_{\text{opt,coll}} = \eta_{\text{opt,0}} \kappa(\theta)\, \eta_{\text{end,loss}}(\theta) \eta_{\text{shadow}}(\theta). \tag{2.2}$$

The collector optical peak efficiency $\eta_{\text{opt,0}}$ accounts for the collector reflectance ρ_{coll}, the intercept factor γ_{coll}, the tracking error η_{track} and the cleanliness factor cf_{coll} and is calculated with Eq. (2.3). The respective values for the Ultimate

Trough collector can be found in Table 2.1 (Riffelmann *et al.*, 2014).

$$\eta_{\text{opt},0} = \rho_{\text{coll}} \gamma_{\text{coll}} \eta_{\text{track}} c f_{\text{coll}}. \tag{2.3}$$

The remaining factors in Eq. (2.2), i.e. the IAM, the end losses and gains as well as the collector shadowing, will be discussed hereafter.

2.2.2 Incidence angle modifier

The IAM describes the variation of performance of the solar collector depending on the incidence angle θ of the sun in relation to the collector's surface. It is an empirical factor that has to be obtained through measurement campaigns for a specific collector. The IAM of the Ultimate Trough collector can be calculated with

$$\kappa(\theta) = a_0 + a_1 \frac{\theta}{\cos(\theta)} + a_2 \frac{\theta^2}{\cos(\theta)}, \tag{2.4}$$

where θ is in radians. The empirical coefficients a_0, a_1 and a_2 of the Ultimate Trough collector were determined through efficiency measurements at FLABEG's demonstration loop over a period of four months (Riffelmann *et al.*, 2014). The respective values for Eq. (2.4) are listed in Table 2.2.

Table 2.2: IAM coefficients of the Ultimate Trough collector (Riffelmann *et al.*, 2014).

Coefficient	Unit	Value
a_0	[-]	1
a_1	[-]	-0.005
a_2	[-]	-0.102

2.2.3 End losses and gains

End losses occur at the end of each SCA whenever the solar irradiance is not perpendicular to the collector aperture area, resulting in a spillage loss as the solar irradiance is reflected past the receiver's end. However, since the end losses of some collectors are partially recovered by adjacent collectors, end gains have to be taken into account as well. The end losses are calculated for each SCA in a loop based on the equation from Lippke (1995) with

$$\eta_{\text{end,loss}}(\theta) = 1 - \frac{f_{\text{avg}} \tan(\theta)}{L_{\text{coll}}} + \eta_{\text{end,gain}}(\theta), \tag{2.5}$$

where L_{coll} is the total length of the collector and f_{avg} is the average focal length of the collector. The last term in Eq. (2.5) accounts for any end gains ($\eta_{\text{end,gain}}$), which is calculated with

$$\eta_{\text{end,gain}}(\theta) = \frac{f_{\text{avg}} \tan(\theta) - L_{\text{SCA,gap}}}{L_{\text{coll}}}, \tag{2.6}$$

where $L_{\text{SCA,gap}}$ is the piping distance between two SCAs. Assuming that the solar field is in the southern hemisphere, the end gain of a SCA equals zero when the SCAs are located at the northernmost end of a collector row (Wagner and Gilman, 2011). Hence, the end gain is zero for SCAs at the loop inlet and outlet for a collector row running in a southern direction from the header piping as well as for SCAs before and after the loop turn-around in case of a collector row running in a northern direction.

2.2.4 Collector shadowing

Collector shadowing generally occurs between adjacent rows during hours where the sun's position is low in the sky, i.e. dusk or dawn (Wagner and Gilman, 2011). The collector row closest to the sun casts a shadow on the collector row behind it and shades a part of its mirrors. The shadowing efficiency can be calculated with (Stuetzle, 2002)

$$\eta_{\text{shadow}}(\theta) = \frac{L_{\text{spacing}} \cos(\theta_z)}{w \cos(\theta)}, \tag{2.7}$$

where L_{spacing} is the spacing between each collector row, θ_z is the zenith angle of the sun (see Appendix B), w is the collector's aperture width and θ is the incidence angle. Collector shadowing can only effectively be reduced by increasing the row spacing since it is desirable to increase the collector aperture width as much as possible in order to maximise the reflective area of a collector.

2.3 Receiver

As previously mentioned, this study uses the Archimede Solar Energy HCEMS-11 receiver for high temperature applications using molten salts. The receiver's technical data is listed in Table 2.3. It consists of an absorber tube made of AISI 321 austenitic stainless steel (Poole, 2017) and an evacuated borosilicate glass envelope. Although the thermal stability limit of the absorber tube's selective coating is 600 °C, the rated thermal limit of the receiver is 550 °C (Archimede Solar Energy, 2017). Therefore, this temperature limit will also be considered as the upper limitation in this study.

2.3.1 Modelling approach

Following the one-dimensional fluid flow approach, which has already been used in studies by Edenburn (1976), Forristall (2003), Wagner and Gilman (2011) and Zaversky *et al.* (2013), the receiver model uses a longitudinal division of each SCA into finite volumes according to the *finite volume method* (FVM). This will be discussed in more detail in section 2.3.2. Each discrete

[4] For a density of 8000 kg/m^3 for AISI 321 (Aerospace Specification Metals, n.d.).

Table 2.3: HCEMS-11 receiver geometry and optical parameters (Archimede Solar Energy, 2017).

Parameter	Variable	Unit	Value
Receiver geometry			
Absorber tube inner diameter	d_2	[mm]	64
Absorber tube outer diameter	d_3	[mm]	70
Absorber tube length	L_{abs}	[m]	4.06
Absorber tube weight[4]	m_{abs}	[kg]	20.5
Absorber tube material	-	[-]	AISI 321
Glass envelope material	-	[-]	borosilicate glass
Thermal stability limit of selective coating	-	[°C]	600
Optical parameters			
Transmittance of glass envelope	τ_{glass}	[%]	96.5
Absorptance of absorber tube	α_{abs}	[%]	95.0
Active length of absorber tube	η_{bellow}	[%]	96.1
Cleanliness factor of glass tube	cf_{glass}	[%]	96.0
Receiver optical efficiency	$\eta_{\text{opt,rec}}$	[%]	84.6

volume has a central node with a representative bulk fluid velocity as well as an average bulk fluid temperature at which the fluid properties are evaluated (see section 2.3.8). The thermal capacitance of the HTF is also assumed to be lumped in this central node. As part of this modelling approach, the flow velocity profile of the HTF in the radial direction is assumed to be uniform and the longitudinal conduction heat transfer of the receiver tube and fluid are neglected. To further simplify the model, an empirical heat loss equation is used to estimate the heat loss of the receiver based on the absorber tube surface temperature and will be discussed in detail in section 2.3.4. As part of the receiver model, the conduction and convective heat transfer in the radial direction for each discrete volume are discussed in sections 2.3.5 and 2.3.6, respectively.

The modelling of the receiver was adapted from the method used in SAM developed by NREL (2018). For coherence, the following section describes the generic modelling approach used in SAM based on the *Technical Manual for the SAM Physical Trough Model* (Wagner and Gilman, 2011), which has been adapted to be specifically used with molten salts (i.e. modified operating strategies and convective heat transfer model) and extended by an empirical heat loss model. SAM uses a one-dimensional model developed by Forristall (2003) with a receiver energy balance as depicted in Figure 2.3a using an iterative approach to solve the system of equations for each temperature of the SCA in the radial direction. This model assumes one central node for the whole SCA, representing the average temperature of the HTF (T_1). However,

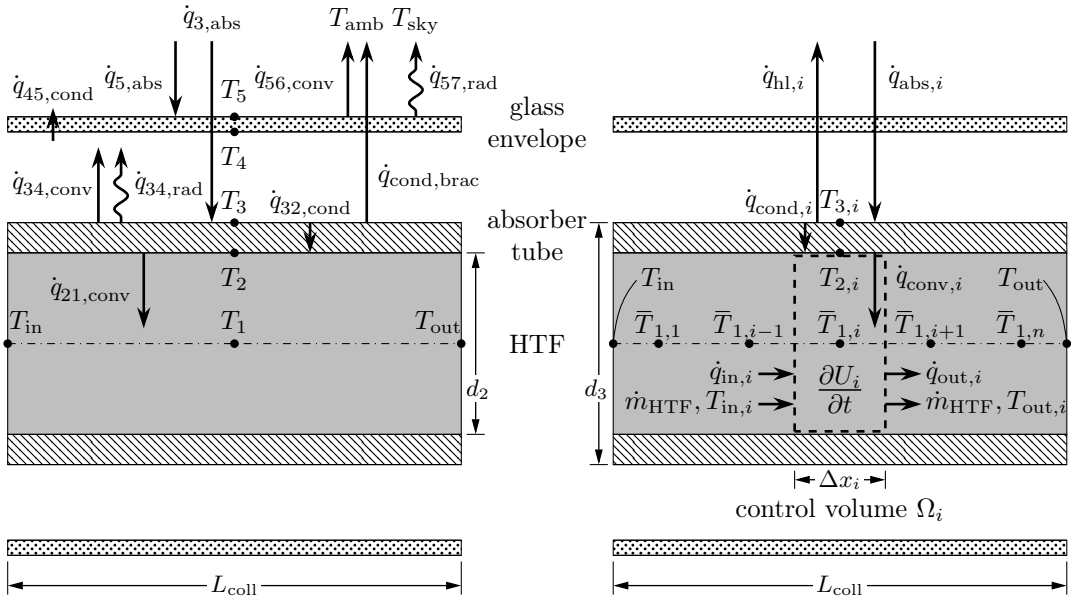

(a) One-dimensional model **(b)** Two-dimensional model

Figure 2.3: Energy balance for (a) a one-dimensional receiver model and (b) the simplified two-dimensional model with longitudinal discretisation into n CVs.

Forristall recommends a two-dimensional model with a division of the receiver into segments of equal length (longitudinal discretisation in flow direction) for higher accuracy. According to analyses conducted by Forristall, this approach also better represents the non-linear temperature distribution of the HTF along the receiver as opposed to the linear temperature changes obtained with the one-dimensional model. Nonetheless, using a two-dimensional model requires more computational effort and therefore time to solve, as the temperature of each receiver segment is iteratively evaluated. Hence, the required simulation time increases significantly with a reduction of the segment lengths.

2.3.2 Receiver energy balance

In order to maintain short simulation times without compromising a high degree of accuracy, this study introduces a simplified two-dimensional receiver model based on an empirical heat loss model, which relates the heat loss to the outer surface temperature of the absorber tube. This approach reduces the number of necessary iterative temperature and heat transfer evaluations by solely calculating the heat loss based on the absorber tube surface temperature, which allows the omission of the evaluation of the inner and outer surface temperature of the glass envelope (T_4 and T_5) and thus, reducing the number of iterations. Therefore, only the inner and outer absorber tube wall temperatures T_2 and T_3 have to be determined iteratively. Following this ap-

proach, Figure 2.4 shows the simplified one-dimensional radial energy balance of the receiver tube of a SCA with the absorbed heat transfer rate $\dot{q}_{\text{abs}}$ into the absorber tube, the convection heat transfer $\dot{q}_{\text{conv}}$ from the absorber tube wall to the HTF, the conduction heat transfer rate $\dot{q}_{\text{cond}}$ and the empirical receiver heat loss $\dot{q}_{\text{hl}}$.

The two-dimensional model (Figure 2.3b) is, in essence, a series of radial one-dimensional models (as depicted in Figure 2.4) connected in longitudinal direction as a result of applying the FVM, which will be discussed in detail in the following section. Starting from the approach of a one-dimensional model (Figure 2.3a), Wagner and Gilman (2011) define the energy balance of the HTF including the inlet heat transfer rate $\dot{q}_{\text{in}}$, the outlet heat transfer rate $\dot{q}_{\text{out}}$, the convection heat transfer rate $\dot{q}_{\text{conv}}$ from the absorber tube wall to the HTF and the change of internal energy $\partial U(t)/\partial t$ as

$$\frac{\partial U(t)}{\partial t} = \dot{q}_{\text{in}} + \dot{q}_{\text{conv}} - \dot{q}_{\text{out}}, \tag{2.8}$$

with

$$\dot{q}_{\text{out}} - \dot{q}_{\text{in}} = m_{\text{HTF}} c_{p,\text{HTF}} v \frac{\partial T(x)}{\partial x}, \tag{2.9}$$

where m_{HTF} is the HTF mass, $c_{p,\text{HTF}}$ the temperature-dependent specific heat capacity of the HTF and v the bulk flow velocity of the fluid. The derivative term represents the temperature gradient in the longitudinal direction of the receiver as a function of length x. Substituting Eq. (2.9) in Eq. (2.8) gives

$$\frac{\partial U(t)}{\partial t} + m_{\text{HTF}} c_{p,\text{HTF}} v \frac{\partial T(x)}{\partial x} = \dot{q}_{\text{conv}}. \tag{2.10}$$

However, simply continuing with this equation would not be sufficient as PTPPs incorporate large masses of HTF and piping, which need to be included to account for transient effects of the system's thermal inertia. Because the

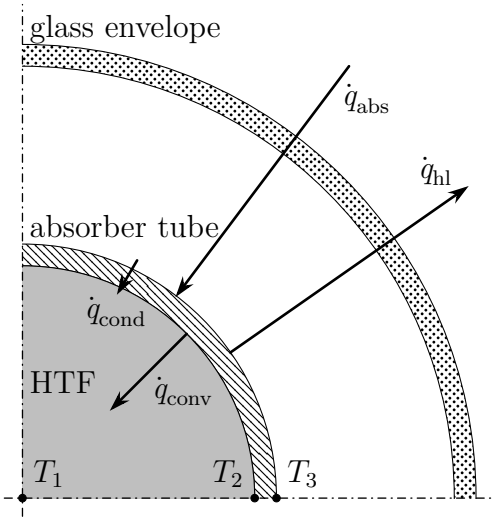

Figure 2.4: Simplified one-dimensional radial energy balance around the receiver.

absorber tube temperature is estimated to be close to the fluid bulk temperature and due to the relatively small ratio of steel mass to HTF mass, the thermal capacitance of the absorber tube is lumped together with the thermal capacitance of the HTF. This simplification is further justified by the low specific heat capacity of the absorber tube, where $c_{p,\text{tube}}\,(500\,^{\circ}\text{C}) = 536\,\text{J/(kg K)}$, compared to e.g. Solar Salt with $c_{p,\text{HTF}}\,(500\,^{\circ}\text{C}) = 1529\,\text{J/(kg K)}$, therefore reducing the effect of the steel piping on the overall thermal inertia of a loop by a factor of approximately 3. Hence, it is assumed that the temperature gradient of the absorber tube follows the temperature variation of the HTF. The assumption of a lumped capacitance model requires that the Biot number is less than 0.1, which results in a temperature difference between the surface and the centre of the tube of not more than 5 % (Mills, 1999). The validity of the lumped capacitance model will be discussed in section 2.3.6. Furthermore, the thermal inertia of the glass envelope can be neglected as it is thermally decoupled from the absorber tube by a vacuum. Hence, the change in internal energy of the HTF as a function of time t can be expressed as:

$$\frac{\partial U(t)}{\partial t} = \left(m_{\text{HTF}} c_{v,\text{HTF}} + m_{\text{tube}} c_{v,\text{tube}}\right) \frac{\partial T(t)}{\partial t}, \tag{2.11}$$

where m_{tube} and $c_{v,\text{tube}}$ are the mass and specific heat capacity of the absorber tube, respectively (Wagner and Gilman, 2011). However, assuming that the density and internal energy are only a function of temperature, both the HTF and the absorber tube are assumed to be incompressible substances and therefore,

$$c_v = c_p. \tag{2.12}$$

Substituting Eqs. (2.11) and (2.12) into Eq. (2.10) yields the governing first order *partial differential equation* (PDE)

$$\left(m_{\text{HTF}} c_{p,\text{HTF}} + m_{\text{tube}} c_{p,\text{tube}}\right) \frac{\partial T(x,t)}{\partial t} + m_{\text{HTF}} c_{p,\text{HTF}} v \frac{\partial T(x,t)}{\partial x} = \dot{q}_{\text{conv}}(x,t), \quad t \geq 0, \quad x \in [0, L_{\text{coll}}], \tag{2.13}$$

with boundary conditions

$$t = 0: \quad \frac{\partial T(t)}{\partial t} = 0, \tag{2.14}$$

$$x = 0: \quad \frac{\partial T(x)}{\partial x} = 0, \tag{2.15}$$

where L_{coll} is the length of a SCA. Hence, the temperature of the fluid is a function of the position x along the collector and progression of time t in dependence of the convection heat transfer rate. This PDE has also been used in studies by Camacho *et al.* (1997) and Zaversky *et al.* (2013). The first term on the left represents the change in temperature of the fluid over time due to the thermal inertia of the absorber tube steel and the fluid itself. Similarly, the second term on the left represents the change in temperature of the fluid along

the length x of the receiver and can be interpreted as a surface flux normal to the absorber tube cross section. Then, $m_{\text{HTF}} c_{p,\text{HTF}} v$ is the advection velocity of the flux. The term on the right is simply the convection heat transfer rate between the inner absorber tube wall and the fluid.

This PDE can be transformed into an *ordinary differential equation* (ODE) by applying the FVM in which a mesh is used to discretise the calculation domain into finite volumes, or *control volumes* (CV), and the solution of the desired variables are calculated at the centre of each discrete volume (vertex-centred). In this discretisation method, the volume integrals of the divergence in the CVs are converted to surface integrals of a tensor field by using the *divergence theorem* (Gauss's theorem) which are then evaluated as surface fluxes at the boundaries of each CV. Since equation (2.13) is in the form of the one-dimensional advection equation in which the properties of the fluid are carried with it from one CV to the next (conservation law), the surface flux entering a volume is equal to the surface flux exiting the previous volume. Hence, this method is *conservative*.

For the FVM, the spatial domain x is divided in the axial direction into n discrete volumes of equal length Δx_i as depicted in Figure 2.5 with

$$0 = x_{\frac{1}{2}} < x_{\frac{3}{2}} < \cdots < x_{n-\frac{1}{2}} < x_{n+\frac{1}{2}} = L_{\text{coll}}, \tag{2.16}$$

$$\Delta x_i = x_{i+\frac{1}{2}} - x_{i-\frac{1}{2}}. \tag{2.17}$$

Each control volume Ω_i is then given by

$$\Omega_i = \left[x_{i-\frac{1}{2}}, x_{i+\frac{1}{2}} \right], \tag{2.18}$$

with volume centre x_i:

$$x_i = \frac{x_{i-\frac{1}{2}} + x_{i+\frac{1}{2}}}{2}. \tag{2.19}$$

This discretisation is also depicted in Figure 2.3b with addition of the second dimension in the radial direction ($T_{2,i}$ and $T_{3,i}$). Hence, the absorber tube wall is also divided into n corresponding segments with inner and outer surface temperatures $T_{2,i}$ and $T_{3,i}$, respectively. Assuming a linear radial temperature distribution, the material properties of the absorber tube wall are evaluated

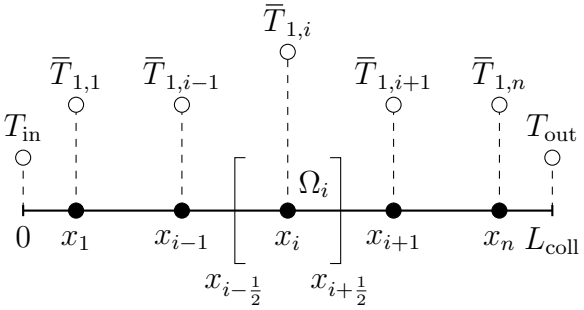

Figure 2.5: One-dimensional discretisation of the spacial domain x for the FVM.

at the temperature in the centre of the wall with

$$T_{\text{abs},i} = \frac{T_{2,i} + T_{3,i}}{2}. \tag{2.20}$$

The procedure to obtain $T_{2,i}$ and $T_{3,i}$ will be discussed in more detail in sections 2.3.5 and 2.3.6. Integration of equation (2.13) over a cell volume $\left[x_{i-\frac{1}{2}}, x_{i+\frac{1}{2}}\right]$ yields

$$\begin{aligned}(m_{\text{HTF},i}c_{p,\text{HTF},i} + m_{\text{tube},i}c_{p,\text{tube},i})\ \frac{\mathrm{d}\overline{T}_i(t)}{\mathrm{d}t}\Delta x_i \\ + m_{\text{HTF},i}c_{p,\text{HTF},i}v_i \int_{x_{i-\frac{1}{2}}}^{x_{i+\frac{1}{2}}} \frac{\partial T(x,t)}{\partial x}\,\mathrm{d}x = \dot{q}_{\text{conv},i}(t)\Delta x_i,\end{aligned} \tag{2.21}$$

where $\overline{T}_i$ is the average fluid temperature in the middle of a CV. Recall that the discretisation is carried out in one dimension where the flux in x direction is by definition equivalent to the divergence of the vector field in the whole CV:

$$\frac{\partial T}{\partial x} \triangleq \nabla \cdot T. \tag{2.22}$$

Evaluating the cell volume integral of the divergence at the cell surfaces according to the divergence theorem, i.e.

$$\iiint_V (\nabla \cdot T)\,\mathrm{d}V = \oiint_S T\,\mathrm{d}S, \tag{2.23}$$

and dividing equation (2.21) by Δx_i yields

$$(m_{\text{HTF},i}c_{p,\text{HTF},i} + m_{\text{tube},i}c_{p,\text{tube},i})\,\frac{\mathrm{d}\overline{T}_i}{\mathrm{d}t} + \frac{m_{\text{HTF},i}c_{p,\text{HTF},i}v_i}{\Delta x_i}\left(T_{i+\frac{1}{2}} - T_{i-\frac{1}{2}}\right) = \dot{q}_{\text{conv},i}. \tag{2.24}$$

Now let

$$T_{i-\frac{1}{2}} =: T_{\text{in},i}, \tag{2.25}$$

$$T_{i+\frac{1}{2}} =: T_{\text{out},i} \tag{2.26}$$

for the respective boundary temperatures of the CV for convenience. As $\overline{T}_i$ is the average fluid temperature in the middle of the CV at x_i it can be rewritten with equations (2.25) and (2.26) as

$$\overline{T}_i =: \overline{T}_{1,i} = \frac{T_{i-\frac{1}{2}} + T_{i+\frac{1}{2}}}{2} = \frac{T_{\text{in},i} + T_{\text{out},i}}{2}. \tag{2.27}$$

$T_{1,i}$ is the representative nodal temperature of the HTF in CV Ω_i at which the fluid properties are evaluated (Figure 2.3b), which is simply the bulk fluid temperature. In addition, the mass flow rate is assumed to be constant in each CV and is simply

$$\dot{m}_{\text{HTF}} = \frac{m_{\text{HTF},i}v_i}{\Delta x_i}. \tag{2.28}$$

Substituting equations (2.25) to (2.28) into equation (2.24) yields

$$\left(m_{\mathrm{HTF},i}c_{p,\mathrm{HTF},i} + m_{\mathrm{tube},i}c_{p,\mathrm{tube},i}\right)\frac{\mathrm{d}\overline{T}_{1,i}}{\mathrm{d}t} + \dot{m}_{\mathrm{HTF}}c_{p,\mathrm{HTF},i}\left(T_{\mathrm{out},i} - T_{\mathrm{in},i}\right) = \dot{q}_{\mathrm{conv},i}. \tag{2.29}$$

Following this approach, Figure 2.3b shows the energy balance of one receiver segment Ω_i with the inlet heat transfer rate $\dot{q}_{\mathrm{in},i}$, the outlet heat transfer rate $\dot{q}_{\mathrm{out},i}$, the absorbed heat transfer rate $\dot{q}_{\mathrm{abs},i}$ into the absorber tube, the convection heat transfer flow $\dot{q}_{\mathrm{conv},i}$ from the absorber tube wall to the HTF, the conduction heat transfer rate $\dot{q}_{\mathrm{cond},i}$ and the receiver heat loss $\dot{q}_{\mathrm{hl},i}$.

As the unknown variable in Eq. (2.29) is the fluid outlet temperature $T_{\mathrm{out},i}$, it can be expressed with equation (2.27) as

$$T_{\mathrm{out},i} = 2\overline{T}_{1,i} - T_{\mathrm{in},i} \tag{2.30}$$

and substituted into Eq. (2.29). Rearranging and solving for the differential term, Eq. (2.29) can be rewritten as

$$\frac{\mathrm{d}\overline{T}_{1,i}}{\mathrm{d}t} = \frac{2\dot{m}_{\mathrm{HTF}}c_{p,\mathrm{HTF},i}\left(T_{\mathrm{in},i} - \overline{T}_{1,i}\right)}{m_{\mathrm{HTF},i}c_{p,\mathrm{HTF},i} + m_{\mathrm{tube},i}c_{p,\mathrm{tube},i}} + \frac{\dot{q}_{\mathrm{conv},i}}{m_{\mathrm{HTF},i}c_{p,\mathrm{HTF},i} + m_{\mathrm{tube},i}c_{p,\mathrm{tube},i}}, \tag{2.31}$$

which is a linear first order differential equation. For convenience, let

$$u_i = \frac{2\dot{m}_{\mathrm{HTF}}c_{p,\mathrm{HTF},i}}{m_{\mathrm{HTF},i}c_{p,\mathrm{HTF},i} + m_{\mathrm{tube},i}c_{p,\mathrm{tube},i}}. \tag{2.32}$$

Separating the variables of Eq. (2.31) and rearranging yields

$$\frac{\mathrm{d}\overline{T}_{1,i}}{\mathrm{d}t} + u_i\overline{T}_{1,i} = u_i\left(T_{\mathrm{in},i} + \frac{\dot{q}_{\mathrm{conv},i}}{2\dot{m}_{\mathrm{HTF}}c_{p,\mathrm{HTF},i}}\right). \tag{2.33}$$

The integrating factor $\mu(t)$ is then

$$\mu(t) = e^{u_i t}, \tag{2.34}$$

where t is the progression of the time step Δt in seconds ($0 \leq t \leq \Delta t$). Multiplying both sides of the differential Eq. (2.33) by the integrating factor and simplifying yields

$$\left(\overline{T}_{1,i}e^{u_i t}\right)' = u_i\left(T_{\mathrm{in},i} + \frac{\dot{q}_{\mathrm{conv},i}}{2\dot{m}_{\mathrm{HTF}}c_{p,\mathrm{HTF},i}}\right)e^{u_i t}. \tag{2.35}$$

After integrating both sides, dividing by the integrating factor $\mu(t)$, substituting u_i and rearranging, Eq. (2.35) is expressed in the form of the general solution for linear first order differential equations:

$$\overline{T}_{1,i} = T_{\mathrm{in},i} + \frac{\dot{q}_{\mathrm{conv},i}}{2\dot{m}_{\mathrm{HTF}}c_{p,\mathrm{HTF},i}} + \mathrm{C}_1 \exp\left(\frac{-2\dot{m}_{\mathrm{HTF}}c_{p,\mathrm{HTF},i}}{m_{\mathrm{HTF},i}c_{p,\mathrm{HTF},i} + m_{\mathrm{tube},i}c_{p,\mathrm{tube},i}}t\right). \tag{2.36}$$

To solve for the unknown constant of integration C_1, one initial condition is required, i.e. the average nodal temperature $\overline{T}_{1,i}$ at the beginning of the time

step is the average temperature $\overline{T}_{0,i}$ at the end of the previous time step:

$$t = 0: \qquad \overline{T}_{0,i} = \overline{T}_{1,i}. \tag{2.37}$$

Hence,

$$\overline{T}_{0,i} = T_{\text{in},i} + \frac{\dot{q}_{\text{conv},i}}{2\dot{m}_{\text{HTF}} c_{p,\text{HTF},i}} + \text{C}_1 e^0, \tag{2.38}$$

$$\text{C}_1 = \overline{T}_{0,i} - T_{\text{in},i} - \frac{\dot{q}_{\text{conv},i}}{2\dot{m}_{\text{HTF}} c_{p,\text{HTF},i}}. \tag{2.39}$$

Substituting C_1 into Eq. (2.36) and substituting $\overline{T}_{1,i}$ with equation (2.27) yields the final equation for the outlet temperature of a CV Ω_i at the end of a time step ($t = \Delta t$), as adapted from Wagner and Gilman (2011):

$$\begin{aligned} T_{\text{out},i}|_{t=\Delta t} = {} & T_{\text{in},i} + \frac{\dot{q}_{\text{conv},i}}{\dot{m}_{\text{HTF}} c_{p,\text{HTF},i}} \\ & + 2\left(\overline{T}_{0,i} - \frac{\dot{q}_{\text{conv},i}}{2\dot{m}_{\text{HTF}} c_{p,\text{HTF},i}}\right) \exp\left(\frac{-2\dot{m}_{\text{HTF}} c_{p,\text{HTF},i}}{m_{\text{HTF},i} c_{p,\text{HTF},i} + m_{\text{tube},i} c_{p,\text{tube},i}} \Delta t\right). \end{aligned} \tag{2.40}$$

2.3.3 Solar heat absorption in absorber tube wall

Similar to the longitudinal discretisation of the receiver tube in section 2.3.2, the concentrated incident solar flux $\dot{q}_{\text{inc}}$ of a SCA — as calculated with Eq. (2.1) — is also divided into n corresponding segments of equal length:

$$\dot{q}_{\text{inc},i} = \frac{\dot{q}_{\text{inc}}}{n}. \tag{2.41}$$

The incident solar flux $\dot{q}_{\text{inc},i}$ on the collector is assumed to be equal for each division i of the collector. Therefore, the concentrated solar flux on the absorber tube $\dot{q}_{\text{abs},i}$ is also circumferentially and longitudinally uniform for each absorber tube segment i. Hence, the circumferential temperature distribution of the absorber tube and the HTF can also be assumed to be uniform. In reality, however, this is not the case as the solar irradiation is concentrated at the bottom of the absorber tube. As a result, the wall temperature at the bottom is significantly higher than at the top of the absorber tube, which can lead to thermal stresses in the material (and possibly damage) and has to be avoided, e.g. by defocusing the solar collector when the maximum operating temperature of the HTF is reached (as will be described in section 2.4.3). During normal operation however, the receiver tube wall temperature difference does not lead to excessive strain of the steel (Viljoen, 2014). A similar effect of high-temperature gradients in the absorber tube can also occur during filling of a loop with hot molten salt (e.g. after draining the loop for maintenance work). In this case, the cold absorber tubes are typically preheated by the FP system in order to avoid high thermal stresses (Kearney *et al.*, 2003). This type of absorber tube preheating has not been explicitly modelled in this study because outages due to maintenance work on the solar field are taken into ac-

Table 2.4: Specific heat loss fitting coefficients for HCEMS-11 receiver tubes with different conditions of vacuum in the annulus (Matino and Maccari, 2015).

Receiver condition	c_1 [W/(m °C)]	c_4 [W/(m °C^4)]	Weighting
Vacuum intact	0.19	7.8×10^{-9}	0.985
Vacuum degraded	0.50	7.9×10^{-9}	0.010
Vacuum lost	1.01	8.0×10^{-9}	0.005

count through a general plant availability factor, which will be introduced in section 2.8.1. Detailed three-dimensional models for the analysis of the non-uniformity of the solar flux on the receiver have been developed by Cheng *et al.* (2010), Wu *et al.* (2014) and Chang *et al.* (2018). However, the integration of a three-dimensional receiver model does not lie within the scope of this work and is therefore not considered.

The absorbed heat transfer rate in the HTF into each absorber tube segment i can be calculated with

$$\dot{q}_{\mathrm{abs},i} = \dot{q}_{\mathrm{inc},i}\eta_{\mathrm{opt,rec}}, \tag{2.42}$$

where the receiver optical efficiency $\eta_{\mathrm{opt,rec}}$ is the product of the transmittance of the glass envelope τ_{glass}, the absorber tube absorptivity α_{abs}, the ratio of bellow length to receiver length η_{bellow} and the cleanliness factor of the glass tube cf_{glass} with the respective optical parameters for the HCEMS-11 receiver tube from Table 2.3:

$$\eta_{\mathrm{opt,rec}} = \tau_{\mathrm{glass}}\alpha_{\mathrm{abs}}\eta_{\mathrm{bellow}}\,cf_{\mathrm{glass}}. \tag{2.43}$$

2.3.4 Empirical heat loss model of absorber tube

In order to reduce the complexity of the model and thus also its required computational effort, the heat loss model is based on an empirical heat loss calculation as suggested by Zaversky *et al.* (2013). The heat loss of the Archimede Solar Energy HCEMS-11 receiver for molten salts has been adapted from Matino and Maccari (2015), who correlated the heat loss as a function of the outer surface temperature of the absorber tube ($T_{3,i}$):

$$\dot{q}_{\mathrm{hl},i} = \left(c_1 T_{3,i} + c_4 T_{3,i}^4\right) \Delta x_i. \tag{2.44}$$

The coefficients c_1 and c_4 have been obtained experimentally under laboratory conditions for various vacuum levels in the receiver and are listed in Table 2.4. According to Matino and Maccari (2015) the coefficient c_1 is linked to the convective heat transfer rate and increases with a decreasing level of vacuum in the annulus (see Figure 2.6). The second term of Eq. (2.44) represents the radiative heat transfer rate. To account for degradation, a weighting factor (listed in Table 2.4) has been introduced to the model to simulate a mix of receivers with the vacuum intact, with a degraded vacuum (~0.1 mbar) and with a broken glass envelope (vacuum lost).

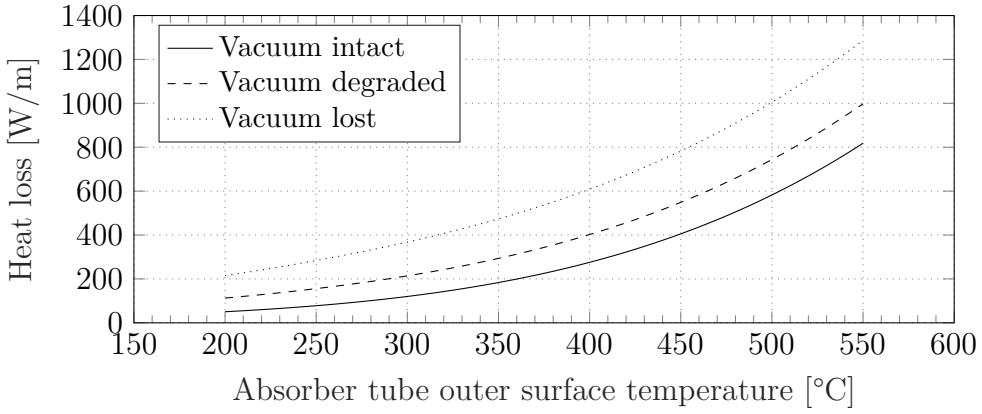

Figure 2.6: Heat loss comparison of the HCEMS-11 receiver with different conditions of the vacuum in the annulus.

As part of the empirical heat loss model, the iterative calculation of the radiation and convection heat loss from the absorber tube to the annulus as well as the conduction and convective heat transfer of the glass envelope are not considered explicitly as they are taken into account in the receiver heat loss equation. This allows the omission of iteratively computing the glass envelope surface temperatures and therefore reduces the required number of iterations during the simulation to obtain the heat loss. The thermal inertia effect of the glass envelope is therefore also neglected.

Heat losses from interconnecting piping, i.e. piping between SCAs, cross-over piping, headers and runners, are considered through a convective heat loss to the ambient air (T_{amb}) with

$$\dot{q}_{\text{hl,piping}} = h_{\text{piping}} A_{\text{piping}} \left(T_{\text{in,piping}} - T_{\text{amb}} \right), \tag{2.45}$$

where h_{piping} is the convective heat loss coefficient, A_{piping} the outer surface area and $T_{\text{in,piping}}$ the inlet temperature of the fluid of the piping, respectively. The convective heat loss coefficient is assumed to be $0.45\,\text{W}/(\text{m}^2\,\text{K})$ for all interconnecting piping as well as the runner and header piping. This heat loss is used to obtain the outlet temperature of the interconnecting piping with

$$T_{\text{out,piping}} = T_{\text{in,piping}} - \frac{\dot{q}_{\text{hl,piping}}}{\dot{m}_{\text{HTF}} c_{p,\text{HTF}}}, \tag{2.46}$$

which in turn is the inlet temperature of the following SCA. Further heat losses from support brackets and expansion bellows are neglected because they are significantly lower than the heat loss from the absorber tube itself. This allows to further reduce the model's complexity and thus its computational effort. The model validation in section 4.2 shows that this assumption is reasonable in terms of the induced error for solar field outlet temperature and thermal output between the model results and the measured data.

2.3.5 Conduction heat transfer through absorber tube

With the solar heat absorption and heat loss model defined, the conduction heat transfer rate across the absorber tube wall is simply the difference of the absorbed solar heat and the heat loss of the discrete absorber tube segment i:

$$\dot{q}_{\text{cond},i} = \dot{q}_{\text{conv},i} = \dot{q}_{\text{abs},i} - \dot{q}_{\text{hl},i}. \tag{2.47}$$

As no further heat losses occur in the absorber tube, the convective heat transfer rate from the absorber tube inner surface into the HTF is equal to the conduction heat transfer rate and will be used in section 2.3.6 to calculate the inner absorber tube wall temperature $T_{2,i}$. Hence, the outer absorber tube wall temperature $T_{3,i}$ can be calculated with Eq. (2.48), where $k_{\text{abs},i}$ is the thermal conductivity of the absorber tube wall segment i and d_2 and d_3 are the inner and outer absorber tube diameters, respectively. The thermal conductivity of the absorber tube is a function of the average wall temperature.

$$T_{3,i} = T_{2,i} + \frac{\dot{q}_{\text{cond},i}}{2\pi k_{\text{abs},i}} \log \frac{d_3}{d_2}. \tag{2.48}$$

2.3.6 Convective heat transfer into the HTF

The heat transferred from the absorber tube inner surface to the HTF by convection can be obtained from Newton's law of cooling:

$$\dot{q}_{\text{conv},i} = h_i A_i \left(T_{2,i} - T_{1,i}\right), \tag{2.49}$$

where h_i is the wall-to-fluid convective heat transfer coefficient, A_i the absorber tube inner cross sectional area and $T_{1,i}$ the bulk fluid temperature in the middle of CV Ω_i. With the convective heat transfer rate from Eq. (2.47), the absorber tube inner surface temperature $T_{2,i}$ can be obtained from Eq. (2.49) with

$$T_{2,i} = T_{1,i} + \frac{\dot{q}_{\text{conv},i}}{h_i A_i}. \tag{2.50}$$

The wall-to-fluid convective heat transfer coefficient h_i is given by

$$h_i = \frac{Nu_i k_{\text{HTF},i}}{d}, \tag{2.51}$$

where Nu_i is the Nusselt number and $k_{\text{HTF},i}$ the thermal conductivity of the HTF in CV Ω_i and d the characteristic length, which in this case corresponds to the inner absorber tube diameter d_2. Correlations for the Nusselt number Nu_i as a function of Re_i and Pr_i were developed by Wu *et al.* (2012) for molten salts from experimental data for transitional flow in Eq. (2.52) and turbulent flow in Eq. (2.53) and are valid for $1.6 < Pr_i < 23.9$:

$$Nu_i = \begin{cases} 0.00154 Re^{1.1} Pr_i^{1/3}, & \text{for } 2300 < Re_i < 10^4 \quad (2.52) \\ 0.02948 Re^{0.787} Pr_i^{1/3}, & \text{for } Re_i \geq 10^4\ . \quad (2.53) \end{cases}$$

This correlation is not valid for laminar flow conditions ($Re_i < 2300$). However, since the Reynolds number can only fall below this value at a minimum

considered mass flow rate of 2 kg/s at temperatures below 225 °C when using Hitec XL as HTF, the Nusselt number for laminar flow can also be approximated with Eq. (2.52). Since these conditions only occur when the solar field is not in operation and the heat transfer is not of particular interest, this proposed approximation of the Nusselt number is satisfactory.

The Reynolds number can be calculated with Eq. (2.54), where $\rho_{\mathrm{HTF},i}$ is the bulk HTF density, v_i the bulk fluid velocity and μ_i the dynamic viscosity of the fluid in CV Ω_i and the Prandtl number is obtained from Eq. (2.55), where $k_{\mathrm{HTF},i}$ is the thermal conductivity of the HTF:

$$Re_i = \frac{\rho_{\mathrm{HTF},i} v_i d_2}{\mu_i}, \tag{2.54}$$

$$Pr_i = \frac{c_{p\mathrm{HTF},i} \mu_i}{k_{\mathrm{HTF},i}}. \tag{2.55}$$

Figure 2.7a shows the Reynolds numbers of the investigated HTFs as a function of the average fluid temperature $T_{1,i}$ at the centre of the CV and their respective thermo-physical properties at an inner tube diameter of $D_2 = 0.064\,\mathrm{m}$ and a velocity of $v_i = 1\,\mathrm{m/s}$. This corresponds to the diameter of the investigated receiver tubes and a velocity that represents a typical flow rate of the HTF during on-sun operation. For the chosen conditions, only in the case of Hitec XL, the Reynolds number is below the limit of $Re_i > 10^4$ for temperatures below approximately 240 °C. However while the solar field is in operation, the fluid temperature is typically above 290 °C and thus does not invalidate the condition for turbulent flow as the fluid's viscosity is significantly reduced at higher temperatures. The Reynolds number only falls below 10^4 during times when the solar field is on standby and therefore does not reduce the heat transfer

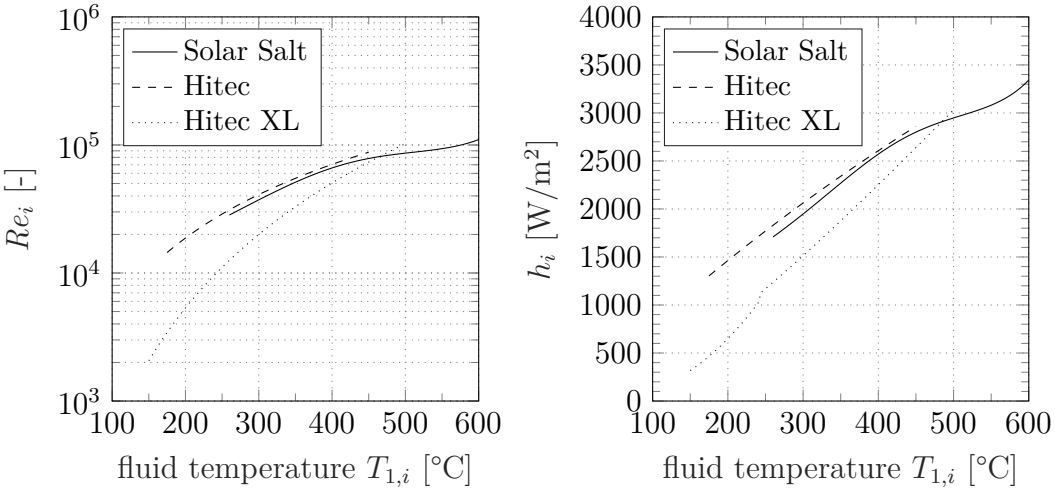

(a) Reynolds number. **(b)** Convective heat transfer coefficient.

Figure 2.7: Reynolds number (a) and convective heat transfer coefficient (b) of molten salt HTFs as a function of fluid temperature $T_{1,i}$ at $v_i = 1\,\mathrm{m/s}$.

coefficient during operation.

For the same conditions, Figure 2.7b shows the heat transfer coefficient of the three HTFs. Solar Salt and Hitec both generally have a higher heat transfer coefficient than Hitec XL, whereby Solar Salt's higher operating temperature enables higher heat transfer coefficients. At low temperatures, the heat transfer coefficient of Hitec XL also reduces due to the transitional flow. However, this is in fact favourable as it reduces the heat loss when the fluid velocity is low when the solar field is not operational, for instance at night or during standby.

In order to confirm the validity of the assumption of the lumped capacitance model, the Biot number Bi_i of the receiver model needs to be calculated with

$$Bi_i = \frac{h_i}{k_{\text{abs},i}} L_\text{c}, \tag{2.56}$$

where h_i is the convective heat transfer coefficient, $k_{\text{abs},i}$ the thermal conductivity of the steel tube and L_c the characteristic length of the absorber tube, which is calculated with

$$L_\text{c} = \frac{V_i}{A_i}. \tag{2.57}$$

Here, V_i is the volume of the absorber tube segment and A_i is the surface area of the absorber tube. With a maximum mass flow rate of 4 kg/s in the measurement data used for the validation in section 4.2 and a thermal conductivity of stainless steel of 22.5 W/(m K) at 550 °C, the absorber tube must be discretised into at least 18 CVs in order to fulfil the condition of $Bi < 0.1$. Therefore, a discretisation into more than 18 CVs is necessary for the model to be valid for the validation with the measurement data. However, in order to also guarantee the validity of the model for situations with higher flow rates (assuming a maximum of 15 kg/s), a minimum of 30 CVs are necessary.

2.3.7 Model solver

In order to accurately model the transient behaviour of a solar collector based on Eq. (2.13), a numerical solution approach is used. Explicit solution methods provide high accuracy and computational advantages in time-dependent solutions if the numerical stability limit can be ensured, i.e. if the *Courant-Friedrichs-Lewy* (CFL) condition is fulfilled. This condition requires that, given a maximum possible bulk fluid flow velocity v, the simulation time step Δt must be chosen small enough so that the fluid flowing through a CV does not leave said CV before the time step is completed. Similarly, if a certain time step size is desired, the CV length Δx has to be chosen large enough to fulfil the same condition. Hence, the CFL condition can be expressed as

$$C = \frac{v \Delta t}{\Delta x} \leq C_\text{max} \tag{2.58}$$

for the one-dimensional case, where C is the Courant number. This number must then be smaller or equal than the maximum allowed Courant number

$C_{\max}$ where for an explicit solver, it is typically assumed that $C_{\max} = 1$.

Assuming a time step size of 10 s (as it is the case in the validation of the model in section 4.2) and a maximum allowable bulk fluid velocity v of 3 m/s, a longitudinal discretisation of the SCA into maximal 8 CVs would be necessary in order to fulfil this condition ($\Delta x = 8.18$ m). Likewise if only one CV for the whole SCA is assumed ($\Delta x = 245.3$ m), the largest possible time step would be 81 s. However, since the model's intended main use is for annual performance simulations, the required time step needs to be considerably larger (e.g. 60 min) in order to save valuable simulation time. Thus, the model requires an implicit solution method in order to also guarantee numerical stability when using large time steps of up to an hour, which would otherwise make it impossible to fulfil the CFL condition. Therefore, the model has been implicitly formulated to approximate the solutions iteratively. This will be discussed below.

The solver of the receiver model is also based on the approach presented by Wagner and Gilman (2011) but has been adapted according to Figure 2.3b to accommodate a series of n one-dimensional radial heat loss models for each CV Ω_i in flow direction. Each following CV uses the outlet temperature from the previous CV as inlet temperature. As such, only the temperatures in radial direction are left to be determined ($T_{2,i}$ and $T_{3,i}$). However, as the outlet fluid temperature $T_{\text{out},i}$ of each CV depends on the receiver heat loss as a function of the absorber temperature $T_{3,i}$ and vice versa, these temperatures can only be evaluated through an implicit set of equations. This modelling approach requires an iterative approximation for each temperature through successive substitution. The model uses the *bisection method* to approximate an initial solution, which is then used as a starting point for the usually faster converging false position method (*regula falsi*). At the beginning of the simulation, the solver requires initial guess values for each node, which are based on the HTF inlet temperature $T_{\text{in},i}$. Guess values in the radial direction are provided as listed in Eq. (2.59) to Eq. (2.61) assuming that the inner and outer absorber tube surface temperature are higher than the fluid temperature:

$$T_{1,i,\text{guess}} = T_{\text{in},i}, \tag{2.59}$$

$$T_{2,i,\text{guess}} = T_{1,i,\text{guess}} + 2\,^{\circ}\text{C}, \tag{2.60}$$

$$T_{3,i,\text{guess}} = T_{2,i,\text{guess}} + 5\,^{\circ}\text{C}. \tag{2.61}$$

Once a heat loss value has been estimated with Eq. (2.44) based on the guessed outer surface temperature of the absorber tube ($T_{3,i,\text{guess}}$), the outlet temperature $T_{\text{out},i,\text{guess}}$ of a CV can be estimated with

$$T_{\text{out},i,\text{guess}} = \frac{\dot{q}_{\text{abs},i}}{\dot{m}_{\text{HTF}}} c_{p,\text{HTF},i} + T_{\text{in},i}. \tag{2.62}$$

Now, assuming a linear temperature distribution within each CV in the axial direction, $T_{1,i}$ is simply the average fluid temperature as

$$T_{1,i} = \frac{T_{\text{in},i} + T_{\text{out},i,\text{guess}}}{2}. \tag{2.63}$$

With this information, $T_{2,i}$ can be estimated with Eq. (2.50). Finally, this temperature is used to update the initial guess value for $T_{3,i}$ with Eq. (2.48) and the iterative process is repeated. The model is converged when the difference between the new value for $T_{3,i}$ and the guessed value of the previous iteration is less than the tolerance $\epsilon = 0.001$. After convergence, the resulting temperature values are used as the new guess values for the following time step.

2.3.8 Heat transfer fluid properties

This study investigates the use of three selected molten salt mixtures, namely *Solar Salt*, *Hitec* and *Hitec XL*, in order to determine the most economically feasible HTF within a Southern African context. Table 2.5 provides an overview of the thermo-physical fluid properties at 300 °C and the costs of each molten salt mixture in comparison to the conventionally used thermal oil *Therminol® VP-1*. All fluid properties are a function of the bulk fluid temperature $T_{1,i}$ at the centre of each CV Ω_i, assuming that the fluid is homogeneously mixed. The temperature-dependent correlations for the thermo-physical fluid properties (i.e. density, specific heat capacity, thermal conductivity and viscosity) of each HTF can be found in Appendix C. However, it should be noted that there is no consensus about the accuracy of the correlations for the specific heat capacity of Solar Salt. Some researchers and manufacturers suggest a temperature-dependent correlation, as for example Serrano-López *et al.* (2013), NREL (2013*b*), Benoit *et al.* (2016) and SQM (2017), but more recently, D'Aguanno *et al.* (2018) have conducted a series of new experiments and found that the specific heat capacity c_p of Solar Salt is not temperature-dependent but rather constant. As there is an ongoing controversy about the respective correlations, more studies are required in order to determine the actual specific heat capacity of Solar Salt as already small deviations can result in a significant over- or underestimation of the annual energy output of CSP plants[5]. Nevertheless, the correlations from Solar Salt's manufacturer, SQM (2017), were used in this study as they are the predominately used correlations in literature and therefore enable the comparability with other studies.

As can be seen in Table 2.5, the freezing point of Solar Salt is the highest of all four HTFs and therefore requires more energy from the FP system to prevent the fluid from freezing in the pipes as compared to the other fluids. Nevertheless, the higher thermal stability limit of Solar Salt enables a larger operating temperature range and thus higher power cycle efficiencies, which compensates for the increased FP energy requirement. In fact, Solar Salt offers the widest range of operating temperatures with a potential temperature difference of 260 °C between the upper and lower recommended operating temperatures. However, since the receiver used in this study has a thermal

[5] D'Aguanno *et al.* (2018) estimate that an overestimation of the specific heat capacity c_p of 5 % results in a electricity output loss of approximately 12 GW h per year for a 50 MW plant with a TES capacity of 15 h.

Table 2.5: Overview of thermo-physical properties and costs of selected HTFs.

Property	Unit	Therminol VP-1[6]	Solar Salt[7]	Hitec[8]	Hitec XL[9]
Freezing point	[°C]	12	221	142	120([10])
Thermal stability limit	[°C]	400	621	538	500
Recommended $T_{\min}$ (T_{fp})	[°C]	50([11])	260	175([11])	150
Recommended $T_{\max}$	[°C]	400	600	450	450([12])
Practical TES ΔT	[°C]	110	260	160	160
Thermo-physical properties at 300 °C					
Density	[kg/m^3]	817	1899	1865	1992
Heat capacity	[J/kgK]	2310	1495	1562	1447
Thermal conductivity	[W/mK]	0.096	0.50	0.39	0.52
Viscosity	[mPa s]	0.23	3.27	3.22	6.37
Costs					
Fluid cost	[$/t]	5150([13])	800([14])	1070([15])	1430([16])
Cost of stored energy[17]	[$/kWh$_{\text{th}}$]	60.2	7.3	15.4	22.6

stability limit of 550 °C, the upper operating temperature of Solar Salt will be limited to this temperature.

Although the specific heat capacities of the three salt mixtures are significantly lower than that of thermal oil, molten salt is the preferred storage medium in PTPPs due to its considerably lower costs. In fact, the cost of Solar Salt for example is 800 $/t (Turchi *et al.*, 2019), which correspond to approximately one sixth of the cost of thermal oil with 5150 $/t, based on Kurup and Turchi (2015) and indexed to 2018 using the *Producer Price Index* (PPI) for aromatic chemicals (BLS, 2019). Further considering the elevated temperature difference achievable in the TES when using molten salt leads to storage costs of 7.3 $/kWh$_{\text{th}}$ for Solar Salt as compared to 60.2 $/kWh$_{\text{th}}$ if thermal oil was used. This corresponds to a cost reduction of 88 % for the stored energy, which is one of the main advantages of using molten salt as storage medium.

[6] Eastman (2019).
[7] SQM (2017).
[8] Coastal Chemical Co. (n.d.).
[9] NREL (2013*b*).
[10] Kearney *et al.* (2003).
[11] NREL (2009).
[12] Grogan (2013).
[13] This is based on Kurup and Turchi (2015) and indexed to 2018 using the PPI for aromatic chemicals (BLS, 2019).
[14] Turchi *et al.* (2019).
[15] This is based on communications with industry experts (Industry Sources, 2018).
[16] Liu *et al.* (2016).
[17] This is based on the heat capacity of the average TES temperature difference (TES ΔT).

2.3.9 Summary of assumptions and simplifications

The receiver model is based on the following assumptions and simplifications:

- The fluid is assumed to be homogeneously mixed within each CV Ω_i where the thermal capacitance is assumed to be lumped at the central node.
- The thermal capacitance of the absorber tube is lumped together with the thermal capacitance of the HTF. This model is valid for a discretisation into at least 30 CVs.
- The receiver is divided into n discrete CVs of equal length Δx_i with a representative bulk average fluid temperature $T_{1,i}$ at the centre of the CV. The temperatures $T_{2,i}$ and $T_{3,i}$ represent the inner and outer surface temperatures of the absorber tube, respectively.
- All fluid properties are a function of the bulk average fluid temperature at the centre x_i of the CV.
- The material properties of the absorber tube are a function of the average wall temperature ($\overline{T}_{\text{abs},i} = (T_{2,i} + T_{3,i})/2$).
- The receiver heat loss is only a function of the outer absorber tube surface temperature $T_{3,i}$.
- Any net longitudinal conduction heat transfer in the absorber tube in the upstream flow direction is considered negligible.
- The longitudinal conduction heat transfer of the receiver and fluid is neglected.
- The conduction and convective heat transfer of the glass envelope are not considered explicitly as they are included in the receiver heat loss equation. The thermal inertia effect of the glass envelope is therefore also neglected.
- The incident solar flux $\dot{q}_{\text{inc},i}$ on the collector is assumed to be equal for each division i of the collector.
- The concentrated solar flux absorbed in the absorber tube, $\dot{q}_{\text{abs},i}$, is assumed to be circumferentially and longitudinally uniform for each CV. Therefore, the circumferential temperature profile in the absorber tube is also assumed to be uniform. Non-concentrated solar flux directly from the sun is also assumed to hit the receiver if the collector is defocused but not shaded.
- The circumferential distribution of the HTF flow and temperature is assumed to be uniform.
- Heat losses from the expansion bellows and support brackets are neglected.
- One loop is modelled representatively for the entire solar field and is then numbered up to account for the actual number of installed loops.

2.4 Solar Field Control and Solar Field Sizing

The following section describes the solar field control, in terms of mass flow rate, FP system and collector defocusing as well as the solar field sizing process, which is needed to calculate the pressure drop across the entire field. First, the solar field control is defined in section 2.4.1, where the mass flow rate is controlled depending on the current operation mode of the solar field. Each solar field operation mode and the necessary conditions that have to be met in order to change operation mode are briefly described. Next, the FP model and the respective freeze protection strategies are presented in section 2.4.2. Furthermore, the collector defocusing approach is presented in section 2.4.3 in order to avoid dangerous overheating of the HTF and the solar field equipment. Lastly, the solar field piping model and pressure drop calculation are presented in section 2.4.4.

2.4.1 Mass flow rate control

The mass flow rate of the solar field is controlled by an iterative feedback controller in TRNSYS (Type 22) that uses the secant method in combination with successive substitution to calculate the appropriate flow rate within the defined limits in order to keep the solar field outlet temperature close to the desired set point. However, depending on the *operation mode* (*OM*), the loop flow rate $\dot{m}_{\text{loop}}$ takes either a fixed minimum or maximum value or is controlled by the controller between the allowable limits. For example, the flow rate during *OM(1)* (freeze protection circulation) is equal to the FP flow rate $\dot{m}_{\text{fp}}$. The pre-set flow rates for each operation mode are as follows:

- *OM(1)*: freeze protection circulation: $\dot{m}_{\text{loop}} = \dot{m}_{\text{fp}}$,
- *OM(2)*: standby circulation: $\dot{m}_{\text{loop}} = \dot{m}_{\text{min}}$,
- *OM(3)*: design circulation: $\dot{m}_{\text{min}} \leq \dot{m}_{\text{loop}} \leq \dot{m}_{\text{max}}$,
- *OM(4)*: collector defocusing: $\dot{m}_{\text{loop}} = \dot{m}_{\text{max}}$.

Table 2.6 lists the allowable limits at design for the respective flow rates. The

Table 2.6: Loop design flow rates.

Parameter	Variable	Unit	Value
Minimum flow rate[18]	$\dot{m}_{\text{min}}$	[kg/s]	2
Maximum flow rate[19]	$\dot{m}_{\text{max}}$	[kg/s]	variable
FP flow rate[20]	$\dot{m}_{\text{fp}}$	[kg/s]	variable (2 to 10)

minimum allowable flow rate $\dot{m}_{\text{min}}$ is assumed to be 2 kg/s. The maximum allowable flow rate in a loop $\dot{m}_{\text{max}}$ is dependent on the nominal thermal power of the power cycle $\dot{Q}_{\text{PB}}$ and the *solar multiple SM* (and hence also the required number of loops N_{loops}). Furthermore, it also depends on the HTF itself, which dictates the design solar field inlet and outlet temperature ($T_{\text{SF,in}}$ and $T_{\text{SF,out}}$) and therefore the average specific heat capacity $c_{p,\text{avg}}$ of the fluid as well. The maximum flow rate is then obtained with

$$\dot{m}_{\text{max}} = \frac{\dot{Q}_{\text{PB}} SM}{N_{\text{loops}} c_{p,\text{avg}} (T_{\text{SF,out}} - T_{\text{SF,in}})}. \tag{2.64}$$

The FP flow rate is varied between 2 kg/s to 10 kg/s throughout the multi-objective optimisation in chapter 5.

Figure 2.8 depicts the flow chart of the solar field control logic, showing the conditions that have to be met in order to change operation mode. Starting from the FP circulation, *OM(1)*, this operation mode is maintained as long as the heat losses from the receiver tubes are higher than the absorbed thermal power into the HTF. If the fluid temperature in any section of a pipe (i.e. receivers, cross-over piping, headers or runners) falls below the FP temperature T_{fp}, the electric FP system is activated in the respective section, which is heating the pipe either through impedance or resistance heating. Depending on the implemented *freeze protection strategy* (FPS), once the solar field outlet temperature cannot be maintained at its desired set point any longer, either hot fluid from the hot tank is mixed into the solar field inlet (FPS2) or the electric FP system is activated throughout the solar field piping. As soon as the solar field outlet temperature is above its defined FP limit and the absorbed thermal power into the HTF is greater than the heat losses from the receiver tubes, the solar field is switched into standby circulation, *OM(2)*.

The low minimum flow rate of 2 kg/s is maintained as long as the outlet temperature is below the hot tank reference temperature $T_{\text{HT,ref}}$, which is typically the case during dusk and dawn as well as during periods of low solar irradiation. This temperature defines the threshold at which the HTF is allowed to be pumped into the hot tank. As long as the fluid temperature is below said set point, the HTF is diverted back to the cold tank. Once the solar field outlet temperature rises above $T_{\text{HT,ref}}$, *OM(3)* design circulation is activated. During this operation mode, the flow rate is controlled by the iterative feedback controller and is varied between the specified limits ($\dot{m}_{\text{min}}$ and $\dot{m}_{\text{max}}$) in order to maintain the nominal solar field temperature $T_{\text{SF,des}}$. With increasing solar irradiation, the flow rate approaches its maximum value. As soon as the maximum flow rate is no longer sufficient to transfer the absorbed heat, the solar field outlet temperature rises above the desired operating tem-

[18] (Maccari *et al.*, 2016).
[19] Depending on the turbine capacity, operating temperature range and solar multiple (Eq. 2.64).
[20] This is varied between 2 kg/s to 10 kg/s in the multi-objective optimisation in chapter 5.

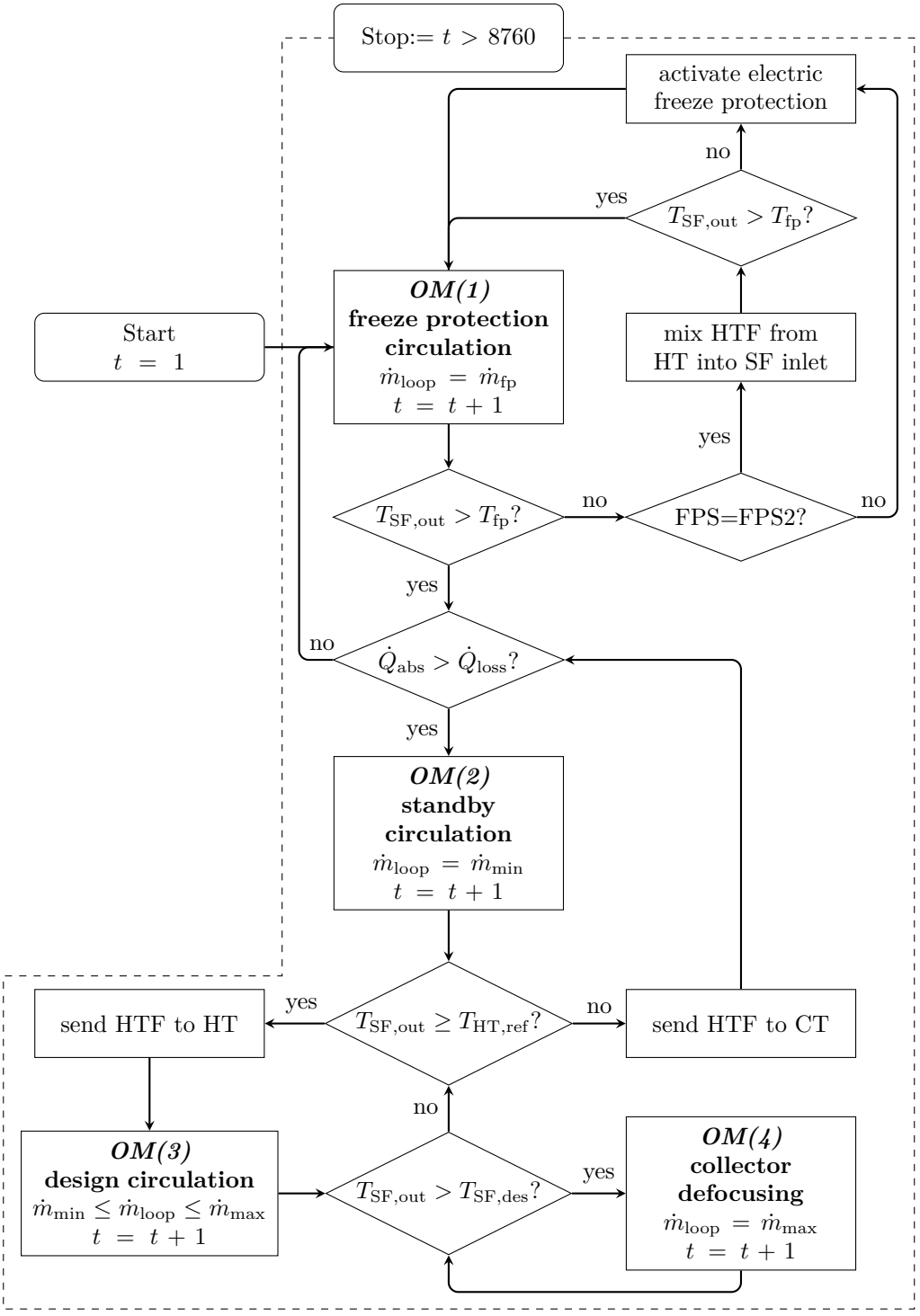

Figure 2.8: Solar field control logic.

perature. In order to avoid high temperatures that can potentially damage the receiver tubes and other equipment, *OM(4)* is entered where the collectors are defocused in order to reduce the reflected solar flux.

A description of the collector defocusing approach is provided in section 2.4.3. *OM(4)* is active until the solar field outlet temperature can be controlled through the flow rate again and *OM(3)* is entered. Lastly, once the fluid outlet temperature falls below the hot tank reference threshold (e.g. at sunset), *OM(2)* is entered and the fluid is directed back to the cold tank. At night, the solar field is switched into *OM(1)* again if the conditions require the FP system to be activated.

2.4.2 Freeze protection model and strategies

The Archimede Solar Energy demonstration plant is equipped with impedance heating in the receiver tubes to protect the HTF from freezing in the pipes. By applying a low voltage to the receivers of a SCA, an electric current is induced in the absorber tube walls. The ohmic resistance of the pipes causes a loss in power that in turn releases energy into the pipe in the form of heat causing a temperature rise in the absorber tube wall. The following sections describe the implemented method for the FP of the receiver tubes as well as of the interconnecting piping. Lastly, two different FP strategies are presented, one relying solely on electric FP and one using thermal energy stored in the hot TES to increase the inlet temperature of the solar field in order to guarantee an outlet temperature above the FP temperature limit of the fluid. In an effort to minimise fossil fuel consumption, this study does not consider any additional gas-fired backup heater for FP. Furthermore, alternative freeze protection methods (as introduced in section 1.2.2) are currently still under development and do not yet constitute a practically proven method on a commercial scale that would be able to eliminate electric heat tracing and are therefore also not investigated here.

Freeze protection model

Since the FP through impedance heating generates heat directly in the absorber tube wall, it is simply implemented as an additional heat source to the incident solar flux in each absorber tube wall segment i when the heat tracing system is active. Thus,

$$\dot{q}_{\mathrm{abs},i} = \dot{q}_{\mathrm{inc},i}\eta_{opt,rec} + \dot{q}_{\mathrm{fp},i}. \tag{2.65}$$

The impedance FP system is primarily used to compensate for the heat loss in the absorber tube wall. The required heat rate $\dot{q}_{\mathrm{fp},i}$ must be slightly higher than the heat loss $\dot{q}_{\mathrm{loss},i}$ in each segment to guarantee that the fluid temperature does not fall below the desired FP temperature T_{fp} (the allowed minimal fluid temperature of each HTF is listed in Table 2.5). However, since the resulting higher absorber tube temperature also automatically results in a higher heat loss, this is an iterative approach where a recalculation of the fluid outlet temperature with the updated heat loss is triggered. This process is repeated until the HTF outlet temperature is equal or above the desired minimal fluid

temperature. The required heat rate from the FP system in each node of the solar collector is simply estimated with

$$\dot{q}_{\mathrm{fp},i} = \frac{T_{\mathrm{fp}}}{T_{\mathrm{out},i}} \dot{q}_{\mathrm{loss},i} \tag{2.66}$$

and is then recalculated until the added heat from the FP system raises the fluid outlet temperature above the minimal fluid temperature T_{fp}.

In addition to the impedance heating system for the receiver tubes, the FP through resistance heating in the interconnecting piping, i.e. piping between SCAs, cross-over piping, headers and runners, has also been taken into account by adding heat once the outlet temperature from Eq. (2.46) falls below the desired FP temperature. Nonetheless, since the required heat from the FP system in the interconnecting piping has been observed to be negligible in the framework of this study, the required additional heat is simply estimated with

$$\dot{q}_{\mathrm{fp,piping}} = \dot{m}_{\mathrm{HTF}} c_{p,\mathrm{HTF}} (T_{\mathrm{fp}} - T_{\mathrm{out,piping}}) \tag{2.67}$$

and does not trigger a whole recalculation of the heat loss but rather adds the additional heat input to the fluid with

$$T_{\mathrm{out,piping}} = \frac{\dot{q}_{\mathrm{fp,piping}}}{\dot{m}_{\mathrm{HTF}} c_{p,\mathrm{HTF}}} + T_{\mathrm{out,piping},0}. \tag{2.68}$$

where $T_{\mathrm{out,piping},0}$ is the outlet temperature obtained from Eq. (2.46) before it is recalculated with Eq. (2.68).

Freeze protection strategies

The baseline approach for the FP system relies on the passive approach proposed by Kearney *et al.* (2003), in which the HTF is circulated from the cold tank through the solar field at night or during periods of low solar irradiation. A relatively high flow rate of 4 kg/s is used in order to guarantee that all components in the solar field are kept warm but leads to increased heat losses overnight. This flow rate also corresponds with the flow rate used in Archimede Solar Energy's demonstration loop for molten salts (Maccari *et al.*, 2016). Since the temperature in the cold tank is ideally around 290 °C, this will be enough in most cases to keep the solar field outlet temperature above the FP temperature. The fluid is then circulated back to the cold tank. Although this approach results in an undesired drop of the cold tank temperature, some energy lost during the night can be recovered in the early morning hours while the solar field is preheated by the sun before nominal operation. As this circulation from the cold tank will not always be sufficient to keep the fluid temperature above its freezing limit at all times during standby of the solar field, an active FP measure is also required.

Two approaches for the active freeze protection strategy can generally be used in PTPPs without requiring a major installation of additional equipment (for example, using a larger drainage tank for mixing as proposed by Hinrichs

et al., 2016) or advanced operational control. The first is typically used in conventional PTPPs using thermal oil as HTF and relies on the electric FP through impedance and resistance heating. Although power plants using thermal oil also typically have a gas-fired backup heater, this study assumes that solely relying on the electric FP is possible under Southern African weather conditions. Additional carbon dioxide emissions can therefore be avoided by omitting such a gas-fired heater. For convenience later on, this strategy will be denoted as *freeze protection strategy 1* and will be referred to as FPS1 from now on. The electric FP is implemented as described in section 2.4.2 and is activated whenever the solar field outlet temperature drops below the FP temperature.

Freeze protection strategy 2 (FPS2) uses the same electric FP approach as in FPS1 but additionally uses the thermal energy stored in the hot tank. By doing so, the solar field inlet temperature can be increased in case the temperature of the fluid in the cold tank is not high enough to guarantee a solar field outlet temperature above the FP temperature T_{fp}. Figure 2.1 on page 22 shows the necessary addition of a three-way valve (in light grey), which allows hot fluid from the hot tank to be mixed with cooler fluid from the cold tank. An iterative feedback controller constantly monitors the solar field outlet temperature and adjusts the flow rate from the hot tank into the solar field inlet in order to keep the outlet temperature above the desired temperature. This approach helps to significantly reduce the usage of the electric FP system as long as there is enough hot fluid available in the hot tank. However, if there is no or only a small amount of hot fluid available in the hot storage tank, the electric FP system has to be turned on regardless. In order to minimise the occurrence of an empty storage tank, this approach reserves a certain percentage of the hot tank volume for the freeze protection strategy ($HT_{\text{level,fp}}$). Ideally, this reserved volume would be different every day, for example, during good weather periods when the reserved percentage can be lowered as it is expected that the FP system will not have to be turned on. However, this approach requires the implementation of a forecasting system, which lies outside the scope of this study. Therefore, a fixed daily reserved percentage is assumed for each power plant simulated in this study. The impact of this percentage is assessed in chapter 5 in order to maximise the net power plant output as a trade-off between thermal energy reserved in the hot tank and electric energy used for FP. Nevertheless, this method depletes the stored energy in the hot tank slightly faster, so that the optimiser converges towards larger storage tanks as compared to FPS1.

2.4.3 Collector defocusing

As mentioned above, in the event that the absorbed solar energy in the solar field requires a mass flow rate that exceeds the maximum allowable value to maintain the nominal solar field outlet temperature, the collectors need to

be defocused in order to avoid overheating of the HTF and the piping. To achieve this, simultaneous partial defocusing of all collectors in a loop is used. Employing this method, the incident solar flux $\dot{q}_{\text{inc}}$ on the receivers is simply scaled with

$$\dot{q}_{\text{inc}} = \dot{q}_{\text{inc}} \frac{\dot{q}_{\text{SF,max}}}{\dot{q}_{\text{SF,eff}}}, \tag{2.69}$$

using the ratio between the maximum allowable solar flux on the receiver $\dot{q}_{\text{SF,max}}$ and the effectively incident solar flux $\dot{q}_{\text{SF,eff}}$. The maximum allowable solar flux corresponds to the maximal possible heat transfer under maximum flow conditions:

$$\dot{q}_{\text{SF,max}} = \dot{m}_{\text{max}} c_{p,\text{HTF,avg}} (T_{\text{SF,des}} - T_{\text{SF,in}}). \tag{2.70}$$

Likewise, the effective solar flux is obtained with

$$\dot{q}_{\text{SF,eff}} = \dot{m}_{\text{loop}} c_{p,\text{HTF,avg}} (T_{\text{SF,out}} - T_{\text{SF,in}}). \tag{2.71}$$

Since this method requires an iterative approach, the incident solar flux is recalculated during each iteration until the solution converges. The required initial guess value for this approach is assumed to be the incident solar flux without collector defocusing.

2.4.4 Solar field sizing and pressure drop model

Apart from the air-cooled condenser, the electricity used by the HTF pumps represents the largest parasitic self-consumption in a PTPP. Therefore, they must be modelled accurately in order to account for the high electricity consumption that affects the net power production. Since the HTF is also pumped through the solar field at night in order to avoid freezing of the fluid in the pipes, the pump parasitic losses occur throughout the whole day but are highest when the solar field is in nominal operation (i.e. the HTF mass flow rate corresponds to the maximum design flow rate).

The following sections provide a short overview of the sizing process to obtain the diameters of the solar field piping, i.e. runners and headers, and the resulting pressure drop in the solar field. The total pressure drop is then used to calculate the required pumping power in section 2.7. The process of sizing the solar field piping and calculating the pressure drop mainly follows the approach from Wagner and Gilman (2011) and are presented in detail in Appendices D and E.

Solar field layout and sizing

The solar field piping model assumes an H-layout with four solar field subsections as illustrated in Figure 2.9. Starting from the power island — where the power block, TES and HTF system are located — at the centre of the plant, the HTF is pumped through two cold runner pipes in a North-South direction. Each runner pipe splits into two cold headers, each running to a

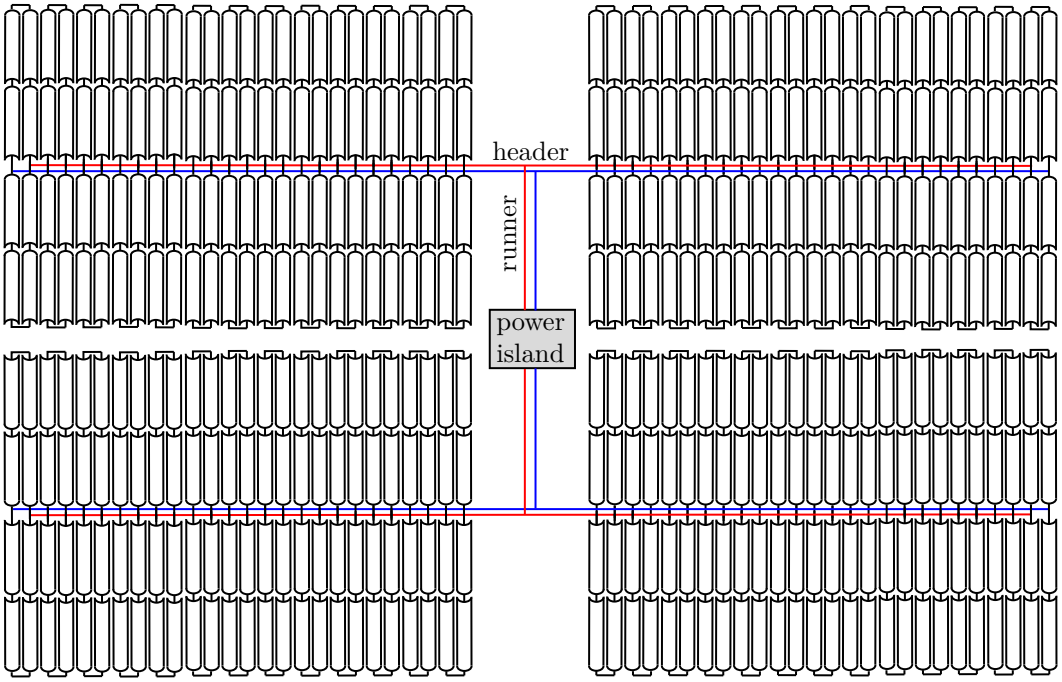

Figure 2.9: Solar field layout with central power island and hot (red) and cold (blue) runners and headers.

solar field subsection in a East-West direction. Each loop, consisting of four SCAs, is connected to a solar field subsection header and is orientated in a North-South direction. Each loop outlet is connected to the hot header, which collects the HTF from all loops and directs it to the hot runner leading back to the power island and into the hot tank.

In order to size the runner and header pipes, an allowable flow velocity range of the fluid is used, hence allowing the calculation of the pipe diameters. Here, a minimum flow velocity $v_{\min}$ of 1 m/s and a maximum flow velocity $v_{\max}$ of 3 m/s are assumed. Based on these flow limitations, the piping diameters can be calculated for the runners with

$$d_{\text{run}} = \sqrt{\frac{4\dot{m}_{\text{run}}}{\rho_{\text{HTF,avg}} v_{\max} \pi}}, \tag{2.72}$$

where $\dot{m}_{\text{run}}$ is the mass flow rate through each runner. Likewise, the diameter for each header section j ($d_{\text{hdr},j}$) can be obtained based on the mass flow rate $\dot{m}_{\text{sec},j,0}$ in the respective header section with

$$d_{\text{hdr},j} = \sqrt{\frac{4\dot{m}_{\text{sec},j,0}}{\rho_{\text{HTF,avg}} v_{\max} \pi}}. \tag{2.73}$$

A detailed description of this sizing process with all its underlying equations is provided in Appendix D.

Pressure drop model

The pressure drop model of the solar field is calculated for each of the three piping subcategories: runners, headers and loops. Furthermore, the pressure drop of pipe fittings (i.e. expansions/contractions, elbows, valves, weldolets and flexible hoses) is also taken into account. The detailed approach is presented in Appendix E. The total pressure drop in the solar field (ΔP_{SF}) can then be calculated as the sum of the pressure drops in each piping subcategory with

$$\Delta P_{\mathrm{SF}} = \Delta P_{\mathrm{loop}} + \Delta P_{\mathrm{hdr,h/c}} + \Delta P_{\mathrm{run,h/c}}, \tag{2.74}$$

where ΔP_{loop} is the pressure drop across the loops. $\Delta P_{\mathrm{hdr,h/c}}$ and $\Delta P_{\mathrm{run,h/c}}$ denote the pressure drops in the hot ($_{\mathrm{h}}$) and cold ($_{\mathrm{c}}$) header piping as well as the runner piping, respectively. ΔP_{SF} is subsequently used in section 2.7 to calculate the solar field pumping power as part of the plant's parasitic consumption.

Land area

To approximate the power plant's land area, the loop length L_{loop} and header pipe length $L_{\mathrm{hdr,base}}$ are needed, which are calculated with Eqs. (E.15) and (E.16) from Appendix E, respectively. The land area A_{land} is calculated with

$$A_{\mathrm{land}} = \left(L_{\mathrm{loop}} L_{\mathrm{hdr,base}} N_{\mathrm{SF,sec}} + A_{\mathrm{PB}}\right)\left(1 + f_{\mathrm{SF}}\right) 10^{-4}\,\mathrm{ha/m^2}, \tag{2.75}$$

and is given in [ha]. The number of solar field sections $N_{\mathrm{SF,sec}}$ is assumed to be limited to four sections (using an H-layout of the solar field). The area occupied by the power island (A_{PB}) is assumed to be $100\,000\,\mathrm{m^2}$, which corresponds to 10 ha. Lastly, the land area is increased by the factor f_{SF}, which is added to account for additional land areas required for roads, transmission lines, pipes, fencing, etc. This factor is assumed to be 20 %. This equation has also been used by Pan *et al.* (2019) to assess the increase of the required land area with increasing installed steam turbine capacities in MSPTPP as compared to central receiver plants.

2.5 Thermal Energy Storage

The TES is modelled as a pair of insulated cylindrical tanks, one cold tank and one hot tank. As opposed to conventional thermal oil PTPPs, using molten salts as HTF enables a direct storage integration. Thus, additional piping and expensive heat exchangers that are required to charge and discharge the TES in thermal oil plants can be omitted. The HTF simply enters the individual tanks either coming from the power block (cold tank) or the solar field (hot tank). Vice versa, the HTF is pumped from the cold tank through the solar field and from the hot tank to the power block (see Figure 2.1 for details).

2.5.1 Storage tank sizing and dynamic modelling

A schematic of the storage tank model is depicted in Figure 2.10. The fluid level in the tank varies during operation between the minimum tank height $h_{\text{tank,min}}$ and the maximum tank height h_{tank}. The minimum fluid height, also known as *heel height*, results from a mechanical limitation of the tank design due to the inlet and outlet pipes of the tank (e.g. the distribution ring header). Thus, a small portion of the fluid volume in the tank is unusable ($V_{\text{tank,min}}$). The fluid in the tanks is assumed to be homogeneously mixed and heat losses only occur to the ambient air. The sizing of the storage tanks is done in DYESOPT based on the user-specified storage full-load hours t_{TES}. Here, the sizing process is formulated in general terms (denoted $_{\text{tank}}$), which can be applied to both the cold and the hot tank with their respective thermo-physical fluid properties.

Multiplying the desired storage full-load hours with the cycle thermal requirement at design yields the thermal capacity of the TES system E_{TES}. The nominal cycle thermal requirement is simply the design gross steam turbine capacity $\dot{W}_{\text{gross}}$ divided by the design-point cycle thermal efficiency η_{PB}. Hence,

$$E_{\text{TES}} = \frac{\dot{W}_{\text{gross}} t_{\text{TES}}}{\eta_{\text{PB}}}. \tag{2.76}$$

The thermal capacity is used to calculate the volume of the tanks, assuming that each tank needs to be able to hold the entire HTF in the TES system:

$$V_{\text{tank}} = \frac{E_{\text{TES}}}{\rho_{\text{HTF}} c_{\text{p,HTF}} (T_{\text{SF,out}} - T_{\text{SF,in}})}. \tag{2.77}$$

Due to the decrease in density with higher temperatures, the hot fluid occupies a larger volume in the tank. Hence, the hot tank needs to be larger than the cold tank to contain the entire fluid volume. Finally, the tank diameter d_{tank}

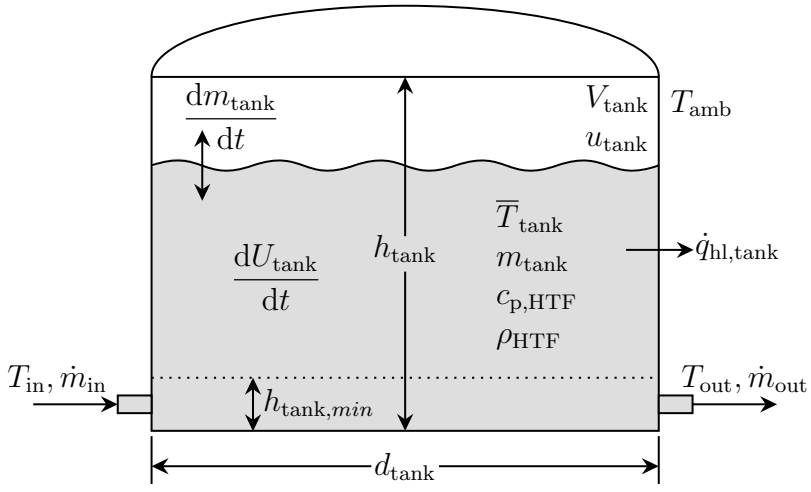

Figure 2.10: TES tank schematic as adapted from Wagner and Gilman (2011).

can be calculated with the tank volume and the user-specified tank height h_{tank}:

$$d_{\text{tank}} = 2\sqrt{\frac{V_{\text{tank}}}{\pi h_{\text{tank}}}}. \tag{2.78}$$

The storage tanks are implemented in TRNSYS by using the variable volume tank model (Type 39) from the standard TRNSYS library. The following section describes the tank model based on the TRNSYS mathematical reference for components (University of Wisconsin-Madison, 2014). The SAM model also uses the same tank model with a slightly modified methodology (Wagner and Gilman, 2011). In order to calculate the fluid temperature in the tank for each time step, an energy balance of the whole tank is required. Since the internal energy $U_{\text{tank}}(t)$, the fluid mass $m_{\text{tank}}(t)$ and the heat loss $\dot{q}_{\text{hl,tank}}(t)$ are all a function of time t, the energy balance of the tank can be defined as a differential equation with

$$\frac{\mathrm{d}\left[U_{\text{tank}}(t)m_{\text{tank}}(t)\right]}{\mathrm{d}t} = \dot{m}_{\text{in}}h(T_{\text{in}}) - \dot{m}_{\text{out}}h[T_{\text{tank}}(t)] - \dot{q}_{\text{hl,tank}}(t). \tag{2.79}$$

Similarly, the mass balance of the tank is simply the difference of inlet and outlet mass flows:

$$\frac{\mathrm{d}m_{\text{tank}}(t)}{\mathrm{d}t} = \dot{m}_{\text{in}} - \dot{m}_{\text{out}}. \tag{2.80}$$

Two instances during each time step are of particular interest, i.e. at the beginning of a time step ($t = 0$) and at the end ($t = \Delta t$). The former is used to define initial conditions for the differential equations, whereas the latter provides information about the state of the system at the end of each time step, which are then used as the initial conditions at the beginning of the next time step. Thus, the solution of Eq. (2.80) for the fluid mass in the tank at the end of the time step ($t = \Delta t$) is

$$m_{\text{tank}} = m_{\text{tank,0}} + \Delta t\left(\dot{m}_{\text{in}} - \dot{m}_{\text{out}}\right), \tag{2.81}$$

where $m_{\text{tank,0}}$ is the fluid mass at the beginning of the time step ($t = 0$). As per Wagner and Gilman (2011), the internal energy of the tank in reference to an arbitrarily chosen reference temperature T_{ref} (which will cancel out in further calculation) can be written as

$$\frac{\mathrm{d}U_{\text{tank}}(t)}{\mathrm{d}t} = c_{\text{p,tank}}(T_{\text{tank}}(t) - T_{\text{ref}}). \tag{2.82}$$

Similarly, the enthalpy $h(t)$ for both the incoming and outgoing mass flow is also a function of temperature with

$$h(t) = c_{\text{p,tank}}(T_{\text{t}} - T_{\text{ref}}), \tag{2.83}$$

where it can be assumed that the specific heat capacity of the fluid does not significantly vary during a time step. Therefore, the same specific heat capacity is used for both the inlet and outlet fluid properties. Lastly, the tank heat loss

to ambient at time t is simply

$$\dot{q}_{\text{hl,tank}}(t) = UA\,(T(t) - T_{\text{amb}})\,, \tag{2.84}$$

where UA is the overall heat transfer coefficient of the tank based on the tank heat loss coefficient u_{tank} (assumed to be $0.4\,\text{W}/(\text{m}^2\,\text{K})$ for both, the hot tank and the cold tank):

$$UA = u_{\text{tank}}\left(2\frac{V_{\text{tank}}}{h_{\text{tank}}} + \pi d_{\text{tank}} h_{\text{tank}}\right). \tag{2.85}$$

Equations (2.81) to (2.84) can now be substituted into Eq. (2.79), which can then be solved for the fluid temperature by enforcing the boundary condition that the fluid temperature T_{tank} at the beginning of the time step is equal to the temperature of the fluid at the end of the previous time step ($T_{\text{tank},0}$):

$$t = 0: \quad T_{\text{tank}} = T_{\text{tank},0}. \tag{2.86}$$

The solution for the fluid temperature at the end of a time step is then

$$T_{\text{tank}|t=\Delta t} = \frac{u_1}{u_2} + \left(T_{\text{tank},0} - \frac{u_1}{u_2}\right)\left(1 + \frac{c_{\text{p,HTF}}\Delta t}{m_{\text{tank},0}}\right)^{\frac{u_2}{u_3}}, \tag{2.87}$$

with

$$u_1 = \dot{m}_{\text{in}} T_{\text{in}} + \frac{UA\,T_{\text{amb}}}{c_{\text{p,HTF}}}, \tag{2.88}$$

$$u_2 = \dot{m}_{\text{in}} + \frac{UA}{c_{\text{p,HTF}}}, \tag{2.89}$$

$$u_3 = \dot{m}_{\text{in}} - \dot{m}_{\text{out}}, \tag{2.90}$$

as per University of Wisconsin-Madison (2014). The final fluid temperature at the end of the time step is then used as the tank temperature at the beginning of the next time step as per Eq. (2.86). However, since the final fluid temperature is not representative for the state of the system during the whole time step, the average fluid temperature is used as the outlet temperature of the tank ($T_{\text{out}} = T_{\text{tank,avg}}$). Integrating Eq. (2.87) over the time step t and dividing by the duration Δt of the time step yields the average fluid temperature in the tank as per University of Wisconsin-Madison (2014) assuming that $T_{\text{tank,avg}}(0) = T_{\text{tank,avg},0}$ at the beginning of the time step as the boundary condition:

$$T_{\text{tank,avg}|t=\Delta t} = \frac{u_1}{u_2} + \frac{m_{\text{tank},0}\left(T_{\text{tank},0} - \frac{u_1}{u_2}\right)}{\Delta t\,(u_3 - u_2)}\left[\left(1 + \frac{c_{\text{p,HTF}}\Delta t}{m_{\text{tank},0}}\right)^{\left(1-\frac{u_2}{u_3}\right)} - 1\right]. \tag{2.91}$$

To calculate the fill level of the tank, the following section shows the process by means of the hot tank, where the generic subscript $_{\text{tank}}$ is replaced with the subscript $_{\text{HT}}$ denoting the hot tank. The fill level HT_{level} of the hot tank is obtained by dividing the average volume of the fluid in the hot tank ($V_{\text{HT,avg}}$)

during a time step by the total volume of the tank:

$$HT_{\text{level}} = \frac{V_{\text{HT,avg}}}{V_{\text{HT}}}. \tag{2.92}$$

The average fluid volume in the tank is simply obtained by dividing the average fluid mass $m_{\text{HT,avg}}$ in the tank by the fluid density evaluated at the average fluid temperature $T_{\text{HT,avg}}$ with the fluid properties from section 2.3.8:

$$V_{\text{HT,avg}} = \frac{m_{\text{HT,avg}}}{\rho_{\text{HTF}}}, \tag{2.93}$$

$$m_{\text{HT,avg}} = \frac{m_{\text{HT,0}} + m_{\text{HT}}}{2}. \tag{2.94}$$

Based on Eq. (2.81), the mass in the hot tank m_{HT} at the end of a time step is

$$m_{\text{HT}} = m_{\text{HT,0}} + \Delta t \left(\dot{m}_{\text{HT,in}} - \dot{m}_{\text{HT,out}}\right). \tag{2.95}$$

Likewise, the fill level of the cold tank (CT_{level}) is calculated analogously to Eqs. (2.92) to (2.95) with the respective variables. Finally, the total mass of the fluid in the storage tanks is obtained by multiplying the volume of the hot tank with the density of the fluid at the storage design temperature ($T_{\text{HT,des}}$):

$$m_{\text{HTF}} = V_{\text{HT}} \rho_{\text{HTF}}. \tag{2.96}$$

2.5.2 Storage dispatch control

Due to the ability of CSP plants to operate as both baseload and peaking power plants, a storage dispatch control strategy is necessary. This control determines the hours during which hot fluid is sent from the hot tank to the steam generator based on a number of criteria. The implemented control logic is shown in Figure 2.11. In the case of baseload operation, the TES dispatch control is straightforward as the power cycle is simply operated whenever there is thermal energy available in the TES. However, in order to avoid starting up the power plant when there is only sufficient energy available for a short time (e.g. 30 minutes) a limitation is put into place where the control logic only allows the operation of the power block when there is a minimum amount of thermal energy available in the hot tank. Here, it is assumed that this minimum corresponds to an equivalent of 1 h of storage time (denoted as $t_{\text{req,PB}}$), which also equals the length of one time step in the simulations.

The required mass necessary in the hot tank to provide the power cycle with enough fluid for one hour ($m_{\text{req,PB}}$) is obtained by multiplying the tank volume at design V_{HT} with the fluid density and the ratio between the minimum storage time $t_{\text{req,PB}}$ required to run the power cycle at the nominal mass flow rate and the design storage hours t_{TES}:

$$m_{\text{req,PB}} = V_{\text{HT}} \rho_{\text{HTF}} \left(\frac{t_{\text{req,PB}}}{t_{\text{TES}}} + \frac{h_{\text{tank,min}}}{h_{\text{tank}}} \right). \tag{2.97}$$

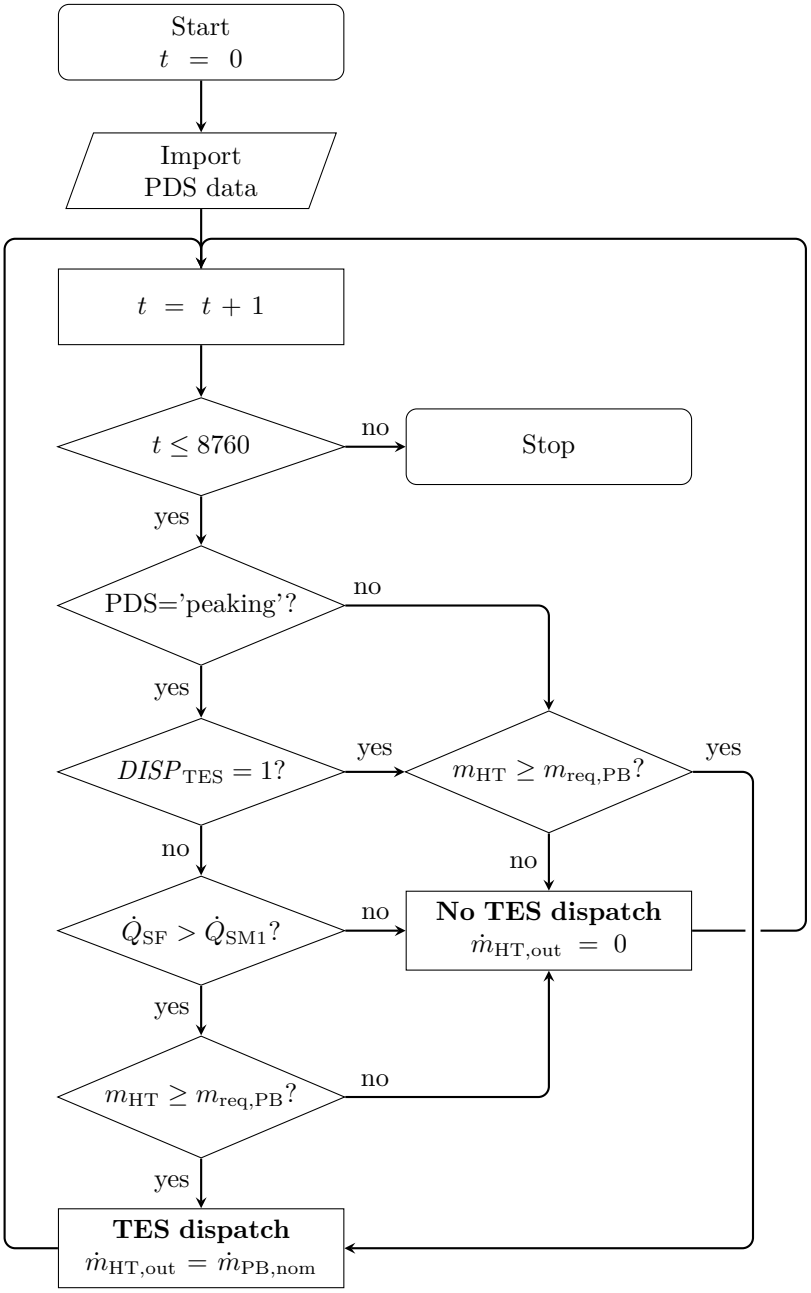

Figure 2.11: TES dispatch control logic.

The ratio between the storage tank fluid minimum height $h_{\text{tank,min}}$ and the tank height h_{tank} is added to account for the unusable amount of salt at the bottom of the tank. If the available salt mass in the HT (m_{HT}) is greater than the salt mass required by the power cycle ($m_{\text{req,PB}}$), the TES is dispatched by pumping the power block's nominal mass flow rate $\dot{m}_{\text{PB,nom}}$ to the steam generator. In the opposite case, no fluid leaves the hot tank and the TES will only be dispatched once enough energy is available in the hot tank.

The same concept of minimum required storage time is also applied to the

peaking strategy once the *predefined dispatch strategy* (PDS) has determined that the current hour is a peaking hour and that the TES should be dispatched ($DISP_{\text{TES}} = 1$). The PDS used in this study has been developed by Guédez *et al.* (2016) and a short summary will be provided here for coherence.

Before the start of the simulation process, this PDS determines on a daily basis during which hours the power cycle should be operated. The decision criterion for this predetermination is first and foremost the tariff available for the respective hours. By ranking the daily hours based on the tariff (highest to lowest), the PDS assigns a priority to hours with higher tariffs. This method requires a tariff structure with different tariffs during different hours of the day (as for example South Africa's two-tier tariff system implemented with BW3) which awards generation during peak times with a tariff 2.7 times higher than the base tariff. This tariff structure will be discussed in more detail in section 3.5.2. Likewise, the PDS can also be used with spot market prices, for example in the case of power plants participating in the *day-ahead market* (DAM) within the *Southern African Power Pool* (SAPP), as discussed in section 3.5.3. After ranking the day hours, the PDS estimates how many TES hours will be available for power generation during a given day based on a simplified solar field conversion efficiency. These available storage hours are then reserved for the hours with the highest tariffs in order to maximise profit. Any remaining hours, during which no thermal energy is available in the TES but the thermal output of the solar field is greater than the power cycle's required power, are assigned for operation as long as there is a tariff available. Hours with a tariff of zero are not served in order to conserve any potential residual energy in the TES for the next day or for FP during the night.

Since the PDS is used to determine the operating hours of the plant before the annual simulation and the efficiency calculation is only based on an estimation, the TES control logic re-evaluates the actual hours of operation during each time step of the simulation based on the flow chart in Figure 2.11. This guarantees that, in the case of a pre-assigned peaking hour where the TES does not actually have enough stored energy available (e.g. due to the usage for FP), the TES is not dispatched.

2.6 Power Cycle

In the power cycle, the hot HTF from the solar field and TES is pumped through the steam generator train, where its thermal energy is transferred from the molten salt side to the feed water side in order to produce steam. The thermal energy of the steam is then converted into mechanical energy through a steam turbine[21] and thereafter into electrical energy by a generator. CSP plants typically use a conventional steam Rankine cycle, which is depicted

[21] Any mentioning of a steam turbine will from now on always be referred to as a turbine.

as a schematic layout in Figure 2.1. The following sections present the Rankine cycle model, the underlying power plant control logic, the modelling of heat rejection using an air-cooled condenser and the electrical generator.

2.6.1 Rankine cycle model

Superheated steam Rankine cycles are the most used thermodynamic cycle not only in commercial CSP plants but also in large-scale conventional power generation systems like nuclear and fossil fuel-fired power stations. Therefore, the Rankine cycle is state-of-the-art and its fundamental functionality will not be discussed further here. Due to the complexity involved in the modelling of Rankine cycles, a number of well validated models for the individual components are available as part of simulation software libraries. To model the Rankine cycle, components from the STEC library are used in this study, as presented below. Due to the high variability of the solar resource in CSP plants, the power output of the steam cycle is highly dependent on the steam quality. Therefore, special consideration needs to be given to the modelling of the off-design performance of the steam turbine, which is presented in section 2.6.2 alongside the power block control logic and the turbine start-up curves.

The conversion efficiency of a Rankine cycle mainly depends on the cycle temperature difference between the superheated steam and the condensate. However, the condensate temperature is generally dependent on the cooling method used (i.e. wet or air-cooled) and with increasing concerns about water availability in arid regions where CSP plants are predominately built[22,23], the trend is to use less efficient air-cooled condensers. Thus, it is necessary to increase the steam temperature in the superheater in order to increase the cycle's efficiency. As mentioned in chapter 1, this can be achieved by using molten salts as HTF, which offer a higher upper temperature limit than the conventionally used thermal oils. In the case of Solar Salt for example, a solar field outlet temperature of 550 °C enables a live steam temperature of 535 °C. The maximum operating temperature also limits the operating pressure, which is typically in the range of 60 bar to 100 bar in CSP plants.

In order to perform a transient simulation of the power cycle, the individual components of the Rankine cycle need to be sized using an iterative approach. This is done through a steady-state design in DYESOPT as described by Ferruzza (2015), where the steam cycle design process is coupled with the design of the HTF side of the steam generator. The temperature, pressure and fluid properties at the inlets and outlets of each component are calculated

[22] In this context see for example Duvenhage (2019) on the strategic management of water resources for CSP plants in South Africa.

[23] A water consumption model considering water usage from the air-cooled condenser, steam cycle makeup, blowdown quench and mirror washing has also been implemented in this study but was beyond the scope of the analysis and is therefore not presented.

with equations from Incropera *et al.* (2007) and Staine (1995). These require several inputs by the user, for example, the temperature gradients in the steam generator or the pressure ratios of the steam turbine in order to calculate the turbine's isentropic efficiency and power output. Based on the resulting thermodynamic conditions, the required steam mass flow rate is approximated iteratively until the calculated power generation of the steam cycle converges to the desired electric power output of the plant. Once the enthalpies at the evaporator, *superheater* (SH) and *reheater* (RH) are known, the design of the HTF cycle is triggered. Based on the thermodynamic states on the steam side of the steam generator, the temperatures and fluid properties on the HTF side can be calculated. The HTF mass flow rate is then determined iteratively until the energy balances on the superheater and reheater on the HTF side converge to the water/steam side. With all mass flow rates and thermodynamic states now defined, the nominal performance parameters of each component can be calculated, e.g. the geometries and heat transfer coefficients of heat exchangers, the required thermal power of the power cycle or the nominal cycle thermal efficiency. This information is then used as input to the individual components for the dynamic modelling.

The dynamic model of the Rankine cycle is implemented in TRNSYS by using components from TRNSYS' *Heat Exchanger* library (University of Wisconsin-Madison, 2014) and the STEC library for solar thermal applications (Schwarzbözl, 2006). The relevant components are; Type 317 for the *preheaters* (PH), Type 320 for the feed water subcoolers, Type 315 for the economiser and superheater, Type 316 for the evaporator and Type 5 for the reheater. For the steam turbine, Type 318 has been used in conjunction with Type 389 for the controlled splitters at the turbine outlets. Lastly, Type 390 has been used for the condensate and feed water pumps. The *air-cooled condenser* (ACC) model has been developed by Guédez *et al.* (2016) and will be discussed in more detail in section 2.6.3. All components used for the transient modelling of the Rankine cycle have been validated in previous studies (for example by Jones *et al.*, 2001) and have been extensively used to study the performance of CSP plants such as in the works of Spelling (2013), Guédez (2016) and Ferruzza (2015). Therefore, these models will not be further described here. However, the turbine off-design operation, start-up times and cool-down periods are of more interest and will be discussed below as well as in section 2.6.2.

The off-design operation of the turbine is modelled through the calculation of a part-load efficiency of each turbine stage based on the approach presented by Lippke (1995). Here, the isentropic efficiency of a turbine stage (η_s) during off-design operation is dependent on the inlet and outlet pressures P_{in} and P_{out} of the turbine stage:

$$\frac{\eta_s}{\eta_{s,0}} = 1 + \alpha \left(\frac{P_{in}/P_{in,0}}{P_{out}/P_{out,0}} - 1 \right)^2 , \tag{2.98}$$

where $\eta_{s,0}$ is the nominal isentropic efficiency and $P_{in,0}$ and $P_{out,0}$ are the inlet and outlet pressures of the turbine stage at design-point conditions. The variable α allows the user to set the dependency of the off-design efficiency on the pressure ratios across each stage. For the purpose of this study, it is assumed that $\alpha = 0.1$ (Lippke, 1995). To calculate the inlet pressure of each stage, *Stodola's cone law*, or law of the ellipse, is used (Lippke, 1995), which relates the pressure difference over a turbine stage to the mass flow ratio of the nominal mass flow rate $\dot{m}_0$ and the off-design mass flow rate $\dot{m}$ with

$$\frac{\dot{m}^2}{\dot{m}_0^2} = \frac{P_{in}^2 - P_{out}^2}{P_{in,0}^2 - P_{out,0}^2}. \tag{2.99}$$

The steam mass flow rate at the turbine inlet is calculated based on the conditions of the molten salt at the steam generator inlet. The inlet pressure is then obtained as a function of the off-design mass flow rate, the outlet pressure and the nominal parameters with

$$P_{in} = \sqrt{\left(\frac{\dot{m}}{\dot{m}_0}\right)^2 \left(P_{in,0}^2 - P_{out,0}^2\right) + P_{out}^2}. \tag{2.100}$$

Since the back-pressure of the turbine is determined by the condenser (saturation pressure), the outlet pressure of the last turbine stage is known. Hence, the outlet pressure of each stage can be calculated, starting from the condenser (assuming no pressure losses between turbine stages). Similarly, the resulting inlet pressure of the first stage is simply the outlet pressure of the steam generator.

With the inner turbine efficiency obtained from Eq. (2.98), the enthalpy at the outlet of the turbine stage (h_{out}) can now be evaluated based on the inlet conditions of the turbine with

$$h_{out} = h_{in} - \eta_s \left(h_{in} - h_{out,s}\right), \tag{2.101}$$

where $h_{out,s}$ is the enthalpy at the turbine's outlet if the process was isentropic. The hourly mechanical power $\dot{W}_{HPT,h}$ of the *high pressure turbine* (HPT) can then be obtained with

$$\dot{W}_{HPT,h} = \dot{m}_{HPT,in,h} \eta_{mech} \left(h_{HPT,in,h} - h_{HPT,out,h}\right) \qquad \text{for } h = 1, \ldots, 8760. \tag{2.102}$$

where $\dot{m}_{HPT,in,h}$ is the steam mass flow rate into the high pressure turbine and η_{mech} is the turbine's mechanical efficiency. $h_{HPT,in,h}$ and $h_{HPT,out,h}$ are the enthalpy values of the steam at the inlet and outlet of the turbine stage, respectively. The mechanical power of the *low pressure turbine* (LPT) is calculated analogously with Eq. (2.102) using the respective values. For simplicity, the intermediate pressure turbine is integrated in this study as part of the LPT.

Finally, the power cycle thermal efficiency η_{PB} is calculated as the ratio of the net electric power output ($\dot{W}_{net}$) and the thermal input to the power block

($\dot{Q}_{\mathrm{PB}}$):

$$\eta_{\mathrm{PB}} = \frac{\dot{W}_{\mathrm{net}}}{\dot{Q}_{\mathrm{PB}}}. \tag{2.103}$$

The net power output is the electric power supplied to the grid, taking into account the parasitic self-consumption of the power block. This is calculated with Eq. (2.127) in section 2.7, which introduces the parasitic consumption.

The power cycle design parameters are summarised in Table 2.7 where the *terminal temperature differences* (TTD) of the individual heat exchangers in the steam generator train are also listed. Two HP and four LP steam extractions are assumed. The mechanical efficiency of the turbine is assumed to be 99 %, whereas the generator's efficiency is 97 %.

Table 2.7: Power cycle design parameters.

Parameter	Variable	Unit	Value
Number of HP steam extractions	-	[−]	2
Number of LP steam extractions[24]	-	[−]	4
TTD of superheater	ΔT_{SH}	[°C]	15
TTD of reheater	ΔT_{RH}	[°C]	15
TTD of economiser	ΔT_{EC}	[°C]	5
TTD of hot preheaters	$\Delta T_{\mathrm{PH,h}}$	[°C]	5
TTD of cold preheaters	$\Delta T_{\mathrm{PH,c}}$	[°C]	3
Mechanical efficiency	η_{mech}	[%]	99
Generator efficiency	η_{gen}	[%]	97

2.6.2 Power block control

The power block control logic depicted in Figure 2.12 is used to control when the power cycle is started up or shut down. The start-up and shut-down decisions are entirely dependent on the mass flow rate into the steam generator system, which is determined by the TES dispatch control presented in section 2.5.2. Once the TES dispatch control has determined that the power block should be operated in the current hour and there is sufficient energy available in the TES, hot HTF is pumped to the steam generator train and the power cycle is started.

The start-up time of the turbine depends on the maximal allowable temperature difference between the metal surface of the turbine and the steam as well as the rate at which the metal temperature can be brought to its nominal value (Ferruzza *et al.*, 2018). This rate depends on the initial turbine metal temperature and is higher the warmer the metal is. Hence, the warmer the turbine is before the start-up, the faster it can be brought up to its nominal

[24] The LP steam extractions include three extractions to preheaters and an additional extraction to the deaerator.

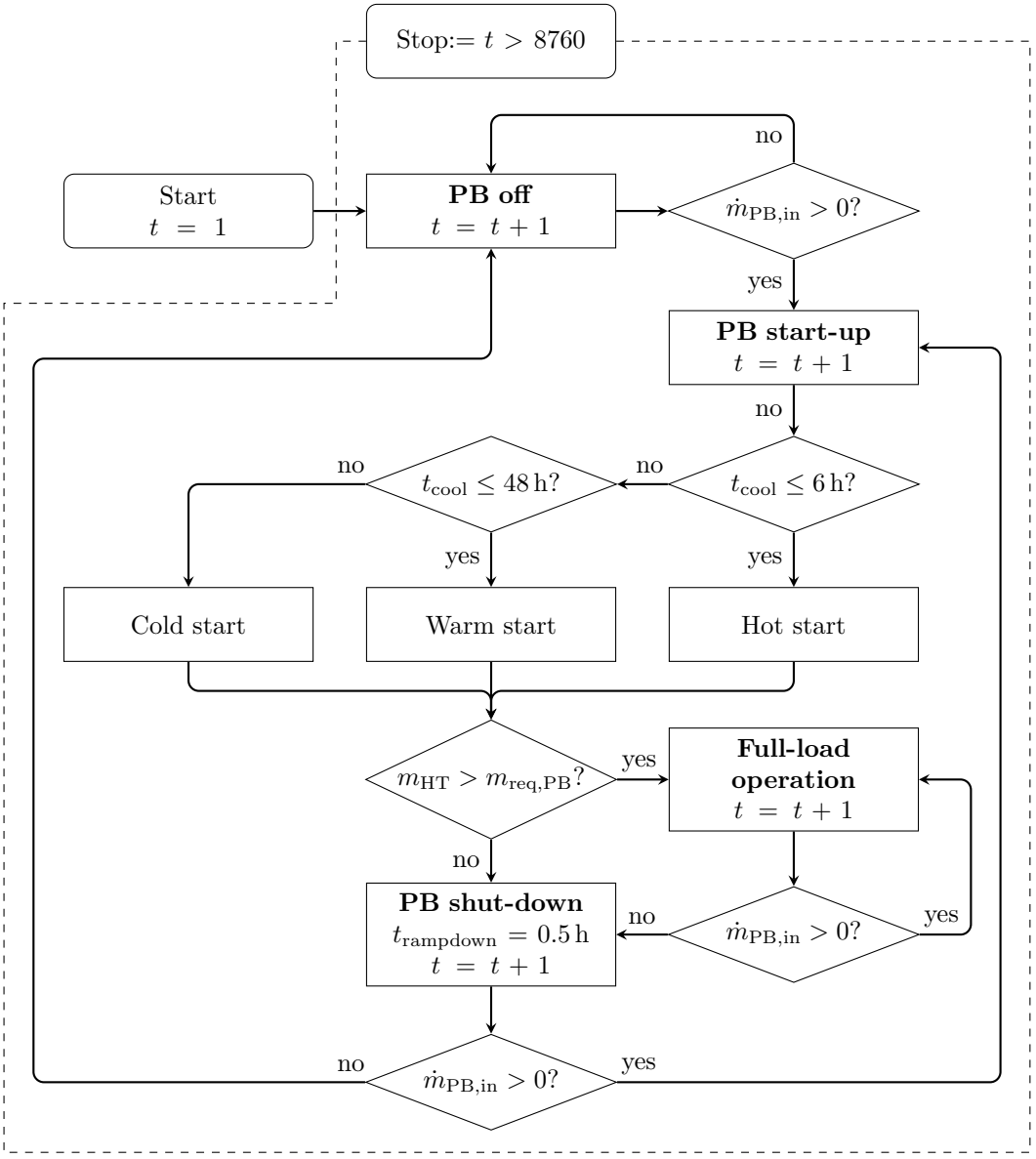

Figure 2.12: Power block control logic.

speed (Topel, 2014). In order to avoid thermal stresses and possible damage of the turbine, start-up curves are used to set the ramp-up rate until the nominal turbine load is reached. In order to bring the turbine to its nominal speed as fast as possible, these curves are determined by the manufacturer by minimising the required start-up time within the allowable thermal stress limits of the turbine. A set of three start-up curves that depend on the metal temperature of the turbine at start-up is typically used, namely for hot, warm and cold start-ups. The three start-up curves as adapted from Spelling *et al.* (2012) can be seen in Figure 2.13. However, instead of using the turbine metal temperature at start-up as the determining factor to choose the appropriate

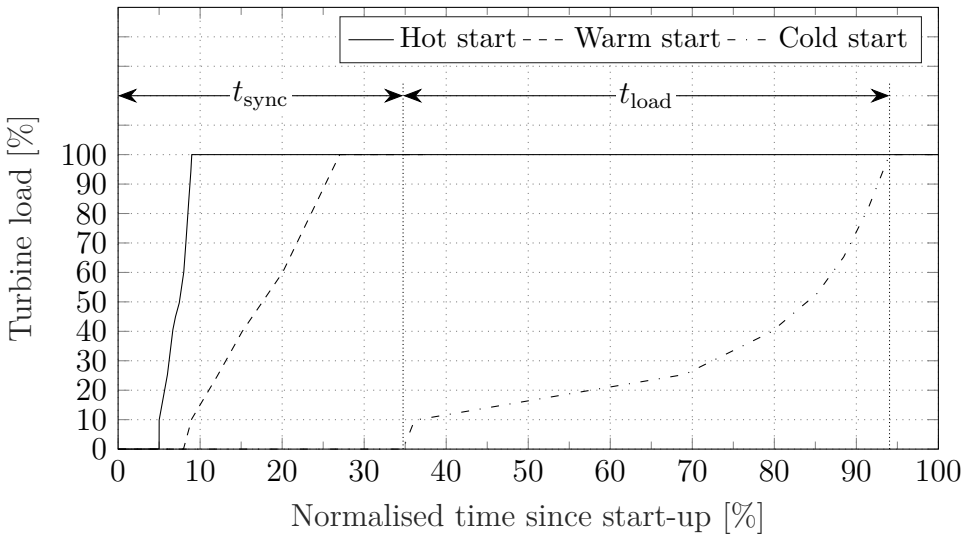

Figure 2.13: Start-up time to reach full turbine load for hot, warm and cold starts. The times for synchronising (t_{sync}) and loading up (t_{load}) the turbine are shown for the cold start as an example (adapted from Spelling *et al.*, 2012).

curve, this study bases the selection on the cool-down time t_{cool} since the turbine was last shut down. Table 2.8 lists the types of turbine starts and their corresponding cool-down periods (Guédez *et al.*, 2014*a*).

The start-up curves consist of two distinct time periods, i.e. the time necessary to reach synchronous speed (t_{sync}) and the time necessary for loading up (t_{load}) the turbine. The two periods are displayed for the case of a cold turbine start in Figure 2.13. In order to model the turbine start-up and shut-down behaviour, the "*turbcontrol*" component (Type 400) from the STEC library has been used as the turbine controller in TRNSYS. This controller has been developed by Jones *et al.* (2001) and uses the approach proposed by Stoddard *et al.* (1987) to introduce synchronisation and load-up delays for the three different types of turbine starts to the model. The turbine reaches its nominal load and starts producing electricity once the synchronisation and load-up periods are completed. If the available salt mass in the hot storage tank drops below the required mass to operate the turbine for one hour ($m_{HT} < m_{req,PB}$) before the synchronisation or load-up has been completed, the start-up is interrupted and the turbine is shut down again. However, since HTF from the hot TES

Table 2.8: Turbine cool-down times since last shut-down and corresponding types of turbine starts (Guédez *et al.*, 2014*a*).

Time since last turbine shut-down	Type of turbine start
$t_{cool} \leq 6\,h$	Hot start
$6\,h < t_{cool} \leq 48\,h$	Warm start
$t_{cool} > 48\,h$	Cold start

is only sent to the power block if there is enough fluid available to run the turbine for one hour, this only happens occasionally. The start-up cycle can also be interrupted if the required superheated steam conditions (temperature or pressure) are not met. Nonetheless, a ramp-down delay (t_{rampdown}) of 0.5 h is used for shutting down the turbine. This ramp-down delay is put in place in order to simulate the balancing of steam temperature and minimum pressure by the plant operator during shut-down in order to extend operation (Jones *et al.*, 2001). During this time, the turbine cannot be restarted when there is suddenly enough salt available in the TES and the power block start-up procedure can only be restarted once the ramp-down time has passed.

During start-up, the design power cycle mass flow rate $\dot{m}_{\text{req,PB}}$ is sent through the steam generator regardless of the type of turbine start. Although the mass flow rate would ideally be ramped up until the nominal mass flow is reached, this study mainly considers a large time step of 1 h, which would result in a mass flow ramp-up during just a fraction of the time step. This leads to an instantaneous jump in the electricity output from the start of the ramp-up phase to full-load operation in TRNSYS. Hence, to compensate for this short-coming, the electricity output is adjusted in post-processing in DYESOPT based on the start-up curves introduced in Figure 2.13. This is to account for the reduced power output due to the start-up delays and the part-load operation of the turbine during ramp-up.

The turbine shut-down is also controlled by the TES dispatch control in Figure 2.11 as it determines the mass flow to the power block based on the PDS or the available salt mass in the storage tank. Hence, if the power block is in operation and there is enough fluid available in the TES to run the power block for one hour but the PDS has determined that the current simulation hour is not a peak or base tariff hour (tariff of zero), no fluid is sent from the TES to the power block and the turbine is therefore shut down. This approach saves thermal energy in the TES for times of higher remuneration and for FP.

2.6.3 Air-cooled condenser

As already mentioned, an ACC is used for the heat rejection in the Rankine cycle. The TRNSYS model used in this study has been developed by Guédez *et al.* (2016) and is presented below. The condenser heat transfer rate is calculated based on the steam mass flow rate $\dot{m}_{\text{steam}}$ through the condenser and the enthalpy difference between the inlet and the outlet of the condenser:

$$\dot{Q}_{\text{CND}} = \dot{m}_{\text{steam}} \left(h_{\text{steam,in}} - h_{\text{steam,out}} \right) . \tag{2.104}$$

Assuming an even distribution of the steam mass flow through the condenser arrays and that the steam is fully condensed at the outlet (saturated liquid: $\chi = 0$), the enthalpy at the condenser outlet is obtained as a function of the saturation temperature T_{sat}:

$$h_{\text{steam,out}} = h \left(T_{\text{sat}}, \chi = 0 \right) . \tag{2.105}$$

The condenser air flow rate required to meet the target condensing temperature is calculated with

$$\dot{m}_{\text{air}} = \frac{\dot{Q}_{\text{CND}}}{c_{p,\text{air}} \left(T_{\text{air,out}} - T_{\text{air,in}}\right)}, \tag{2.106}$$

using the condenser heat transfer rate from Eq. (2.104) and the inlet and outlet air temperature. If the required air flow rate exceeds the condenser's maximum possible air flow rate, the condensing temperature is simply estimated based on the maximum air flow rate as per Eq. (2.110). The condensing pressure P_{sat} is determined as a function of the calculated saturation temperature. The condenser outlet temperature $T_{\text{air,out}}$ is calculated with

$$T_{\text{air,out}} = T_{\text{sat}} - T_{\text{TTD}}, \tag{2.107}$$

where T_{TTD} is the design terminal temperature difference (TTD) of the condenser. This represents the temperature difference between the steam saturation temperature T_{sat} at the corresponding saturation pressure P_{sat} and the outlet cooling water temperature, which in this case is assumed to correspond to the condenser outlet air temperature $T_{\text{air,out}}$. A typical range for the terminal temperature difference of surface condensers is 2 °C to 4 °C (Conradie and Kröger, 1996). With the required air flow from Eq. (2.106) and the specific heat capacity of the air, the condenser effectiveness can be calculated according to Conradie and Kröger (1996) with

$$\epsilon = 1 - \exp\left(-\frac{UA}{\dot{m}_{\text{air}} c_{p,\text{air}}}\right), \tag{2.108}$$

where UA is the overall heat transfer coefficient of the condenser. To obtain the condensing temperature and pressure, a simultaneous solution of Eqs. (2.104) to (2.108) is required. For off-design operation, this model uses a power-law relation to scale the condenser's overall heat transfer coefficient UA based on the reference value at design (UA_{ref}):

$$UA = UA_{\text{ref}} \left(\frac{\dot{m}_{\text{air}}}{\dot{m}_{\text{air,max}}}\right)^{UA_{\text{exp}}}. \tag{2.109}$$

The overall heat transfer coefficient is also linked to the ratio of the air mass flow rate through the condenser ($\dot{m}_{\text{air}}$) and the maximum possible air flow at design ($\dot{m}_{\text{air,max}}$). The maximum air flow is calculated with

$$\dot{m}_{\text{air,max}} = \frac{\dot{Q}_{\text{CND,des}}}{c_{p,\text{air}} \Delta T_{\text{air,nom}}}, \tag{2.110}$$

where $\dot{Q}_{\text{CND,des}}$ is the heat transfer through the condenser at design and is calculated with Eq. (2.104) under nominal conditions, $c_{p,\text{air}}$ is the specific heat capacity of air and $\Delta T_{\text{air,nom}}$ is the nominal air temperature difference between inlet and outlet of the fan. The scaling exponent UA_{exp} in Eq. (2.109) is assumed to be 0.8 and UA_{ref} is calculated based on Conradie and Kröger (1996) with

$$UA_{\text{ref}} = -\frac{\dot{m}_{\text{air,max}}\left(1-\epsilon_{\text{des}}\right)}{c_{p,\text{air}}}, \tag{2.111}$$

The effectiveness of the condenser at design (ϵ_{des}) is defined as the ratio of the heat transfer through the condenser from Eq. (2.104) at design conditions and the maximum possible heat transfer rate of the cooling air flow with

$$\epsilon_{\text{des}} = \frac{\dot{Q}_{\text{CND,des}}}{\dot{m}_{\text{air,max}} c_{p,\text{air}} \Delta T_{\text{split}}}, \tag{2.112}$$

as adapted from Patnode (2006). The nominal ACC split ΔT_{split} is the temperature difference between the condensing temperature and the ambient dry air temperature at design:

$$\Delta T_{\text{split}} = T_{\text{sat}} - T_{\text{dry}}. \tag{2.113}$$

2.6.4 Generator

The steam turbine is connected through a shaft to the *generator* (G) (see Figure 2.1), which converts the mechanical energy from the turbine into electrical energy. The hourly gross electricity output $\dot{W}_{\text{gross},h}$ of the power plant is calculated as the sum of each turbine stage's mechanical power from Eq. (2.102), multiplied by the generator efficiency η_{gen}, which is assumed to be 97 %:

$$\dot{W}_{\text{gross},h} = \left(\dot{W}_{\text{HPT},h} + \dot{W}_{\text{LPT},h}\right)\eta_{\text{gen}} \qquad \text{for } h = 1,\ldots,8760. \tag{2.114}$$

2.7 Parasitic Consumption

During the operation of CSP plants, auxiliary systems (such as the solar field pump and FP system) continuously use electric energy which reduces the net electric output of the power plant. This parasitic self-consumption needs to be taken into account as it reduces the power plant's overall *solar-to-electric* (S2E) efficiency. The largest load in an air-cooled plant are typically the condenser fans, followed by the solar field pump, which is kept operational throughout the night to circulate the HTF in order to keep all the components warm. A large share of parasitic consumption also falls on the FP system since large thermal losses in the solar field need to be compensated through impedance and resistance heating. The total parasitic load $\dot{W}_{\text{paras}}$ of the power plant is calculated as the sum of the loads of the individual auxiliary systems with

$$\dot{W}_{\text{paras}} = \dot{W}_{\text{pump,SF}} + \dot{W}_{\text{pump,TES}} + \dot{W}_{\text{pump,PB}} + \dot{W}_{\text{ACC}} + \dot{W}_{\text{fp}} + \dot{W}_{\text{track}}. \tag{2.115}$$

These systems include the solar field pump ($\dot{W}_{\text{pump,SF}}$), TES pump ($\dot{W}_{\text{pump,TES}}$), deaerator and condensate pump as part of the power block ($\dot{W}_{\text{pump,PB}}$), condenser fan ($\dot{W}_{\text{ACC}}$), FP system ($\dot{W}_{\text{fp}}$) and the tracking of the solar collectors ($\dot{W}_{\text{track}}$). The respective parasitic loads will be presented in the following sections.

Pumping power

The required pumping power of each pump in the power plant can be calculated with Eqs. (2.116) to (2.118). The work done by the solar field pump is determined based on the pressure drop ΔP_{SF} across the solar field (see Appendix E for details), the HTF mass flow rate $\dot{m}_{\mathrm{SF}}$, the HTF density $\rho_{\mathrm{CT,out}}$ at the outlet of the cold tank and the solar field pump efficiency η_{pump} with

$$\dot{W}_{\mathrm{pump,SF}} = \frac{\Delta P_{\mathrm{SF}} \dot{m}_{\mathrm{SF}}}{\eta_{\mathrm{pump}} \rho_{\mathrm{CT,out}}}. \tag{2.116}$$

The pump efficiency (including the electric motor) is assumed to be 85 % for all pumps. The electric power required for pumping in the power block is calculated as the sum of the power of the deaerator pump and the condensate pump with

$$\dot{W}_{\mathrm{pump,PB}} = \frac{\Delta P_{\mathrm{FW}} \dot{m}_{\mathrm{FW}}}{\eta_{\mathrm{pump}} \rho_{\mathrm{FW}}} + \frac{\Delta P_{\mathrm{CND}} \dot{m}_{\mathrm{CND}}}{\eta_{\mathrm{pump}} \rho_{\mathrm{CND}}}, \tag{2.117}$$

where ΔP_{D} is the feed water pressure drop in the deaerator, $\dot{m}_{\mathrm{FW}}$ is the feed water flow rate, η_{pump} is the pump efficiency, ΔP_{CND} is the pressure drop across the condenser and $\dot{m}_{\mathrm{CND}}$ is the condensate mass flow rate.

Lastly, the pumping power of the TES pump ($\dot{W}_{\mathrm{pump,TES}}$) is calculated based on the HTF mass flow rate at the hot tank outlet ($\dot{m}_{\mathrm{HT,out}}$), the specific TES pump coefficient $C_{\mathrm{pump,TES}}$, which is assumed to be 550 J/kg (Wagner and Gilman, 2011), and the time step Δt of the simulation in [s]:

$$\dot{W}_{\mathrm{pump,TES}} = \dot{m}_{\mathrm{HT,out}} \frac{C_{\mathrm{pump,TES}}}{\Delta t}. \tag{2.118}$$

Condenser fans

The condenser fans are responsible for the majority of the parasitic consumption in air-cooled power plants. This results in a reduction of the net electric output of the plant, which is caused by a significantly larger load in comparison to a wet-cooled design. Therefore, larger gross turbine capacities are typically required in order to maintain the same net capacity of a similarly sized wet-cooled power plant (Burkhardt *et al.*, 2011). This increases the investment costs of the air-cooled design since a larger turbine also requires a larger solar field and TES system. Nevertheless, the increased capital costs can be offset by increased energy production of the air-cooled design on cool days. Despite the less efficient power cycle of air-cooled plants, the parasitic load of the air-cooled condenser is lower than that of a wet-cooled design on cool days, which results in a higher net output of the plant. According to Burkhardt *et al.* (2011), an increase of 3 % in the annual energy production is seen compared to a wet-cooled design.

The calculation of the power consumption of the condenser fans uses a power-law relation that estimates the condenser power $\dot{W}_{\mathrm{ACC}}$ based on the

maximum reference value $\dot{W}_{\mathrm{ACC,max}}$ and the air mass flow ratio that is scaled by the UA scaling exponent UA_{exp} with:

$$\dot{W}_{\mathrm{ACC}} = \dot{W}_{\mathrm{ACC,max}} \left(\frac{\dot{m}_{\mathrm{air}}}{\dot{m}_{\mathrm{air,max}}} \right)^{UA_{\mathrm{exp}}}. \tag{2.119}$$

The maximum air flow rate at design ($\dot{m}_{\mathrm{air,max}}$) is calculated with Eq. (2.110) and the maximum fan power is obtained from

$$\dot{W}_{\mathrm{ACC,max}} = \frac{\Delta P_{\mathrm{fan}} \dot{V}_{\mathrm{air,max}}}{\eta_{\mathrm{fan}}}. \tag{2.120}$$

The fan static pressure rise at design (ΔP_{fan}) and the fan static efficiency (η_{fan}) are assumed to be 120 Pa and 60 %, respectively. The maximum air volume flow is calculated with

$$\dot{V}_{\mathrm{air,max}} = \dot{m}_{\mathrm{air,max}} \frac{\mathrm{R}_{\mathrm{air}} \left(T_{\mathrm{dry}} + 273.15\,^{\circ}\mathrm{C} \right)}{P_{\mathrm{amb}}}, \tag{2.121}$$

where the dry ambient air temperature T_{dry} and ambient pressure P_{amb} at design are assumed to be 35 °C and 10^5 Pa, respectively. The design parameters for the fan power consumption are listed in Table 2.9.

Table 2.9: ACC design parameters for fan power consumption calculation.

Parameter	Variable	Unit	Value
Fan static pressure rise	ΔP_{fan}	[Pa]	120
Fan static efficiency	η_{fan}	[%]	60
Dry ambient air temperature at design	T_{dry}	[°C]	35
Ambient pressure at design	P_{amb}	[Pa]	10^5
Specific heat capacity of air	$c_{p,\mathrm{air}}$	[J/(kg K)]	1000
Gas constant of air	$\mathrm{R}_{\mathrm{air}}$	[J/(kg K)]	287

Freeze protection

The parasitic power of the FP system $\dot{W}_{\mathrm{fp}}$ is the sum of the required power of the impedance heating system in the solar collectors ($\dot{W}_{\mathrm{fp,loop}}$) and of the resistance heating system in the interconnecting piping ($\dot{W}_{\mathrm{fp,piping}}$), which consists of the piping between collectors, cross-over piping, headers and runners:

$$\dot{W}_{\mathrm{fp}} = \dot{W}_{\mathrm{fp,loop}} + \dot{W}_{\mathrm{fp,piping}}. \tag{2.122}$$

According to Kearney *et al.* (2003), the electric power needed to heat an absorber tube is

$$\frac{m_{\mathrm{tube}} c_{p,\mathrm{tube}} \Delta T}{t} = \frac{I^2 \rho L_{\mathrm{tube}}}{A_{\mathrm{tube}}}, \tag{2.123}$$

where m_{tube} is the absorber tube mass, $c_{p,\mathrm{tube}}$ is the specific heat capacity of the absorber tube, ΔT is the temperature change due to heat tracing, t is the heating time, I is the impedance current, ρ is the electrical resistivity of the

absorber tube, L_{tube} is the length of the absorber tube and finally, A_{tube} is the metal cross-section of the absorber tube. Assuming a maximum impedance current of 400 A and an electrical resistivity of $7.2 \times 10^{-7}\,\Omega\,\text{m}$ for AISI 321 (Aerospace Specification Metals, n.d.), the maximal heating power of a SCA is 44.5 kW_{th}. This is enough to pre-heat the receiver tubes in approximately 30 minutes by 140 °C, assuming a specific heat capacity $c_{p,\text{tube}}$ of the absorber tube of 500 J/(kg K) (Aerospace Specification Metals, n.d.). This would be the case, for example, when pre-heating the absorber tubes from the minimum fluid temperature of Hitec XL (150 °C) to the operating temperature of 290 °C in the morning to avoid thermal stresses in the material. Likewise, the maximum power density of the impedance heating system is ~180 W/m which is enough to compensate for the heat loss up to an absorber tube temperature of 345 °C.

Since the thermal and electrical power in Eq. (2.123) are directly equated, the parasitic consumption of the impedance FP system $\dot{W}_{\text{fp,loop}}$ can be assumed to be equal to the sum of the FP heat transfer $\dot{q}_{\text{fp},i,j}$ of each segment n of all N_{SCA} collectors in a loop times the total number of loops in the solar field (N_{loop}):

$$\dot{W}_{\text{fp,loop}} = N_{\text{loop}} \sum_{j=1}^{N_{\text{SCA}}} \sum_{i=1}^{n} \dot{q}_{\text{fp},i,j}. \tag{2.124}$$

Similarly, the required electrical power for the resistance heating in the interconnecting piping is the sum of the required FP heat transfer rates $\dot{q}_{\text{fp,piping}}$ from Eq. (2.67) of each subcategory (i.e. from the piping connecting the collectors $\dot{q}_{\text{fp,coll}}$, cross-over piping $\dot{q}_{\text{fp,COP}}$, headers $\dot{q}_{\text{fp,hdr}}$ and runners $\dot{q}_{\text{fp,run}}$):

$$\dot{W}_{\text{fp,piping}} = \dot{q}_{\text{fp,coll}} + \dot{q}_{\text{fp,COP}} + \dot{q}_{\text{fp,hdr}} + \dot{q}_{\text{fp,run}}. \tag{2.125}$$

Solar field tracking

For the solar field tracking, linear actuators are typically used to accurately move the solar collectors into the required position. The parasitic load of the solar field tracking mechanism can be calculated with:

$$\dot{W}_{\text{track}} = C_{\text{track}} N_{\text{SCA}} N_{\text{loops}} \tag{2.126}$$

for N_{loops} loops with N_{SCA} solar collectors per loop. The tracking power coefficient (C_{track}) is assumed to be 125 W per SCA (Wagner and Gilman, 2011). Since the SCAs are standing still at night and during periods where the solar field is not in operation, the parasitic load from tracking only applies during hours of active tracking of the sun.

2.8 Technical Performance Indicators

Finally, in order to assess the technical and economic performance of PTPPs, the technical performance indicators need to be defined. The key indicators used in this study are the net electric energy output of the plant, the capacity

factor, the solar field efficiency and the solar-to-electric efficiency, which will be discussed hereinafter. These indicators have been chosen because they allow a high-level comparison of the overall technical plant performance when analysing a large range of different power plant configurations and operating strategies under different tariff structures. These indicators will be used in section 5.2 for a sensitivity analysis in order to identify design parameters that have the largest impact on the technical performance of a power plant.

2.8.1 Net electric energy output

The net electric energy output of the power plant is simply the difference between the generator's gross power output $\dot{W}_{\text{gross},h}$ from Eq. (2.114) and the parasitic power $\dot{W}_{\text{paras},h}$, multiplied by the time step Δt of the simulation in [h] and a factor for the plant availability & maintenance:

$$\dot{E}_{\text{net},h} = \left(\dot{W}_{\text{gross},h} - \dot{W}_{\text{paras},h}\right) \Delta t f_{\text{avail}} \qquad \text{for } h = 1, \ldots, 8760. \tag{2.127}$$

Since the time step in the annual performance evaluations is generally assumed to be one hour, the rate of work done per hour also equals the electric energy during said hour. The factor for the plant availability and maintenance accounts for periods of down-time of the turbine during which no electricity is generated and is assumed to be 96 %. This factor is applied in the form of a constant loss during each hour of the year.

The annually generated net electricity $E_{\text{net},t}$ in year t is then the sum of the hourly generated electricity $E_{\text{net},t,h}$ with

$$E_{\text{net},t} = \sum_{h=1}^{8760} E_{\text{net},t,h} \qquad \text{for } t = 1, \ldots, n_{\text{op}}, \tag{2.128}$$

where $E_{\text{net},t,h}$ is assumed to degrade with a degradation rate r_{deg} of 0.1 %/a based on the hourly generated electricity in year one ($E_{\text{net},h}$) from Eq. 2.127:

$$E_{\text{net},t,h} = E_{\text{net},h}(1 - r_{\text{deg}})^{t-1} \qquad \text{for } t = 1, \ldots, n_{\text{op}};\ h = 1, \ldots, 8760. \tag{2.129}$$

2.8.2 Capacity factor

The capacity factor is used to indicate the ratio between the power plant's maximum possible generation capacity and the actual generation over the period of a year (8760 h). Based on the annual electricity output in year one ($E_{\text{net},1}$) calculated with Eq. (2.128) and the gross turbine capacity at design ($\dot{W}_{\text{gross}}$), the capacity factor is given by

$$f_{\text{cap}} = \frac{E_{\text{net},1}}{\dot{W}_{\text{gross}} 8760\,\text{h}}. \tag{2.130}$$

2.8.3 Solar field efficiency

The solar field efficiency relates the effectiveness of the solar collectors and receivers to convert the solar irradiance into thermal energy. Hence, the solar field efficiency η_{SF} is calculated with

$$\eta_{\text{SF}} = \frac{\dot{Q}_{\text{SF}}}{I_{\text{b}} A_{\text{SF}}}, \tag{2.131}$$

where $\dot{Q}_{\text{SF}}$ is the thermal output of the solar field, I_{b} is the beam irradiance and A_{SF} is the total aperture area of the solar field.

2.8.4 Solar-to-electric efficiency

Lastly, the overall power plant efficiency is measured in terms of the solar-to-electric efficiency η_{S2E}, which indicates the effectiveness of the plant to convert solar irradiance into electric energy. The solar-to-electric efficiency is then simply the ratio between the net power plant output $\dot{W}_{\text{net}}$ and the product of the beam irradiance and the total solar field aperture area:

$$\eta_{\text{S2E}} = \frac{\dot{W}_{\text{net}}}{I_{\text{b}} A_{\text{SF}}}. \tag{2.132}$$

2.9 Summary

In this chapter, a detailed two-dimensional solar collector model — based on the Ultimate Trough collector in combination with the HCEMS-11 receiver — was presented for the use with molten salts as HTF. Alongside the conduction and convection heat transfer of the receiver, a simplification of the receiver heat loss calculation was introduced that uses an empirical correlation of the heat loss with the outer surface temperature of the absorber tube. In order to further simplify the model, the thermal capacitance of the HTF and the absorber tube are assumed to be lumped together. This assumption was validated through the Biot number which requires each SCA to be discretised into at least 30 CVs.

Next, the solar field control, layout, sizing and pressure drop were presented alongside two FPSs. FPS1 entirely relies on electric FP through impedance and resistance heating of the solar field piping, whereas FPS2 additionally uses thermal energy stored in the hot tank to prevent freezing of the HTF. The remaining component models for the TES and power block were presented including their respective controls and operating strategies. A description of the parasitic consumption from pumps, condenser fans, FP and solar field tracking is also provided. Finally, the key technical performance indicators (i.e. the net electric energy output, capacity factor, solar field efficiency and solar-to-electric efficiency) were defined and will be used in chapter 6 for the multi-objective optimisation of MSPTPPs.

Chapter 3

Economic Model

In the following sections, a 2018-cost model for *molten salt parabolic trough power plants* (MSPTPP) in Southern Africa is formulated. The economic model calculates the direct and indirect capital costs based on specific investment costs for the power plant components and considers location-dependent financing costs and inflation rates for South Africa and Namibia. *Power purchase agreement* (PPA) tariffs for the baseload and two-tier tariff structures correspond to the average tariffs paid through the *Renewable Energy Independent Power Producer Procurement* (REIPPPP) in 2018 as reported by the Department of Energy (2019*a*). *Day-ahead market* (DAM) prices are based on the effective hourly prices of 2018 for Eskom's control area which includes South Africa and Namibia (SAPP, 2020). All values reported in ZAR refer to *South African Rand* and values in $ refer to *United States Dollar* (USD).

3.1 Currency and Inflation

The economic model uses a mix of both ZAR and USD based data from different years. In order to formulate a cost model for 2018, all costs and tariffs were indexed and deflated to 2018. The capital cost data is based on specific costs for the power plant components in USD and has been indexed to $\$_{2018}$ using the *Chemical Engineering Plant Cost Index* (CEPCI) from Chemical Engineering (2018) or the Producer Price Index (BLS, 2019) where applicable. The financial boundary conditions for the tariffs, operating costs and financing costs are location-tailored to South Africa and Namibia and are ZAR-based. This also includes PPA tariffs and DAM prices.

All cost data that was only available in $ was converted to ZAR using the yearly average exchange rate of 2018 (X-Rates, 2019*c*). By doing so, the economic model is ZAR-based and uses South African and Namibian inflation rates to calculate the financial metrics of the power plants in ZAR. However, all costs and tariffs are expressed in $\$_{2018}$ throughout this study in order to allow an easier comparison with other studies. Finally, the results of the economic

assessment (i.e. the financial metrics) were converted post-simulation from ZAR to $ using the average exchange rate of 2018 (X-Rates, 2019*c*). This enables the comparability of the results from this study with data reported in international studies. The additional inflation of the USD has not been taken into account. Hence, the model is ZAR-based but expressed in USD terms for 2018.

3.2 Capital Costs

The *capital expenditure* (CAPEX) of a power plant represents the total installed costs in year zero and is calculated with Eq. (3.1). This includes the direct capital costs (C_{direct}) for components, infrastructure and installation as well as indirect capital costs (C_{indirect}) that cannot be attributed to a specific component, such as land costs. Lastly, short-term construction financing costs (C_{con}) are also assumed to be included as part of the capital costs.

$$CAPEX = C_{\text{direct}} + C_{\text{indirect}} + C_{\text{con}}. \tag{3.1}$$

3.2.1 Direct and indirect capital costs

The direct capital costs include equipment costs for the solar field (C_{SF}), the TES (C_{TES}), the power block (C_{PB}), the *balance of plant* (BOP) (C_{BOP}) and the transmission line to the closest substation (C_{trans}). The direct capital costs are calculated with

$$C_{\text{direct}} = (C_{\text{SF}} + C_{\text{TES}} + C_{\text{PB}} + C_{\text{BOP}} + C_{\text{trans}})(1 + f_{\text{cont}}). \tag{3.2}$$

Contingencies for unexpected cost uncertainties are included as a percentage of the total equipment costs through the factor f_{cont}. A contingency of 7 % is assumed throughout this study (NREL, 2018). The individual equipment costs are discussed in sections 3.2.2 to 3.2.5.

Indirect capital costs include the costs of land (C_{land}), engineering, procurement and construction costs (C_{EPC}) and the sales tax ($C_{\text{tax,sales}}$). These indirect capital costs are discussed in sections 3.2.6 to 3.2.8:

$$C_{\text{indirect}} = C_{\text{land}} + C_{\text{EPC}} + C_{\text{tax,sales}}. \tag{3.3}$$

The construction financing costs are calculated with

$$C_{\text{con}} = \frac{n_{\text{con}}}{2} i_{\text{con}} (C_{\text{direct}} + C_{\text{indirect}}) + f_{\text{upfront}} (C_{\text{direct}} + C_{\text{indirect}}), \tag{3.4}$$

assuming a construction period n_{con} of two years, where i_{con} is the annual interest rate assuming that the total construction balance is only outstanding for half of the construction period (NREL, 2018) and f_{upfront} is the up-front fee for the construction financing. The construction financing costs are assumed to be 4 % for the interest rate and 1 % for the up-front fee (NREL, 2018).

The general equation for calculating the cost C_{comp} of each plant component of size X_{comp} is based on SAM's cost scaling model (NREL, 2013*a*) with

$$C_{\text{comp}} = c_{\text{comp}}^{\text{ref}} X_{\text{comp}}^{\text{ref}} \left(\frac{X_{\text{comp}}}{X_{\text{comp}}^{\text{ref}}} \right)^{s_{\text{comp}}}, \tag{3.5}$$

where the reference specific direct component costs $c_{\text{comp}}^{\text{ref}}$ (as reported in Table 3.1) are scaled based on the reference component size $X_{\text{comp}}^{\text{ref}}$, using the scaling exponent s_{comp}. The specific component costs for the site preparation, power block, balance of plant and TES are based on SAM's parabolic trough and central receiver plant cost assumptions for 2018 (Turchi *et al.*, 2019). The reference component sizes for the cost scaling of these components are based on SAM's reference parabolic trough plant with 111 MW gross turbine capacity, 6 h TES and a solar multiple of 2, as well as SAM's central receiver reference plant with 115 MW gross turbine capacity, 10 h TES and a solar multiple of 2.4, where applicable (Turchi *et al.*, 2019).

The SCA and HTF costs are based on DLR's parabolic trough cost assumptions for 2015, using a reference plant with 160 MW gross turbine capacity, 7.5 h TES and a solar multiple of 2 (Dieckmann *et al.*, 2017). The DLR cost data for 2018 has been calculated by applying the cost reductions proposed by Dieckmann *et al.* (2017) from 2015 to 2025, assuming a linear learning curve and indexing it from 2015 to 2018 using the CEPCI (Chemical Engineering, 2018). All cost scaling exponents have been taken from NREL (2013*a*).

For comparison (and later use in section 4.3), the component costs of a thermal oil PTPP are also listed in Table 3.1. This data is based on the same cost data references as discussed above. The costs for the power block and balance of plant are significantly lower for thermal oil PTPPs due to the lower temperature and pressure levels in the steam cycle as compared to a MSPTPP. Therefore, cheaper materials (and thinner piping wall sizes) can be used in the power block piping and steam generator. Although Solar Salt is assumed to be used as the storage medium in the TES, the lower operating temperature difference of thermal oil PTPPs also reduces the thermal energy storage capacity of the TES, which leads to higher storage system costs (excluding the fluid). In contrast, it is assumed according to Dieckmann *et al.* (2017) that the HTF system costs of a thermal oil PTPP are equal to those of a power plant using molten salt as HTF. The researchers suggest that the costs saved from omitting the TES heat exchangers in a molten salt PTPP are offset by increased costs due to additional piping and freeze protection equipment when using molten salt as HTF (e.g. more expensive materials and higher costs of valves).

Lastly, a so-called location factor of 10 % (f_{loc}) is added to the direct capital costs of the SCAs, TES, power block and balance of plant due to the high costs incurred due to the typically required import of specialised equipment (e.g. receivers, turbine, heat exchangers, generator, drives etc.) into Southern Africa as well as to factor in higher costs for local raw materials, which can be

Table 3.1: Summary of the specific direct and indirect component cost assumptions and scaling exponents for CAPEX calculation in $\$_{2018}$ (Dieckmann *et al.*, 2017; Turchi *et al.*, 2019; NREL, 2013*a*; Telsnig *et al.*, 2013; Industry Sources, 2018; Liu *et al.*, 2016; Poole, 2017). All cost data indexed to 2018 using the CEPCI (Chemical Engineering, 2018).

Parameter	Unit	$c_{\text{comp}}^{\text{ref}}$ / f_{fin}				s_{comp} [-]
Direct capital costs						
Site preparation	[\$/m^2]	25				0.9
Solar collector arrays	[\$/m^2]	150.5				-
HTF system (excl. fluid)	[\$/m^2]	41.2				0.9
Transmission line	[mil. \$/km]	1.32				-
Contingencies	[%]	7				-
Heat transfer fluid		Thermal oil	Solar Salt	Hitec	Hitec XL	
Power block	[\$/kW$_{\text{gross}}$]	910	1040	1040	1040	0.8
Balance of plant	[\$/kW$_{\text{gross}}$]	90	290	290	290	0.8
Fluid costs	[\$/t]	5150	800	1071	1430	-
TES (excl. fluid)[1]	[\$/kWh$_{\text{th}}$]	38.8	13.4	21.1	23.2	0.8
Indirect capital costs						
Land	[\$/m^2]	0.2				-
EPC	[%]	11				0.9
Sales tax	[%]	15				-

over 20 % more expensive than in overseas countries (GIZ, 2013). These higher material costs, combined with a lower local labour productivity, as compared to Europe or the United States, can result in 5 % to 300 % higher overall costs in South Africa (GIZ, 2013). However, a 300 % increase in costs is not expected to be realistic for the entire power plant costs but rather only single components. Hence, a location factor that represents a 10 % addition to the direct capital costs can be assumed to be adequate and optimistic. The overall cost assumptions are validated against existing CSP projects in South Africa in section 4.3, namely, the Bokpoort and Kathu parabolic trough plants.

[1] For thermal oil, the specific TES costs were estimated by subtracting the HTF costs from SAM's reference PTPP with a TES capacity of 943 MW h$_{\text{th}}$ and a salt mass of 27 400 t (Turchi *et al.*, 2019). For the molten salts, the specific TES costs were estimated by subtracting the HTF costs from SAM's reference central receiver plant with a TES capacity of 2350 MW h$_{\text{th}}$ and a salt mass of 27 400 t (Turchi *et al.*, 2019). This was then adjusted to match the equivalent storage capacity with the respective operating temperature difference and heat capacity of the various HTFs (see Table 2.5).

3.2.2 Solar field

The capital costs of the solar field (C_{SF}) include the costs for site preparation (C_{site}), the SCAs (C_{SCA}) and the HTF system ($C_{\mathrm{HTF,sys}}$). They are calculated with

$$C_{\mathrm{SF}} = C_{\mathrm{site}} + C_{\mathrm{SCA}} + C_{\mathrm{HTF,sys}}. \tag{3.6}$$

The individual cost items are discussed below, including a description of the cost reduction of the SCAs through production volume scaling.

Site preparation

The site preparation costs include costs for clearing, levelling and terracing of the site as well as for infrastructure such as roads, fences, water supply, drainage and wind protection. The site preparation costs are based on SAM's cost assumptions for PTPPs and are scaled based on the reference reflective solar field area $A_{\mathrm{refl}}^{\mathrm{ref}}$ of SAM's reference parabolic trough plant with 949 888 m^2 (Turchi *et al.*, 2019):

$$C_{\mathrm{site}} = c_{\mathrm{site}}^{\mathrm{ref}} A_{\mathrm{refl}}^{\mathrm{ref}} \left(\frac{A_{\mathrm{refl}}}{A_{\mathrm{refl}}^{\mathrm{ref}}} \right)^{s_{\mathrm{site}}}. \tag{3.7}$$

Solar collector array

The capital costs of the SCAs (C_{SCA}) are calculated based on the total reflective solar field aperture area A_{refl} with

$$C_{\mathrm{SCA}} = c_{\mathrm{SCA}} A_{\mathrm{refl}}, \tag{3.8}$$

where c_{SCA} is the sum of the specific sub-component costs for the Ultimate Trough collector from Dieckmann *et al.* (2017). These include the collector structure, receivers, mirrors, drives, cabling, pylons and foundations. Since SCA costs are reduced with an increasing volume of production due to the economy of scale effect, the SCA costs are scaled based on the respective production volume. This production volume scaling uses the progress ratio approach from Sargent & Lundy (2003) which allows the estimation of the cost reduction for each doubling of the cumulative production volume based on the number of SCAs (N_{SCA}). Furthermore, a location factor f_{loc} of 10 % is applied to account for the increased material and import costs in Southern Africa as discussed at the end of section 3.2.1. Thus, the specific SCA costs, including the production volume scaling effect and the location factor, are calculated with

$$\begin{aligned} \{\text{specific cost}\} &= \{\text{reference cost}\} \cdot \{\text{volume scaling}\} \cdot \{\text{location factor}\} \\ c_{\mathrm{SCA}} &= \sum_{i=1}^{n} c_{\mathrm{SCA},i}^{\mathrm{ref}} \cdot pr_i^{\log_2 \frac{N_{\mathrm{SCA}}}{N_{\mathrm{SCA}}^{\mathrm{ref}}}} \cdot (1 + f_{\mathrm{loc}}). \end{aligned} \tag{3.9}$$

The specific SCA sub-component costs $c^{\text{ref}}_{\text{SCA},i}$ are listed in Table 3.2 together with the corresponding progress ratios pr_i. The reference production volume of SCAs ($N^{\text{ref}}_{\text{SCA}}$) from Dieckmann *et al.* (2017) is 880. Compared to the DLR costs of 150.5 \$/m^2, this results in specific SCA costs of 165.6 \$/m^2 including the location factor of 10 % for the same solar field size in Southern Africa. The specific SCA costs are shown in Figure 3.1 as a function of the production volume. It can be seen that the specific SCA costs reduce exponentially with an increasing SCA production volume, approaching a minimum of 150 \$/m^2. In terms of individual component costs, no single component can be identified of which the costs are significantly more sensitive to an increasing production volume compared to any other component.

Table 3.2: Specific direct SCA component costs[2] (Dieckmann *et al.*, 2017) and progress ratios (Sargent & Lundy, 2003).

SCA component i	$c^{\text{ref}}_{\text{SCA},i}$ [\$/m^2]	pr_i [-]
Collector structure	67.2	0.92
Receivers	26.6	0.92
Mirrors	22.8	0.92
Pylons & foundations	22.4	0.92
Drives	7.1	0.94
Cabling	4.4	1.00
Total specific SCA cost ($c^{\text{ref}}_{\text{SCA}}$)	150.5	-

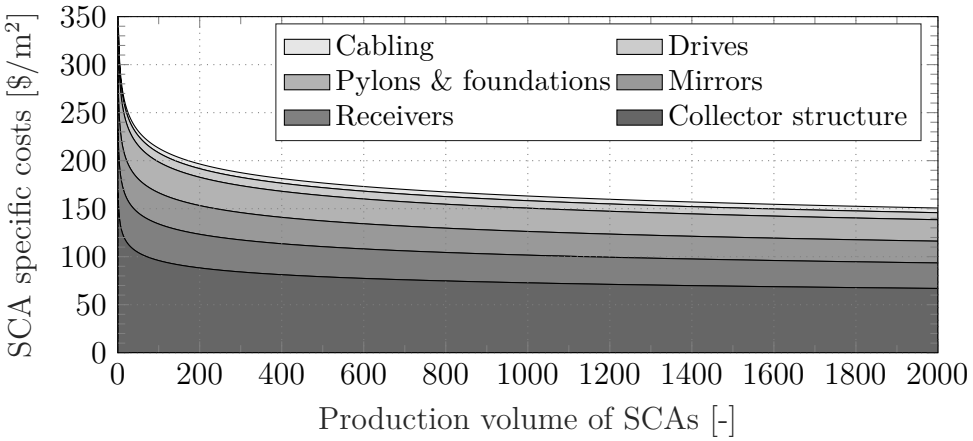

Figure 3.1: Specific SCA costs as a function of production volume.

[2] DLR cost data for 2018 has been calculated by applying the cost reductions proposed by Dieckmann *et al.* (2017) from 2015 to 2025, assuming a linear learning curve and indexing it from 2015 to 2018 using the CEPCI (Chemical Engineering, 2018).

HTF system

The HTF system includes the freeze protection system, ullage system, HTF pumps, expansion vessels, solar field runner and header piping, power block piping, foundations and support structures (Kurup and Turchi, 2015). The HTF system costs $C_{\mathrm{HTF,sys}}$ are calculated with Eq. (3.10), based on the specific costs $c^{\mathrm{ref}}_{\mathrm{HTF,sys}}$ from the DLR cost data (Dieckmann *et al.*, 2017) which are scaled according to the reference reflective solar field area $A^{\mathrm{ref}}_{\mathrm{refl}}$ of 1 510 000 m^2. The location factor of 10 % also applies here.

$$C_{\mathrm{HTF,sys}} = c^{\mathrm{ref}}_{\mathrm{HTF,sys}} A^{\mathrm{ref}}_{\mathrm{refl}} \left(\frac{A_{\mathrm{refl}}}{A^{\mathrm{ref}}_{\mathrm{refl}}} \right)^{s_{\mathrm{HTF,sys}}} (1 + f_{\mathrm{loc}}) + C_{\mathrm{HTF,SF}}. \tag{3.10}$$

The HTF costs $C_{\mathrm{HTF,SF}}$ are calculated based on the total fluid mass $m_{\mathrm{HTF,SF}}$ in the solar field and HTF system at design with

$$C_{\mathrm{HTF,SF}} = c^{\mathrm{ref}}_{\mathrm{HTF}} m_{\mathrm{HTF,SF}}, \tag{3.11}$$

where

$$c^{\mathrm{ref}}_{\mathrm{HTF}} = \begin{cases} 800\,\$/\mathrm{t}, & \text{for Solar Salt (Turchi } \textit{et al.}\text{, 2019)} \\ 1071\,\$/\mathrm{t}, & \text{for Hitec (Industry Sources, 2018)} \\ 1430\,\$/\mathrm{t}, & \text{for Hitec XL (Liu } \textit{et al.}\text{, 2016).} \end{cases} \tag{3.12}$$

The HTF system costs, including the fluid costs in Table 3.1, are indicated based on the HTF system costs from Dieckmann *et al.* (2017) plus the fluid costs assuming that an HTF volume in the solar field of 4458 m^3 for a plant corresponding to SAM's reference parabolic trough plant with 949 888 m^2 reflective aperture area. The total HTF system costs in the model are based on the actual calculated fluid mass in the solar field as per Eq. (3.10).

3.2.3 Thermal energy storage

The TES costs (C_{TES}), including the hot and cold storage tanks, immersion heaters and the storage fluid, are based on the cost assumptions of SAM's central receiver reference plant with a reference TES capacity $E^{\mathrm{ref}}_{\mathrm{TES}}$ of 2350 MWh$_{\mathrm{th}}$ (Turchi *et al.*, 2019). This is due to the direct storage integration as opposed to SAM's reference parabolic trough plant, which uses thermal oil as HTF and therefore has an indirect TES. These costs have been adjusted to the respective operating temperature difference and heat capacity of the various HTFs for the use in MSPTPPs (see Table 2.5). The location factor of 10 % is also applied here:

$$C_{\mathrm{TES}} = c^{\mathrm{ref}}_{\mathrm{TES}} E^{\mathrm{ref}}_{\mathrm{TES}} \left(\frac{E_{\mathrm{TES}}}{E^{\mathrm{ref}}_{\mathrm{TES}}} \right)^{s_{\mathrm{TES}}} (1 + f_{\mathrm{loc}}) + C_{\mathrm{HTF,TES}}, \tag{3.13}$$

with

$$c_{\mathrm{TES}}^{\mathrm{ref}} = \begin{cases} 13.4\,\$/\mathrm{kWh_{th}}, & \text{for Solar Salt,} \\ 21.1\,\$/\mathrm{kWh_{th}}, & \text{for Hitec,} \\ 23.2\,\$/\mathrm{kWh_{th}}, & \text{for Hitec XL.} \end{cases} \tag{3.14}$$

Similar to the HTF system costs, the fluid costs for the TES are calculated based on the total HTF mass at design in the cold and hot storage tanks with

$$C_{\mathrm{HTF,TES}} = c_{\mathrm{HTF}}^{\mathrm{ref}} m_{\mathrm{HTF,TES}}, \tag{3.15}$$

where the storage medium costs $c_{\mathrm{HTF}}^{\mathrm{ref}}$ are given in Eq. (3.12). The TES costs, including the fluid costs in Table 3.1, are indicated for SAM's reference central receiver plant (115 MW gross power output, 10 h TES and solar multiple of 2.4) with a TES capacity of 2350 MW $\mathrm{h_{th}}$ and adjusted to the respective operating temperature difference and heat capacity of the various HTFs. The total TES costs in the model are based on the actual calculated fluid mass in the TES as per Eq. (3.13).

3.2.4 Power block and balance of plant

The costs for the power block (C_{PB}) and balance of plant (C_{BOP}) are also based on the cost assumptions from Turchi *et al.* (2019) for an air-cooled power cycle of SAM's reference central receiver plant due to the similar temperature and pressure levels when using molten salts as HTF as opposed to using thermal oil. This reference plant has a gross turbine output $\dot{W}_{\mathrm{PB}}^{\mathrm{ref}}$ of 115 000 kW and the specific power block costs $c_{\mathrm{gross}}^{\mathrm{ref}}$ are 1040 $\$/\mathrm{kW_{gross}}$. Thus, the power block costs are calculated with

$$C_{\mathrm{PB}} = c_{\mathrm{PB}}^{\mathrm{ref}} \dot{W}_{\mathrm{gross}}^{\mathrm{ref}} \left(\frac{\dot{W}_{\mathrm{gross}}}{\dot{W}_{\mathrm{gross}}^{\mathrm{ref}}} \right)^{s_{\mathrm{PB}}} (1 + f_{\mathrm{loc}}). \tag{3.16}$$

Similarly, the balance of plant costs are calculated based on the same reference plant:

$$C_{\mathrm{BOP}} = c_{\mathrm{BOP}}^{\mathrm{ref}} \dot{W}_{\mathrm{gross}}^{\mathrm{ref}} \left(\frac{\dot{W}_{\mathrm{gross}}}{\dot{W}_{\mathrm{gross}}^{\mathrm{ref}}} \right)^{s_{\mathrm{BOP}}} (1 + f_{\mathrm{loc}}). \tag{3.17}$$

3.2.5 Transmission line

The REIPPPP requires a connection agreement between the IPP and Eskom in which the IPPs are responsible for the costs of transmission lines connecting the power plant to the nearest suitable substation (Eberhard and Naude, 2016). Telsnig *et al.* (2013) estimated the specific costs of a transmission line ($c_{\mathrm{trans}}^{\mathrm{ref}}$) to be 17.3 mil. ZAR/km in $\mathrm{ZAR_{2010}}$. This corresponds to approximately 1.32 mil. $/km (deflated and converted to $\$_{2018}$[3]). The reference length of the

[3] This has been done using the inflation rates from StatsSA (2020) and assuming a yearly average exchange rate of 13.242 ZAR/$ in 2018 (X-Rates, 2019*c*).

transmission line ($L^{\text{ref}}_{\text{trans}}$) is assumed to be the average length of the transmission lines of all CSP projects built in South Africa which is 5.33 km. Table 3.3 lists the lengths of the transmission lines for each project. The cost of the transmission line to the closest substation (C_{trans}) is then calculated with

$$C_{\text{trans}} = c^{\text{ref}}_{\text{trans}} L^{\text{ref}}_{\text{trans}}. \tag{3.18}$$

Table 3.3: Transmission line lengths of built CSP projects in South Africa.

Project	Length [km]	Source
KaXu	1	Engineering News (2015)
Khi	5	Engineering News (2015)
Bokpoort	1	The World Bank (2007)
Xina	3	New Energy Update (2017)
Ilanga	14	Savannah Environmental (2011)
Kathu	8	De Klerk (2016)
Average ($L^{\text{ref}}_{\text{trans}}$)	5.33	-

3.2.6 Land

The costs for the land area (C_{land}) are calculated based on the required land area of the power plant from Eq. (2.75) with

$$C_{\text{land}} = c^{\text{ref}}_{\text{land}} A_{\text{land}}, \tag{3.19}$$

where the land costs $c^{\text{ref}}_{\text{land}}$ are assumed to be 0.2 \$/m^2 based on advertised farm land for sale in the area of Upington, South Africa (Poole, 2017).

3.2.7 Engineering, procurement and construction

The *engineering, procurement and construction* (EPC) costs refer to the costs related to the design and construction of a power plant. This may include costs for engineering, project and construction management, permitting, commissioning and start-up, staff training and legal fees. Here, it is assumed that the EPC costs (f_{EPC}) are 11 % of the direct capital costs (NREL, 2018). Thus by using the capital costs of 624.7 mil. \$ of SAM's reference parabolic trough plant ($C^{\text{ref}}_{\text{direct}}$) from Turchi *et al.* (2019), the EPC costs are calculated with

$$C_{\text{EPC}} = f_{\text{EPC}} C^{\text{ref}}_{\text{direct}} \left(\frac{C_{\text{direct}}}{C^{\text{ref}}_{\text{direct}}} \right)^{s_{\text{EPC}}}. \tag{3.20}$$

3.2.8 Sales tax

The sales tax ($f_{\text{tax,sales}}$) for the sale of goods and services is 15 % in both South Africa and Namibia (Trading Economics, 2019*a*,*b*) and is calculated with

$$C_{\text{tax,sales}} = f_{\text{tax,sales}} \beta_{\text{direct}} C_{\text{direct}}, \tag{3.21}$$

where the calculation basis β_{direct} is 80 % of the direct capital costs C_{direct}. The sales tax value is also used for the income tax calculation in section 3.3.2.

3.3 Operating Costs

The operating costs $C_{\text{op},t}$ of a CSP plant include the annual operation and maintenance costs ($OPEX_t$), income tax ($C_{\text{tax},t}$), debt payments ($C_{\text{dp},t}$) and interest payments ($C_{\text{int},t}$) which are calculated annually with Eq. (3.22) for the duration of the operational lifetime of the power plant (n_{op}). Unless stated otherwise, the operational lifetime is assumed to be 20 years which corresponds to the duration of the PPAs under the REIPPPP. The *operation and maintenance costs* (OPEX) and tax liability are discussed in sections 3.3.1 to 3.3.2 and the annual debt and interest payments in section 3.4.1.

$$C_{\text{op},t} = OPEX_t + C_{\text{tax},t} + C_{\text{dp},t} + C_{\text{int},t} \qquad \text{for } t = 1, \ldots, n_{\text{op}}. \tag{3.22}$$

3.3.1 Operation and maintenance costs

The annual operation and maintenance costs $OPEX_t$ of the power plant include fixed costs $C_{\text{fix},t}$ by installed net capacity ($\dot{W}_{\text{net}}$), variable costs $C_{\text{var},t}$ by net electric output ($E_{\text{net},t}$) and insurance costs $C_{\text{ins},t}$ as a percentage of the direct capital costs (C_{direct}) with

$$OPEX_t = C_{\text{fix},t} + C_{\text{var},t} + C_{\text{ins},t} \qquad \text{for } t = 1, \ldots, n_{\text{op}}, \tag{3.23}$$

where the costs are inflated for each year t with the inflation rate r_{infl}:

$$C_{\text{fix},t} = c_{\text{fix}} \dot{W}_{\text{net}} (1 + r_{\text{infl}})^{t-1} \qquad \text{for } t = 1, \ldots, n_{\text{op}}, \tag{3.24}$$

$$C_{\text{var},t} = c_{\text{var}} E_{\text{net},t} (1 + r_{\text{infl}})^{t-1} \qquad \text{for } t = 1, \ldots, n_{\text{op}}, \tag{3.25}$$

$$C_{\text{ins},t} = f_{\text{ins}} C_{\text{direct}} (1 + r_{\text{infl}})^{t-1} \qquad \text{for } t = 1, \ldots, n_{\text{op}}. \tag{3.26}$$

Table 3.4 lists the fixed and variable operation and maintenance costs as well as the annual insurance rate (Turchi *et al.*, 2019). The inflation rate is assumed to

Table 3.4: Operation and maintenance cost assumptions (Turchi *et al.*, 2019).

Parameter	Variable	Unit	c_{comp} / f_{fin}
Fixed costs	c_{fix}	[\$/kW$_{\text{net}}$]	66
Variable costs	c_{var}	[\$/kWh$_{\text{e,net}}$]	4
Insurance rate	f_{ins}	[%]	0.5

be 4.7 % for South Africa and 4.3 % for Namibia (Trading Economics, 2019*a*,*b*). As already mentioned in section 3.1, the additional inflation of the USD was not considered in this study. Therefore, the economic model is based on ZAR terms but is expressed in USD to enable the comparability with international studies.

3.3.2 Tax liability and benefits

The annual revenue from the sale of electricity is subject to income tax. The taxable income that serves as the basis for the income tax is reduced by expenses and deductions, such as the OPEX, depreciation and interest payments.

Revenue

The revenue R_t is the sum of the hourly electricity sale, either in the form of a tariff from a PPA or a trading price from a spot market like the DAM. The revenue in year t is calculated with

$$R_t = \sum_{h=1}^{8760} p_{\mathrm{el},t,h} E_{\mathrm{net},t,h} \qquad \text{for } t = 1, \ldots, n_\mathrm{op}, \tag{3.27}$$

where $p_{\mathrm{el},t,h}$ is the hourly electricity tariff in year t which is escalated annually by the escalation rate r_esc with

$$p_{\mathrm{el},t,h} = p_{\mathrm{el},h}(1 + r_\mathrm{esc})^{t-1} \qquad \text{for } t = 1, \ldots, n_\mathrm{op};\ h = 1, \ldots, 8760. \tag{3.28}$$

Here, $p_{\mathrm{el},h}$ is the electricity tariff in year one. Similarly, $E_{\mathrm{net},t,h}$ is the hourly generated electricity in year t, including degradation as per Eq. (2.129).

Depreciation

According to section 12B of the amended South African *Income Tax Act 58 of 1962* (Republic of South Africa, 1962), an accelerated depreciation is available for renewable energy projects including CSP. This permits a depreciation of 50 % of the CAPEX in the first year of operation, 30 % in the following year and 20 % in the third year. In the case of Namibia, the capital costs of machinery and equipment can be depreciated in three equal amounts over three years, beginning in the year of the investment (EY, 2019). Therefore, the depreciation basis is the project's *CAPEX* from Eq. (3.1) and since both countries allow an accelerated depreciation over a period of three years, the depreciation period is $n_\mathrm{depr} = 3$. The depreciation value in year t is then

$$C_{\mathrm{depr},t} = CAPEX\, r_{\mathrm{depr},t} \qquad \text{for } t = 1, \ldots, n_\mathrm{depr}, \tag{3.29}$$

where the depreciation rate $r_{\mathrm{depr},t}$ in each year corresponds to the values as reported in Table 3.5 for the respective countries.

Table 3.5: Annual depreciation rates for South Africa and Namibia.

	$r_{\text{depr},t}$ [%]	
Year t	South Africa	Namibia
1	50	33.33
2	30	33.33
3	20	33.33

Income tax

The annual income tax $C_{\text{tax},t}$ is calculated based on the total taxable income TI_t and the income tax rate r_{tax}, which is 28 % in South Africa and 32 % in Namibia (Trading Economics, 2019*a*,*b*):

$$C_{\text{tax},t} = TI_t r_{\text{tax}}. \tag{3.30}$$

The taxable income includes the revenue from all sources — in this case only from the sale of electricity — and is reduced by expenses and deductions such as the OPEX, depreciation, interest payments and the sales tax as per Eq. (3.31). The latter is assumed to be payable as a one-time tax in year one of operation and is calculated with Eq. (3.21). Since the taxable income is reduced by large deductions from depreciation and sales tax (especially during the first years of operation), it can be negative, resulting in a tax benefit.

$$TI_t = R_t - OPEX_t - C_{\text{depr},t} - C_{\text{int},t} - C_{\text{tax,sales},t} \qquad \text{for } t = 1, \ldots, n_{\text{op}}. \tag{3.31}$$

3.3.3 Decommissioning costs

Finally, decommissioning costs are strictly speaking also part of the operating costs but are considered as a separate cost item in order to make a clear distinction between the operating costs during the operational lifetime of the plant and the costs during the decommissioning period. The decommissioning costs are calculated based on the total capital costs of the power plant with

$$C_{\text{dec}} = f_{\text{dec}} CAPEX, \tag{3.32}$$

where f_{dec} is assumed to be 2.5 % (Harnmeijer and Ibikunle, 2014). The decommissioning costs are split equally over the decommissioning period n_{dec} after the operational lifetime n_{op} of the power plant. A decommissioning period of 2 years is assumed throughout this study.

An exemplary project after-tax cash flow of a MSPTPP with 150 MW gross power output, a TES of 12 h and a solar multiple of 2.5 is shown in Figure 3.2. This illustrates the individual incoming and outgoing costs discussed in the previous sections for the entire economic lifetime of the power plant. It should be noted that the outgoing cash flow during the construction period, which is the total CAPEX of the plant, is divided into debt (C_{debt})

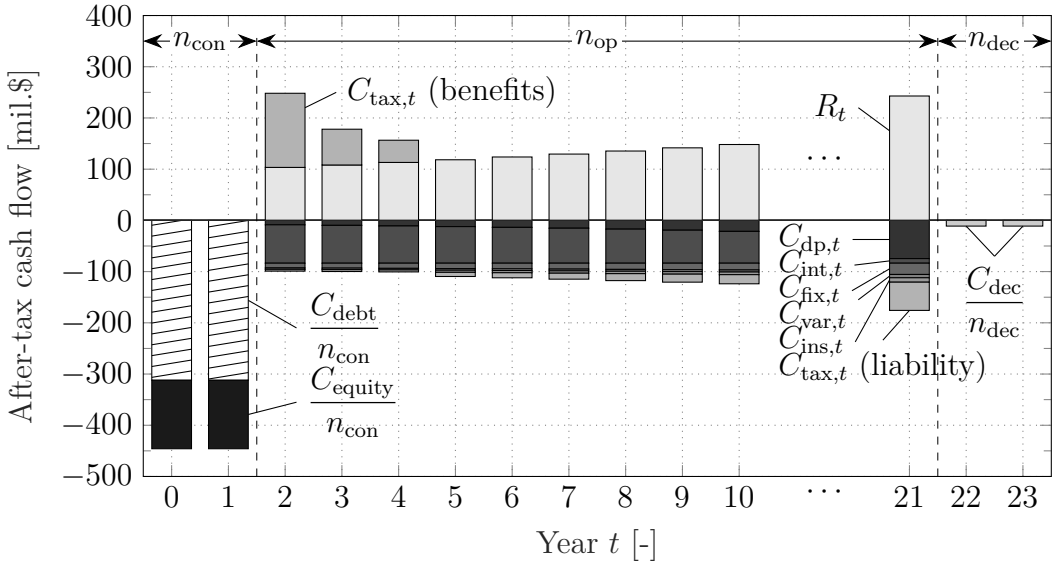

Figure 3.2: Exemplary project after-tax cash flow during the lifetime of a MSPTPP in South Africa with 150 MW gross power output, a TES of 12 h and a solar multiple of 2.5 (adapted from Spelling, 2013, with own calculations).

and equity (C_{eq}). The respective financing costs related to the issuance of debt and equity are presented in the following section.

3.4 Financing Costs

In order to finance CSP projects, a developer typically requires equity investors and debt lenders to raise capital. Due to the high risks involved in CSP project development, the financing costs make up a large portion of the total project costs linked to the high interest rates and expected returns on equity. This has a significant impact on the LCOE and considering financing costs in the economic model is therefore imperative. The following sections discuss the debt and equity financing as well as their effect on the overall financing costs.

3.4.1 Debt financing

The main providers of debt financing under South Africa's REIPPPP were the "big four" local commercial banks, i.e. ABSA, Rand Merchant Bank, Nedbank and Standard Bank. Additional debt financing was provided by the Industrial Development Corporation of South Africa, the Development Bank of South Africa and Investec (Baker, 2015). Renewable energy project financing is usually structured at a debt to equity ratio of 70/30 (Mendonça *et al.*, 2009) due to the high upfront CAPEX. Projects under the REIPPPP in South Africa are sometimes even structured at a debt to equity ratio of 80/20 (Baker, 2015). However, Table 3.6 shows the debt to equity ratios of CSP plants in South

Table 3.6: Capital costs and debt/equity shares of existing CSP projects in South Africa[4] (The World Bank, 2019).

Parameter	Unit	KaXu	Khi	Bokpoort	Xina	Ilanga	Kathu
Capital costs	[mil. $]	844	424	498	854	688	779
Debt	[mil. $]	633	318	349	618	470	608
Equity	[mil. $]	211	106	149	236	218	171
Debt share	[%]	75	75	70	72	68	78
Equity share	[%]	25	25	30	28	32	22
Average debt/equity	[%]			73/27			

Africa where the highest debt share is 78 % (Kathu Solar Park). The reason for such high debt shares is the lower cost of debt as compared to the cost of equity. Hence, the average cost of funding reduces the more debt there is, resulting in lower overall project costs and a higher return on equity. This so-called leverage effect is normally used in order to optimise the capital structure of CSP plants by maximising the share of debt.

Debt tenors typically range from 15 years to 18 years (WWF, 2014*a*). However, Baker (2015) has found that the debt tenor for projects under the REIPPPP is 20 years on average with a debt interest rate of 12 % (k_{debt}). This can be considered a conservative value considering that the prime interest rate in South Africa fluctuated between 9.75 % and 10.5 % between 2016 and 2018 (South African Reserve Bank, 2020) and assuming a markup for increased risk due to the lower maturity level of MSPTPPs as compared to state-of-the-art thermal oil plants. Additional risk categories, such as grid integration risk, power market risk, political risk and currency risk are the main factors that result in an increase of the debt interest rate in South Africa (UNDP, 2014). Similarly, the prime interest rate in Namibia fluctuated between 10.25 % and 10.75 % during the same period (Trading Economics, 2020) and the assumed cost of debt of 12 % can therefore also be considered reasonable. These debt financing costs will be used throughout the study unless stated otherwise.

The debt principal at the time of investment ($t = 0$) is calculated based on the total capital costs $CAPEX$ and the share of debt w_{debt} with

$$C_{\text{debt},0} = CAPEX\, w_{\text{debt}}. \tag{3.33}$$

Assuming equal payments (standard amortisation) for the debt repayment, the annual principal payment amount C_{pp} is calculated using the annuity method, distributing the total amount of debt and interest equally over the period of the debt tenor (n_{debt}):

$$C_{\text{pp}} = C_{\text{debt},0} \frac{k_{\text{debt}}}{1 - (1 + k_{\text{debt}})^{n_{\text{debt}}}}. \tag{3.34}$$

[4] Data for Redstone (BW3.5) is not available at the time of writing due to a two-year delay in financial close attributed to the refusal by Eskom to sign the PPA (SolarPACES, 2018).

This fixed amount is paid annually towards the debt and consists of the debt payments $C_{\mathrm{dp},t}$ and interest payments $C_{\mathrm{int},t}$, which are calculated with Eqs. (3.35) and (3.36), respectively. The remaining debt $C_{\mathrm{debt},t}$ in year t is then calculated with Eq. (3.37).

$$C_{\mathrm{dp},t} = C_{\mathrm{pp}} - C_{\mathrm{int},t} \qquad \text{for } t = 1, \ldots, n_{\mathrm{debt}}, \tag{3.35}$$

$$C_{\mathrm{int},t} = C_{\mathrm{debt},t} k_{\mathrm{debt}} \qquad \text{for } t = 1, \ldots, n_{\mathrm{debt}}, \tag{3.36}$$

$$C_{\mathrm{debt},t} = C_{\mathrm{debt},t-1} - C_{\mathrm{dp},t} \qquad \text{for } t = 1, \ldots, n_{\mathrm{debt}}. \tag{3.37}$$

Although a maximisation of the debt share is desired to fully make use of the leverage effect, attention has to be paid if a high debt results in annual debt payments exceeding the net operating income. To avoid an inability to service the debt, the *debt service coverage ratio* (DSCR) is introduced. It is a measure of the availability of cash to pay the debt and interest in each year t for the duration of the debt tenor (n_{debt}). The DSCR is calculated as the ratio of the net operating income before tax and the sum of debt and interest payments:

$$DSCR_t = \frac{R_t - OPEX_t}{C_{\mathrm{dp},t} + C_{\mathrm{int},t}} \qquad \text{for } t = 1, \ldots, n_{\mathrm{debt}}. \tag{3.38}$$

Typical values for the DSCR in the electricity sector range from 1.2 to 1.5 (Kistner and Price, 1999; Hirsch *et al.*, 2017; Sklar-Chik *et al.*, 2016). For the purpose of this study, a DSCR of 1.2 is assumed. Using this DSCR as a minimum allowable value, the maximum possible share of debt in the project financing that fulfils this condition is calculated.

3.4.2 Equity financing

To make up the balance between the total capital costs and the debt, equity financing is required. A project consortium between the developer and equity investors is usually formed where dividends are split among the equity investors. The developer's equity shares range between 15 % to 51 % in the built CSP plants in South Africa and the rest is mainly made up by private and public investment corporations, the Industrial Development Corporation of South Africa, the South African government employees pension fund and community trusts (Ministry of Energy, 2018).

The risk for equity investors is far greater than for debt lenders since they are the last to receive any financial revenue from the project. Therefore, their expected rate of return is typically higher than the debt financing rate and can be up to 18 % in South Africa for some projects (WWF, 2014*a*; Lazard, 2017). This equity return is assumed throughout this study unless stated otherwise. Table 3.7 provides a summary of the debt and equity financing assumptions. The required equity investment C_{eq} is simply calculated as the balance of the total funding based on the calculated share of debt (w_{debt}):

$$C_{\mathrm{eq}} = CAPEX\,(1 - w_{\mathrm{debt}})\,. \tag{3.39}$$

Table 3.7: Debt and equity assumptions.

Parameter	Variable	Unit	Value	Source
Share of debt	w_{debt}	[%]	variable	-
Share of equity	w_{eq}	[%]	variable	-
Cost of debt	k_{debt}	[%]	12	Baker (2015)
Cost of equity	k_{eq}	[%]	18	WWF (2014*a*); Lazard (2017)
Debt tenor	n_{debt}	[a]	20	Baker (2015)
DSCR (min.)	*DSCR*	[-]	1.2	Kistner and Price (1999); Hirsch *et al.* (2017); Sklar-Chik *et al.* (2016)

As previously mentioned, the financing structure has a significant effect on the LCOE (which will be presented in detail in section 3.6.1). A cost break-down of the pre-tax LCOE into capital costs, operating costs and financing costs (debt and equity) is shown in Figure 3.3 for different debt/equity ratios. It becomes evident that the financing costs make up the majority of the LCOE, which shows the importance of accurate economic modelling and the use of well-founded financial assumptions. Furthermore, it can be seen that the overall LCOE decreases with an increasing share of debt due to the lower cost of the debt. The same effect takes place for the equity financing cost which increases significantly with an increasing share of equity. Using the assumptions for the cost of debt and equity from above, the equity financing cost already exceeds the debt financing cost at a debt/equity ratio of 60/40.

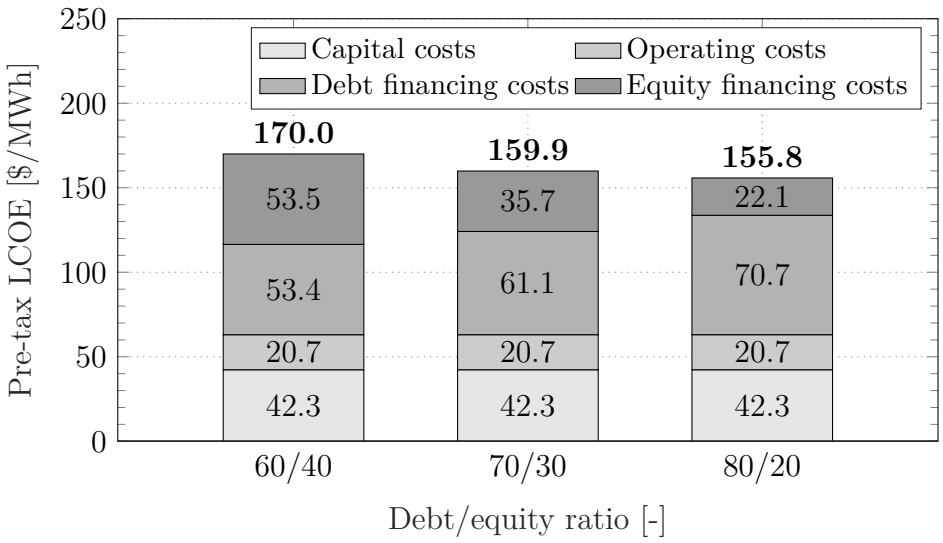

Figure 3.3: Exemplary impact of financing costs on LCOE for various debt/equity ratios for a MSPTPP with 150 MW gross power output, a TES of 12 h and a solar multiple of 2.5 ($k_{\text{debt}} = 12\,\%$; $k_{\text{eq}} = 18\,\%$).

3.4.3 Weighted average cost of capital

The *weighted average cost of capital* (WACC) represents the long-term minimum required return of a company based on all its assets (i.e. debt, equity, preferred stock etc.). It is often referred to as the aggregated cost of all the company's sources of capital and is calculated with

$$WACC_{\text{nom}} = w_{\text{debt}} k_{\text{debt}} (1 - r_{\text{tax}}) + w_{\text{eq}} k_{\text{eq}}, \tag{3.40}$$

where w_{debt} and w_{eq} are the share of debt and equity, respectively, k_{debt} is the debt interest rate and k_{eq} is the cost of equity as per Table 3.7. The corporate income tax rate r_{tax} from section 3.3.2 effectively reduces the cost of capital because interest payments are tax deductible. As the interest and tax rates are location-dependent due to the corporate income tax rate and the general investment climate (regarding the interest rates), the WACC is defined by the external market and not by the company. Therefore, the WACC in Southern Africa is significantly higher than compared to other countries which results in a considerably higher LCOE[5]. In fact with the assumptions from above, the nominal WACC is 11.45 % in South Africa and 11.11 % in Namibia for a typical debt/equity ratio of 70/30. In comparison, the WACC of the *Dubai Electricity & Water Authority* (DEWA) combined tower and trough plant *DEWA IV* in Dubai is estimated to be below 3 % for the same debt/equity ratio (Lilliestam and Pitz-Paal, 2018). Although the DNI in Dubai is comparatively low with values between 2000 kWh/m^{2}a and 2200 kWh/m^{2}a, the project consortium of ACWA (Saudi Arabia) and Shanghai Power (China) is profiting from "very good financing conditions" (Lilliestam and Pitz-Paal, 2018). In combination with an "extraordinarily long PPA duration of 35 years" (Lilliestam and Pitz-Paal, 2018), this leads to the awarded PPA tariff of 73 $/MWh which, at the time, was the lowest tariff ever awarded for CSP plants. If similar financing conditions were possible in Southern Africa (in combination with the high solar resource of up to 3200 kWh/m^{2}a), even lower PPA tariffs can be expected. Therefore, the current investment and risk climate in Southern Africa poses the largest barrier for cheap electricity from CSP plants.

For the sake of completeness and by taking the expectations of inflation into account, the real WACC can be calculated with the Fisher equation based on the country-specific inflation rate r_{infl}:

$$WACC_{\text{real}} = \frac{(1 + WACC_{\text{nom}})}{(1 + r_{\text{infl}})} - 1. \tag{3.41}$$

3.5 Tariffs and Trading Prices

Remuneration for electricity generation from renewable energy projects in South Africa is organised through the REIPPPP which requests bid tariffs

[5] For a comparison of the effect of location-dependent interest and inflation rates on the LCOE of PTPPs see, for example, Pan *et al.* (2018*b*).

from project developers through bid windows. Successful bids are awarded a PPA of 20 years between the developer and the off-taker which is the state-owned utility Eskom. A comparison between the average awarded tariffs per technology is shown in Figure 1.3 and discussed in section 1.2.5. The first two bid windows received a fixed tariff (baseload generation), whereas the tariff structure was changed to a two-tier tariff in the last two bid windows (peaking generation). For the latter, the base tariff from off-peak times is inflated by a factor of 2.7 for generation during peak hours but no tariff is paid during a low-demand period at night. The following sections present the two tariff structures considered in this study as well as a third option in the form of spot market trading prices.

3.5.1 Baseload tariff

The average baseload tariffs from the first two bid windows were 296.8 \$/MWh and 277.9 \$/MWh (Department of Energy, 2018)[6]. However as this fixed tariff has been changed to a two-tier tariff structure starting with BW3, there is currently no such tariff available. Additionally and considering the technology learning rate from the bid windows, it is evident that a significantly lower tariff is possible and simply using the tariff from BW2 would not be reasonable. Therefore, the base tariff from the two-tier tariff structure during off-peak times serves as a suitable reference point for baseload generation. Hence, the baseload tariff is assumed to be 150.3 \$/MWh in this study.

3.5.2 Two-tier tariff

The two-tier tariff structure consists of a base tariff of 150.3 \$/MWh which is paid during off-peak times from 5:00 to 16:30 and 21:30 to 22:00. During peak hours from 16:30 to 21:30, the base tariff is inflated by 270 %, resulting in a tariff of 405.8 \$/MWh. During low demand hours between 22:00 and 5:00, the tariff is zero. Table 3.8 provides a summary of the two-tier tariff structure. Under this tariff structure, a plant operator will try to maximise revenue through generation during periods with a tariff greater than zero and avoid

Table 3.8: Two-tier tariff structure (Department of Energy, 2019*a*).

Period	Time [h]	Tariff [\$/MWh]
Off-peak	05:00–16:30 21:30–22:00	150.3
Peak	16:30–21:30	405.8
Night	22:00–05:00	0.0

[6] Yearly average exchange rate of 13.242 ZAR/\$ in 2018 (X-Rates, 2019*c*).

generation during night-time (i.e. peaking operation). Assuming a constant power output, the average tariff is 225.5 $/MWh which is considerably higher compared to the assumed baseload tariff of 150.3 $/MWh.

3.5.3 Day-ahead trading price

As there are currently no PPA tariffs available for CSP in Namibia, an optimistic alternative is the participation in a spot market, such as the DAM within the SAPP. For this, the hourly DAM trading prices from 2018 are used as input to the model (SAPP, 2020). With all tariff scenarios now defined, Figure 3.4 shows a comparison of the two tariff structures and the DAM trading price in relation to the DNI. It can be seen that the two tariff structures follow a clearly defined pattern and are significantly higher than the DAM trading prices. In fact, the yearly average DAM trading price in 2018 was

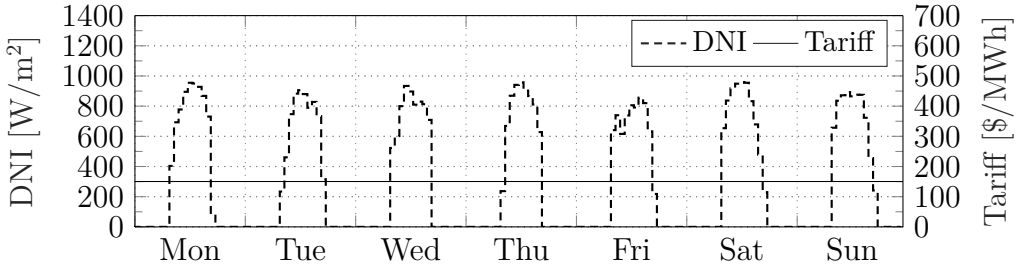

(a) Baseload tariff.

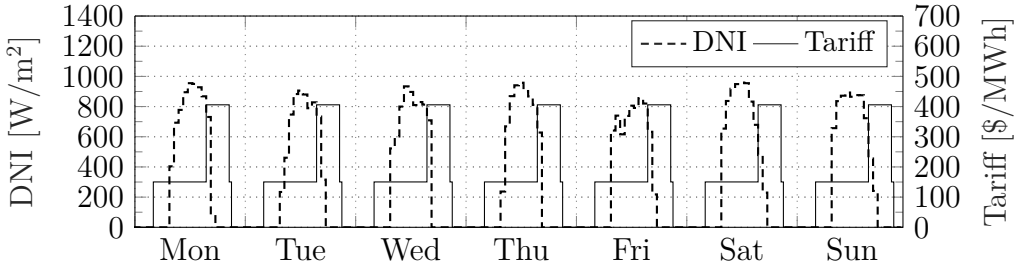

(b) Two-tier tariff.

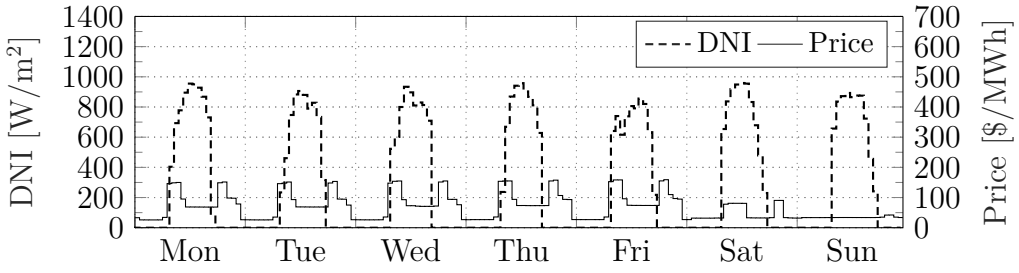

(c) Day-ahead market trading prices.

Figure 3.4: Tariffs and DAM trading prices in comparison with the DNI during a typical winter week.

49.7 $/MWh. Furthermore, the daily DAM trading prices are highly volatile and are generally lower during the weekend when demand is low. This makes it significantly more challenging for CSP plants to operate under these conditions since a high degree of operational flexibility is required and the electricity price is considerably lower than the tariffs available through a PPA.

3.5.4 Tariff escalation

As part of the REIPPPP, the PPA tariffs are inflation-adjusted each year (Eberhard and Naude, 2016; WWF, 2014*a*). This can be seen in Figure 3.5, where the annual tariff increase of BW3.5 is shown in comparison to the historic *Consumer Price Index* (CPI) from StatsSA (2020). The yearly tariff increase mostly coincides with the yearly average CPI with the exception of 2015, where the tariff has been increased by over 11 %. Hence, the PPA tariff escalation rate $r_{\mathrm{esc,PPA}}$ used for the escalation with Eq. (3.28) is simply assumed to correspond to the inflation rate r_{infl}, which was 4.7 % in South Africa and 4.3 % in Namibia during 2018 (Trading Economics, 2019*a*,*b*). The hourly electricity price ($p_{\mathrm{el},h}$) is either the hourly PPA tariff or the DAM trading price in year one.

Figure 3.6 shows the DAM trading price trend since 2017. The average prices in 2017 and 2018 are considerably lower than, for instance, in 2019 and 2020. Furthermore, a steep increase up to 120 $/MWh can be observed in early 2020. Such high trading prices would potentially enable CSP plants to participate in the trading market without having to rely on PPA tariffs. Looking at the trend of the DAM trading prices, an average annual increase of 16 % can be observed in the last three years. However, such a high annual increase is not expected to occur in the long-term. Therefore, an annual increase of 5 % is assumed in this study for DAM prices.

Figure 3.7 shows an exemplary tariff escalation for the baseload scenario in South Africa. It can be seen that the tariff is increased annually by the

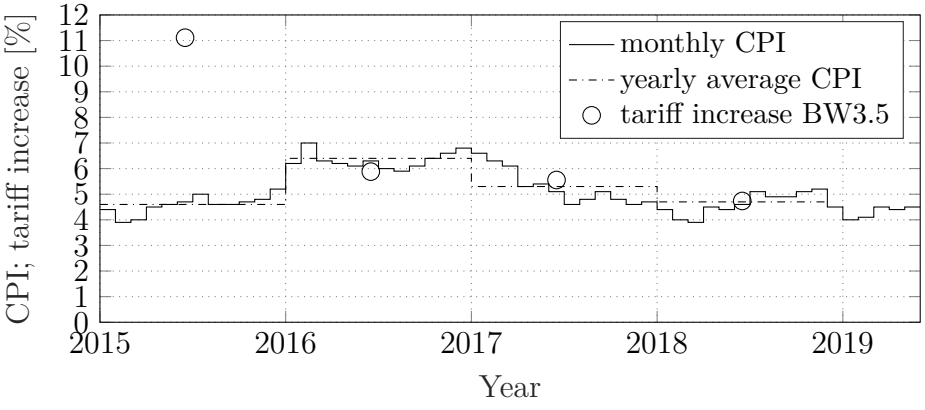

Figure 3.5: CPI for South Africa and yearly average tariff increase in bid window 3.5 (StatsSA, 2020; Department of Energy, 2019*a*)

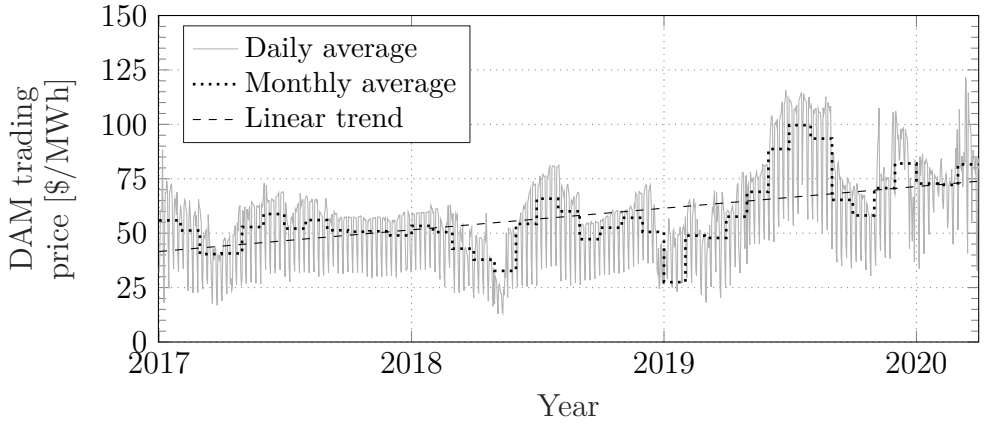

Figure 3.6: Daily and monthly average DAM trading prices (deflated to $\$_{2018}$) from 2017 to March 2020 for South Africa and Namibia (SAPP, 2020).

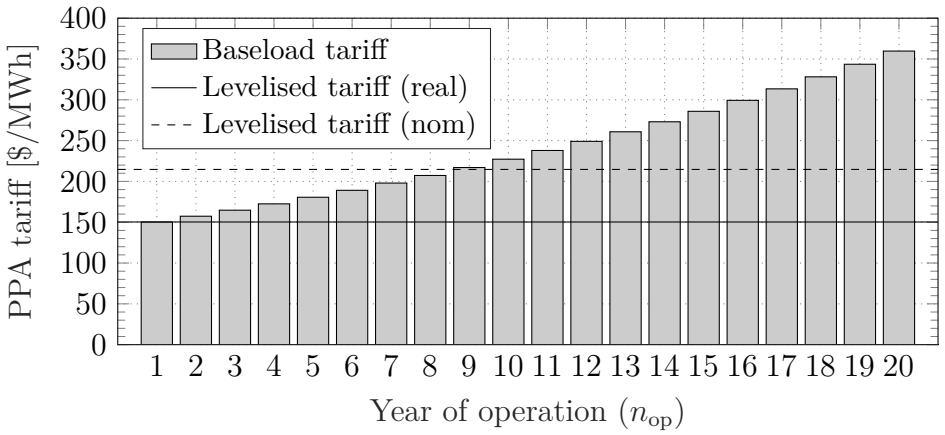

Figure 3.7: PPA tariff escalation of the baseload tariff structure in South Africa.

escalation rate based on the tariff in the previous year and reaches a maximum of 359.7 \$/MWh. To express the escalating tariff as a single value over the complete lifetime of a PPA including inflation, the nominal levelised PPA tariff ($p_{\text{PPA,lev,nom},h}$) can be used. This value represents the total monetary value of a PPA (revenue) over the financial lifetime of the PPA based on the nominal discount rate d_{nom}. The nominal discount rate is simply assumed to be the nominal WACC from Eq. 3.40 throughout this study. The nominal levelised PPA tariff is calculated with

$$p_{\text{PPA,lev,nom},h} = \frac{\sum_{t=1}^{n_{\text{op}}} \frac{R_t}{(1+d_{\text{nom}})^t}}{\sum_{t=1}^{n_{\text{op}}} \frac{E_{\text{net},t}}{(1+d_{\text{nom}})^t}}. \tag{3.42}$$

The real levelised PPA tariff simply corresponds to the starting tariff in year one since it does not take inflation effects into account. The nominal discount rate d_{nom} can be calculated from the relation between the real discount rate d_{real} and the inflation rate r_{infl} with

$$d_{\text{nom}} = (1 + d_{\text{real}})(1 + r_{\text{infl}}) - 1. \tag{3.43}$$

The nominal levelised tariff of the baseload tariff structure is 214.7 \$/MWh when assuming a constant annual electricity output with constant revenue streams and a nominal discount rate of 11.45 %. This corresponds to a constant currency value in nominal terms, i.e. taking inflation into account. In contrast to that, Figure 3.8 shows the tariff escalation of the two-tier tariff structure in South Africa. The base and peak tariffs represent tariffs during off-peak and peak times (as presented in section 3.5.2), respectively. The average tariff is simply the weighted average of the two base and peak tariffs assuming a constant power output (except during times where the tariff is zero) and is 225.5 \$/MWh. The peak tariff is escalated to 971.2 \$/MWh in year 20 which also leads to a considerably higher average tariff of 539.6 \$/MWh compared to the baseload tariff structure. Similarly, the levelised nominal tariff is 322.1 \$/MWh which is approximately 50 % higher than the levelised tariff of the baseload tariff structure. Hence, the expected revenue under the two-tier tariff is significantly higher which leads to higher returns on the investment.

Finally, with all economic parameters now defined, Table 3.9 provides a summary of the main financial parameter assumptions of the cost model.

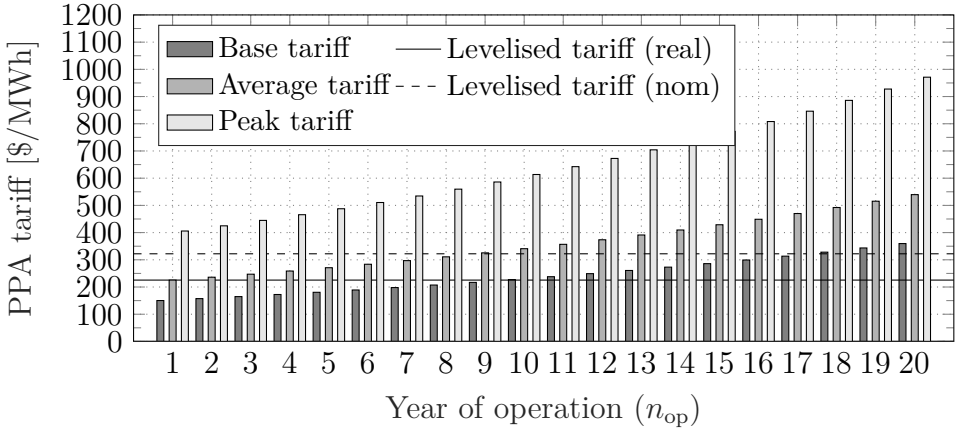

Figure 3.8: PPA tariff escalation of the two-tier tariff structure in South Africa.

Table 3.9: Summary of main financial parameter assumptions for 2018.

Parameter	Variable	Unit	Value	
Construction duration	n_{con}	[a]	2	
Operational lifetime	n_{op}	[a]	20	
Decommissioning duration	n_{dec}	[a]	2	
Decommissioning costs[7]	f_{dec}	[%]	2.5	
PPA tariff (first year)[8]	$p_{\text{el,PPA}}$	[$/MWh]	150.3	
DAM trading price[9]	$p_{\text{el,DAM}}$	[$/MWh]	variable	
DAM price escalation rate[10]	$r_{\text{esc,DAM}}$	[%/a]	5	
Location			South Africa	Namibia
Inflation rate[11]	r_{infl}	[%/a]	4.7	4.3
Real discount rate[12]	d_{real}	[%/a]	6.45	6.53
Nominal discount rate[12]	d_{nom}	[%/a]	11.45	11.11
Income tax rate[11]	r_{tax}	[%/a]	28	32
PPA tariff escalation rate[13]	$r_{\text{esc,PPA}}$	[%/a]	4.7	4.3

3.6 Economic Performance Indicators

For the assessment of the economic performance of MSPTPPs, the economic performance indicators need to be defined. The key indicators used in this study are the LCOE, the *net present value* (NPV) and the IRR which will be discussed hereinafter. It should be noted that the financial metrics used in this study only consider the revenue from the sale of electricity and do not take any further revenue streams (e.g. from complementary, regulatory and ancillary services) into account (Guédez, 2016; De Meyer, 2018). Due to the flexibility of CSP plants with TES, they can be operated as baseload, intermittent as well as peaking plants. The latter can especially add significant value to the electric system during demand peaks (De Meyer *et al.*, 2017). As such, the REIPPPP acknowledges the value of CSP during system peak times by inflating the base tariff by a factor of 2.7. Nevertheless, any additional value contributed to the electric system is currently not promoted through specific policies and hence cannot be quantified sufficiently to be included in this study. Therefore, the metrics reported here are purely based on the project's costs and the sale of electricity and are likely to improve once the value of CSP is adequately accounted for.

[7] Harnmeijer and Ibikunle (2014).
[8] Fixed tariff in baseload tariff structure and base tariff in two-tier tariff structure.
[9] The yearly average DAM trading price in 2018 is 49.7 $/MWh.
[10] For scenarios using DAM trading prices as input.
[11] Trading Economics (2019*a*,*b*).
[12] Assuming a debt/equity ratio of 70/30, cost of debt of 12 % and cost of equity of 18 %.
[13] For scenarios with a fixed term PPA and a baseload or two-tier tariff structure.

3.6.1 Levelised cost of electricity

One of the most commonly used measures for the economic performance of renewable energy projects is the LCOE. The LCOE is expressed as the costs of a project over the total project lifetime in \$/MWh of generated electricity. The calculation of the LCOE in this study is based on a discounted cash flow analysis over the financial lifetime of the project including the operation and decommissioning phase. Based on the approach from SAM (NREL, 2018), all costs are discounted to present value using the nominal discount rate d_{nom} from Table 3.9. The nominal discount rate d_{nom} can be calculated from the relation between the real discount rate d_{real} and the inflation rate r_{infl} with Eq. (3.43). In this study, the real and nominal discount rates are simply assumed to be the real and nominal WACC from Eq. (3.40) and (3.41), respectively. Assuming a debt/equity ratio of 70/30, a cost of debt of 12 % and a cost of equity of 18 %, the real and nominal WACC in South Africa are 6.45 % and 11.45 %, respectively. Due to a lower inflation rate but higher income tax rate, the real and nominal WACC in Namibia are 6.53 % and 11.11 %, respectively. However, the WACC is different for every project as the debt/equity ratio is calculated to satisfy the minimum allowable DSCR. To account for inflation, the LCOE is calculated in real terms, which results in a constant, inflation-adjusted value. With all the discount rates now defined, the $LCOE_{\text{real}}$ is given by

$$LCOE_{\text{real}} = \frac{C_{\text{equity}} + \sum_{t=1}^{n_{\text{op}}+n_{\text{dec}}} \frac{C_{\text{op},t} + C_{\text{dec},t}}{(1+d_{\text{nom}})^t}}{\sum_{t=1}^{n_{\text{op}}} \frac{E_{\text{net},t}}{(1+d_{\text{real}})^t}}, \tag{3.44}$$

where C_{equity} is the amount of equity investment in the first year and $C_{\text{op},t}$ are the annual project costs in year t as calculated with Eq. (3.22). The decommissioning costs $C_{\text{dec},t}$ are only due after the operational lifetime n_{op} of the plant. The annual costs are discounted with the nominal discount rate because the costs are in nominal terms and include the effect of inflation as introduced in Eqs. (3.24) to (3.26). The levelised costs also include benefits, such as depreciation and tax credits, which effectively reduce the annual project costs. The annually generated net electricity $E_{\text{net},t}$ is calculated with Eq. (2.128). Whenever the LCOE is mentioned in this study, it is referred to the real LCOE from Eq. (3.44) unless stated otherwise.

Additionally, it should be noted that Eq. (3.44) is discounted over a period of $n_{\text{op}} + n_{\text{dec}}$, which allows the inclusion of the decommissioning costs after the operational lifetime n_{op} of the power plant, assuming a duration of the decommissioning phase n_{dec} of two years. The decommissioning costs C_{dec} are calculated with Eq. (3.32).

The LCOE as a performance metric should be used very carefully as var-

ious calculation methods exist that consequently yield different results. For instance, a simplified method using an assumed WACC as the discount rate d is often used in the estimation of the LCOE as, for example, in reports by IRENA (2018), Kost *et al.* (2018) and in the CSP.guru project database (Lilliestam *et al.*, 2017, 2018). For the sake of completeness, this LCOE (referred to as *simplified LCOE* in this study) is calculated based on the overnight $CAPEX$, the annual operation and maintenance costs $OPEX_t$ from Eq. (3.23):

$$LCOE_{\text{simple}} = \frac{CAPEX + \sum_{t=1}^{n_{\text{op}}} \frac{OPEX_t}{(1+d)^t}}{\sum_{t=1}^{n_{\text{op}}} \frac{E_{\text{net},t}}{(1+d)^t}} \tag{3.45}$$

and is used in section 4.3 in order to allow a comparison with power plants currently operational or under construction in South Africa with data from Lilliestam *et al.* (2018). In order to obtain a comparable result, a discount rate d of 10 % and a financial lifetime of 25 years are assumed in accordance with the assumptions used by Lilliestam *et al.* (2018). This corresponds to the typical expectation of economic lifetime of CSP plants found in literature. These assumptions are also identical to the values used by IRENA (2018) for the calculation of the LCOE of renewable power generation costs in non-OECD countries. In addition to the above mentioned difference, it should be noted that a real LCOE can never be compared to a nominal LCOE as the real LCOE is inflation-adjusted and the nominal LCOE is calculated in terms of current currency value (NREL, 2018).

Lastly, the LCOE in this study only takes the costs of the power plant itself into account and neither extends to include externalities (environmental or non-environmental impacts), such as land use, water and supply security, nor considers overall system costs, e.g. transmission, distribution and marketing costs (Sklar-Chik *et al.*, 2016). Although a more accurate calculation of the LCOE is desired by including the aforementioned costs, this is beyond the scope of this study and is therefore not accounted for.

3.6.2 Net present value

The NPV is widely used in the economic assessment of projects and is a measure of all future cash flows over the entire economic lifetime of a project in terms of present value. A project is typically considered economically feasible if the NPV is greater than zero. However, all financial metrics should always be evaluated complementary to each other as opposed to focusing only on a single metric. For example, a project with a low LCOE can still lead to a negative NPV or have an IRR below the desired target. Considering cash inflows (revenue) and cash outflows (equity, operating costs and decommission-

ing costs) during three distinct periods of a CSP plant's economic lifetime (i.e. construction, operation and decommissioning), the NPV is calculated with

$$NPV = -\sum_{t=0}^{n_{\text{con}}-1} \frac{C_{\text{equity}}}{n_{\text{con}}(1+d_{\text{nom}})^t} + \sum_{t=n_{\text{con}}}^{n_{\text{con}}+n_{\text{op}}-1} \frac{R_{\text{t}} - C_{\text{op},t}}{(1+d_{\text{nom}})^t} - \sum_{t=n_{\text{con}}+n_{\text{op}}}^{n_{\text{con}}+n_{\text{op}}+n_{\text{dec}}-1} \frac{C_{\text{dec},t}}{n_{\text{dec}}(1+d_{\text{nom}})^t}, \quad (3.46)$$

where C_{equity} is the equity investment that is assumed to be distributed equally over the construction period n_{con}. As previously mentioned in section 3.6.1, the nominal discount rate d_{nom} is simply the nominal WACC. The revenue R_{t} in each year is calculated with Eq. (3.27). The revenue is reduced by the after-tax operating cost $C_{\text{op},t}$ which are calculated with Eq. (3.22). The last term of Eq. (3.46) includes the decommissioning costs $C_{\text{dec},t}$ from Eq. (3.32) during the decommissioning period n_{dec} and are assumed to be equally distributed over the decommissioning period.

3.6.3 Internal rate of return

The last key economic performance indicator is the IRR. The IRR is the *nominal* discount rate at which the present value of future positive cash flows is equal to the future negative cash flows. In other terms, it is simply the discount rate at which the NPV, as defined in Eq. (3.46), is zero over the lifetime of the project. Since the NPV also considers the profit generated during the lifetime of a project, the IRR is a profit-based indicator and, unlike the LCOE, takes the value of dispatchability through FITs into account (Guédez *et al.*, 2016). Therefore, the IRR is a useful measure in addition to the LCOE and NPV in order to assess a project's profitability.

There are two relevant IRRs, the project IRR (IRR_{proj}) and the equity IRR (IRR_{eq}). The project IRR gives the rate of return of the whole project, assuming that there is no debt in the project financing. In other words, it does not include costs for financing (i.e. debt and equity costs) and is calculated over the lifetime of the project with

$$NPV = 0 = -\sum_{t=0}^{n_{\text{con}}-1} \frac{CAPEX}{n_{\text{con}}(1+IRR_{\text{proj}})^t} + \sum_{t=n_{\text{con}}}^{n_{\text{con}}+n_{\text{op}}-1} \frac{R_{\text{t}} - OPEX_{,t}}{(1+IRR_{\text{proj}})^t} - \sum_{t=n_{\text{con}}+n_{\text{op}}}^{n_{\text{con}}+n_{\text{op}}+n_{\text{dec}}-1} \frac{C_{\text{dec},t}}{n_{\text{dec}}(1+IRR_{\text{proj}})^t}. \quad (3.47)$$

The equity IRR, on the other hand, only considers the cash flow for the equity shareholders, i.e. the after-tax revenue, operating expenses and debt payments (including interest):

$$NPV = 0 = -\sum_{t=0}^{n_{\text{con}}-1} \frac{C_{\text{equity}}}{n_{\text{con}}(1+IRR_{\text{eq}})^t} + \sum_{t=n_{\text{con}}}^{n_{\text{con}}+n_{\text{op}}-1} \frac{R_{\text{t}} - C_{\text{op},t}}{(1+IRR_{\text{eq}})^t} - \sum_{t=n_{\text{con}}+n_{\text{op}}}^{n_{\text{con}}+n_{\text{op}}+n_{\text{dec}}-1} \frac{C_{\text{dec},t}}{n_{\text{dec}}(1+IRR_{\text{eq}})^t}. \quad (3.48)$$

The IRR excludes any external factors, such as inflation or financial risk, and should be higher than the WACC of a company to make a project profitable. An equity IRR of 16 % to 20 % is typically expected from IPP projects (Kistner and Price, 1999). For convenience, the equity IRR (IRR_{eq}) is simply referred to as IRR in this study as it provides more information on a project's feasibility due to the consideration of capital costs.

Similarly, by substituting Eq. (3.27) into Eq. (3.47) and denoting the electricity price $p_{\text{el},t,h}$ as the required PPA tariff $p_{\text{PPA,req}t,h}$, yields

$$NPV = 0 = -\sum_{t=0}^{n_{\text{con}}-1} \frac{C_{\text{equity}}}{n_{\text{con}}(1+IRR_{\text{targ}})^t} + \sum_{t=n_{\text{con}}}^{n_{\text{con}}+n_{\text{op}}-1} \frac{\sum_{h=1}^{8760}(p_{\text{el},t,h}E_{\text{net},t,h}) - C_{\text{op},t}}{(1+IRR_{\text{targ}})^t} - \sum_{t=n_{\text{con}}+n_{\text{op}}}^{n_{\text{con}}+n_{\text{op}}+n_{\text{dec}}-1} \frac{C_{\text{dec},t}}{n_{\text{dec}}(1+IRR_{\text{targ}})^t}, \quad (3.49)$$

which can be used to calculate the bidding PPA tariff that is necessary to achieve a predefined target IRR for a given capital structure and cash flow by solving for the required PPA tariff $p_{\text{PPA,req}t,h}$ (Guédez, 2016). Analogously to the calculation of the IRR, this can be achieved by solving for the electricity price that corresponds to a NPV of zero with the desired IRR. However, this approach can only be used in order to obtain a minimum possible bidding price for a baseload tariff structure as the price is calculated as a levelised tariff over the complete lifetime of a project in real terms.

Alternatively, Eq. (3.49) can also be used by policy makers to calculate the lowest possible PPA tariff that would make the NPV of a CSP project zero. For this, the target IRR in Eq. (3.49) is simply assumed to be the nominal discount rate d_{nom} which is simply the nominal WACC in this study. However, this approach requires a carefully selected nominal discount rate and the effectively proposed PPA tariff should be higher than the calculated minimal value to also allow the CSP plant to generate some profit.

3.7 Cost Projections Until 2050 Through Learning Rates

This section introduces the method used to project the future costs and LCOE of MSPTPPs from present to 2050. Based on the assumption that the costs of a power plant reduce continuously the more power plants are built, the effect of this economy of scale can be used to project the future cost development. The cost reduction of power plants can be characterised by so-called learning curves, which describe the reduction of costs as a function of the cumulative installed capacity as a result of the experience gained from past projects. Figure 3.9 plots the weighted average of the total installed costs of CSP plants in log-log space for two datasets. The first is based on data from Lilliestam *et al.* (2018) for plants installed between 2007 and 2020. After deflating the capital costs to $\$_{2018}$, the annual weighted average costs have been calculated. The second set uses the weighted average costs of global CSP plants as reported by IRENA (2019) with the cumulative installed capacity in each year based on data from NREL (2020). The learning curve for both datasets is plotted as a straight line in log-log space since it is based on a logarithmic function. The slope of the learning curves can be converted to a *learning rate* (LR), which can be interpreted as a cost reduction of future installations in percent each time the cumulative installed capacity doubles. It can be seen that the total installed costs from Lilliestam *et al.* (2018) are on average 13 % lower than the costs reported by IRENA (2019). However, both learning curves have a clear downward trend of the total installed costs with increasing installed capacity.

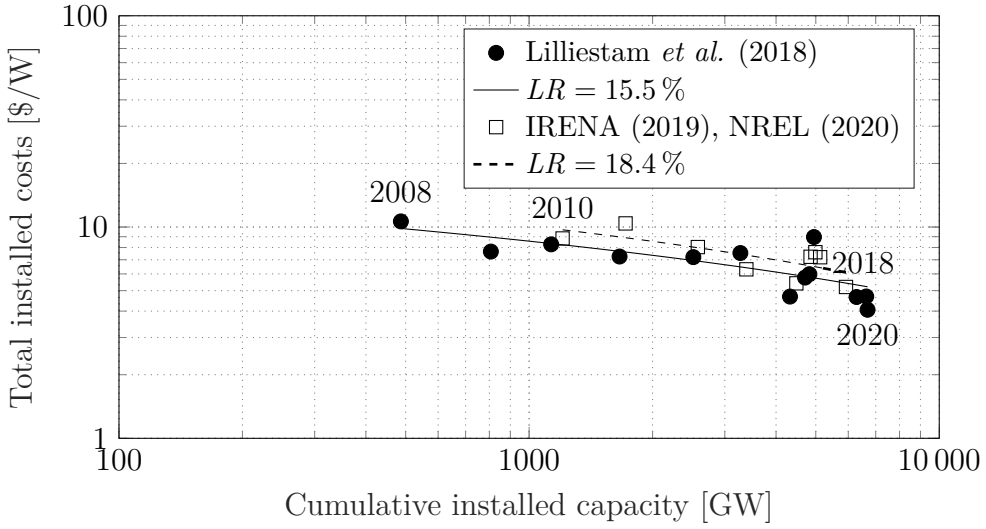

Figure 3.9: Learning curves of total installed costs of CSP plants based on data from Lilliestam *et al.* (2018) between 2008 and 2020 (deflated to $\$_{2018}$) and IRENA (2019) between 2010 and 2018 with cumulative installed capacity from NREL (2020).

Nevertheless, the data from Lilliestam *et al.* (2018) shows that the costs decrease slower with a LR of 15.5 %. In contrast, the data from IRENA (2019) has a LR of 18.4 % which means that the installed costs decrease faster with each doubling of the globally installed capacity.

Assuming 2018 as the base year, the learning curves can be used to express the costs c_t in any given year t as a function of the learning rate LR, the total installed costs c_{2018} and the cumulative installed capacity $\dot{W}_{2018}$ in the base year with Eq. (3.50) from Trieb (2004):

$$c_t = c_{2018} \left(\frac{\dot{W}_t}{\dot{W}_{2018}} \right)^{\frac{\log(1-LR)}{\log 2}} \qquad \text{for } t = 2018, \ldots, 2050. \tag{3.50}$$

Here, the total installed costs c are given in \$/kW and the cumulative installed capacity $\dot{W}$ is expressed in GW. In order to calculate future costs, the future cumulative installed capacity needs to be known or estimated. For that purpose, roadmap scenarios and forecasts can be used to project the future CSP deployment. Figure 3.10 shows the projected cumulative installed CSP

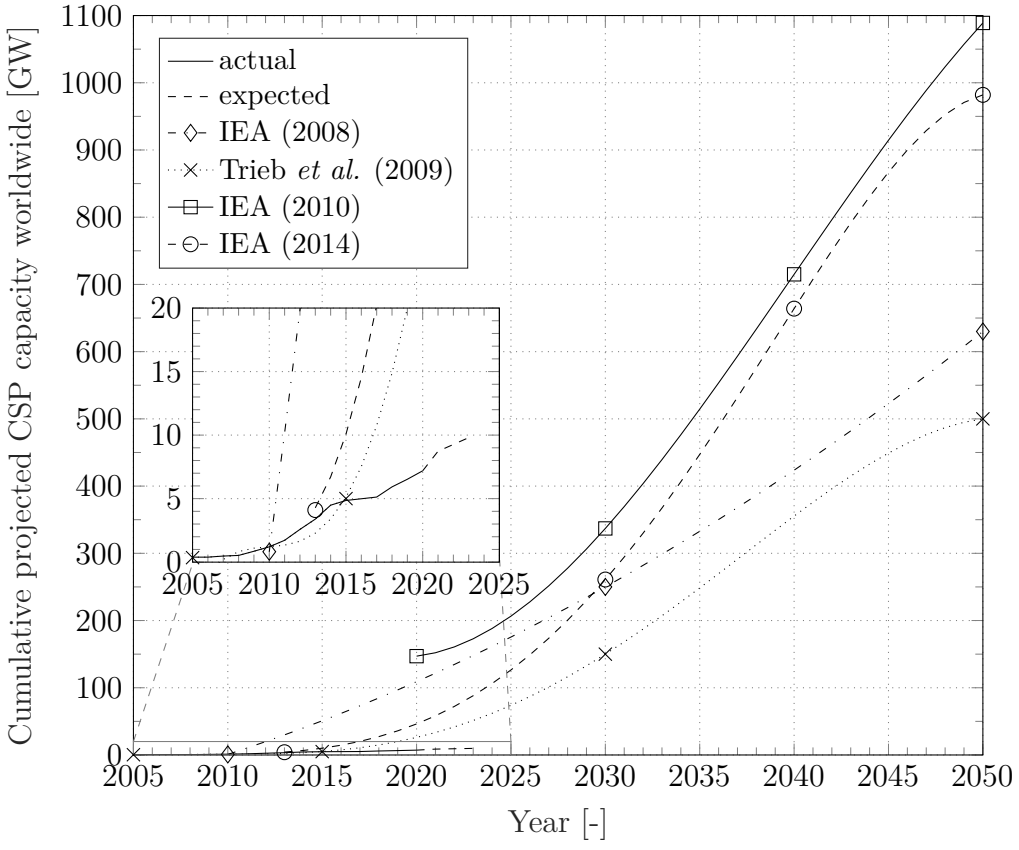

Figure 3.10: Projected cumulative installed CSP capacity worldwide until 2050 and close-up of actual installed capacity until 2020.

capacity until 2050 according to four roadmap scenarios, i.e. IEA (2008), IEA (2010), IEA (2014) and Trieb *et al.* (2009). The respective projected CSP capacities are listed in Table 3.10. The graph is extended by the actually installed capacity until 2020 as well as the expected capacity until 2023 as per Figure 1.1a (NREL, 2020). It can be seen that all projections fail to match the actual progression of CSP deployment until 2020 by assuming a rapid increase in annual installations. However, the projection by Trieb *et al.* (2009) appears to represent the most moderate and realistic scenario for the CSP expansion until 2050. Hence, this projection is selected to forecast the cost development until 2050. To obtain the annual cumulative installed capacity for this scenario, the values from Table 3.10 have been fitted with a fourth grade polynomial as a function of year t for $2018 < t < 2050$:

$$\dot{W}_t = -0.00052t^4 + 4.214t^3 - 1.279 \times 10^4\, t^2 + 1.725 \times 10^7\, t - 8.728 \times 10^9. \quad (3.51)$$

Now, with the costs in 2018 and the future cumulative installed capacities defined, the costs c_t in any given year t can be calculated. These costs are then used to calculate the LCOE for future plants using a variation of the simplified LCOE method from Eq. (3.45):

$$LCOE_t = \frac{c_t + \sum_{j=1}^{n_{\text{op}}} \frac{OPEX_{t,j}}{(1+d)^j}}{\sum_{j=1}^{n_{\text{op}}} \frac{e_{\text{net},j}(1-r_{\text{deg}})^{j-1}}{(1+d)^j}} \qquad \text{for } t = 2018, \ldots, 2050, \quad (3.52)$$

where $e_{\text{net},j}$ is the specific annual generated electricity per installed capacity in [kWh/kW]. As CSP plants experience a yearly reduction in power production due to degradation, the generated electricity is reduced annually by the degradation factor r_{deg} which is assumed to be 0.1 % per year. The useful lifetime of the power plant (n_{op}) is assumed to be 30 years which has also been used in studies by Hernández-Moro and Martínez-Duart (2012) and Kost *et al.* (2018). Some studies suggest an economic lifetime of 25 years (e.g. IRENA (2019), Lilliestam and Pitz-Paal (2018), Parrado *et al.* (2016) and Kost *et al.* (2013)) but as the recent DEWA bid for the combined tower and trough plant *DEWA IV*

Table 3.10: Projected cumulative installed CSP capacity until 2050 for each scenario/forecast.

Scenario/forecast	Unit	2005	2010	2013	2015	2020	2030	2040	2050
IEA (2008)	[GW]	-	0.82	-	-	-	250	-	630
Trieb *et al.* (2009)	[GW]	0.354	-	-	5	-	150	-	500
IEA (2010)	[GW]	-	-	-	-	147	337	715	1089
IEA (2014)	[GW]	-	-	4.1	-	-	261	664	982

has obtained a PPA for 35 years (Lilliestam and Pitz-Paal, 2018), the trend goes towards longer-running PPAs. Hence, assuming a financial lifetime of 30 years is more likely to be representative for future power plants. The discount rate d is assumed to be 10 % which is in line with studies conducted by IRENA (2019), Hernández-Moro and Martínez-Duart (2012), Parrado *et al.* (2016) and Lilliestam *et al.* (2018) (for non-OECD countries). For comparison, Kost *et al.* (2013) assume a nominal WACC of 9.7 % as the discount rate, whereas Kost *et al.* (2018) assume a WACC of 7.9 % for CSP plants. Lastly, the annual operation and maintenance costs $OPEX_{t,j}$ can be estimated with

$$OPEX_{t,j} = (f_{\mathrm{OPEX}} + f_{\mathrm{ins}})\, c_t \qquad \text{for } t = 2018, \ldots, 2050, \tag{3.53}$$

where the operation and maintenance costs factor f_{OPEX} and the insurance costs factor f_{ins} are assumed to be 1.5 % and 0.5 % of the specific capital costs c_t in year t, respectively. These annual operating expenses are not adjusted by inflation. Therefore, the LCOE for the projection until 2050 is given in real terms (constant $\$_{2018}$) in order to avoid distortion of the data by using a possibly wrong value for the inflation which cannot be estimated with a high level of confidence. This also enables a better comparison of the LCOE of CSP with the costs of other technologies, e.g. coal-fired power plants.

Finally, a suitable LR has to be chosen in order to estimate the costs of CSP with increasing deployment based on Eq. (3.50). A large variety of LRs for CSP can be found in literature. Trieb *et al.* (2009) suggest a LR of 10 % for the solar field, 8 % for the TES and 2 % for the power block. Kost *et al.* (2013) calculated the average LR of the entire power plant, yielding an average of 7.5 %. Similarly, Kost *et al.* (2018) estimated a LR of 7.5 % for CSP in an average cost development scenario. Hernández-Moro and Martínez-Duart (2012) suggest a LR of 12 % based on data from the SEGS plants and Craig *et al.* (2017) proposed a LR of 11.4 % for South Africa. Similarly, Platzer and Dinter (2016) estimate that LRs of at least 10 % to 15 % are possible for CSP plants. However, recent analyses have suggested that the LR has increased to above 20 % since 2013 (Lilliestam *et al.*, 2017). Likewise, IRENA (2018) found that the LR of CSP is 30 % with the expected deployment in the period of 2010–2020 and that 30 % would also be possible in the period of 2010–2022 when considering the recent record-bid of 73 $/MWh (Lilliestam and Pitz-Paal, 2018) in Dubai. Based on this optimistic outlook of recent studies and record-low bidding prices, this study assumes a LR of 20 % but will also consider a more conservative scenario with a LR of 10 % in section 6.4.

3.8 Summary

A detailed 2018-cost model for MSPTPPs in Southern Africa was presented. The model takes into account direct and indirect capital costs for equipment, infrastructure, contingencies and EPC, as well as operating costs that include

OPEX, insurance, and taxes. The financing costs for CSP projects in Southern Africa are assumed to be 12 % for debt and 18 % for equity financing. It was shown that — within the financial boundary conditions in Southern Africa — the financing costs make up the largest cost share of the LCOE and an optimised financing structure is required in order to significantly reduce a project's LCOE.

In order to analyse the effect of tariff structures on the economic feasibility of CSP plants, a baseload and a two-tier tariff structure are used for baseload and peaking operation, respectively. All tariffs are assumed to be escalated annually to account for inflation. Additionally, the DAM trading prices of 2018 will be used in chapter 6 to investigate the potential spot market participation of MSPTPPs. Next, key economic performance indicators (i.e. LCOE, NPV and IRR) were defined that enable the identification of power plant configurations and operational parameter set points that lead to an optimised financial feasibility in chapter 6. Lastly, a method to project the future costs and LCOE of MSPTPPs by 2050 in Southern Africa was presented. Using the learning curve approach, the expected cost reduction of CSP plants by 2050 is estimated based on the projected global CSP capacity installed by 2050.

Chapter 4

Model Validation[1]

In order to confirm the accuracy of the developed model, a validation study is necessary. However as there are currently no comparable MSPTPPs in operation, there is a lack of useful data available for the validation. Hence, an initial validation of the model with the open-source simulation software SAM (NREL, 2018) is carried out. Next, measurement data from a molten salt test loop in Massa Martana, Italy, is used to validate the empirical heat loss model of the receiver tubes. Lastly, the results from the model are compared to financial data from two PTPPs in South Africa in order to validate the economic model.

4.1 Validation with SAM

SAM is widely considered as a well validated tool in academia for performance analyses of CSP plants. Although the software allows the use of commercially available molten salts like Solar Salt, Hitec and Hitec XL, the operating strategy and control system is not advantageous for this type of HTF. The original intention of use was for thermal oils, which have a considerably lower freezing temperature than molten salts (12 °C compared to between 120 °C and 220 °C depending on the salt), making the need to continuously recirculate the HTF through the solar field at night a less prioritised requirement. However, molten salts are limited by their high freezing temperature. One possible FP method is to recirculate the fluid from the cold tank as investigated by Kearney *et al.* (2003) and Poole (2017). SAM does not offer the option to direct the HTF from the solar field outlet to the cold tank but rather circulates it directly back to the solar field. Thus, an improved operating control allowing the recirculation from the cold tank is required. Furthermore, SAM does not allow the user to specify a dedicated flow rate for FP but rather uses the minimum flow rate instead. This assumption might be valid in order to minimise the heat

[1] Parts of this chapter have previously been published in Pan *et al.* (2018*a*) or have been submitted for publication (see Pan *et al.*, 2021).

loss in the solar field during the night but a higher flow rate would guarantee that the entire solar field piping stayed warm throughout the night.

Another limiting factor of SAM is the discretisation of the SCAs into only one node per SCA. As shown by Zaversky *et al.* (2013); Yebra *et al.* (2008, 2010); Hirsch *et al.* (2005); Spelling *et al.* (2012) and Gálvez-Carrillo *et al.* (2009), a smaller spatial resolution of the SCAs leads to a more confident representation of the transient response of the solar field. When using molten salts, a precise prediction of the solar field's thermal inertia is necessary to accurately predict when the FP system needs to be activated to avoid freezing of the fluid in the pipes. Hence, a more flexible and adjustable model that allows specific user-inputs is favourable. The model developed in this study aims at providing a PTPP model specifically for the usage of molten salts as HTF and to provide the user with more possibilities to replicate their desired plant design.

The validation of the entire plant model has been carried out with SAM for the three different salt mixtures. The model error has been calculated in terms of the *root-mean-square error* (RMSE), which is a common indicator used to quantify the accuracy of transient models. In its general form, this error represents the standard deviation of the residuals between a typically measured outlet temperature $T_{\text{out,m},j}$ and the simulated outlet temperature $T_{\text{out,s},j}$ for N data points and is given by

$$RMSE = \sqrt{\frac{\sum_{j=1}^{N} \left(T_{\text{out,s},j} - T_{\text{out,m},j}\right)^2}{N}}. \tag{4.1}$$

However in this case both outlet temperatures were simulated, the RMSE is calculated based on the two simulated outlet temperatures of the two models. The RMSE penalises large errors more than small ones because the differences of the measurement and prediction are squared before they are averaged. This could be an important feature in e.g. control design studies, where a model representing transient changes more accurately is desired. In contrast, the *mean absolute error* (MAE) measures the average magnitude of the error induced in the model and can be calculated with

$$MAE = \frac{\sum_{j=1}^{N} \left|T_{\text{out,s},j} - T_{\text{out,m},j}\right|}{N}. \tag{4.2}$$

Because the MAE is less sensitive to outliers than the RMSE, it is also often used to assess the error of a model and will therefore be included. The complete validation with SAM is discussed in detail in Pan *et al.* (2018*a*). Nevertheless, a brief summary of the key results obtained from this validation is provided hereafter. However, since the validation with another computer software lies outside the main objective of this study, the complete validation with SAM is discussed in detail in Appendix F. Nevertheless, a brief summary of the key results obtained from this validation is provided hereafter for coherence.

The power plant for the validation has a gross turbine capacity of 55 MW,

a solar multiple of 1.6 and 6 h of TES capacity. The power cycle is assumed to have a thermal efficiency of 37 % with a boiler pressure of 100 bar. The validation has shown that the model performs well with Solar Salt as HTF with a MAE of the loop outlet temperature of 2.51 °C but produces considerably larger errors when using Hitec or Hitec XL. The main reason for the increased errors with these two HTFs has been found to be due to the empirical heat loss model that underestimates the heat loss at lower temperatures as compared to SAM. Additionally, the model neglects heat losses from expansion bellows and support brackets which would reduce the absorbed thermal energy in the HTF. This also leads to higher errors for all other performance indicators as shown in Table F.3. Furthermore, the net electricity output of the model shows a similar behaviour to the output from SAM with some discrepancies happening during the start-up and shut-down periods. The variation of the net power output during operation is mainly due to the solar field pump and ACC parasitics. However, with MAEs between 1.48 MW and 3.68 MW (or 2.7 % and 6.7 % of the installed capacity of 55 MW) for the net power output with Solar Salt, the model shows a good agreement with the results from SAM. It has been found that the TES was charged earlier in the day in the model and the fill level was generally higher as compared to SAM. This can be attributed to the two very different TES integrations and dispatch strategies. Unfortunately, this is a result of the limitations of both SAM and the model that cannot be easily altered in order to align the two TES integrations. However, various adaptations have been implemented in the model to facilitate molten salts and their specific operation requirements. The results show that the recirculation from the cold tank keeps the fluid temperature above the FP temperature during some nights and thus reduces the need for electric impedance heating.

Finally, it can be concluded that the results obtained from the model are in good agreement with the results from SAM. In order to further confirm the model's accuracy, a validation with real measurement data is desirable. This validation will be carried out in the following section.

4.2 Solar Field Validation with Measurement Data

The following sections discuss the validation of the solar field model with measurement data from a molten salt test loop. A comparison of the measured and simulated fluid outlet temperature of each SCA as well as a validation of the loop thermal output are provided. The effect of decreasing levels of discretisation on the loop outlet temperature is discussed in order to assess the accuracy of the model in terms of the transient response and the induced error. Additionally, the effect of the number of CVs per SCA on the required simulation time (computational effort) is also investigated. The complete val-

idation with the measurement data is discussed in more detail in Pan *et al.* (2021).

4.2.1 The Archimede Solar Energy demonstration plant

The data used for the validation has been provided by Archimede Solar Energy, which is based in Massa Martana, Italy. The company produces the *HCEMS-11* receiver tube, which has been specifically designed for use with molten salts as HTFs for temperatures of up to 550 °C (Archimede Solar Energy, 2017). Archimede Solar Energy has been operating the first standalone molten salt parabolic trough demonstration plant since 2013 and has proven the viability of using molten salts — in this case Solar Salt (60 % $NaNO_3$, 40 % KNO_3) — as HTF for standard sized CSP plants (Maccari *et al.*, 2015). Tests involving critical situations for the safe and reliable operation of the plant such as thawing and freezing of the HTF in the receiver tubes as well as long term high temperature operation and thermal cycling have been completed successfully (Maccari *et al.*, 2015; Matino and Maccari, 2015).

The test facility consists of a single north-south oriented loop of six SCAs with a total of 144 HCEs as well as a cold and hot tank of 25 m^3 each. The main design data of the solar collector loop is listed in Table 4.1. In order to prevent the HTF from freezing, the receiver tubes and flexible hoses can be heated through *impedance heating* while the residual piping and valves are fitted with mineral insulating cables for resistance heating.

Table 4.1: Archimede Solar Energy demonstration plant design data (Maccari *et al.*, 2015).

Parameter	Unit	Value
Solar field		
SCA length	[m]	100.33
Collector aperture width	[m]	5.96
Loop net aperture area	[m^2]	3398.4
Focal length	[m]	1.81
Number of SCAs in a loop	[-]	6
Design inlet temperature	[°C]	290
Design outlet temperature	[°C]	550
Design thermal output	[kW_{th}]	1900

4.2.2 Test loop measurement data

The measurement data has been collected over a period of 23.5 hours from 2nd April 2015 at 23:15 to 3rd April 2015 at 22:45 local solar time. All data

has been recorded with a time step size of 10 s, which is also set as the simulation time step. The DNI is shown in Figure 4.1 alongside the product of the DNI with the cosine of the incidence angle θ in order to demonstrate the amount of usable irradiance on the SCAs, thus taking into account the cosine losses. Additionally, Figure 4.2 shows the ambient air temperature and wind speed during the measurement period. It can be seen that the solar irradiance steadily increased right from sunrise around 6:20 with only some small disturbances due to clouds at around 11:30 until it reached it's maximum of 955 $\mathrm{W/m^2}$ around 13:00. Towards the end of the day, some cloud-cover reduced the DNI from 15:30 until sunset at 18:00. Similarly, the ambient air cools down during the night and reaches its lowest value of 3 °C at 6:00. As the sun rises shortly after, the air is heated up quickly and the highest air temperature is reached with 19.6 °C just before 16:00. Thereafter, the sky is covered with some clouds and the air temperature starts to fall. Immediately after dusk, the temperature starts to plummet. The wind speed during the measurement period is highly volatile but is relatively low throughout the day except for the period from the late morning until the evening. The range of the wind speed is 0.09 m/s to 8.3 m/s.

Figure 4.3 shows the collected measurement data for the loop inlet and outlet temperature (T_{in} and T_{out}), mass flow $\dot{m}$, number of focused collectors N_{SCA} and electrical power of the FP system P_{fp}. The inlet temperature T_{in} has been directly measured at the inlet of SCA 1 while the outlet temperature T_{out} has been measured directly at the outlet of SCA 6. The mass flow rate of the HTF has been kept constant at approximately 3.7 kg/s throughout the duration of the experiment when the solar field was not in focus. As soon as the collectors were turned into focus, the controller reduced the mass flow in order to keep the outlet temperature at the set point of 550 °C.

All collectors were focused simultaneously around 10:30 and remained in focus until a successive defocusing sequence was carried out after 14:00, starting with SCA 6. This is especially useful for validating the effect of such operational interventions on the accuracy of the model. Shortly after all collectors were defocused they were all turned back into the focal point at the same time. The following focus/defocus operations at around 15:15 were the result of keeping the mass flow constant at 3.6 kg/s and the HTF consequently surpassing its set outlet temperature. In an attempt to reduce the solar energy input on the receiver tubes, the SCAs were defocused arbitrarily. As soon as the cloud-cover started to form, all SCAs were focused again in order to be able to validate the effect of intermittent solar irradiance on the performance of the model. At the end of the day, all SCAs were defocused again.

Figure 4.3 shows the effect of all the changes in operation on the fluid outlet temperature. Prior to the on-sun operation of the solar field, the outlet temperature decreased steadily until it approached the lower temperature set point and impedance heating was activated at 00:10. The impedance heating in the absorber tubes resulted in an increase of the outlet temperature above

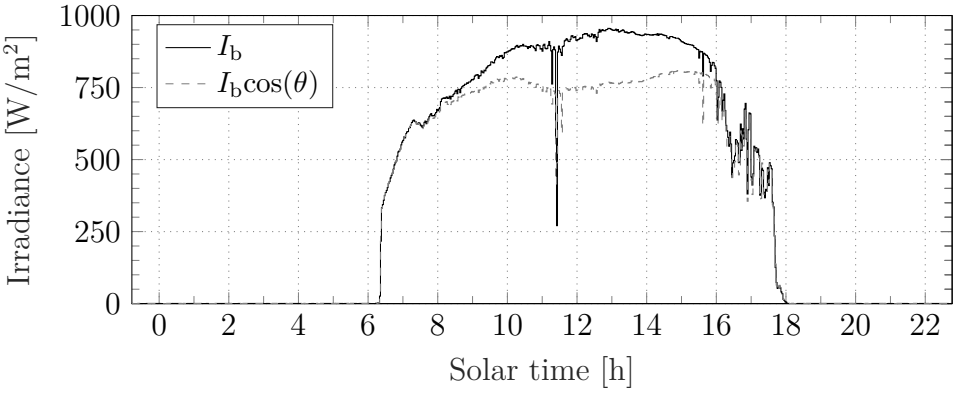

Figure 4.1: DNI and DNI after cosine losses on 3rd April 2015.

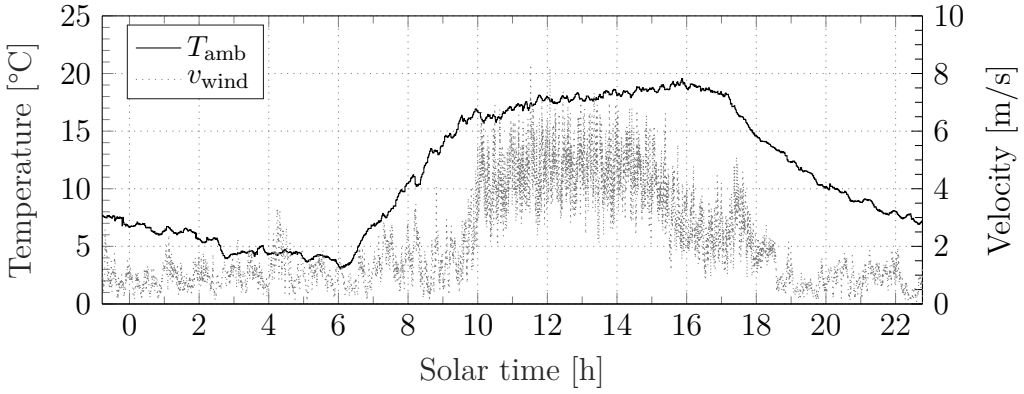

Figure 4.2: Ambient air temperature and wind speed on 3rd April 2015.

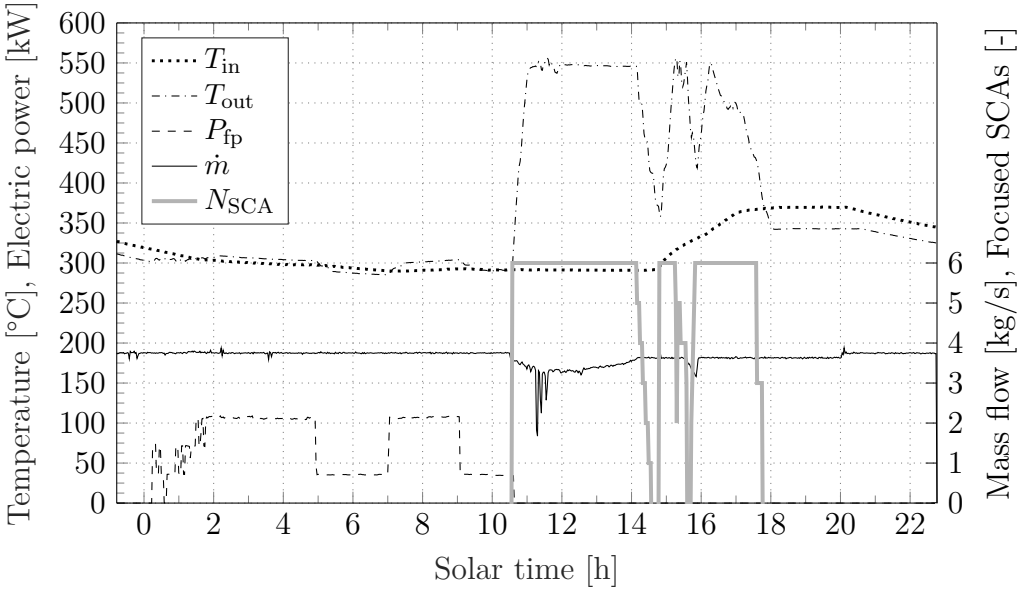

Figure 4.3: Measurement data of the Archimede Solar Energy demonstration plant on 3rd April 2015.

the fluid inlet temperature at around 2:00. As soon as the impedance heating power input was reduced at 5:00, the outlet temperature again fell below the inlet temperature. The same process was repeated at 7:00 when the outlet temperature decreased below 290 °C.

Furthermore, it can be seen that the inlet temperature starts to steadily increase at around 14:30. This is due to the fact that the air cooler rejecting the heat produced in the solar field was already operating at full capacity and the cold tank has been nearly fully emptied. Therefore, the fluid returning to the loop could not be cooled down to the desired 290 °C and the inlet temperature increased until sunset.

4.2.3 Validation setup

Recall that the modelling approach presented in section 2.3.2 required a discretisation of the spatial domain of the receiver into a number of discrete volumes, i.e. CVs, along the receiver axis. The more CVs that the receiver is divided into, the smaller these volumes get and the numerical solution approaches the analytic solution of the underlying differential equation. Choosing an appropriate number of divisions strongly depends on the intended purpose of the study. Control design studies, for example, typically require a higher spatial resolution in order to accurately reproduce the transient response of the solar collector. For this purpose, Yebra *et al.* (2010) recommend a spatial resolution of 7.3 m to 18.3 m for a parabolic trough collector using thermal oil as HTF, whereas Hirsch *et al.* (2005) recommend 10 m. Similarly, Zaversky *et al.* (2013) also recommend a division of the SCA into intervals of 10 m for molten salt applications. Yebra *et al.* (2008) proposed a model for DSG and recommend a higher spatial resolution of 2.5 m to 5.6 m because the model needs to replicate the dominant dynamics of the solar collector more accurately in the case of DSG.

In contrast, the accurate reproduction of the transient response of the SCA does not generally play a central role when conducting dynamic performance simulations. These types of simulations are usually conducted to assess the annual yield of a CSP plant and use large time steps of up to an hour in order to keep the computational effort low. For that purpose, SAM uses only one CV per SCA, leading to a relatively low spatial resolution that is determined by the user input of the collector length. Similarly, Llorente García *et al.* (2011) also recommend a relatively large level of discretisation of 150 m per CV. In contrast, Spelling *et al.* (2012) used a spatial resolution of only 20 m and Zaversky *et al.* (2013) proposed a CV size of approximately 16 m. According to the researchers, this represents a good trade-off between model accuracy and simulation speed that is suitable for most transient simulation purposes.

As previously mentioned in section 2.3.7, the model is implicitly formulated in order to allow the use of large time steps whereby the limitation through the CFL condition does not apply. This also enables the use of smaller CVs.

Hence, the present study assumes a division into 40 CVs per SCA, thus fulfilling the condition of the Biot number for the lumped capacitance model that required a minimum division into 30 CVs per SCA. This corresponds to a spatial resolution of 2.5 m per CV. As compared to the spatial resolutions used in the studies mentioned above, this is a relatively small receiver segment length, which can be assumed to lead to a significantly more accurate approximation of the loop outlet temperature. Therefore, the main validation process has been conducted with 40 CVs per SCA in section 4.2.4 and has subsequently been gradually reduced to up to 1 CV in order to collect information on the effect of larger CVs on the accuracy of the model (see section 4.2.5). Furthermore, section 4.2.7 discusses the use of large time step sizes of up to 60 min on the accuracy of the model.

4.2.4 Comparison of the measured and simulated fluid outlet temperature

A comparison of the measured and simulated loop outlet temperature can be seen in Figure 4.4. An overall good agreement of the simulated values with the

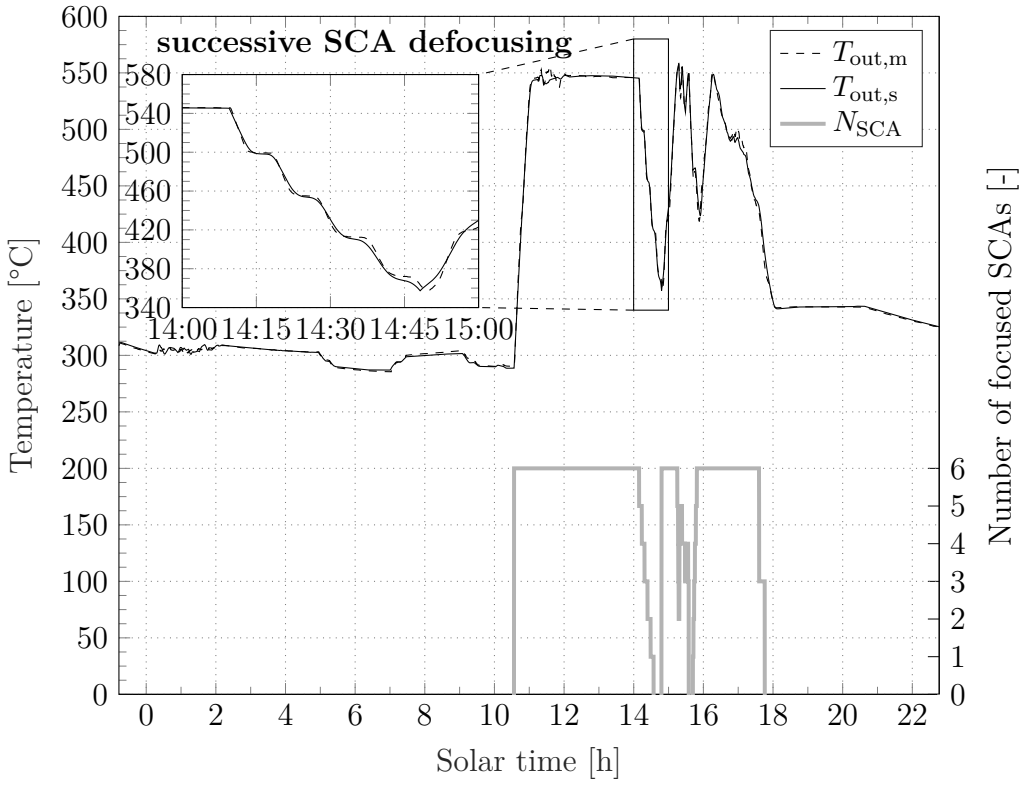

Figure 4.4: Comparison of measured and simulated HTF outlet temperature of the loop with close-up of successive SCA defocusing and number of focused SCAs in the loop with 40 CVs per SCA.

measured data can be observed over the entire measurement period apart from a short mismatch at around 11:30 that is caused by the fluctuating DNI. The impedance heating is first activated just after midnight (see Figure 4.3) and is alternately switched between its three power states, i.e. low, medium and high power to heat the HTF. Shortly before 2:00, the electrical power input into the absorber tubes is kept constant at its highest power setting, maintaining an elevated outlet temperature. At 5:00, it is switched to the lower setting which results in a fast decrease of the HTF outlet temperature. As the warmer fluid is still slowly propagating through the SCAs followed by cooler fluid, the thermal inertia of the SCAs causes a delay in the cool-down of each SCA, resulting in a "stepped" outlet temperature profile at the exit of the last SCA. The slope of the outlet temperature during the second high-intensity impedance heating phase (from 7:00 to 9:00) is increasing — as compared to the decreasing slope of the first phase. This is due to the presence of non-concentrated solar irradiance on the receiver tube as the sun had already risen but the collectors were still defocused. Note that switching the impedance heating into its high power setting leads to the same temperature step as described during the cool-down.

In order to shed some light on the effect of the successive defocusing sequence at 14:00, Figure 4.4 includes a close-up view of said period. Here, the fluid outlet temperature profile is rigorously reproduced after consecutively turning each SCA out of focus as well as when the collectors are all simultaneously focused at start-up. Furthermore, the outlet temperature is kept relatively constant close to the set point of 550 °C throughout the operation from 11:00 to 14:00. Only during times of intermittent solar irradiation at 11:30 and again from just before 17:00 is there a slight mismatch between the simulated and measured values due to an overestimation of the heat loss in the cross-over piping.

4.2.5 Model error

As introduced in section 4.1, two indicators have been used to quantify the accuracy of the transient model, namely the RMSE from Eq. (4.1) and the MAE from Eq. (4.2). The RMSE of the model with the highest discretisation level, i.e. 40 CVs, has been calculated to be 2.57 °C. Compared to the measured average loop outlet temperature of 370.2 °C, this corresponds to a relative error of 0.69 %. Likewise, the MAE is 1.56 °C. These errors confirm that the model is meticulously calculating the loop outlet temperature and accurately reproducing the transient behaviour of the solar collector.

However, the high spatial resolution of 2.5 m per CV requires a considerable amount of computational effort. At a time step of 10 s, the model requires 27.6 s to simulate the investigated 23.5 h period with a standard desktop computer with 3.40 GHz. Extrapolating this time requirement to a full annual performance simulation, the simulation time would amount to approximately 2.8 h. Since this is an infeasibly long time requirement (especially for the in-

tended use of the model for multi-objective optimisation studies that require well above 5000 simulation runs per optimisation), the number of CVs per SCA has been gradually reduced in order to reduce the number of iterative systems of equations in the model. The resulting spatial resolutions and their respective RMSE and MAE are depicted in Table 4.2. It can be seen that the RMSE and MAE increase with the reduction of CVs per SCA, leading to a maximum RMSE of 3.68 °C and a MAE of 2.20 °C for the lowest level of discretisation of 1 CV per SCA. This corresponds to a relative error of 0.99 % compared to the measured average loop outlet temperature. Contrastingly, Table 4.2 also shows the required simulation time for each discretisation level, where using only 1 CV per SCA can reduce the simulation time to 7.6 s for the investigated 23.5 h period. Thus, the estimated computational time required for an annual performance evaluation would be 0.8 h. This is, however, still impractically long for the intended use of the model in multi-objective optimisation studies due to the very small time step of 10 s. Hence, a large time step of 1 h is required for this kind of analyses. The effect of increasing the time step on the model performance is discussed in section 4.2.7.

The model errors reported in Table 4.2 all lie below a relative error of 1 % so that the model can still be considered to perform well even for low spatial resolutions of up to 100 m. Additionally considering an uncertainty range of the measurement data of ±2 °C, the MAE lies within the temperature sensor's uncertainty range up to a division into 2 CVs. Only the model with 1 CV has a MAE greater than the uncertainty range of the measurement data. The larger errors induced in the model by the lower discretisation levels can therefore be assumed to be sufficiently low to be feasible in annual performance evaluations. It must be noted that, as introduced in section 2.3.6, the lumped capacitance model is only valid for a minimum of 18 CVs with a maximum mass flow rate of 4 kg/s as observed in the measurement data. Although the receiver tube model is not valid for a discretisation into less than 20 CVs, the model errors in Table 4.2 show that using less CVs does not result in a significantly higher error as compared to the case with a highest spatial resolution.

Table 4.2: Validation results of loop outlet temperature for a decreasing number of CVs per SCA and corresponding time requirement to simulate a day and a year.

Number of CVs [-]	Spatial resolution [m]	RMSE [°C]	MAE [°C]	Relative error [%]	Req. simulation time	
					day [s]	year [h]
40	2.5	2.57	1.56	0.69	27.6	2.8
20	5	2.61	1.57	0.71	17.8	1.8
10	10	2.74	1.61	0.74	12.6	1.3
5	20	2.84	1.66	0.77	10.3	1.0
2	50	3.12	1.83	0.84	8.4	0.9
1	100	3.68	2.20	0.99	7.6	0.8

With a relative error below 1 % for all levels of discretisation, it can be assumed that using only one CV leads to sufficiently accurate results. This can also be seen in Figure 4.5, where the measured loop outlet temperature during on-sun operation of the solar collectors is shown in comparison to the simulated outlet temperature for discretisation levels of 1 CV and 5 CVs per SCA. Although the discretisation into 1 CV shows a good agreement with the measured data, the thermal response for this case is significantly slower, i.e. the time constant of the model increases with a decrease in spatial resolution). This is especially evident during the defocusing period between 14:00 and 15:00, where the simulated loop outlet temperature lags behind the measured one. However, this is not the case for the discretisation into 5 CVs, which shows a very good agreement with the measurement data. Therefore, a discretisation into 5 CVs per SCA (spatial resolution of 20 m) represents a feasible compromise between model accuracy and simulation time while having a RMSE below 3 °C.

Table 4.3 shows the model error of the loop thermal energy, thermal output and thermal efficiency for decreasing levels of discretisation. The error of the total loop thermal energy during the measurement period is between 1.54 % and 2.71 % with decreasing spatial resolution. As already mentioned, the empirical heat loss model underestimates the heat loss which results in an increased energy production of the loop. This can also be seen when looking at the RMSE of the loop thermal output, where the overestimation of the thermal output in the most detailed model results in a RMSE of 20.4 kW. However, considering the loop's design thermal output of 1900 kW (Maccari *et al.*, 2015), this leads to a relative error of 1.07 % which is acceptable. Similarly, the relative error for decreasing levels of discretisation ranges from 0.84 % to 1.33 %. Lastly, the RMSE of the loop conversion efficiency ranges from

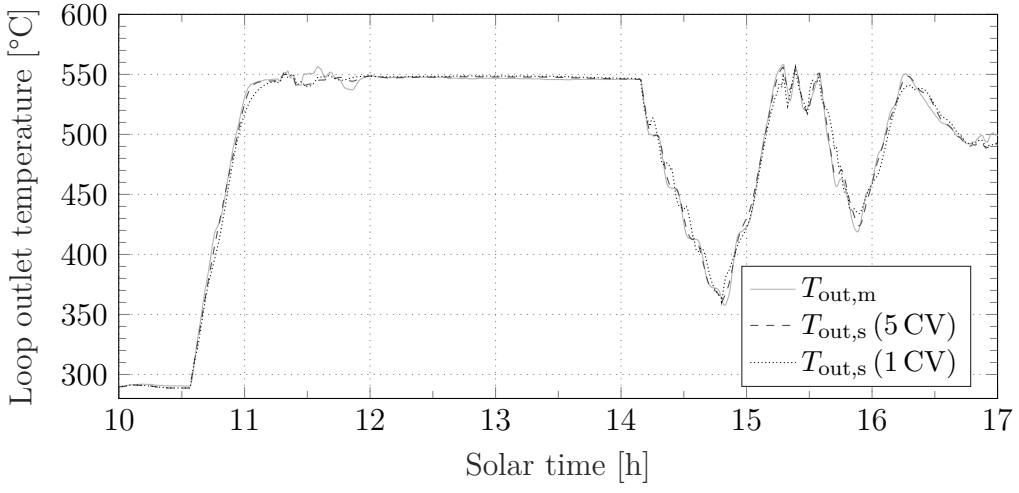

Figure 4.5: Comparison of measured and simulated loop outlet temperatures for discretisation levels of 1 CV and 5 CVs per SCA.

Table 4.3: Model error of loop thermal energy, thermal output and conversion efficiency for decreasing levels of discretisation.

	Thermal energy		Thermal output			Conversion efficiency		
CVs [-]	Total energy [MW h]	Error [%]	RMSE [kW]	MAE [kW]	Error[2] [%]	RMSE [%]	MAE [%]	Error[3] [%]
measured	7.730	-	-	-	-	-	-	-
40	7.849	1.54	20.4	5.0	1.07	2.16	0.30	3.28
20	7.845	1.49	16.0	4.8	0.84	2.50	0.33	3.79
10	7.853	1.59	16.1	5.1	0.85	2.51	0.34	3.81
5	7.863	1.72	16.7	5.5	0.88	2.62	0.37	3.98
2	7.894	2.12	19.8	6.8	1.04	2.64	0.41	4.01
1	7.940	2.71	25.2	8.7	1.33	3.05	0.51	4.63

2.16 % to 3.05 %. Considering the loop's peak efficiency of 65.9 % during the measurement period, this results in a relative error between 3.28 % and 4.63 %. Although the model is theoretically not valid for a discretisation below 20 CVs, it can be seen that the induced error is acceptable even when using only 1 CV per SCA. Nevertheless, discretisation into at least 5 CVs is recommended as a good trade-off between model accuracy and simulation time.

4.2.6 Loop thermal output

Additionally to the solar field outlet temperature, the thermal output of the loop has been investigated. Figure 4.6 shows the loop thermal output of the model and the test loop for two periods of interest. The first is a period during the night when the impedance heating is active as shown in Figure 4.6a. It can be seen that there is good agreement between the model and the measured data when the thermal output is greater than zero. Contrary to this when the solar field outlet temperature is lower than the inlet temperature (negative thermal output), the model overestimates the thermal output. This can be attributed to the empirical heat loss model which does not factor in ambient conditions like air temperature or wind speed. Although the wind speed was below 4 m/s during this period, the ambient air temperature dropped to 3 °C just before sunrise at 6:30 (see Figure 4.2). Hence, it is clear that the empirical heat loss model needs to be further improved in order to also capture the effect of ambient conditions on the heat loss. Furthermore, the model neglects heat losses from expansion bellows and support brackets which would increase the overall heat loss. Nevertheless as the heat loss from the support brackets and expansion bellows mainly depends on the receiver temperature, it is negligible during this period because the solar field is operating at its lower design tem-

[2] Compared to the loop design thermal output of 1900 kW.
[3] Compared to the peak conversion efficiency of the loop during that day of 65.9 %.

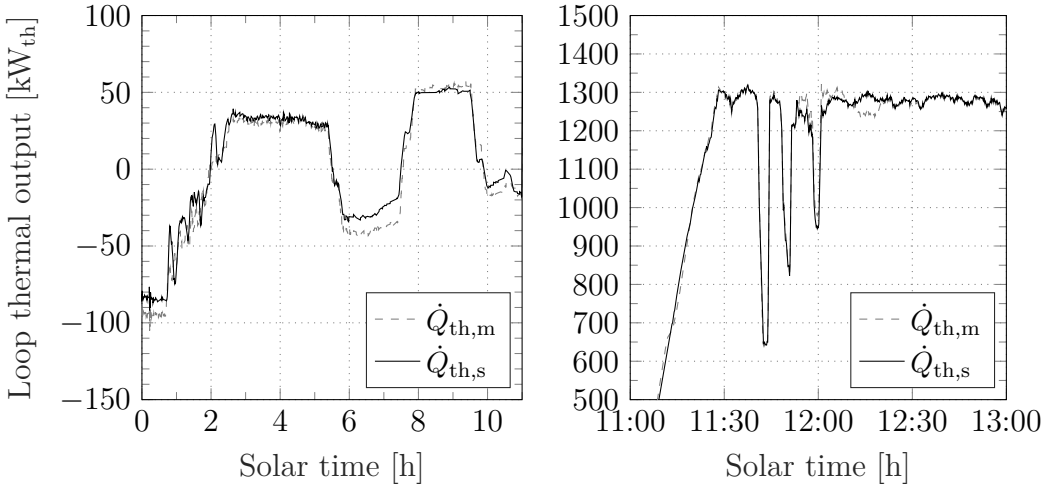

(a) Night-time. **(b)** Highly intermittent solar irradiance.

Figure 4.6: Comparison of measured and simulated loop thermal output with 40 CVs per SCA during (a) night and (b) highly intermittent solar irradiance.

perature of 290 °C. Figure 4.6 also confirms the accuracy of the FP system implemented in the model as it is the only heat input to the fluid during this period, showing good agreement between the simulated and measured thermal output of the loop.

The second period of interest is during on-sun operation of the collector as shown in Figure 4.6b. The simulated thermal output of the loop matches the measured data well during most of the period, i.e. during the start-up phase of the collectors and the intermittent solar irradiance until approximately 12:00. Thereafter, the thermal output of the model fluctuates around the measured values until approximately 12:30. In this case, the discrepancy of the simulated data is caused by high wind speeds during this period with a peak of 8.3 m/s (as seen in Figure 4.2). As mentioned above, the empirical heat loss model does not account for ambient conditions and is thus recommended to be extended to include the influence of the ambient air temperature and wind speed in a future study. Although the heat losses from expansion bellows and support brackets would be the highest during this period with the solar field operating at its upper design temperature of 550 °C, it can be seen that the omission of these heat losses does not significantly affect the loop thermal output. Hence, it can be assumed that the assumption to neglect these heat losses is justified.

Nevertheless, the MAE of the model over the entire period is 13.75 kW whereas the RMSE is 34.8 kW. The latter corresponds to 1.83 % of the loop's nominal thermal output of 1900 kW which shows that the simplified empirical heat loss model produces satisfactory results. Additionally, the total thermal energy output of the loop during the day is 7.90 MW h. This is 2.2 % larger than the measured thermal output of 7.73 MW h. Hence, it can be concluded that the thermal output of the loop is modelled accurately. Consequentially,

the outlet temperature and mass flow rate can also be considered to be accurately modelled by implication.

4.2.7 Model performance with large time step sizes

It is common practice for CSP yield analyses to conduct annual performance simulations based on hourly weather data due to the limited availability of the solar resource data as well as the computational time requirement. Hence, a certain error is inherent to any hourly performance simulation due to the nature of the modelling approach with large temporal resolution. As mentioned before, the implicit modelling approach guarantees numerical stability and allows the choice of large time steps. In order to assess their effect on the loop outlet temperature, the simulations have been repeated for time steps of 5, 15, 30 and 60 minutes. This has been done by dividing the whole measurement period into the corresponding time intervals and creating "snapshots" of the measurement data (i.e. inlet temperature, DNI, mass flow, impedance heating power, etc.) at the end of each time step as would be the case when using hourly DNI data from a typical meteorological year file. The results for a time step of 60 min is shown in Figure 4.7.

Compared to the measured outlet temperature with a 10 s interval, the simulation with a time step of 60 min does not accurately reproduce the loop outlet temperature due to the low temporal resolution. However, the relative error of the cumulative thermal energy between the simulated values and the measured data is only 1.3 %. Here, deviations from the measured data in the positive direction during one time step are cancelled out by deviations in the negative direction during another time step, leading to a sum that approximates the measured data (similar to the *Riemann sum* for numerical

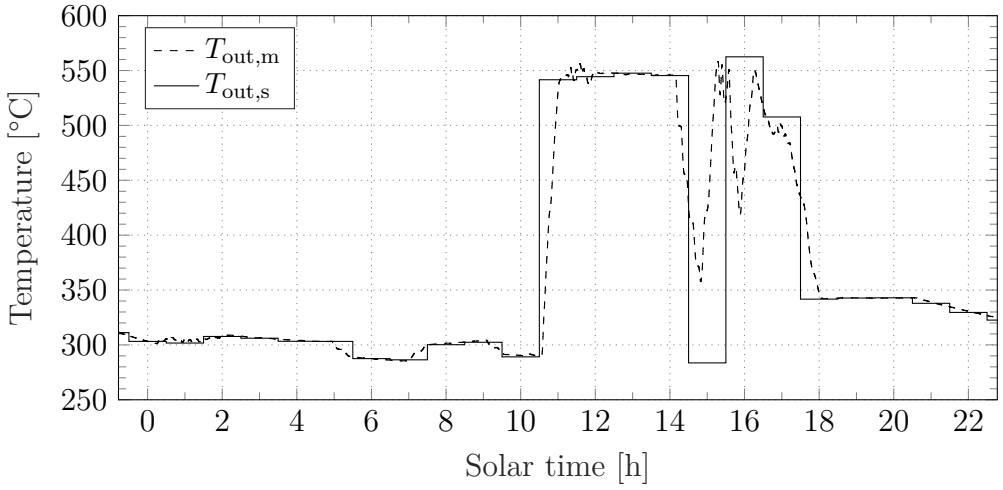

Figure 4.7: Comparison of measured and simulated loop outlet temperatures for a time step size of 60 min with discretisation into 40 CVs per SCA.

approximation of integrals by a finite sum of rectangles). However, this relatively small error will likely be considerably higher during times of highly intermittent DNI. Table 4.4 shows that the errors between the model with the investigated time steps and the measured data lie within an acceptable range of −7.8 % to 1.3 %. Thus, it can be concluded that the developed model is suitable for use in annual performance evaluations with time steps of up to 60 min.

Table 4.4: Errors of thermal energy delivered by the loop for time steps of 5, 15, 30 and 60 min as compared to the measured data (discretisation into 40 CVs).

Time step size	Loop thermal energy [MW h]	Error [%]
10 s (measured)	7.73	-
10 s	7.90	2.2
5 min	7.63	−1.3
15 min	7.77	0.5
30 min	7.12	−7.8
60 min	7.83	1.3

4.3 Validation of Power Plant Performance and Cost Model

In order to validate the overall power plant performance and the cost model introduced in chapter 3, this section compares the results from the developed model with data from two power plants currently in operation in South Africa, namely, Bokpoort and Kathu. However, both power plants use thermal oil as HTF and different collectors. Therefore, the model was adapted accordingly, which will be discussed below and followed by a comparison of the results.

4.3.1 Model adaptations

Due to the fact that both Bokpoort and Kathu use thermal oil as HTF in combination with different solar collectors, a direct comparison with the model presented in chapter 2 is not possible. Furthermore, Bokpoort uses a wet-cooled condenser for the power cycle, whereas the model and Kathu use an air-cooled condenser. Hence, a model for thermal oil PTPPs that was previously developed by Ferruzza *et al.* (2017) has been used for the wet-cooled condenser and the solar field, adding the indirect storage integration through heat exchangers. This model has been validated by Ferruzza *et al.* (2017) with a maximum error of 8.9 % in yearly electricity production. As the two power plants in question use a different type of collector and receiver than those presented as part of the model in chapter 2, their respective parameters have

been introduced to the model. This will be discussed in more detail at the beginning of sections 4.3.2 and 4.3.3. Furthermore, HTF properties for thermal oil (*Therminol® VP-1*) have been added. These thermo-physical fluid property correlations are listed in Appendix C. The remaining parts of the power plant have been left unchanged (i.e. the power block, TES, freeze protection system, solar field layout design etc.). It should also be noted that Bokpoort was awarded under BW2 and is therefore operated as a baseload power plant. In contrast, Kathu was part of BW3.5 and is therefore only operated during the day and evening due to the two-tier tariff. Hence, the operating strategy of each power plant matched in the model.

4.3.2 Comparison with Bokpoort

Bokpoort is a 55 MW (gross) thermal oil power plant in Groblershoop, Northern Cape, South Africa. Developed by ACWA Power, it started operation in 2016. The plant has an indirect TES of 9.3 h (Solar Salt) and uses the SenerTrough in conjunction with Schott's PTR70 receiver (NREL, 2020). Data for the collector has been taken from Castañeda *et al.* (2003), Relloso *et al.* (2011), Stolten and Scherer (2013) and GIZ (2014), whereas the data of the receiver has been taken from Schott (2013). It should be noted that the empirical heat loss model introduced in section 2.3.4 is based on correlations specific to Archimede Solar Energy's HCEMS-11 receiver from Eq. (2.44) and is therefore not valid for Schott's PTR70 receiver. Hence, the heat loss correlation based on the absorber tube surface temperature T_3 developed by Burkholder and Kutscher (2009) for Schott's PTR70 receiver has been used instead:

$$\dot{q}'_{\mathrm{hl}} = 0.141 T_3 + \left(6.48 \times 10^{-9}\right) T_3^4. \tag{4.3}$$

This correlation has been obtained by measuring the electric power required to maintain a set temperature from 100 °C to 500 °C in increments of 50 °C. Figure 4.8 shows the heat loss normalised per meter receiver length for both receivers. The heat loss of Archimede Solar Energy's HCEMS-11 receiver is higher than Schott's PTR70 receiver and the difference between the two increases with increasing absorber tube temperature. This is due to the second term in Eq. (2.44) and (4.3) which represents the receiver's radiative heat transfer rate that increases to the power of four with increasing absorber temperature.

In order to validate the model, key design and performance metrics of Bokpoort are compared to the results obtained from the model. Table 4.5 lists Bokpoort's plant design data as well as technical and financial performance indicators in comparison to the model's calculations. The net turbine capacity of Bokpoort is 50 MW, whereas the model estimates it to be 50.4 MW. This corresponds to an overestimation of 0.8 % mainly caused by an underestimation of the parasitic consumption. This, in turn, also leads to an overestimation by 0.7 % of the annual electricity production. Bokpoort's solar field has a total

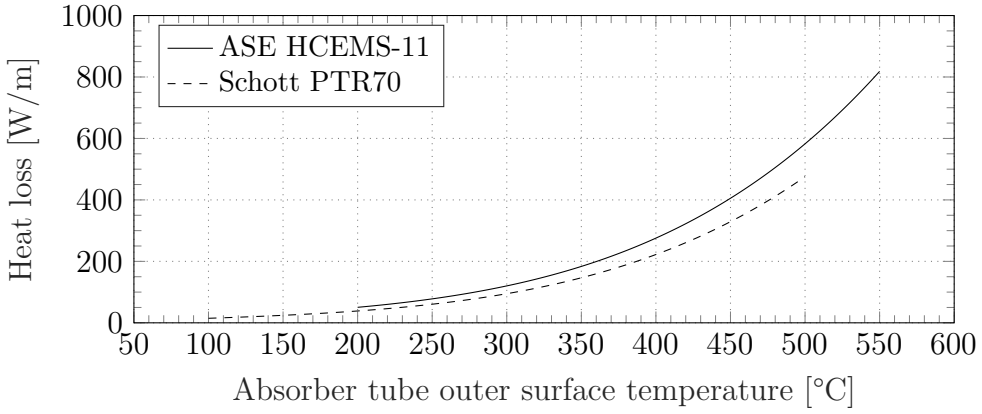

Figure 4.8: Heat loss comparison of the Archimede Solar Energy HCEMS-11 receiver (Matino and Maccari, 2015) with Schott's PTR70 receiver (Burkholder and Kutscher, 2009).

Table 4.5: Technical and economic performance indicators of Bokpoort for the validation of the power cycle and cost model of the parabolic trough model (cost data indexed to $\$_{2017}$).

Parameter	Unit	Bokpoort	Model	Rel. error
Net turbine capacity	[MW]	50([4])	50.4	0.8 %
Annual electricity production	[GW h]	230([4])	231.5	0.7 %
Total reflective aperture area	[km^2]	0.588([4])	0.588	-
Land area	[ha]	250([5])	242.6	−3.0 %
TES capacity	[MW h$_{th}$]	1300([4])	1339.4	3.0 %
TES salt inventory	[t]	38100([6])	40926	7.4 %
Live steam flow rate	[kg/s]	60([6])	59.1	1.5 %
Capacity factor (net)	[%]	52.5([7])	52.4	−0.2 %
CAPEX	[mil. $]	575.8([7])	542.0	−5.9 %
OPEX	[mil. $/a]	8.6([7])	6.6	−23.3 %
LCOE ($d = 5\,\%$)[8]	[$/MWh]	215.2([7])	206.0	−4.3 %
LCOE ($d = 10\,\%$)[8]	[$/MWh]	313.3([7])	297.6	−5.0 %

reflective area of 0.588 km^2 and occupies a land area of 250 ha. The land area of the model is calculated based on Eq. (2.75) and is underestimated by −3 %. The total reflective area is a result of the input in terms of the number of loops which is 180 in the case of Bokpoort (Bhula, 2017). Therefore, there is

[4] NREL (2020).
[5] Jeal (2017).
[6] Bhula (2017).
[7] Lilliestam *et al.* (2018).
[8] This is based on 25 years operational lifetime and a discount rate of 5 % and 10 %, respectively, as per the reference LCOE calculation method. This excludes decommissioning costs because the reference LCOE is only based on overnight CAPEX.

no deviation between the model and the actual plant. The TES capacity and TES salt inventory are overestimated by 3.0 % and 7.4 %, respectively. The live steam flow rate deviates by 1.5 % from the reported value of 60 kg/s. It should be noted that some of the design values of Bokpoort might have been rounded to the nearest tens, hundreds or thousands digit for convenience of reporting. Similarly, some reported values — for example the annual electricity production and consequently the capacity factor as well — are estimates themselves to represent the plant's target performance and are therefore also sometimes rounded. Hence, the calculated errors of the model can in reality be higher or lower. Nevertheless, it can be concluded that the model performs well and estimates the plant design data within an acceptable margin of error.

For the financial data of Bokpoort, estimates from Lilliestam *et al.* (2018) have been taken. As this data is reported in $\$_{2017}$, all financial assumptions from chapter 3 have been indexed to $\$_{2017}$ using the CEPCI (Chemical Engineering, 2018). Furthermore, Lilliestam *et al.* (2018) use the simplified LCOE calculation method as introduced in section 3.6.1 and assume a discount rate of 5 and 10 % as well as a financial lifetime of the project of 25 years. Therefore, the same assumptions have been made in the model to allow comparison.

The CAPEX of Bokpoort is reported to be 575.8 mil. \$, whereas the model estimates it to be 542.0 mil. \$ which corresponds to a relative error of −5.9 %. Recall that the CAPEX is increased by 10 % in the model (see section 3.2) in order to take into account import costs for special equipment as well as to factor in higher costs for local raw materials and lower local labour productivity. As the actual CAPEX of Bokpoort is more than 5 % larger than estimated by the model, it can be concluded that the assumed location factor is conservative but adequate. The overall CAPEX calculation underestimates the actual investment costs and can therefore be considered optimistic. However, one has to bear in mind that this was one of the first CSP plants built in South Africa under BW2, leading to higher investment costs as compared to later projects (mainly due to the need to establish infrastructure and train local workers). Additionally, the remote location of Bokpoort — located approximately 40 km of dirt road away from the closest town (Groblershoop) and 115 km from the next major city (Upington) — requires the entire staff to be housed and catered for in a container settlement on-site, leading to higher investment and operational costs that are not explicitly considered in the model.

The OPEX is underestimated by 23.3 %. This high discrepancy can be explained through the two different methods of calculating the OPEX. Lilliestam *et al.* (2018) simply assume the OPEX to be 1.5 % of the CAPEX, whereas it is calculated here based on a mix of fixed costs by capacity and variable costs by generation in the model (see section 3.3.1). Furthermore, Bokpoort was among the earlier projects in South Africa under BW2 and it is likely that its OPEX is higher than in later projects due to the initial necessity of job creation in the area. This required extensive training of local plant operators and technicians as well as flying in experienced plant operators from abroad

for the first months of operation in order to achieve a knowledge transfer.

Finally, combining the CAPEX, OPEX and annual electricity production leads to a LCOE of 215.2 \$/MWh for Bokpoort with a discount rate of 5 %. Compared to that, the average bidding tariff in BW2 was 3500 ZAR/MWh (Department of Energy, 2018), corresponding to 271.4 \$/MWh in $\$_{2017}$[9] which is higher than the estimated LCOE of Bokpoort. However, the PPA term with Eskom is only 20 years, thus increasing the LCOE to 238.4 \$/MWh. Nevertheless, this is still below the PPA tariff in BW2 which leaves enough room to generate profit for the developer. Hence, the estimates for the LCOE by Lilliestam *et al.* (2018) can be assumed to be reliable. The LCOE calculated by the model is 206.0 \$/MWh which corresponds with a relative error of −4.3 %. This increased error is mainly due to the underestimation of the CAPEX and OPEX mentioned above since the OPEX in the reference data is also just an estimation based on an annual percentage of the CAPEX. Likewise, the LCOE assuming a discount rate of 10 % is 313.3 \$/MWh for Bokpoort and 297.6 \$/MWh in the model. With a relative error of −5 % it can be concluded that the economic model is optimistic but produces acceptable results and confirms that the assumptions made in chapter 3 are reasonable.

4.3.3 Comparison with Kathu

Similarly to the previous comparison with Bokpoort, the results from the model are compared with the technical and economic performance metrics of the Kathu power plant near Kuruman in Northern Cape, South Africa. This thermal oil PTPP has a net turbine capacity of 100 MW with a TES of 4.5 hours (NREL, 2020) and is air-cooled. It began operation in January 2019 and is estimated to supply 500 GW h per year to the grid (Acciona, 2019). The solar field consists of 250 loops of SENERtrough-2 collectors amounting to a total of 1.047 km^2 reflective area on 400 ha of land area (SENER, 2019). The receivers used are Rioglass PTR70-4G, which is technically identical to Schott's PTR70 receiver after Rioglass has acquired Schott Solar's receiver business in 2015 (Rioglass, 2015). Data for modelling the collector was taken from Rodriguez-Sanchez and Rosengarten (2015), GIZ (2014) and Donga and Kumar (2019), whereas data from Rioglass (2020) was used for the receiver. Additionally, the heat loss correlation from Eq. (4.3) was used to calculate the receiver heat losses. Because Kathu has been awarded in BW3.5 of the REIPPPP, it receives a two-tier tariff and is therefore not usually operated during the night. The respective operating strategy was thus used in the model.

Table 4.6 shows the technical and financial performance indicators of Kathu in comparison to the results obtained from the model. Similarly to the comparison with Bokpoort, the net turbine capacity and annual electricity pro-

[9] Yearly average exchange rate of 12.896 ZAR/\$ in 2017 (X-Rates, 2019*a*).

Table 4.6: Technical and economic performance indicators of Kathu for the validation of the power cycle and cost model of the parabolic trough model (cost data indexed to $\$_{2017}$).

Parameter	Unit	Kathu	Model	Rel. error
Net turbine capacity	[MW]	100([10])	100.8	0.8 %
Annual electricity production	[GW h]	500([11])	503.7	0.7 %
Total reflective aperture area	[km^2]	1.047([12])	1.047	-
Land area	[ha]	400([12])	426.5	6.6 %
TES capacity	[MW h$_{th}$]	1550([12])	1527.4	−1.5 %
TES salt inventory	[t]	45000([10])	41265	−8.3 %
Live steam flow rate	[kg/s]	n.a.([13])	142	n.a.
Capacity factor (net)	[%]	56.4([10])	57.0	1.1 %
CAPEX	[mil. $]	902.1([7])	882.4	−2.2 %
OPEX	[mil. $/a]	13.5([7])	13	−3.7 %
LCOE ($d = 5\,\%$)[14]	[$/MWh]	155.1([7])	150.2	−3.2 %
LCOE ($d = 10\,\%$)[14]	[$/MWh]	225.8([7])	218.9	−3.1 %

duction are overestimated by 0.8 % and 0.7 %, respectively. This can again be attributed to the underestimation of the parasitic consumption at design in the model. On the other hand, the land area is 6.6 % larger in the model. The TES capacity has a relative error of −1.5 %, whereas the error for TES salt inventory is significantly higher with −8.3 %. This can likely be attributed to an additional safety margin for the amount of salt used in Kathu, which is not taken into account in the model. No data has been found for the live steam flow rate but it has been calculated to be 142 kg/s.

The capacity factor of 56.4 % reported by De Klerk (2016) refers to the net turbine capacity of 100 MW including a reduction in availability due to scheduled and unscheduled maintenance. Hence, the capacity factor of the model is also stated as a net value and is 57 %, resulting in a relative error of 1.1 %. With a capacity factor of 56.4 %, the estimated annual net electricity production would likely be 494.1 GW h instead of 500 GW h as reported by Acciona (2019). This relatively small difference can be attributed to the rounding to the nearest hundred and can be neglected due to the relatively low error.

The investment costs of Kathu are reported to be 12 bil. ZAR (Fin24, 2016), which corresponds to 902.1 mil. $ in $\$_{2017}$ (Lilliestam *et al.*, 2018). The CAPEX is estimated to be 882.4 mil. $ by the model, leading to an underestimation of

[10] De Klerk (2016).
[11] Acciona (2019).
[12] SENER (2019).
[13] No information available.
[14] This is based on 25 years operational lifetime and a discount rate of 5 % and 10 %, respectively, as per the reference LCOE calculation method. This excludes decommissioning costs because the reference LCOE is only based on overnight CAPEX.

2.2 %. However, the CAPEX calculation of the model also includes additional costs as, for example, the cost of a 8 km transmission line to connect to the existing 132 kV Eskom line (De Klerk, 2016) as per section 3.2.5. Similarly to Bokpoort, the investment costs are underestimated although a location factor of 10 % for import of special equipment, higher costs for raw materials and lower local labour productivity has been applied on the direct investment costs of the solar field, HTF system, TES and power block (see section 3.2). Again, this confirms that the usage of this additional cost factor is adequate and the estimate of 10 % is reasonable. The OPEX of Kathu is estimated to be 13.5 mil. $ per year by Lilliestam *et al.* (2018), whereas it is calculated to be 13 mil. $ in the model. Contrary to the large error for the OPEX in the case of Bokpoort, the estimation for Kathu yields a relative error of just −3.7 %.

Based on the overnight CAPEX and the estimated annual electricity production of 500 GW h, Lilliestam *et al.* (2018) estimate the LCOE of Kathu to be 155.1 $/MWh considering a discount rate of 5 %, a payback period of 25 years and annual OPEX of 1.5 % of the CAPEX (Lilliestam and Pitz-Paal, 2018). Provided that the base tariff of the REIPPPP BW3.5 is 147.3 $/MWh (Department of Energy, 2018) (fully indexed and converted to $\$_{2017}$[15]), the LCOE reported in Lilliestam *et al.* (2018) can be considered to be a good estimate. Additionally, the base tariff is inflated by a factor of 2.7 during peak hours from 16:30 to 21:30, whereas the tariff is 0 ZAR/MWh during the night time from 22:00 to 5:00. Due to the rather small TES of 4.5 h of Kathu, the operation of the power plant can be assumed to be targeting the peak hours in order to increase the profit of the plant. Hence, the average tariff can be estimated to be higher than 147.3 $/MWh which further validates the LCOE estimate of 155.1 $/MWh. In fact, the average tariff is 221.0 $/MWh when assuming continuous operation only during the hours with a remuneration tariff, which is also higher than the LCOE estimation using a discount rate of 10 %. In comparison to the LCOE estimated by Lilliestam *et al.* (2018), the LCOE calculated by the model using the same simplified method as in the data reference is 150.2 $/MWh, yielding a relative error of −3.2 %. Using a discount rate of 10 % yields a marginally smaller error of −3.1 %. Hence, it can be concluded that the calculated LCOE is reasonable and the model is sufficiently accurate in both the estimation of the annual electricity production, the calculation of the plant's CAPEX and thus, the LCOE.

4.4 Summary

Due to the lack of available data for MSPTPPs, the validation of the entire plant model has been carried out with SAM for three different salts. The results show that the model performs well with Solar Salt as HTF with a MAE of 2.51 °C for the outlet temperature of the solar field. Using Hitec or Hitec XL

[15] Yearly average exchange rate of 12.896 ZAR/$ in 2017 (X-Rates, 2019*a*).

leads to larger errors, mainly due to the underestimation of the heat losses in the model as compared to SAM. Although the model neglects heat losses from expansion bellows and support brackets, a validation with measurement data showed that this simplification is justifiable. The validation with SAM also confirmed the accuracy of the model in terms of net power output with MAEs between 1.48 and 3.68 MW (2.7 and 6.7 % of the installed capacity of 55 MW), which is due to different start-up and shut-down approaches as well as the TES fill level. The latter was found to have the largest mismatch between the model and SAM which is a result of the different TES dispatch strategies and FP integrations. Nevertheless, it can be concluded that the results obtained from the model are in good agreement with the results from SAM.

To further validate the solar field model and its usage of an empirical heat loss model, a validation with measurement data from a test loop using Solar Salt as HTF has been carried out. The simulation results show very good agreement with the measurement data over the investigated period and the transient response of the solar collector is accurately reproduced. Likewise, the integration of the FP model has been also shown to produce accurate results. Nevertheless, an adaptation of the empirical heat loss model to include the effects of ambient conditions on the receiver heat loss is recommended. Furthermore, it has been shown that neglecting the heat losses from expansion bellows and support brackets does not significantly affect the thermal output of the loop.

In order to reduce the computational effort of the model, the level of discretisation of the collector has been varied, representing a decrease in the amount of CVs from 40 per SCA down to 1 per SCA. The highest level of detail (40 CVs per SCA) takes approximately 2.8 h for an annual simulation with a time step of 10 s, whereas only using 1 CV per SCA requires 0.8 h. The reduced computational effort is traded in for a higher error but a feasible compromise between model error and simulation time has been found to be a division of the SCA into 5 CVs. This leads to a RMSE below 3 °C at a simulation time of 1 h. However, the usage of such a small time step is only recommended for control design studies and larger time steps of one hour are typically used for annual performance evaluations. Therefore, an analysis with the use of large time steps up to 1 h has been carried out. It was shown that the errors of the loop thermal output between the model and the measured data lie within an acceptable range of −7.8 % to 1.3 %. Thus, it can be concluded that the developed model is suitable for use in annual performance evaluations.

Lastly, to validate the overall power plant model as well as the economic model, a comparison with data from two real power plants in South Africa has been done. Since these plants use thermal oil as HTF as well as different collectors and receivers, the model has been adapted accordingly by implementing an indirect TES, the appropriate collectors and receivers as well as the fluid properties of thermal oil. The results show that both the technical and financial performance indicators calculated by the model match the data

from the real power plants with acceptable errors. In fact, the maximum error for the LCOE is $-5\,\%$ in the case of Bokpoort and $-3.2\,\%$ for Kathu. Considering the LCOE as a reasonable measure for the overall technical and financial performance of a power plant, it can be concluded that the model's accuracy is highly acceptable. Furthermore, it has been shown that the assumed location factor of $10\,\%$ applied to the direct investment costs is conservative, yet reasonable.

Chapter 5

Multi-objective Optimisation[1]

In this chapter, the technical and economic performance assessment of MSPTPPs are combined to investigate the feasibility of different plant designs and operating strategies under location-tailored boundary conditions. A sensitivity analysis is carried out in order to assess the impact of key design variables on the technical and economic performance. Lastly, a multi-objective optimisation algorithm is introduced that will be used in chapter 6 to identify power plant configurations and operational parameter set points that lead to the best trade-offs between two optimisation objectives.

5.1 Reference Plant

As part of the study's objectives (presented in section 1.4), a sensitivity analysis is conducted in section 5.2 in order to assess the impact of key technical and financial parameters on the efficiency and profitability of a MSPTPP. For this, a reference plant is required to serve as a base case. As there are currently no MSPTPPs in operation that could serve as such a reference, a reasonably sized power plant configuration that would be technically feasible and financially viable is assumed.

5.1.1 Plant design and financial parameters

The main technical design parameters of the reference plant are provided in Table 5.1. The plant is assumed to be located in Upington, South Africa, and uses Solar Salt as HTF. It is operated as a baseload power plant and relies on FPS1, as introduced in section 2.4.2. The plant has a gross turbine capacity of 150 MW and the HPT and LPT inlet pressures are set to 100 bar and 16.5 bar, respectively. The nominal power cycle thermal efficiency is 38.5 %. The solar field has a collector row spacing of 30 m and a relatively small solar multiple of 2.5 that was chosen in order to reduce the CAPEX. The minimum

[1] Parts of this chapter have been published in Pan *et al.* (2018*b*).

Table 5.1: Technical design parameters and nominal values of the reference plant.

Design parameter	Variable	Unit	Value
Power block			
Gross power output	$\dot{W}_{\text{gross}}$	[MW]	150
HPT inlet pressure	$P_{\text{HPT,in}}$	[bar]	100
LPT inlet pressure	$P_{\text{LPT,in}}$	[bar]	16.5
Solar field			
Solar multiple	SM	[–]	2.5
Row spacing	L_{spacing}	[m]	30
Minimum loop flow rate	$\dot{m}_{\text{min}}$	[kg/s]	2
FP loop flow rate	$\dot{m}_{\text{fp}}$	[kg/s]	4
FP temperature	T_{fp}	[°C]	260
Thermal energy storage			
TES capacity	t_{TES}	[h]	12
HT reference temperature	$T_{\text{HT,ref}}$	[°C]	480
TES dispatch strategy	-	[–]	baseload
Air-cooled condenser			
Dry air temperature at design	T_{dry}	[°C]	35
Terminal temperature difference	T_{TTD}	[°C]	2
Nominal air temperature difference	$\Delta T_{\text{air,nom}}$	[°C]	28
Nominal values			
PB cycle thermal efficiency	$\eta_{\text{PB,th}}$	[%]	38.5
SF conversion efficiency	η_{SF}	[%]	70.6

loop flow rate is fixed at 2 kg/s, whereas the flow rate during FP operation is limited to 4 kg/s in order to guarantee that all of the piping equipment is kept warm throughout the night. Due to the high freezing point of Solar Salt, the FP temperature is set at 260 °C in the reference plant. However, Pan *et al.* (2018*b*) have shown that increasing the FP temperature to 265 °C leads to lower LCOEs in larger power plants. The effect of the choice of this temperature set point will be analysed in more detail in section 6.2.2. With the above design parameters, the nominal solar field (SF) conversion efficiency is 70.6 % under design conditions (at 12:00 on spring equinox with a design DNI of 900 W/m^2).

Due to the baseload operation strategy of the reference plant, a relatively large storage system with 12 h storage time is assumed. The hot tank reference temperature $T_{\text{HT,ref}}$ (which defines the temperature threshold above which the HTF exiting the solar field is pumped into the hot tank instead of being recirculated to the cold tank) is set to 480 °C. Although Poole (2017) recommends

a higher temperature of 530 °C in order to avoid the reduction in heat storage capacity of the hot tank, a significantly lower value is used here since it is assumed that the large TES is able to compensate for much of the lost storage capacity simply by being able to fill the hot tank earlier in the day. A closer look at the effect of this temperature on the power plant's performance will be provided through a multi-objective optimisation in section 6.2.2 where this theory will be confirmed.

For the ACC, a dry air temperature at design of 35 °C and a terminal temperature difference of 2 °C are assumed. The nominal air temperature difference between the inlet and outlet of the condenser's air side is 28 °C.

Regarding the financing costs, a debt to equity ratio of 70/30 is assumed. Combined with the financial parameter assumptions from Table 3.9, this leads to a real and nominal WACC of 6.45 % and 11.45 %, respectively.

5.1.2 Technical and economic performance indicators

Based on the technical and economic design parameters introduced above, Table 5.2 shows a summary of the key performance indicators of the reference plant. The annual net power output is 688.1 GW h and the average power cycle efficiency is 37.4 %. Combined with an average solar field efficiency of 54.60 %, the solar-to-electric efficiency is 19.15 %. Although the implemented TES of 12 h is relatively large, the capacity factor is only 54.83 %. This is mainly due to the relatively small solar field in comparison to the large TES. However, this was chosen in order to reduce the CAPEX, which is 891.7 mil. $. Combined with an OPEX of 15.7 mil. $, the LCOE of the reference plant is 129.8 $/MWh which is significantly lower than the baseload tariff of 150.3 $/MWh. In fact, the minimum required tariff that has to be paid in order for the power plant to be financially feasible is 132.5 $/MWh based on Eq. (3.49). Compared to the nominal WACC of 11.45 %, the IRR is sufficiently higher at 14.75 % which leads to a NPV of 51.8 mil. $.

Table 5.2: Technical and economic key performance indicators of the reference plant.

Parameter	Variable	Unit	Value
Annual net power output	E_{net}	[GW h]	688.1
Average solar field efficiency	η_{SF}	[%]	54.60
Solar-to-electric efficiency	η_{S2E}	[%]	19.15
Capacity factor	f_{cap}	[%]	54.83
Capital costs	$CAPEX$	[mil.$]	891.7
Levelised cost of electricity	$LCOE$	[$/MWh]	129.8
Internal rate of return	IRR	[%]	14.75
Net present value	NPV	[mil.$]	51.8

5.2 Sensitivity Analysis

To assess the impact of key technical and economic parameter assumptions on the efficiency and profitability of a MSPTPP, a sensitivity analysis is carried out. By varying a series of design parameters one at the time, the respective effect on the technical and economic performance of the plant is assessed. For this, the reference plant from the previous section is used as a base case and potential improvements can be easily identified. Furthermore, the sensitivity analysis is used to test the robustness of the model towards uncertainties of the input data. By doing so, parameter inputs can be identified that should be chosen very carefully if they have a significant impact on the overall plant performance. Lastly, the sensitivity analysis is also used to select appropriate ranges of the input variables for the multi-objective optimisation in section 5.3.

5.2.1 Gross turbine capacity, TES size and solar multiple

The design parameters with the largest impact on the technical and economic performance indicators of solar thermal power plants are typically the gross turbine capacity, the TES full load hours and the solar multiple. However as these design parameters define the overall size of the power plant, the variation of one parameter requires an adaptation of the other two parameters in order to obtain appropriately sized components. Thus, simply varying only one parameter at the time does not provide a sufficiently accurate representation of the model's sensitivity to these design variables and they should always be varied as a set of three. As the impact of these parameters on the technical and economic performance of power plants is already known and has been the subject of several studies (see for example the works of Boukelia *et al.*, 2015*b*; Guédez, 2016; Pan *et al.*, 2019), they are only discussed briefly here. The respective impact of the gross turbine capacity, TES size and solar multiple on the LCOE and solar-to-electric efficiency will be compared to the impact of the variation of other design variables in section 5.2.5.

Figure 5.1 shows the sensitivity of the technical performance parameters to the variation of the gross turbine capacity, TES size and solar multiple. Naturally, the annual net electricity output increases with increasing component sizes. However, increasing the turbine capacity of the reference plant results in a decrease of the solar field efficiency and therefore also the solar-to-electric efficiency and capacity factor. This is due to significantly higher heat losses and pumping power requirements in large solar fields as well as a relative increase of the condenser power consumption with increasing turbine capacities due to larger air volume flow requirements.

Compared to the reference plant, increasing the TES time not only results in an increase of the annual net electricity output but also of the solar field and solar-to-electric efficiencies. This is due to the fact that less energy needs

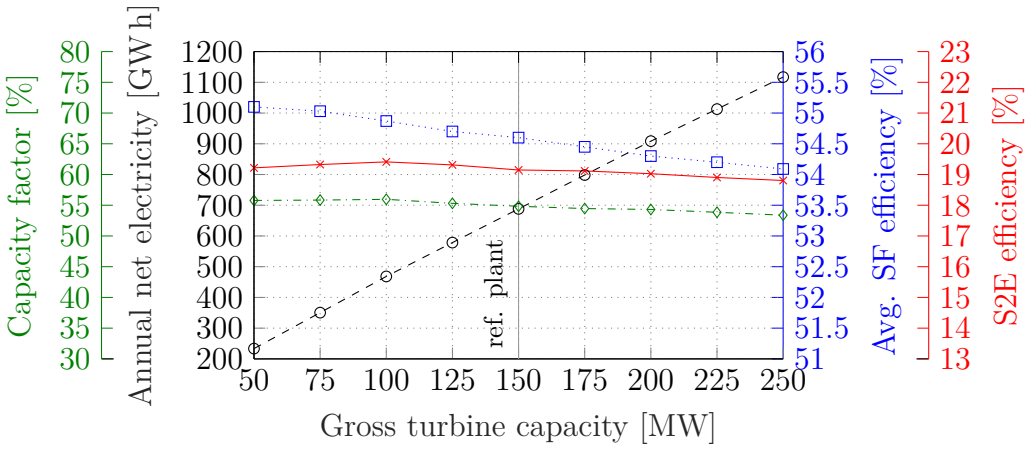

(a) Gross turbine capacity.

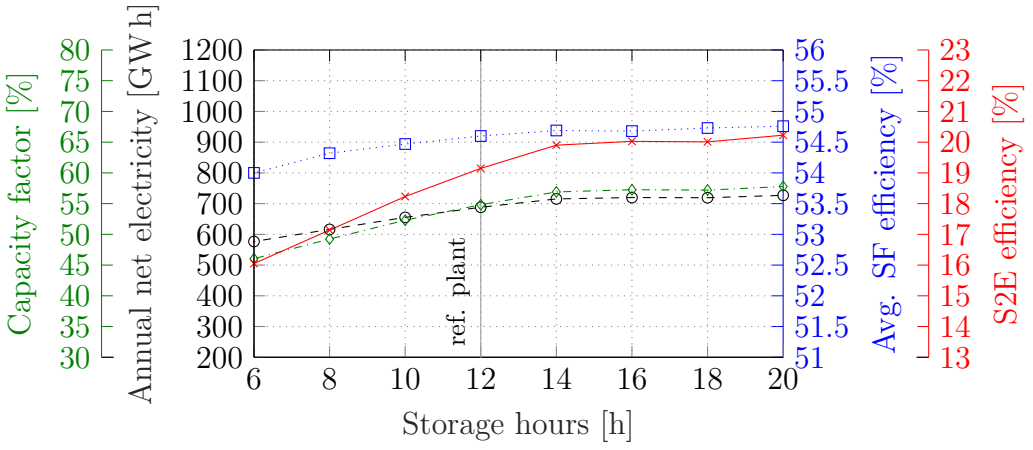

(b) Thermal energy storage full load hours.

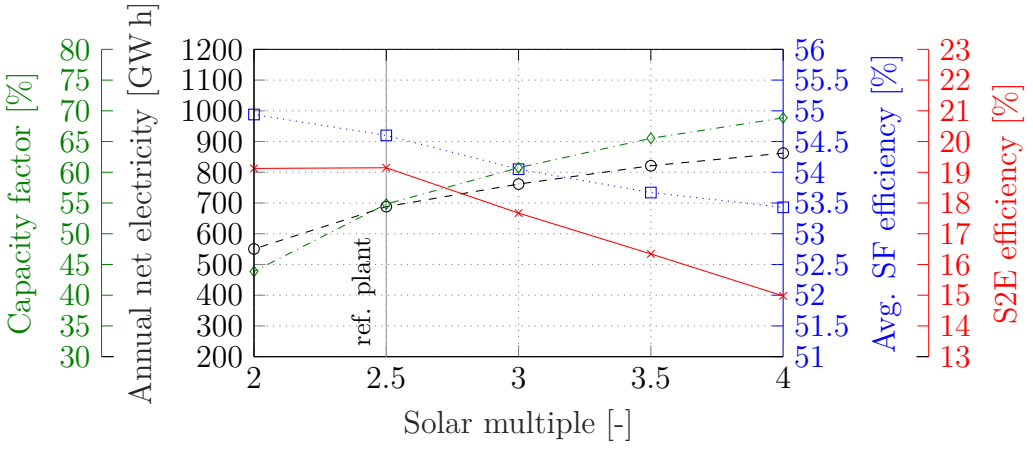

(c) Solar multiple.

Figure 5.1: Sensitivity of technical performance indicators to the variation of the (a) gross turbine capacity, (b) TES full load hours and (c) solar multiple.

to dumped with increasing TES sizes and therefore more thermal energy is available for power production. Here, a TES size of 20 h results in the highest solar-to-electric efficiency of 20.2 %. In contrast, the reverse effect takes place when increasing the solar multiple of the reference plant, which results in a decrease of the solar field and solar-to-electric efficiencies. Although the net power output increases, implementing a larger solar field without increasing the TES time leads to a significant increase of energy dumping in the solar field and must be avoided. Therefore, it can be concluded that a carefully selected combination of these three design parameters is required in order to improve the technical performance indicators.

Regarding the economic performance indicators, Figure 5.2 shows their sensitivity to the variation of the gross turbine capacity, TES size and solar multiple. It can be seen that the LCOE is most sensitive to the installed turbine capacity. Nevertheless, increasing the solar multiple or TES size also results in a significant reduction of the LCOE as well as an improved IRR and NPV. In fact, increasing the turbine capacity of the reference plant to 250 MW results in an LCOE of 125.7 $/MWh and an IRR of 16.7 %. The CAPEX is directly proportional to the power plant size and simply increases linearly with increasing system sizes. However, similar to the conclusion drawn above, the goal is to find a combination of component sizes that maximises the financial feasibility of CSP plants, which can, for example, be obtained through an optimisation study. This will be presented in detail in section 5.3.

5.2.2 Freeze protection temperature threshold

In order to provide insight into the sensitivity of operational input parameter set points of MSPTPPs, one important parameter is the FP temperature threshold. As shown by Pan *et al.* (2018*b*), the FP temperature for molten salts should be chosen close to the design solar field inlet temperature. Although the freezing point of all salt mixtures in this study is significantly lower than the solar field inlet temperature, a higher temperature is desired in order to avoid the cold tank cooling down too much during the night. In fact, Pan *et al.* (2018*b*) recommend a FP temperature between 260 °C and 265 °C for Solar Salt. Similar results can be seen in Figure 5.3, where the impact of the FP temperature on the technical and economic power plant performance is shown.

Although the average solar field efficiency decreases with a higher FP temperature — due to the increased heat losses in the solar field caused by the higher average fluid temperature — the annual net electric output increases (Figure 5.3a). This is because the cold tank temperature remains closer to the desired solar field inlet temperature. Therefore, power production can start earlier in the morning, leading to an increase of the gross and net power output of the plant. This can be seen in Figure 5.4, where the net electricity output is shown for both a power plant with a freeze protection temperature threshold

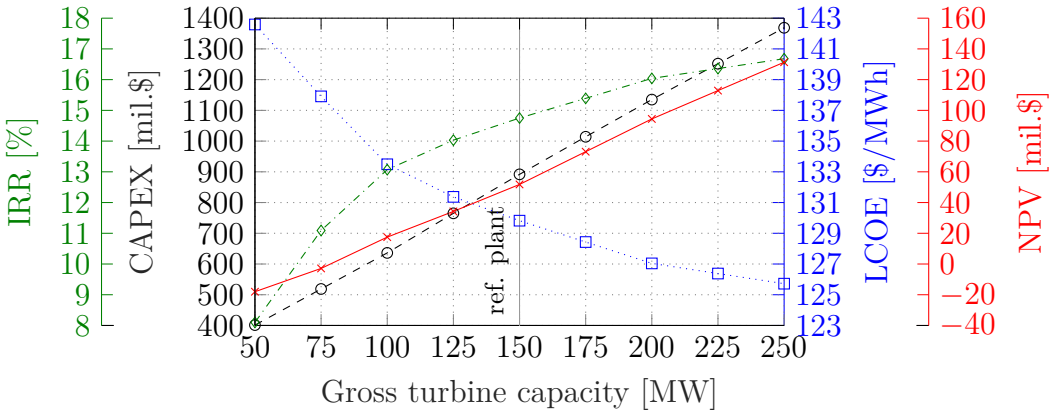

(a) Gross turbine capacity.

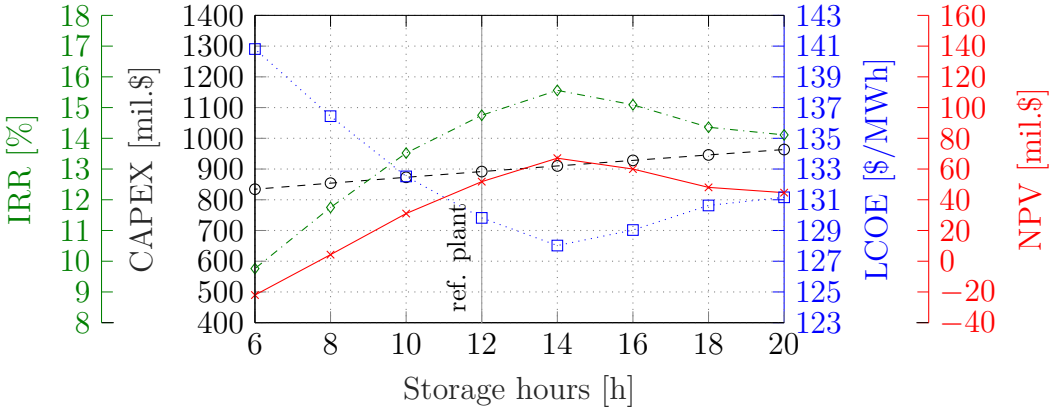

(b) Thermal energy storage full load hours.

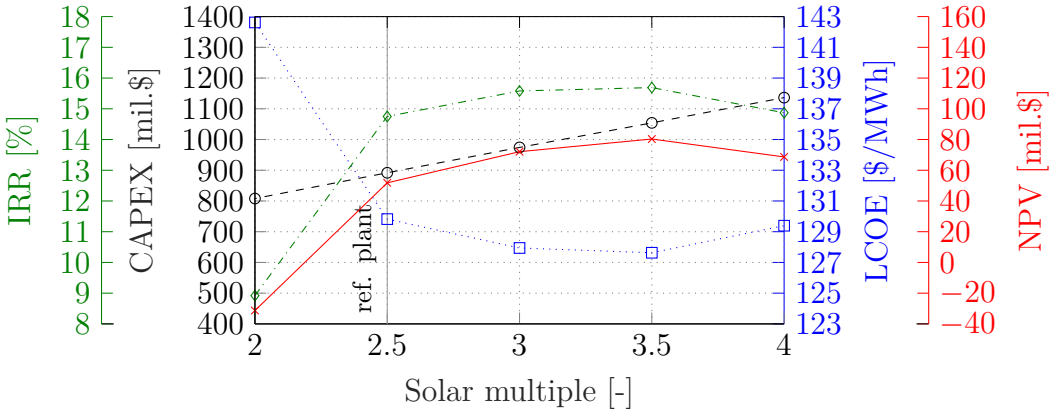

(c) Solar multiple.

Figure 5.2: Sensitivity of economic performance indicators to the variation of the (a) gross turbine capacity, (b) TES full load hours and (c) solar multiple.

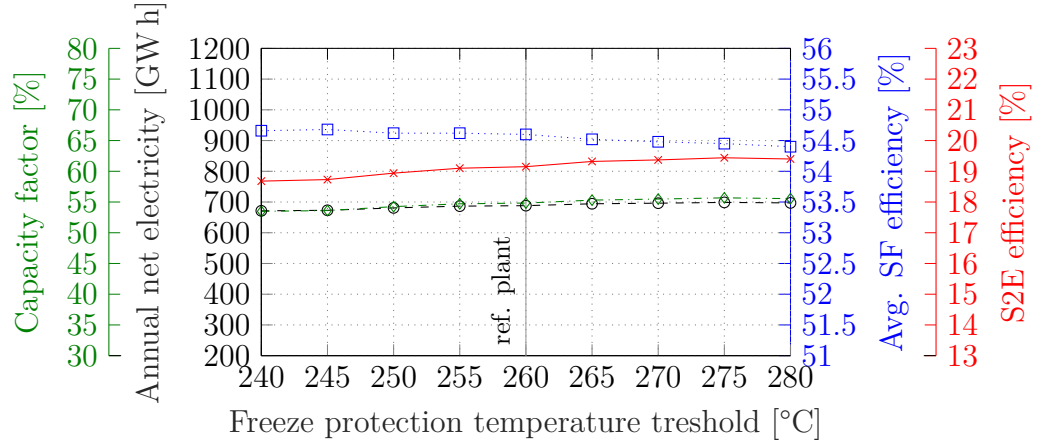

(a) Technical performance indicators.

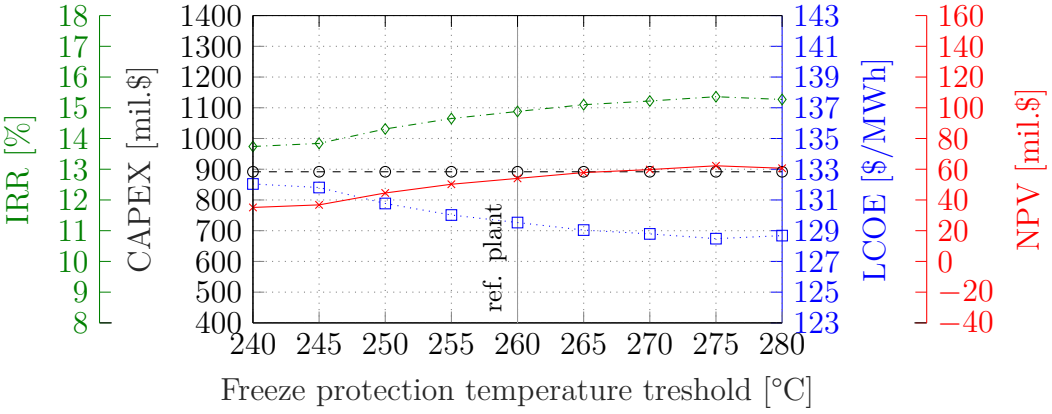

(b) Economic performance indicators.

Figure 5.3: Sensitivity of (a) technical performance indicators and (b) economic performance indicators to the variation of the FP temperature.

of 260 °C and one with 280 °C. For the latter case, the solar field outlet temperature is slightly higher during the start of the solar field operation in the morning. Therefore, the TES is filled faster and the result is an earlier start of turbine operation as well as a prolonged power output after sunset. Although the parasitic consumption for electric heat tracing increases with incrementing freeze protection temperatures (see for example the large difference in net power output during the night in Figure 5.4), the total net energy output also increases in this case due to an earlier start of generation.

As the CAPEX is not sensitive to the freeze protection temperature set point (see Figure 5.3b), the LCOE decreases with a rising freeze protection temperature due to the increased electricity output. The lowest LCOE is achieved with a freeze protection temperature of 275 °C and is 128.5 $/MWh. Therefore, it can be concluded that the freeze protection temperature should not be lowered close to the salt's freezing point but should rather be close

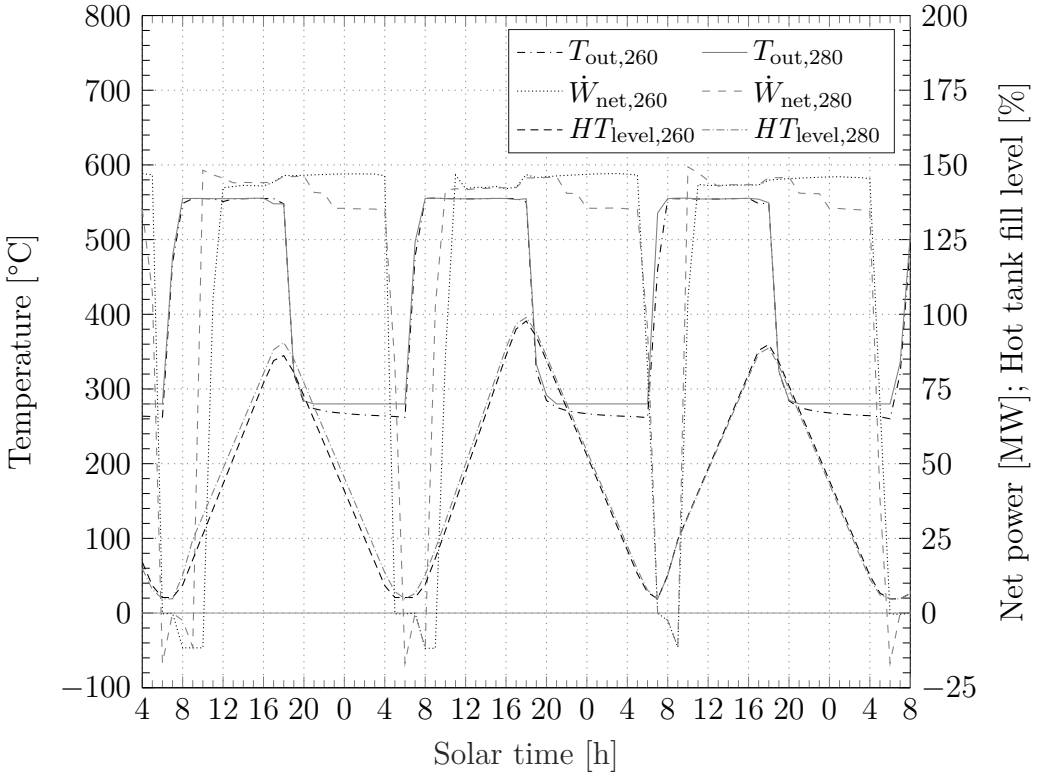

Figure 5.4: Comparison of the net power output of a power plant using a freeze protection temperature threshold of 260 °C to one using 280 °C.

to the solar field inlet temperature. It should be noted, however, that power plant configurations with different design and operational parameter values can result in the reverse effect. Therefore, a closer look into the effect of the freeze protection temperature threshold is required and will be provided in section 6.2.2.

5.2.3 Hot tank fill level reserved for freeze protection

In order to assess the impact on the performance of the power plant depending on the freeze protection strategy used, the sensitivity analysis also includes a variation of the hot tank fill level reserved for FP (Figure 5.5). For this, the freeze protection strategy of the reference plant was changed from FPS1 to FPS2 in order to allow mixing from the hot tank. As part of this freeze protection strategy, a portion of the hot tank is reserved for FP. It can be seen in Figure 5.5a that increasing the reserved percentage of the hot tank leads to a slight decrease of the average solar field efficiency. This is caused by a higher average solar field temperature caused by the advanced freeze protection strategy approach which results in higher heat losses. Furthermore, an increased dumping of solar energy takes place as the hot tank has effectively less storage volume capacity available that needs to be filled. Therefore, the

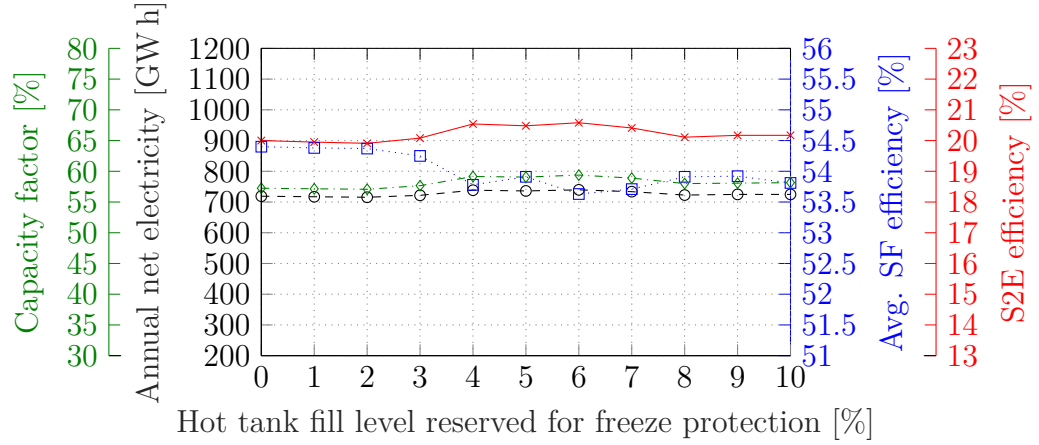

(a) Technical performance indicators.

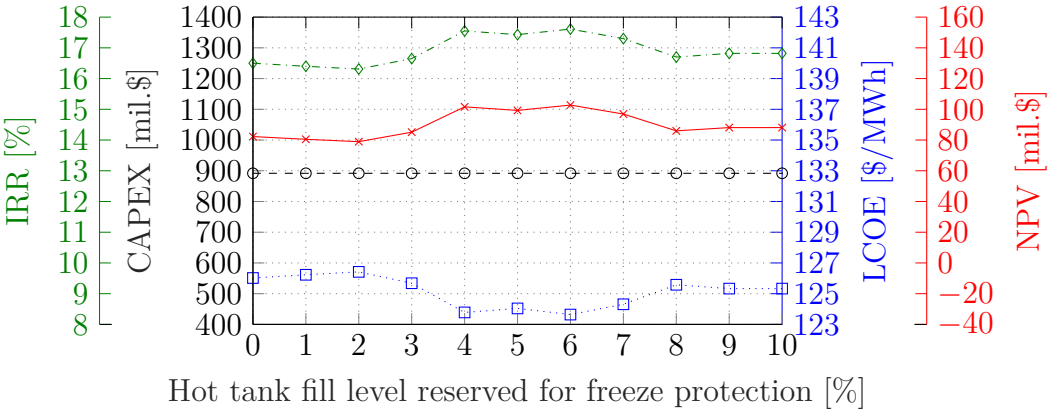

(b) Economic performance indicators.

Figure 5.5: Sensitivity of (a) technical performance indicators and (b) economic performance indicators to the variation of the hot tank fill level reserved for FP.

TES is filled faster the higher the reserved fill level for FP is. However, the annual net electricity output increases with an increasing hot tank fill level as the electric FP energy requirement is significantly reduced using FPS2. This, in turn, also leads to an increase of the solar-to-electric efficiency and therefore also a decrease of the LCOE with higher fill level values reserved in the hot tank.

As the reference plant used FPS1, no direct comparison of the performance indicators can be made. However, it can be seen that a significant reduction of the LCOE to between 123.6 $/MWh and 126.4 $/MWh is achieved when using FPS2 (compared to an LCOE of 129.8 $/MWh when using FPS1). Therefore, it can be assumed that FPS2 is the superior FP approach. Nevertheless, this will be discussed in more detail in section 6.2.1.

5.2.4 High pressure turbine inlet pressure

The Rankine cycle efficiency can typically be increased by raising the design boiler pressure. Therefore, the HPT inlet pressure was varied between 60 bar and 110 bar in order to show the effect of different turbine pressures on the power plant performance (Figure 5.6). Although a higher live steam pressure results in a higher power cycle efficiency, Figure 5.6b shows that the LCOE is lower compared to the reference plant if the HPT inlet pressure is reduced to 80 bar or 90 bar. The reason for this is that a lower live steam pressure results in a lower economiser inlet temperature which leads to a higher total heat rate required in the power block to reach the desired steam temperature. As the solar multiple is fixed in this sensitivity analysis and only the HPT inlet pressure is varied, more loops are needed in the solar field to cover the higher heat required by the power block. Therefore, the resulting larger solar

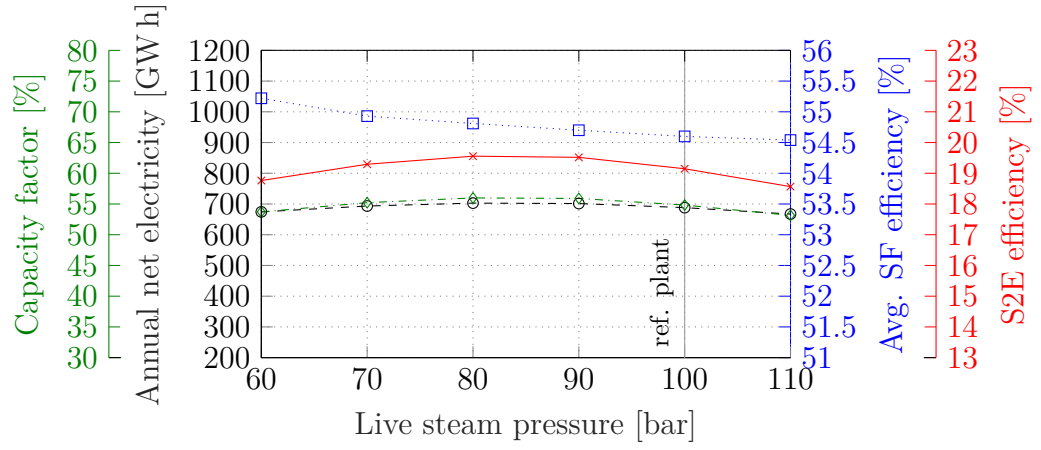

(a) Technical performance indicators.

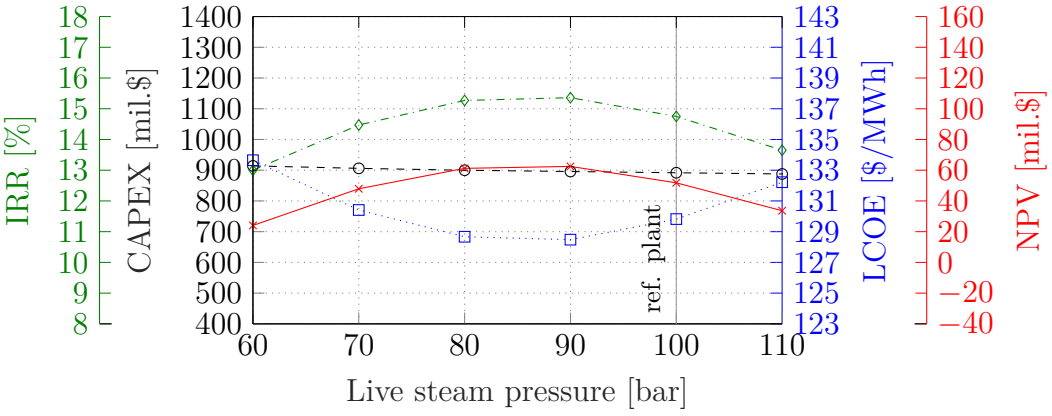

(b) Economic performance indicators.

Figure 5.6: Sensitivity of (a) technical performance indicators and (b) economic performance indicators to the variation of the HPT inlet pressure.

field can also provide more energy to the TES which increases the overall energy production. As a result, the LCOE is reduced although the power block efficiency is lower than with a higher HPT inlet pressure.

The power cycle efficiency also depends on the extraction pressure for the reheater (i.e. the LPT inlet pressure). As an increasing HPT inlet pressure leads to a higher evaporation pressure and temperature, a pinch point violation can be expected in the evaporator since the temperature gradient of the hot molten salt stream remains the same. Therefore, a steam cycle optimisation of the HPT inlet pressure and the extraction pressure for a gross turbine capacity of 150 MW has been carried out using Solar Salt as HTF. Figure 5.7 shows the resulting power cycle efficiencies for the respective inlet pressures. It can be seen that an increasing HPT inlet pressure leads to a pinch-point violation in combination with high LPT inlet pressures. Therefore, a higher LPT inlet pressure is preferable which also requires a HPT inlet pressure below approximately 140 bar in order to achieve a high power block efficiency. The maximum possible power cycle efficiency of 38.99 % in this case can be achieved with a HPT inlet pressure of 122.5 bar and a LPT inlet pressure of 14.4 bar.

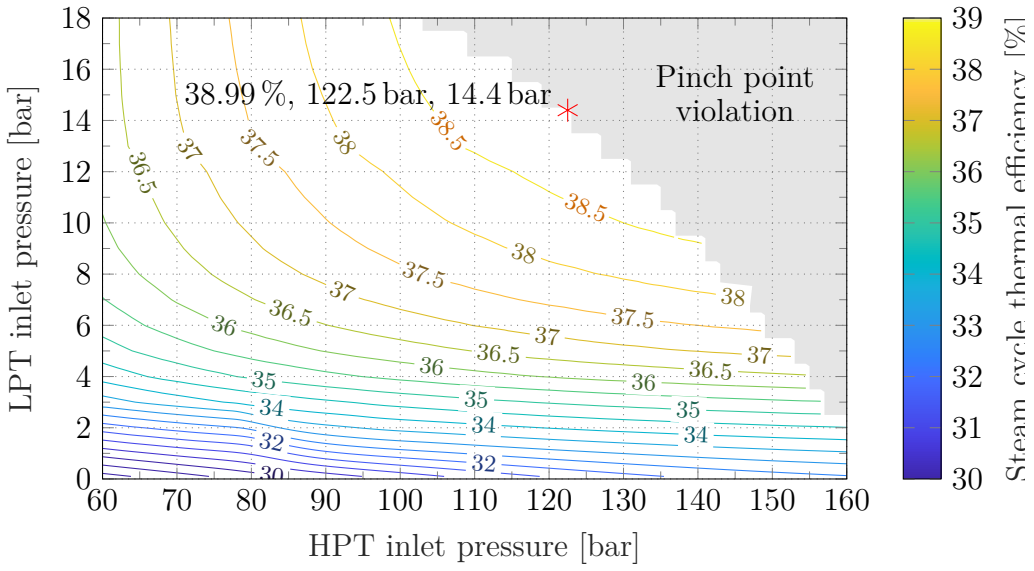

Figure 5.7: Sensitivity of PB thermal efficiency as a function of HP and LP steam turbine inlet pressures for a 150 MW gross turbine capacity using Solar Salt as HTF.

5.2.5 Summary of LCOE and solar-to-electric efficiency improvements

A summary of the highest possible improvements of the LCOE and solar-to-electric efficiency relative to the reference plant is provided in Figure 5.8 for all parameters varied during the sensitivity analysis. It can be seen that the

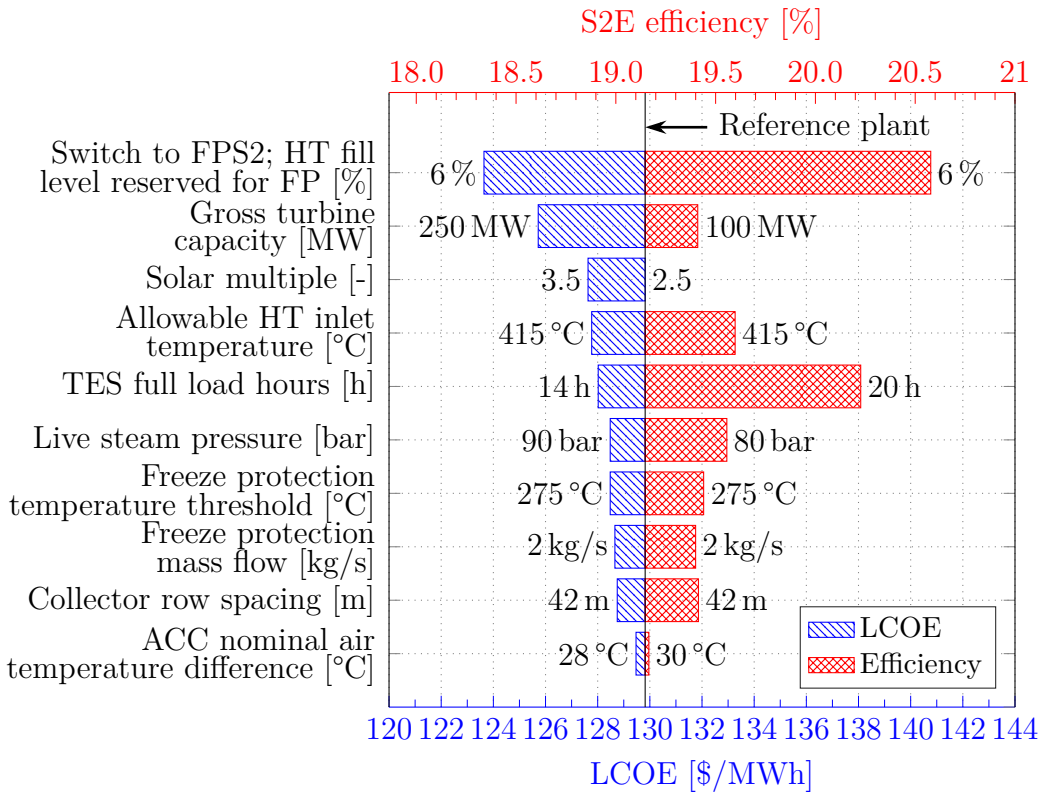

Figure 5.8: Comparison of highest possible improvements of LCOE and solar-to-electric efficiency relative to the reference plant based on each investigated sensitivity variable (sorted by descending impact on LCOE). The values next to each bar represent the design parameter with which the improvement is achieved.

switch to FPS2 yields the highest improvement of both the LCOE and solar-to-electric efficiency compared to the reference plant. Through this, an LCOE reduction of up to 5 % is possible, whereby the solar-to-electric efficiency can be increased from 19.15 % to 20.58 % (corresponding to an increase of 7.5 %). As discussed in section 5.2.1, a variation of the gross turbine capacity, TES full load hours and solar multiple has also been performed. As these three design parameters significantly affect the overall size of a power plant, they also have a large impact on the LCOE. Here, a gross turbine capacity of 250 MW leads to a LCOE reduction of approximately 3 %. Similarly, a larger solar multiple and TES capacity also reduce the LCOE. The latter also results in a significant increase of the solar-to-electric efficiency if a TES of 20 h is implemented. Lastly, operational parameter set points like the allowable hot tank inlet temperature, FP mass flow rate, collector row spacing and ACC nominal air temperature difference can also be optimised in order to achieve lower LCOEs. The corresponding impact of these design parameters on the technical and economic performance indicators is depicted in Appendix G.

In light of all the potential technical and economic performance improve-

ments from Figure 5.8, an even higher LCOE reduction can be expected through a combined variation of several or all design parameters at once. This can be achieved through a multi-objective optimisation, where a series of design variables are varied throughout the optimisation in order to find combinations that lead to a minimised LCOE (for example). This optimisation approach will be introduced in section 5.3.

5.2.6 Financial parameters

Lastly, a sensitivity analysis on the financial parameter assumptions was carried out to assess the robustness of the model to uncertainties from the input data. For this, the main financial parameters from chapter 3 have been varied by ±40 % of the assumptions used for the reference plant in section 5.1. The results are shown in Figure 5.9 for the IRR and LCOE. It can be seen that the model is highly sensitive to the debt interest rate, the PPA tariff and the economic lifetime of the plant. Figure 5.9a shows that the IRR is reduced

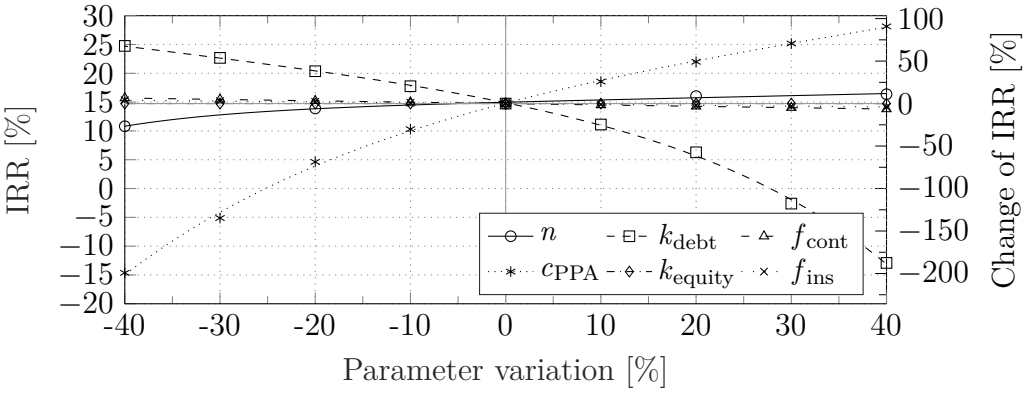

(a) Internal rate of return.

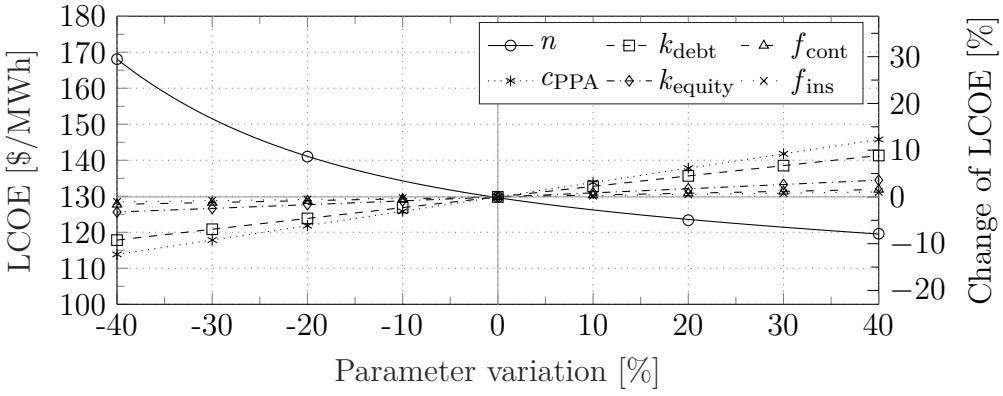

(b) Levelised cost of electricity.

Figure 5.9: Sensitivity analysis of financial input parameters and their impact on economic key performance indicators.

by up to 185 % compared to the reference plant if the debt interest rate is increased by 40 %. However, decreasing it by 40 % only increases the IRR by approximately 70 %. The PPA tariff, on the other hand, has the opposite effect where an increase of 40 % results in an approximately 90 % higher IRR.

Figure 5.9b shows the impact of the economic parameter assumptions on the LCOE. Here, the economic lifetime of the power plant (defined by its PPA duration) has the largest impact on the LCOE, followed by the PPA tariff and the debt interest rate. Increasing the economic lifetime of the power plant and decreasing the debt interest rate both lead to a LCOE reduction of up to 10 %. Therefore, long PPA terms of over 30 years in combination with debt interest rates below 12 % are recommended. Interestingly though, a higher PPA tariff has a negative effect on the LCOE which results in an increase thereof. This is because a higher PPA tariff increases the revenue and ultimately also the tax liability, which drives the LCOE up.

However as the financial boundary conditions are set by the external market, the economic assumptions from Table 3.9 are considered to have a low level of uncertainty as they are well-referenced in literature (Baker, 2015; WWF, 2014*a*; Lazard, 2017). Therefore, they are not varied throughout the optimisation process described in the following section unless stated otherwise.

5.3 Multi-objective Optimisation Approach

When looking at complex energy systems like solar thermal power plants, traditional optimisation techniques are not sufficient since the consideration of several optimisation objectives (e.g. maximise electricity production, minimise CAPEX, maximise IRR, minimise fossil fuel consumption, etc.) is sometimes required. However, these objectives will likely be conflicting so that no single optimal solution can be found. Furthermore as the variation of one design parameter often requires other parameters to be changed as well, a number of input parameters (so-called *decision variables*) need to be varied throughout the optimisation in order to produce reasonable designs. For this purpose, multi-objective optimisation algorithms can be used which allow for the variation of a number of decision variables at once to find the optimal trade-off between two contradictory objectives.

5.3.1 Multi-objective optimiser

Due to the complex nature of energy systems, advanced methods and algorithms are required for optimisation studies. In order to find optimal power plant configurations that satisfy multiple operational or economic performance objectives, a multi-objective optimiser is used. The optimiser used in this study has been developed at the Swiss Federal Institute of Technology Lausanne (EPFL) and a detailed description of this optimisation method can be

found in Leyland (2002) and Molyneaux (2002). The multi-objective optimiser uses a population-based evolutionary algorithm for the simultaneous optimisation of two objectives by varying several input parameters (decision variables) within specified limits and calculating the respective objectives.

The multi-objective optimiser is implemented as a part of DYESOPT (see section 2.1) and has previously been used to study solar thermal power plants by, for example, Spelling (2013) and Guédez (2016). It is based on an evolutionary algorithm that generates an initial *population*, which is moved towards a set of optimal designs through evolution. This initial population consists of, for instance, 100 designs, each based on decision variables that are randomly picked within the specified limits. After calculating the objectives of each design using the technical and economic model developed in this study, individuals that are outperformed by any other individual in both objectives are assigned a low rank. Better performing designs are assigned a higher rank. A random selection process is then used in order to select *parent* designs, where higher ranking individuals have a higher probability of being selected as a parent. The resulting parent population is then used to generate *child* designs. During this process, natural evolution is mimicked by allowing mutation, recombination and selection to take place, making sure that each child is unique. Each child of the parent population has parts of its parent's design. If the child's design outperforms the objectives of the parents, the parents are discarded and the child becomes a parent, thus, creating a new generation of parent designs and subsequent child designs. This process is repeated until a so-called *Pareto-optimal front* is formed, which will be discussed in section 5.3.2.

Decision variables

As shown in the sensitivity analysis in section 5.2, varying design parameters and operational set points can lead to improvements in terms of technical and economic performance. However instead of only varying one parameter at the time, the multi-objective optimisation approach allows the variation of several parameters at once. For this, key decision variables like, for example, the TES full load hours, solar field size and the FP temperature are varied between specified limits to derive plant configurations in terms of component sizes and operational parameter set points that lead to an optimal trade-off between two objectives. The decision variables and their respective range of values are listed in Table 5.3. The specified ranges correspond to the same limits as in the sensitivity analysis since using some unlikely values for certain parameters can potentially lead to unexpected performance improvements.

Although the sensitivity analysis in section 5.2 has shown that the model is most sensitive to the economic parameter assumptions, these parameters are not varied since they are set by the external market. The uncertainties of the economic parameters are low as the duration of the PPAs and the respective

Table 5.3: Decision variables, operating strategies and objective functions for the multi-objective optimisation.

Decision variables		Variable	Unit	Range
Gross turbine capacity		$\dot{W}_{\text{gross}}$	[MW]	50-250
Solar multiple		SM	[–]	1-4
TES capacity		t_{TES}	[h]	2-24
Collector row spacing		L_{spacing}	[m]	10-50
Allowable HT inlet temperature[2]		$T_{\text{HT,ref}}$	[°C]	300-440/540
FP mass flow rate		$\dot{m}_{\text{fp}}$	[kg/s]	2-10
HPT inlet pressure		$P_{\text{HPT,in}}$	[bar]	60-120
LPT inlet pressure		$P_{\text{LPT,in}}$	[bar]	0.5-18
ACC nominal air temperature difference		$\Delta T_{\text{air,nom}}$	[°C]	10-30
ACC terminal temperature difference		T_{TTD}	[°C]	1-6
HT level reserved for FP[3]		$HT_{\text{level,fp}}$	[%]	5-25
FP temperature	Solar Salt	T_{fp}	[°C]	250-285
	Hitec	T_{fp}	[°C]	160-285
	Hitec XL	T_{fp}	[°C]	140-285
Operating strategies		Variable	Unit	Strategy
TES dispatch strategy		-	[–]	baseload; peaking
Freeze protection strategy		-	[–]	FPS1; FPS2
Objective functions		Variable	Unit	Objective
Capital costs		$CAPEX$	[mil.$]	min.
Internal rate of return		IRR	[%]	max.

tariffs are based on actual data from the REIPPPP (Department of Energy, 2019*a*). Similarly, well-founded interest rates and costs of capital have been chosen in chapter 3 based on reported values in literature (Baker, 2015; WWF, 2014*a*; Lazard, 2017). However in order to show the potential feasibility of CSP plants with favourable financial conditions, lower financing costs and longer PPA terms have been assumed for some optimisations which will be clearly indicated in the following chapter.

Apart from varying the technical decision variables, the optimisations are also carried out for different operating strategies. These include the two TES dispatch strategies (baseload and peaking operation), as well as the two freeze protection strategies, i.e. FPS1 and FPS2. Lastly, a division of the SCA into 5 CVs is used throughout the optimisation process. This provides a reasonable trade-off between simulation accuracy and computational effort as shown in section 4.2.

[2] Maximum temperature of 540 °C for Solar Salt and 440 °C for Hitec and Hitec XL.
[3] Only in the case of FPS2.

Conflicting performance objectives

Since the operational objectives of CSP plants are typically conflicting (e.g. maximise profit, maximise electricity generation, minimise CAPEX, minimise fossil fuel consumption, minimise turbine stops), simultaneously fulfilling several objectives becomes a challenge in terms of plant design. As described above, a multi-objective optimiser can be used to find trade-offs of optimal designs that satisfy two objectives at once. For this, two conflicting objectives need to be defined. If the objectives are not conflicting, a single optimal solution can be found and a conventional optimisation approach with only one objective should be used.

The optimisations in this study are carried out by minimising the CAPEX and maximising the IRR (see Table 5.3) which can be conflicting objectives for investors and decision makers in CSP projects (Guédez *et al.*, 2016). A cheaper plant will produce less energy and thus have a low IRR, whereas a plant that achieves a higher IRR will be more expensive. Since the CAPEX and its attached risks represent a major barrier for investors willing to finance CSP projects (Guédez *et al.*, 2016), minimising it allows the finding of high-performing power plant configurations at minimised costs. Although minimising the LCOE would also be a suitable objective for the optimisation, the IRR is a profit-based indicator that takes the value of dispatchability into account. This is preferable in this study as different tariff structures are compared. However, since a project with a high IRR also typically has a low LCOE, the influence of the decision variables on the LCOE can also be evaluated with the results from the optimisation.

5.3.2 Pareto-optimal front

As previously mentioned, the multi-objective optimiser allows the user to optimise several operational or economic objectives at once by achieving Pareto-optimality which represents an optimal trade-off between two objectives (Pareto, 1896). The result of the multi-objective optimiser is a scatter plot in which the objectives of the individual designs are displayed as shown in Figure 5.10 for an exemplary optimisation. Each marker represents a power plant configuration with a unique combination of equipment sizing and operating parameter set points within the specified limits of the decision variables (see Table 5.3). It can be seen that, based on the objectives of the randomly generated first generation, no optimal trade-off can be determined. With every new generation of designs, the objectives improve and a front starts to form, representing a trade-off of solutions. However, the multi-objective optimiser reaches a point where no significant improvements of the two objectives are achieved with additional generations (see Figure 5.10) and the optimisation is empirically converged. The objectives of the last generation form a curve (here, 60 generations) that represents the optimal trade-off between the two

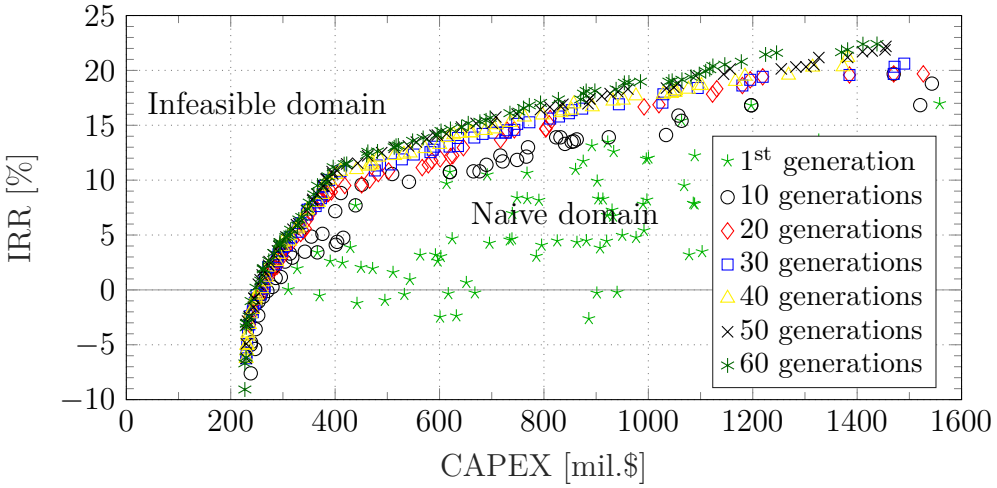

Figure 5.10: Effect of number of generations on the Pareto front as an optimal trade-off between CAPEX and IRR (adapted from Augsburger, 2013).

objectives, the so-called Pareto-optimal front. Along this curve, each point is considered optimal as no other design exists that is simultaneously better in both objectives. Therefore above the Pareto front lies the *infeasible domain*, where no power plant design exists that can achieve both a lower CAPEX and a higher IRR than any design on the Pareto front. Every generation of designs below the Pareto-front is part of the *naive domain*. Within this domain, every design is outperformed by designs on the Pareto front, meaning that there are designs that either have a lower CAPEX or a higher IRR.

As the optimisation process requires a significant computational effort[4], an empirical maximum limit of 5760 evaluations — using an initial population size of 96 power plant designs and allowing 60 generations — has been set, assuming that, after so many generations, any further improvements of a following generation's objectives can be considered insignificantly better than the previous generation's objectives as shown in Figure 5.10.

5.4 Summary

In this chapter, the impact of key design variables on the technical and economic performance of MSPTPPs was investigated in comparison to a reference plant. By varying a series of plant design parameters one at the time, the feasibility of different plant designs, operating strategies and financial parameter assumptions was assessed. It was shown that switching from FPS1 to FPS2

[4] For example, on a standard desktop computer with a 3.40 GHz processor, an optimisation with 6000 evaluations takes approximately two to three weeks to complete, depending on the complexity of the underlying dynamic performance model (i.e. the number of CVs per SCA or the freeze protection strategy used).

yields the largest improvement of both the LCOE and solar-to-electric efficiency, followed by increasing the gross turbine capacity, TES size and solar multiple. Additionally, operational parameters like the FP temperature or mass flow rate can also be optimised in order to further reduce the LCOE. Lastly, a multi-objective optimiser using a population-based evolutionary algorithm was introduced for the optimisation of MSPTPPs. This allows the variation of several decision variables at once, which is used in the following chapter to identify power plant configurations and operational parameter set points that lead to the best trade-offs between two optimisation objectives.

Chapter 6

Results and Discussion

The developed MSPTPP model is used in this section for multi-objective optimisations. This allows for the variation of a number of decision variables at once in order to find the optimal trade-off between two contradictory objectives. Firstly, three different HTFs and two freeze protection strategies are compared to identify the most cost-effective strategy. Secondly, a range of optimal power plant configurations and operational parameter set points are proposed for the different freeze protection strategies as well as for baseload and two-tier tariff structures. Thirdly, recommendations regarding tariff structures, PPA tariffs and a potential spot market participation are given. Fourthly, a projection of the LCOE evolution of MSPTPPs until 2050 is provided.

6.1 Preferred Heat Transfer Fluid

In order to determine the preferred HTF for a more efficient and profitable operation of MSPTPPs in Southern Africa, a multi-objective optimisation has been carried out for each of the salt candidates, i.e. Solar Salt, Hitec and Hitec XL. As the climatic conditions at the two selected locations (Upington in South Africa and Kokerboom in Namibia) are similar, South Africa has been chosen as the location for this optimisation. Nevertheless, the results from this South African optimisation are also representative of Namibia as the financial conditions in both countries will not have a direct effect on the performance of the individual HTF but rather leads to a proportional shift of the Pareto-optimal front. The power plants are assumed to operate under the baseload tariff introduced in section 3.5.1 and use FPS1 for FP.

Figure 6.1 presents the results of the multi-objective optimisation for the three investigated HTFs. In Figure 6.1a, the LCOE is plotted against the CAPEX of the simulated plants, showing the optimal trade-off between the two conflicting objectives of minimising the LCOE and minimising the CAPEX. It can be seen that Solar Salt offers the lowest LCOE with a minimum

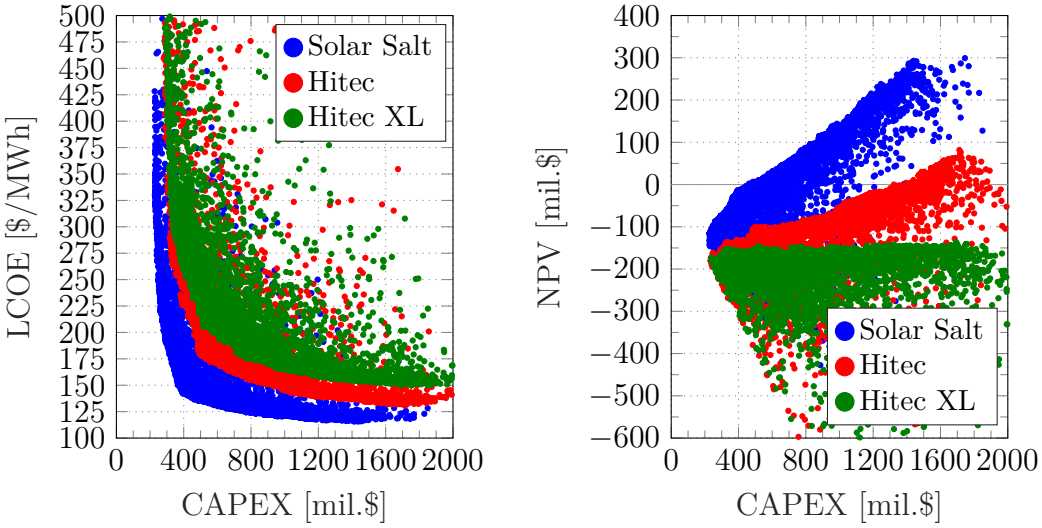

(a) LCOE-CAPEX trade-off for Solar Salt, Hitec and Hitec XL.

(b) NPV-CAPEX trade-off for Solar Salt, Hitec and Hitec XL.

Figure 6.1: Comparison of trade-offs for the three investigated HTFs in terms of (a) LCOE-CAPEX and (b) NPV-CAPEX.

of 115.8 $/MWh, followed by Hitec with 130.8 $/MWh and Hitec XL with 149.8 $/MWh. The LCOE reduces rapidly with an increase in CAPEX up to approximately 400 mil. $ to 600 mil. $ in all three cases and only slower thereafter. An increase in CAPEX is directly linked to a larger power plant in terms of turbine capacity, TES full load hours and solar field size. Therefore, larger plants are obviously favourable under baseload operation since they are able to maximise the power production, which in turn also leads to a lower LCOE. Additionally, it can also be seen that Solar Salt reaches lower LCOEs at the same investment costs when using the other HTFs. This is mainly due to the reduced specific investment costs linked to Solar Salt as discussed in section 3.2, the higher operating temperature range and thus, efficiency.

Although LCOEs below the levelised PPA tariff of 150.3 $/kWh are possible with all three fluids, this is not a guarantee that the plants will be profitable. As previously mentioned in section 3.6.1, the LCOE only reflects the present value of the costs of producing electricity but does not indicate how much revenue or profit can ultimately be generated. Therefore, the NPV can be used (for instance) to assess the plants' economic feasibility. The NPV of the individual HTFs is shown in Figure 6.1b. Power plants using Solar Salt reach a positive NPV starting from investment costs of 400 mil. $ and a high NPV of up to 300 mil. $ can be achieved with an increasing power plant size due to the baseload tariff structure. Using Hitec as HTF requires considerably larger power plants with significantly higher investment costs of at least 1300 mil. $ in order to generate enough electricity to achieve a NPV larger than zero. Although profitable power plant configurations are therefore possible, the rel-

atively high capital costs pose a substantial barrier to developers and lenders, which makes it impossible that such large sums will be invested (especially considering the relatively low NPV that the investment will achieve). Lastly, in the case of Hitec XL, no power plant configuration has been found that offers economic feasibility. This clearly shows that Solar Salt is the preferred HTF for use in MSPTPPs in Southern Africa. Therefore, this study will not further consider Hitec and Hitec XL as viable options and only Solar Salt is used for the remaining optimisations and analyses.

6.2 Effect of Freeze Protection Strategy on Plant Performance

In order to assess which freeze protection strategy performs better under baseload or peaking operation, a multi-objective optimisation has been performed for each freeze protection strategy using both the baseload and two-tier tariff structure. The objectives were again to minimise the CAPEX while at the same time maximise the IRR and thus, the profitability of the power plants. The decision variables that have been varied throughout the optimisation process were the same as introduced in Table 5.3. Section 6.2.1 discusses the results of this optimisation by comparing the LCOE, IRR, NPV and the required electric energy for FP of the two strategies. Thereafter, section 6.2.2 provides more details on the optimal parameter set points that lead to an improved LCOE in MSPTPPs.

6.2.1 Preferred freeze protection strategy

As shown in section 2.4.2, two approaches for the FP strategy were implemented in TRNSYS. In the first strategy, *FPS1*, fluid from the solar field outlet is circulated back to the cold tank while the solar field is in standby. By doing so, it uses the thermal energy stored in the cold tank, which is usually kept at a temperature around 290 °C, to keep the solar field warm. Typically, this inlet temperature is high enough to maintain an outlet temperature above the FP threshold temperature. However, in the case when the HTF temperature drops below the FP set point, this strategy relies entirely on electric FP through impedance and resistance heating. Furthermore, it has been shown in Pan *et al.* (2018*a*) that this approach leads to a gradual cooling of the cold tank throughout the night so that any energy lost (during the night) needs to be recuperated in the early morning before normal operation can begin. Nevertheless, this same approach can also be used in combination with the allowable hot tank inlet temperature to raise the cold tank's temperature in the late afternoon or during periods of low solar irradiance. The higher this allowable hot tank temperature is chosen, the more hot fluid is circulated to the cold tank from the solar field. This approach is especially useful during

the hours just before sunset to raise the cold tank's temperature, which will in turn help in keeping the solar field outlet temperature above its desired threshold.

Analogously to this freeze protection strategy, FPS2 is based on the same approach but also uses thermal energy stored in the hot tank for FP. Once the fluid temperature in the cold tank is no longer high enough to maintain the desired solar field outlet temperature, a mixing valve between the cold tank and the solar field inlet is used to mix hot fluid from the hot tank with the fluid from the cold tank in order to raise the solar field inlet temperature. However, this method requires a sufficient amount of hot fluid stored in the hot tank that needs to be reserved for this purpose. By doing so, a significant amount of thermal energy capacity of the TES is no longer useful for power production, which can reduce the overall net energy output of the plant. However, this approach reduces the necessary amount of energy consumed by the electric FP system by using thermal energy instead and the reduced TES capacity can be off-set by simply building a slightly larger TES. In the case where there is not enough thermal energy available in the hot tank, this strategy also relies on conventional electric FP.

Using both freeze protection strategies in the optimisation, a comparison can be made in order to identify the more efficient strategy for both, baseload and peaking operation. Figure 6.2a shows the results of the optimisation using the baseload tariff. It can be seen that both FP strategies lead to similar internal rates of return for relatively small power plants[1] with investment costs of up to 400 mil. $. For larger power plants, FPS2 yields higher IRRs than FPS2 the higher the CAPEX get. An IRR of up to 30.1 % is possible with FPS2 in comparison to a maximum of 22.4 % with FPS1. For comparison, an IRR between 16 % and 20 % is typically expected for IPP projects according to Kistner and Price (1999). In contrast, Figure 6.2b shows the performance of the two FP strategies under the two-tier structure. Besides the significantly higher internal rates of return — which are a direct result of the favourable peaking tariff that will be discussed in more detail in section 6.3 — it can be seen that FPS1 performs significantly better in smaller power plants with investment costs of up to 600 mil. $. For larger power plants, both FP strategies are suitable to achieve IRRs of up to 77 %. Furthermore, it can be seen that medium-sized power plants with a CAPEX of between 600 and 800 mil. $ yield the highest IRRs under the two-tier tariff structure. Although this tariff has a period of no remuneration during the night, power plants with relatively large storage sizes between 8 h and 14 h lead to higher IRRs. This can be explained by the fact that these large TES capacities help to bridge the night time to

[1] As the CAPEX is directly linked to the size of the turbine, the solar multiple and the TES capacity, a "small" power plant refers to a plant with a small CAPEX and therefore also a small turbine capacity, solar multiple and TES size. Vice versa, a "large" power plant simply refers to a plant with a high CAPEX and therefore a large turbine capacity, solar multiple and TES size.

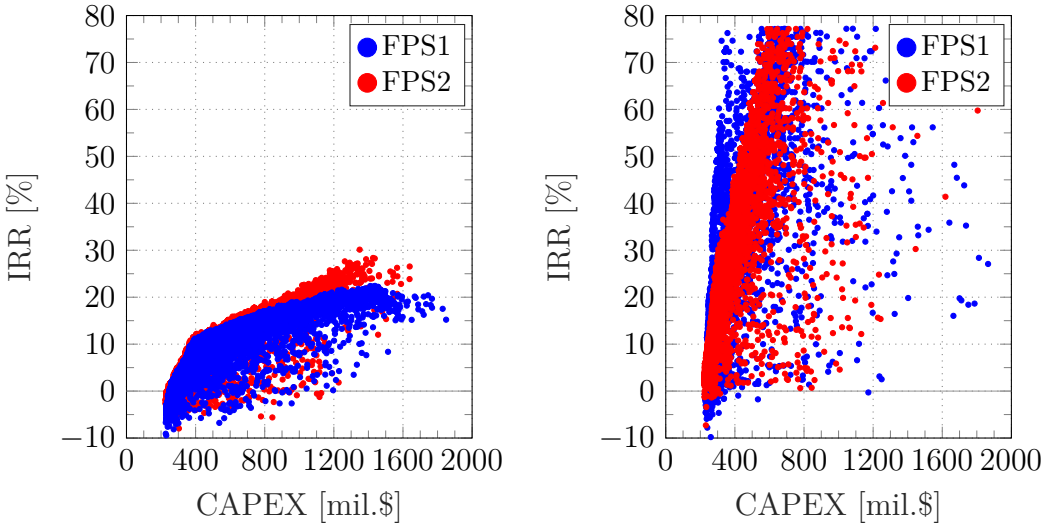

(a) Baseload tariff. **(b)** Peaking tariff.

Figure 6.2: IRR-CAPEX trade-off of the two freeze protection strategies.

start power production in the early morning hours before sunrise. Furthermore, larger storage tanks also facilitate the reduction in electric energy for the FP system in both FP strategies which ultimately leads to a higher net energy output.

Although the IRR can be used to indicate the expected profitability of a power plant, one needs to bear in mind that, as explained in section 3.6.3, the IRR should be higher than the WACC in order to be financially feasible. However, this is not easily possible with a large number of power plants where every single one has a different WACC due to the varying financing structures. Hence, the NPV can be used to assess whether a power plant will be profitable. A NPV greater than zero indicates an IRR higher than the WACC. Figure 6.3a shows the NPV of the two FP strategies for baseload operation. Similar to the IRR, the difference in NPV between FPS1 and FPS2 increases with larger power plants with FPS2 representing the more effective freeze protection strategy. Power plants with a high CAPEX comprise of larger solar fields and TES systems that enable a higher energy output and are less sensitive to extraction of thermal energy from the hot tank for FP. Therefore, FPS2 yields better results than FPS1 with increasing system sizes. Nevertheless, power plants with investment costs above 400 mil. $ are needed for both FP strategies to reach a NPV above zero. In contrast, the relatively high IRRs achieved under the two-tier tariff structure also lead to high NPVs, which is shown in Figure 6.3b. For both FP strategies, small power plants with a CAPEX above 250 mil. $ already provide an economically feasible option. For these small plants, however, FPS1 is favourable because they generally comprise of a smaller TES that will otherwise be depleted faster under FPS2. For larger power plants with a CAPEX of above 500 mil. $, FPS2 is recommended as it results in higher IRRs

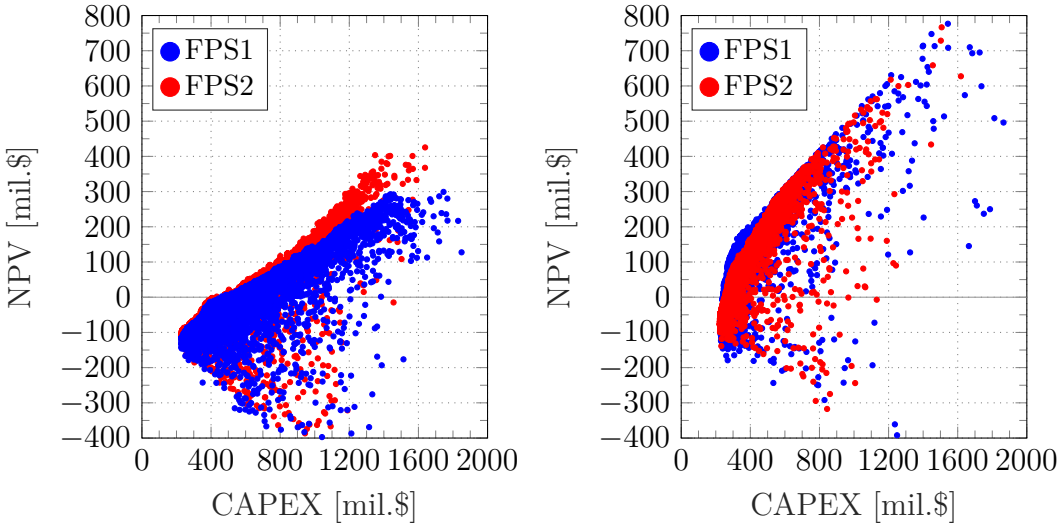

(a) Baseload tariff. **(b)** Peaking tariff.

Figure 6.3: Influence of the freeze protection strategy on the NPV of power plants.

and lower LCOEs, as will be shown in the following section.

Figure 6.4 shows a comparison of the LCOE between the two tariff structures for each FP strategy. Although the two-tier tariff yields higher IRRs and NPVs than the baseload tariff, the latter enables significantly lower LCOEs. In fact, with a minimum of 108.9 $/MWh under FPS2, a 7 % lower LCOE is possible with the baseload tariff as compared to the two-tier tariff with a minimum LCOE of 125 $/MWh. In terms of preferred FP strategy, FPS2 leads to a slightly lower LCOE than FPS1 under baseload operation due to the re-

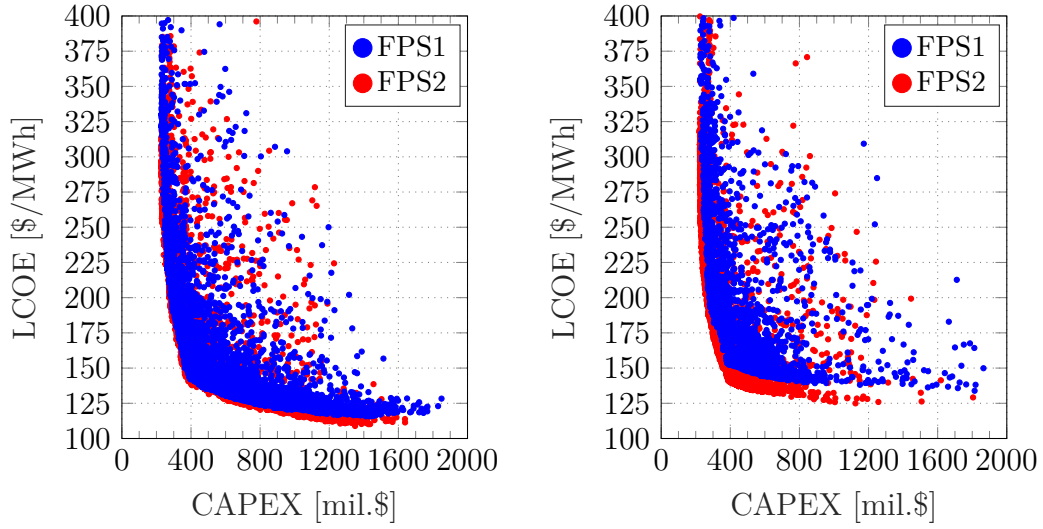

(a) Baseload tariff. **(b)** Peaking tariff.

Figure 6.4: LCOE-CAPEX trade-off of the two freeze protection strategies.

sulting higher net energy output with increasing system sizes (as previously discussed). Similarly, in the case of the peaking operation, FPS2 yields a significantly lower LCOE than FPS1, which is also linked to the fact that power plants with larger TES systems enable a higher energy output and are able to provide the majority of the thermal energy required for the freeze protection system, thus, reducing the need for electric FP.

In order to assess the effect of the two FP strategies on the energy requirement of the electric FP system, Figure 6.5a shows the share of FP energy (E_{fp}) of the total net energy (E_{net}) and the corresponding LCOE for both FP strategies under baseload operation. Here, the advantage of FPS2 over FPS1 can be seen as the energy requirement for electric FP ranges between 0 % and 10 %, whereas FPS1 can lead to an electric energy requirement of up to approximately 15 % of the total net energy output. In comparison, the energy requirement for electric FP under the two-tier tariff (Figure 6.5b) lies within the same ranges as under the baseload tariff with FPS2, leading to a reduction in consumption of the electric FP system. Furthermore, FPS2 leads to an increased operational flexibility as there is always some energy available in the hot tank, which can, for instance, also be used for short-term power production as operating reserve if requested by the grid operator.

To put the advantage of FPS2 into perspective, Figure 6.6 shows a direct comparison of the solar-to-electric efficiencies that can be reached with the respective FP strategies (under baseload operation). Under FPS1, the maximum possible solar-to-electric efficiency is 20.81 %, whereas efficiencies of up to 21.59 % are possible with FPS2. It can be seen in Figure 6.6a that the best-performing power plants under FPS1 on the Pareto front are power

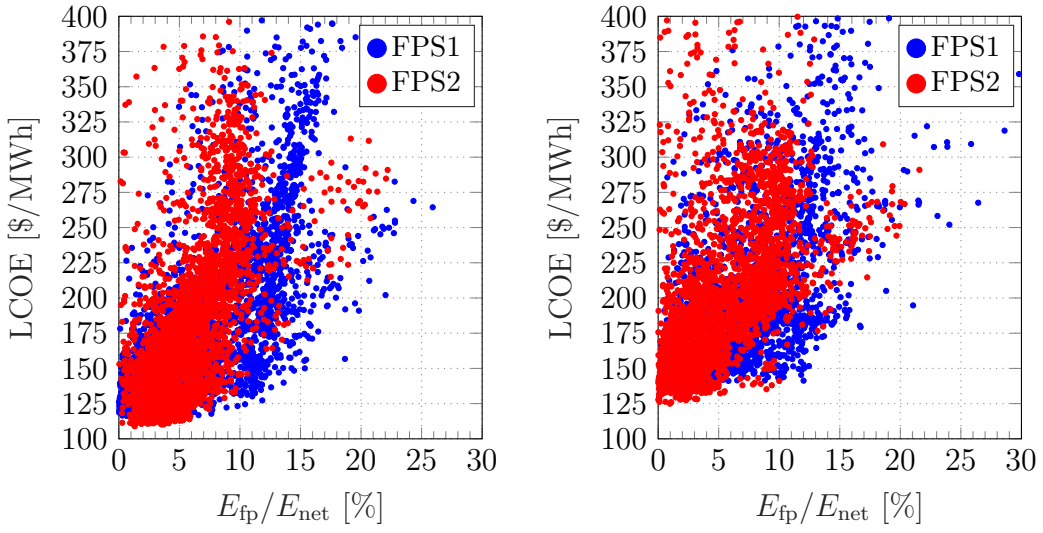

(a) Baseload tariff. **(b)** Peaking tariff.

Figure 6.5: LCOE and the corresponding energy requirement for FP per net electric output of the two freeze protection strategies.

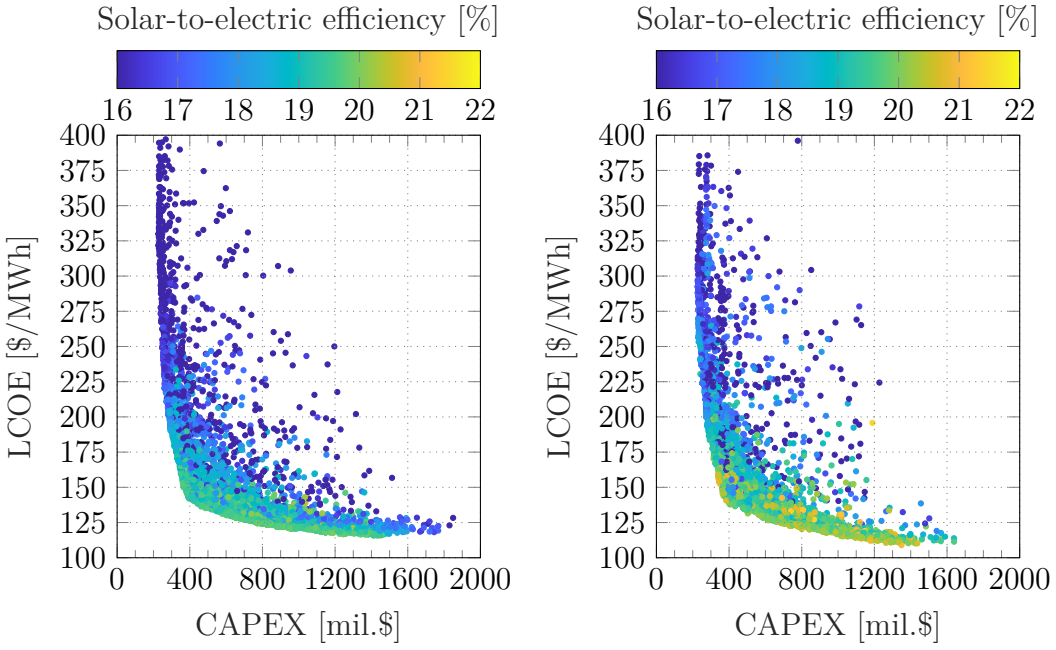

(a) FPS1. **(b)** FPS2.

Figure 6.6: Trade-off of LCOE-CAPEX and corresponding average solar-to-electric efficiencies for baseload power plants using (a) FPS1 and (b) FPS2.

plants with a CAPEX between 300 mil. $ and 1500 mil. $ with values between 19 % and 19.8 %. The solar-to-electric efficiency decreases for very large power plants due to the increased heat losses in the respectively large solar fields. Nevertheless, a lower LCOE can be achieved with large power plants, due to the significantly larger turbine and TES capacities that enables an increased power output and capacity factor. Figure 6.6b shows a similar trend when using FPS2, although the overall solar-to-electric efficiencies are consistently higher than under FPS1. Here, efficiencies between 20 % and 21.6 % are possible for small to medium-sized power plants. Very large power plants with a CAPEX of above 1300 mil. $, on the other hand, experience a loss in efficiency due to the increased heat losses that are inherent to larger solar fields. The solar-to-electric efficiencies of these plants fall below 20 % but an increased power output due to the large turbine and TES capacities leads to the lowest LCOEs in this comparison.

Interestingly, there is a great variation in the optimal HPT inlet pressure between the two freeze protection strategies in terms of both power block efficiency and LCOE. This is illustrated in Figure 6.7 where the highest power cycle efficiencies can be achieved with an HPT inlet pressure between 80 bar and 110 bar when using FPS1. Furthermore, this pressure range also leads to the lowest LCOE values for FPS1. Under this strategy, the maximum average cycle efficiency is 37.9 %. In contrast, the optimal HPT inlet pressure using FPS2 should be chosen considerably lower, i.e. between 65 bar and 85 bar (Fig-

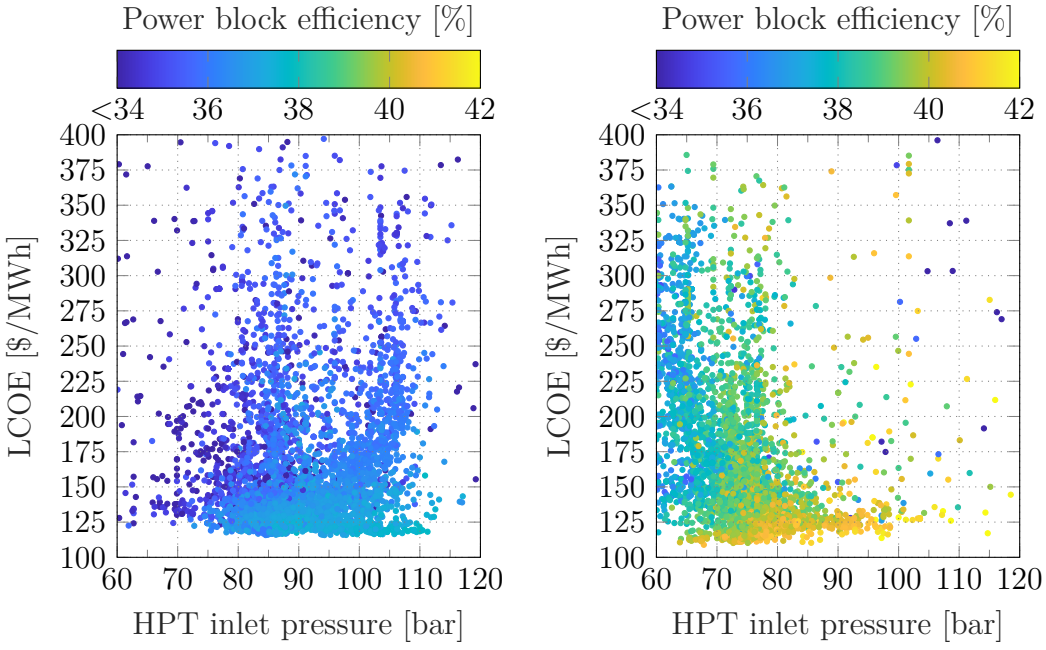

(a) FPS1. **(b)** FPS2.

Figure 6.7: Influence of the HPT inlet pressure on the LCOE and average power block efficiency for baseload power plants using (a) FPS1 and (b) FPS2.

ure 6.7b). Although higher steam pressures result in higher cycle efficiencies in both cases, this pressure range enables significantly lower LCOEs under FPS2. This can be explained when looking at the allowable inlet temperature of the hot tank in Figure 6.8. Under FPS2, an allowable inlet temperature of the hot tank between 420 °C and 480 °C leads to the lowest LCOEs and highest power cycle efficiencies. In contrast, using FPS1 requires lower hot tank inlet temperatures between 380 °C and 450 °C in order to minimise the LCOE and maximise the power block efficiency. The higher hot tank inlet temperatures using FPS2 also have an effect on the optimal LPT inlet pressure by requiring higher pressures. In order to prevent a pinch point violation, lower HPT inlet pressures are thusly required (see Figure 5.7). Furthermore, as discussed in section 5.2.4, the resulting lower inlet temperature to the economiser with lower HPT inlet pressures leads to a larger solar field. This then results in more energy being sent to the TES and an overall increased energy output. Therefore, the optimiser converges towards lower HPT inlet pressures although the resulting power block efficiency is lower, as compared with higher HPT inlet pressures.

Using FPS2, power block efficiencies of up to 42 % can be achieved (see Figure 6.7), which is approximately 4 percentage points higher than under FPS1. The reason for this large difference in efficiency lies in the allowable inlet temperature of the hot tank. Theoretically, the higher this temperature is set, the higher the average HTF temperature in the hot tank and is therefore

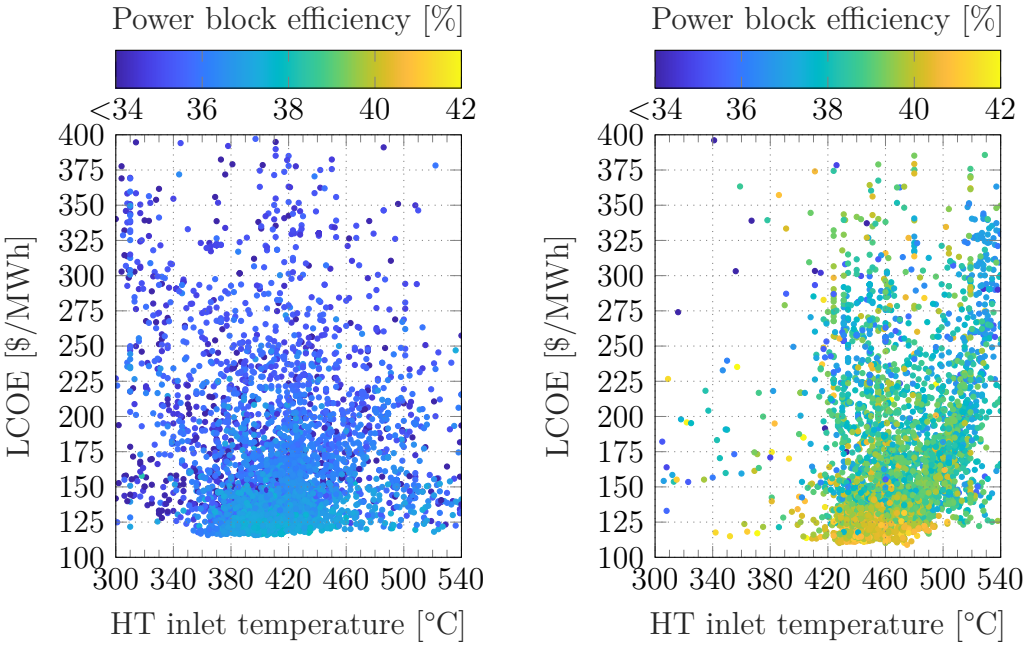

(a) FPS1. **(b)** FPS2.

Figure 6.8: Influence of the hot tank allowable inlet temperature on the LCOE and average power block efficiency for baseload power plants using (a) FPS1 and (b) FPS2.

also higher in the steam generator. Furthermore, a higher TES temperature also increases the thermal storage capacity of the hot tank. Nevertheless, the allowable inlet temperature has to be chosen carefully since it affects a number of other components in the power plant, e.g. the cold tank temperature which in turn also affects the energy requirement for FP as discussed at the beginning of this section. As the performance of the FP system is also dependent on the standby mass flow rate, for example, these parameters mutually affect each other. Therefore by allowing the optimiser to vary the allowable inlet temperature of the hot tank between the specified limits from Table 5.3, a large number of combinations with other decision variables can be tested and their effect on the LCOE can be assessed. The results are shown in Figure 6.8 for both FP strategies. The resulting higher TES temperatures under FPS2 therefore also lead to an increased power cycle efficiency as compared to FPS1 and an overall higher solar-to-electric efficiency as discussed earlier.

Finally, it can be concluded that FPS2 offers the most advantages in terms of electric energy requirement reduction and an overall increase in financial viability due to increased efficiency of the power plants under both the baseload and two-tier tariff structure. Hence, FPS2 is selected as the preferred strategy for the remaining optimisations in the following sections.

6.2.2 Optimal parameters for freeze protection system

With FPS2 being the preferred freeze protection strategy, the optimal parameter set points for this strategy can be determined for both the baseload and peaking operation based on the optimisation results from the previous section. These include the FP temperature threshold at which the electric FP system is activated, the FP mass flow rate during standby of the solar field and the hot tank level that is reserved for FP. Depending on the TES dispatch strategy (which is determined by the tariff structure) the optimal set points can be determined that lead to a more efficient power plant operation and thus higher profitability.

Baseload tariff

The LCOE-CAPEX trade-off under the baseload tariff is shown in Figure 6.9. The figures also shows the respective FP temperature threshold and FP mass flow rate that enable a reduction in LCOE. It can be seen that small power plants (below a CAPEX of 400 mil. $) achieve the lowest LCOEs with a FP temperature below 260 °C and a FP mass flow rate between 3 kg/s and 6 kg/s. Although the recommended minimum operating temperature for Solar Salt is 260 °C, reducing the FP temperature by up to 10 °C can increase the energy output of small plants. Nevertheless, this is tied to an increased risk of the

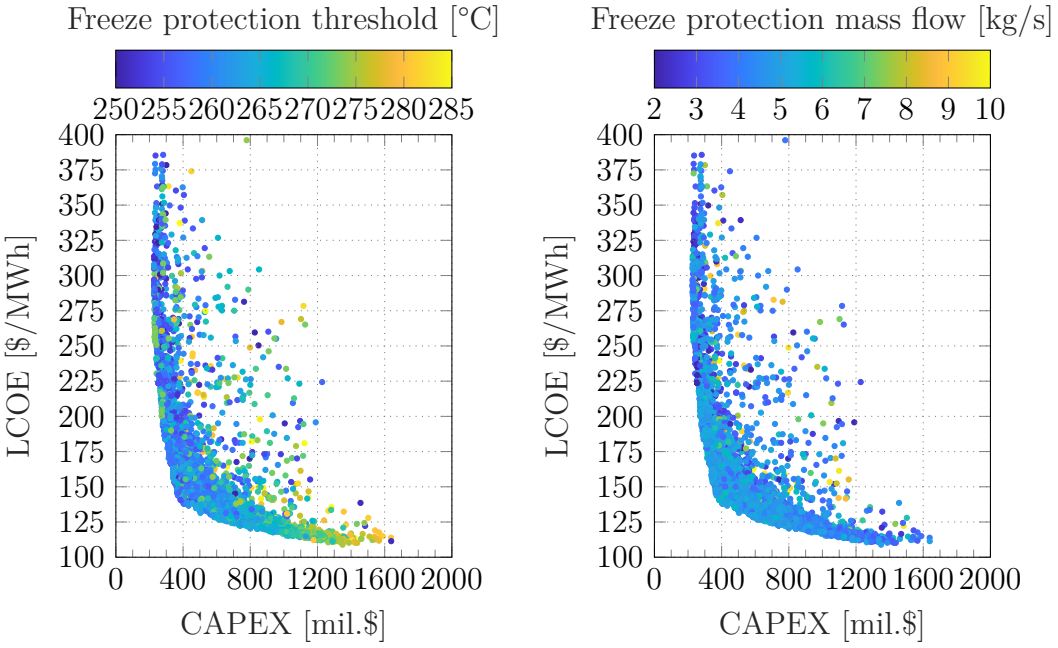

(a) FP temperature threshold.

(b) FP mass flow rate.

Figure 6.9: Trade-off of LCOE-CAPEX and influence of (a) the FP temperature threshold and (b) the FP mass flow rate under the baseload tariff.

HTF to freeze in the pipes in the case of a fault. Therefore as a FP temperature of 260 °C leads to a only marginally higher LCOE, this temperature is recommended for smaller plants. As can be seen in Figure 6.10 (where the LCOE-CAPEX trade-off is shown in terms of the installed gross turbine and TES capacity) the power plants below a CAPEX of 400 mil. $ comprise a turbine capacity of 50 MW in combination with a TES capacity of between 2 h and 14 h capacity. Therefore for plants with a capacity of 50 MW, the optimal FP temperature does not directly depend on the size of the TES. With increasing plant size, however, the optimal FP temperature threshold also increases so that the optimum lies between 260 and 270 °C for plants with a CAPEX of up to 1000 mil. $. Above a CAPEX of 1000 mil. $ (turbine capacities above 150 MW), temperatures above 270 °C and, in some cases, even over 280 °C result in the lowest LCOEs. Such high temperatures for the FP can be explained through the fact that these plants also feature a large TES of above 14 h, as shown in Figure 6.10b. This large hot tank enables a continuous mixing of hot fluid from the hot tank. In conjunction with the high FP temperature set point, this leads to the cold tank temperature staying close to its desired temperature of 290 °C which ultimately increases the plant efficiency. In terms of the FP mass flow rate during the solar field standby, the optimum flow rate varies between 4 kg/s and 6 kg/s for all plant sizes as shown in Figure 6.9b. However in the case of very large power plants that also have a high FP tem-

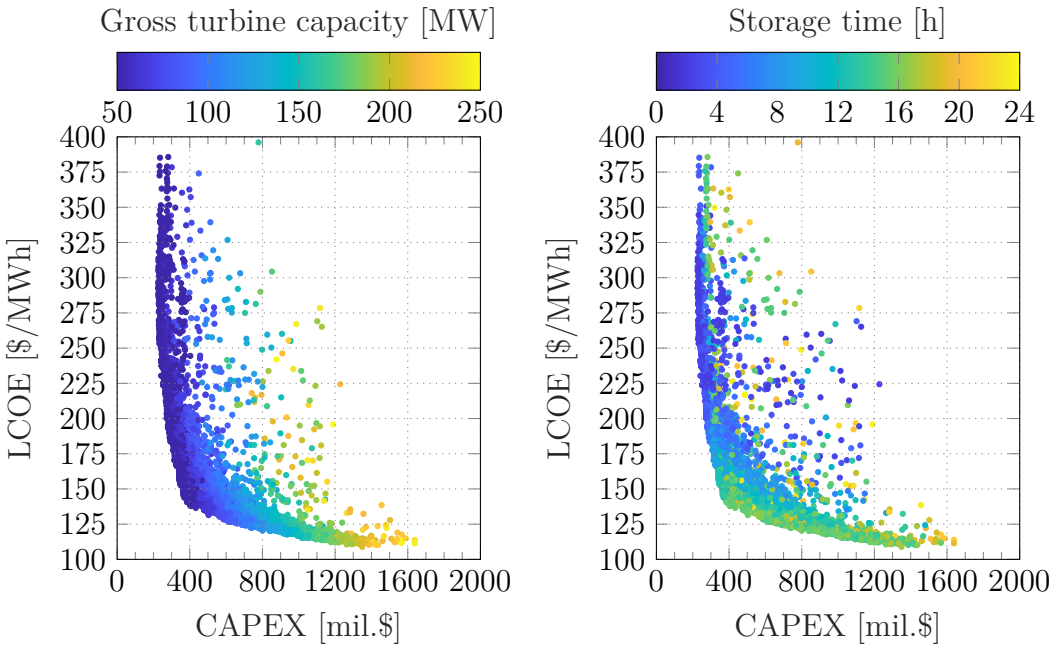

(a) Installed gross turbine capacity. **(b)** TES capacity.

Figure 6.10: Trade-off of LCOE-CAPEX and influence of (a) the gross turbine capacity and (b) the TES capacity under the baseload tariff.

perature (towards the right of the graph), the optimal FP flow rate is between 3 kg/s and 4 kg/s to compensate for the higher heat losses in the solar field resulting from the increased fluid temperatures.

Figure 6.11 shows the LCOE-CAPEX trade-off in terms of the hot tank fill level that is reserved for FP and the relative amount of energy requirement for the electric FP under FPS2. Since FPS2 requires a certain percentage of the hot tank fill level to be reserved for FP, Figure 6.11a shows that a value between 3 % and 6 % yields the lowest LCOEs on the Pareto front. The weighted average reserved fill level for FP is 5.5 %. Hence, reserving a TES fill level of only 5 % can lead to a significant decrease of the LCOE which justifies a potential over-sizing of the TES by approximately 5 %.

Lastly, the LCOE naturally decreases with a decreasing energy consumption of the FP system, which makes up approximately 1 % to 4 % of the total net energy output in the case of the best performing power plants on the Pareto front (turbine capacities above 50 MW with TES sizes above 7 h). However even when using FPS2, the need for electric FP cannot be completely eliminated since it is still required during some hours of the year.

To summarise, it can be concluded that a combination of turbine capacities above 100 MW and a TES size of between 14 h and 16 h are recommended in order to minimise the LCOE. Furthermore, a FP temperature threshold

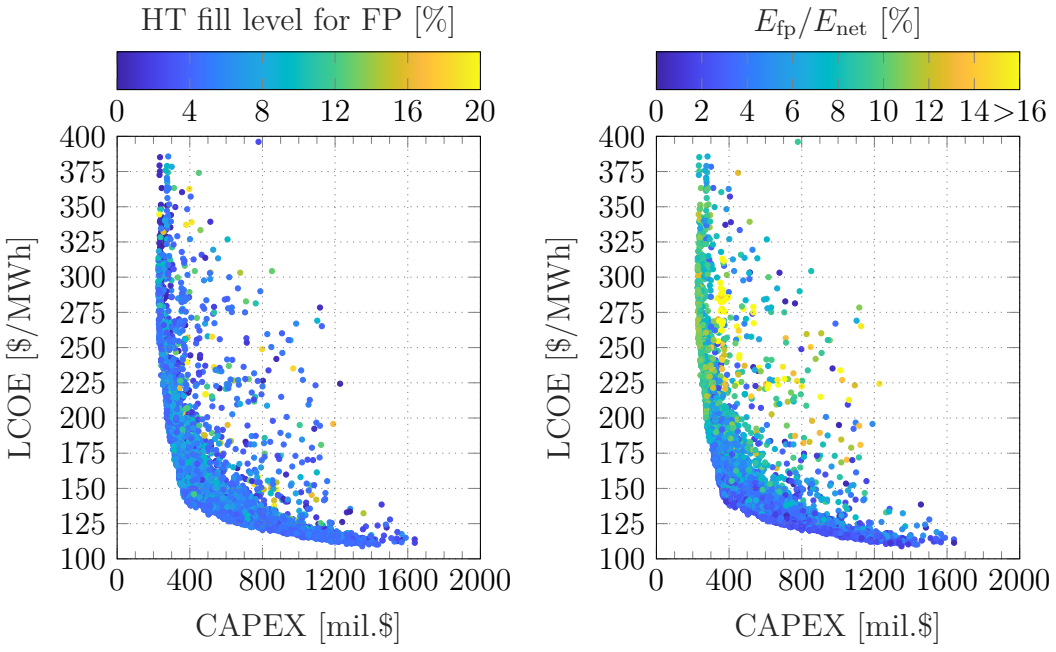

(a) Hot tank fill level reserved for FP.

(b) Share of the energy requirement for FP of the total net energy output.

Figure 6.11: Trade-off of LCOE-CAPEX and influence of (a) the hot tank fill level reserved for FP and (b) the share of the energy requirement for FP of the total net energy output under the baseload tariff.

between 260 °C and 270 °C and a mass flow rate between 4 kg/s and 6 kg/s are recommended for baseload operation. The required hot tank fill level reserved for FP under FPS2 should be limited to below 5 %.

Two-tier tariff

Under the two-tier tariff, small turbine capacities of below 100 MW are favourable in terms of LCOE reduction as shown in Figure 6.12a. A further reduction of the LCOE is possible with turbine capacities of up to 200 MW but comes at considerably larger investment costs. Although the two-tier tariff rewards power generation during peak hours in the evening and discourages power generation at night through a tariff of zero, Figure 6.12b indicates that large TES capacities are nonetheless the key to LCOE reduction. Here, large TES sizes of up to 23 h have been found to have a positive effect on the LCOE due to the fact that the non-generation period over night can be bridged more easily to restart power generation in the early morning hours before the sun rises. Furthermore, larger TES capacities are beneficial to the approach of FPS2, which reserves a percentage of the storage tank capacity for FP. This is exacerbated by the FP temperature threshold, shown in Figure 6.13a, which should be chosen lower the larger the TES is.

The optimal FP temperature threshold for small plants with a CAPEX of up to 350 mil. $ (TES capacities below 10 h) lies in the range of 270 °C to

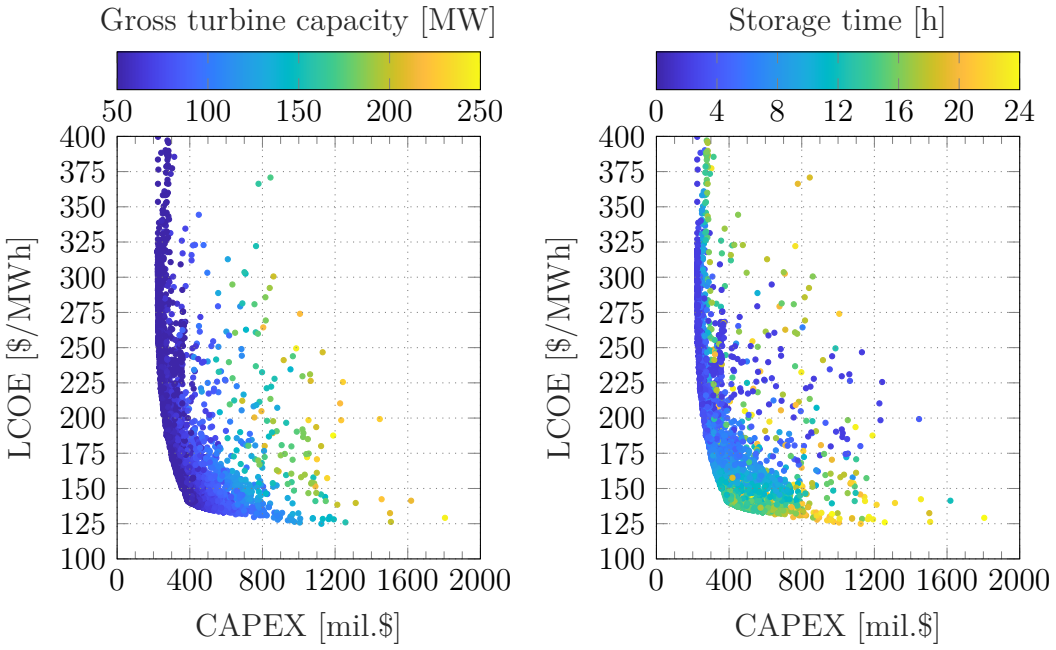

(a) Installed gross turbine capacity. **(b)** TES capacity.

Figure 6.12: Trade-off of LCOE-CAPEX and influence of (a) the gross turbine capacity and (b) the TES capacity under the two-tier tariff.

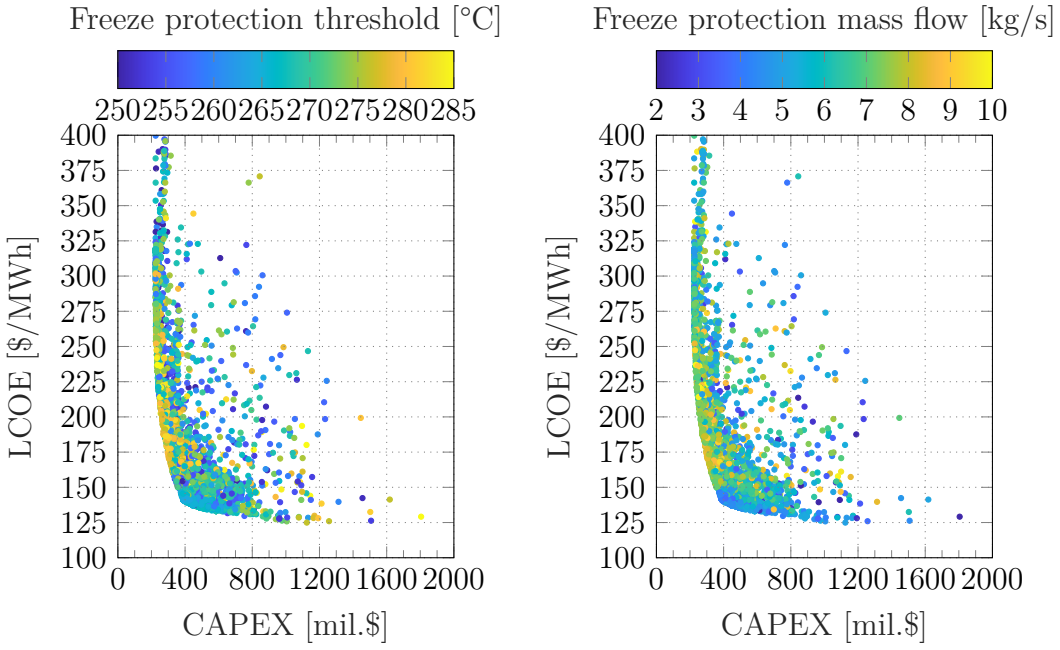

(a) FP temperature threshold.

(b) FP mass flow rate.

Figure 6.13: Trade-off of LCOE-CAPEX and influence of (a) the FP temperature threshold and (b) the FP mass flow rate under the two-tier tariff.

280 °C, with some plants even requiring a FP temperature of 284 °C. All of these plants on the Pareto front feature a gross turbine capacity of 50 MW, whereas their TES capacity varies between 2 h and 10 h. With increasing TES capacities, however, the optimal FP temperature threshold decreases to values between 265 °C and 270 °C. Similarly, the optimal FP mass flow rate is between 6 kg/s and 9 kg/s for small plants with a CAPEX of up to 350 mil. $ and reduces to 4 kg/s to 6 kg/s with increasing TES capacities (Figure 6.13b). Although a significantly lower flow rate of 2 kg/s would result in a reduction of heat losses in the solar field, the optimisation procedure has determined that larger flow rates, in combination with the variation of other decision variables, are beneficial in terms of LCOE reduction. Due to the implementation of FPS2, the flow rate can be higher than 2 kg/s since the relatively large TES tanks in larger systems store enough energy that can compensate for the heat losses incurred by higher flow rates. In fact, Figure 6.14a shows that power plants with smaller TES systems (CAPEX below 350 mil. $) require between 5 % and 11 % of the hot tank fill level to be reserved for FP in order to compensate for the heat losses induced by the elevated flow rates. With TES capacities above 10 h, however, the optimal required hot tank fill level reserved for FP reduces to below 1 %. As a result of these large storage tanks when using FPS2, the share of the energy requirement for electric FP of the total amount of net electric energy lies between 0.1 % and 3 % (Figure 6.14b). In comparison, TES capacities below 10 h result in a considerably higher electric energy requirement

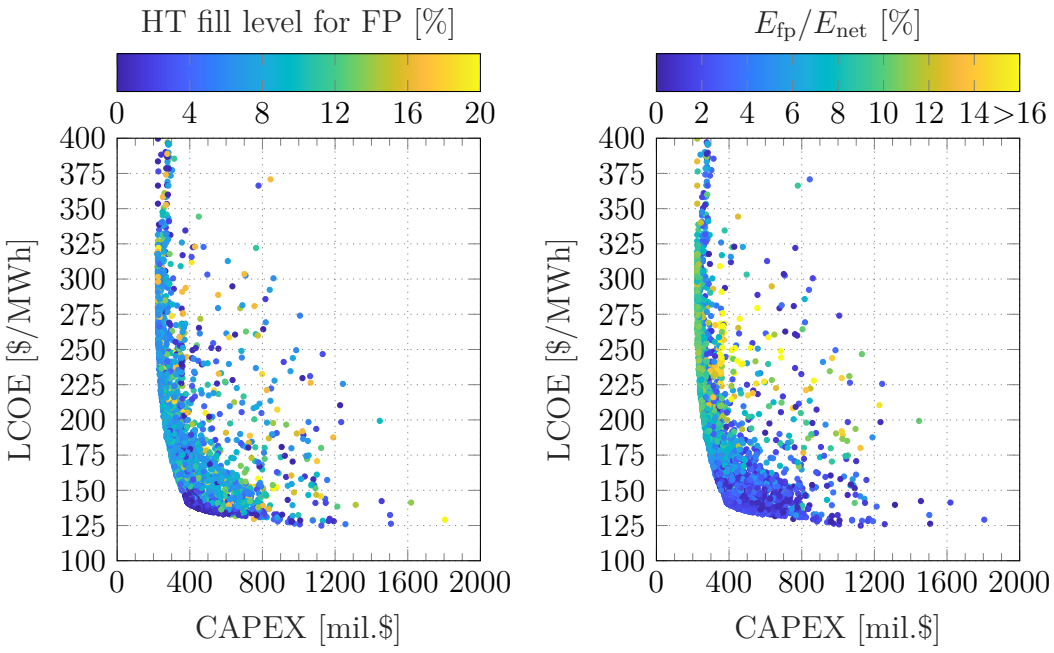

(a) Hot tank fill level reserved for FP.

(b) Share of the energy requirement for FP of the total net energy output.

Figure 6.14: Trade-off of LCOE-CAPEX and influence of (a) the hot tank fill level reserved for FP and (b) the share of the energy requirement for FP of the total net energy output under the two-tier tariff.

of between 4 % and 10 % in combination with a high reserved hot tank fill level for FP.

To conclude, in the case of a two-tier tariff as currently available in South Africa, the recommended turbine capacity is below 100 MW in combination with a TES capacity of between 13 h and 20 h — which is counterintuitively large for this tariff structure — in order to minimise the LCOE. Using the proposed FPS2 approach for freeze protection, a FP temperature threshold of 265 °C to 270 °C is recommended for these power plant configurations in combination with a solar field standby mass flow rate of between 4 kg/s and 6 kg/s. Lastly, the hot tank fill level reserved for FP can be lowered to below 1 % due to the large storage capacities.

6.3 Recommendations for MSPTPPs in Southern Africa

The following sections provide a number of recommendations for the deployment of MSPTPPs in South Africa and Namibia, discussing the effect of the tariff structure on the power plants' LCOE in section 6.3.1, the minimum possible PPA tariff under current financial conditions in section 6.3.2 and a possi-

ble participation in the day-ahead market under favourable financial boundary conditions in section 6.3.3.

6.3.1 Tariff structures

Comparing the results of the multi-objective optimisation of power plants under the baseload and two-tier tariff structure using FPS2 from section 6.2, Figure 6.15 shows that a baseload tariff enables significantly lower LCOEs as compared to a two-tier tariff structure. However, an IRR of up to 77.2 % can be achieved through the two-tier tariff, making use of the inflated tariff during peak hours. In comparison, the maximum possible IRR under baseload operation is 30.1 %. Thus, the two-tier tariff structure is advantageous from the view-point of developers, leading to a high IRR and thus profit, but a significantly lower tariff could be paid by the government or the off-taking utility if a baseload tariff was implemented. In fact, Figure 6.16 depicts the levelised PPA tariff (in real terms) of both tariff structures. Since the baseload tariff is fixed, the levelised PPA price without inflation is simply the tariff itself, i.e. 150.3 $/MWh. However due to the varying tariff depending on the time of day under the two-tier tariff structure, the levelised PPA price ranges from 181.6 $/MWh to 264.5 $/MWh with a median of 212.3 $/MWh. Considering the minimum value, this corresponds to an approximately 20 % higher tariff than the base tariff. Therefore from the view-point of the government, a baseload tariff scheme should be envisioned due to the significantly lower possible tariff. Furthermore, this would aid the ageing power system in adding

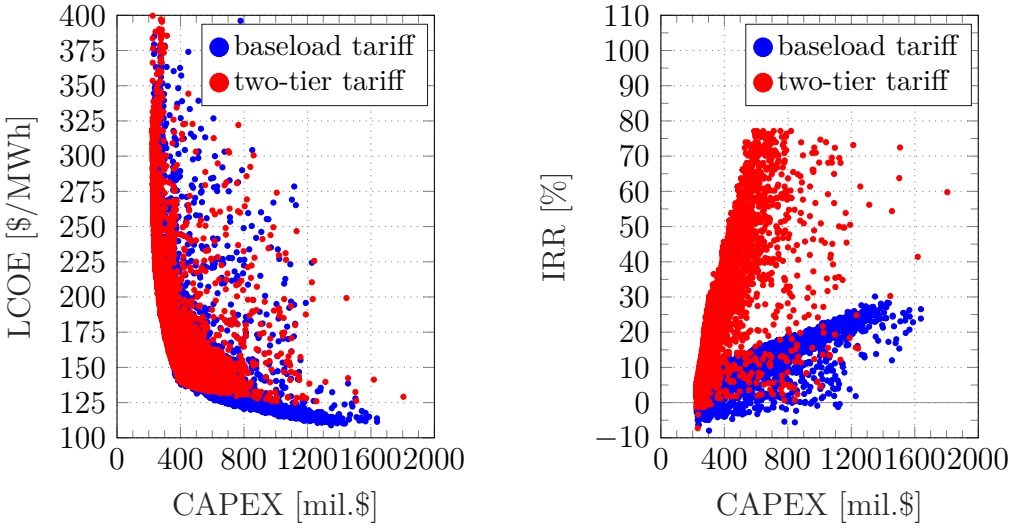

(a) LCOE-CAPEX trade-off for baseload and two-tier tariff.

(b) IRR-CAPEX trade-off for baseload and two-tier tariff.

Figure 6.15: Comparison of trade-offs for baseload and two-tier tariff structure in terms of (a) IRR-CAPEX and (b) LCOE-CAPEX.

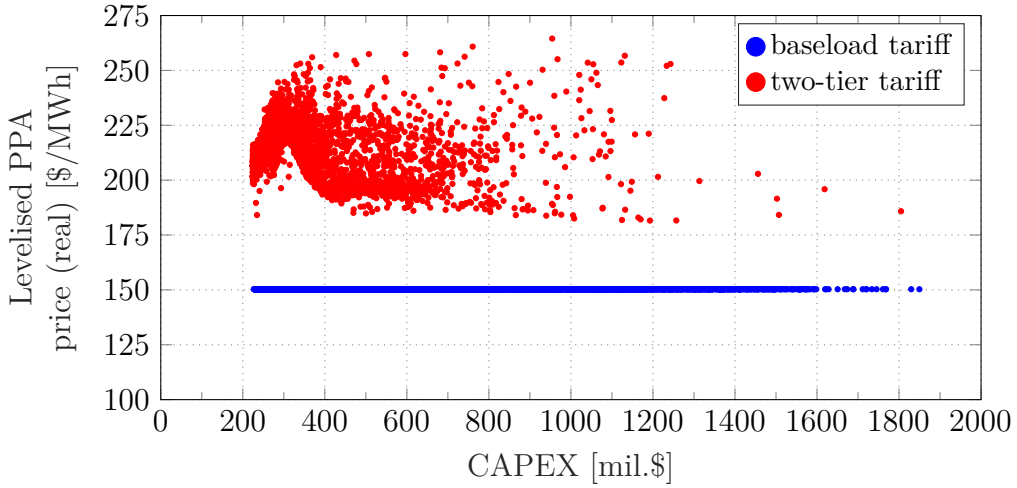

Figure 6.16: Comparison of levelised PPA price (real) for baseload and two-tier tariff structures.

urgently needed new baseload capacity to the supply mix. A successive substitution of old coal power plants can be supported by building CSP plants that have been shown to operate as baseload plants with the additional advantage of providing a high degree of operational flexibility in order to also act as peaking plants if required. A comparison of the LCOE projection of CSP plants and coal-fired power plants until 2050 is provided in section 6.4.

Lastly, Figure 6.17 shows the simplified LCOE for MSPTPPs under baseload and two-tier tariffs in comparison to currently operational CSP plants in South Africa. The simplified LCOE has been used in order to allow comparability with the LCOE data for South African CSP projects from Lilliestam *et al.* (2018). It can be seen that a reduction of the LCOE has been achieved with every new power plant installation, with Kathu providing the lowest LCOE of 225.8 $/MWh. In comparison, significantly lower LCOEs can be achieved under both tariff structures when using MSPTPPs with a minimum of 138.1 $/MWh for baseload and 154.6 $/MWh for peaking power plants. Therefore, it can be concluded that MSPTPPs offer a viable alternative to conventional CSP plants for future PPA auctions.

Considering only parabolic trough plants from the bidding rounds under the REIPPPP, the LCOE reduced by 33 % between BW1 (336.7 $/MWh) and BW3.5 (225.8 $/MWh). Figure 6.18 shows the LCOE of each bid window and the reduction compared to the previous rounds. Using this data to project the current cost trajectory of PTPPs in South Africa leads to an expected LCOE reduction of approximately 30 % in a future hypothetical bid window. This cost reduction translates to a LCOE of 155.8 $/MWh. According to Figure 6.17, MSPTPPs are a suitable technology that can offer such low LCOEs. However, a LCOE below 155.8 $/MWh can only be achieved if a baseload tariff

[2] The year in parentheses indicates the start of commercial operation (NREL, 2020).

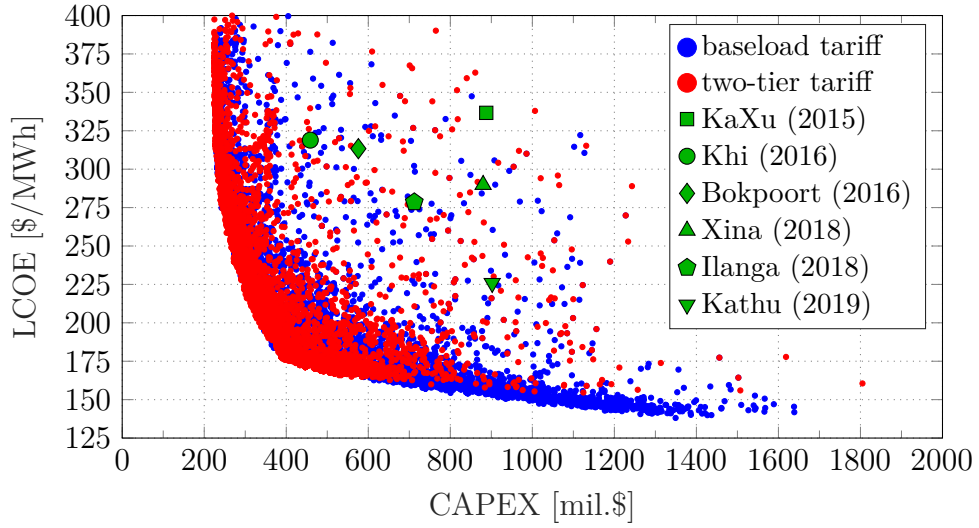

Figure 6.17: LCOE-CAPEX trade-off for baseload and two-tier tariff structure in comparison to operational CSP plants in South Africa[2](Lilliestam *et al.*, 2018). To ensure comparability of the data, the LCOE corresponds to the simplified LCOE as calculated with Eq. (3.45) ($d = 10\,\%$, $n_{\text{op}} = 25$ years).

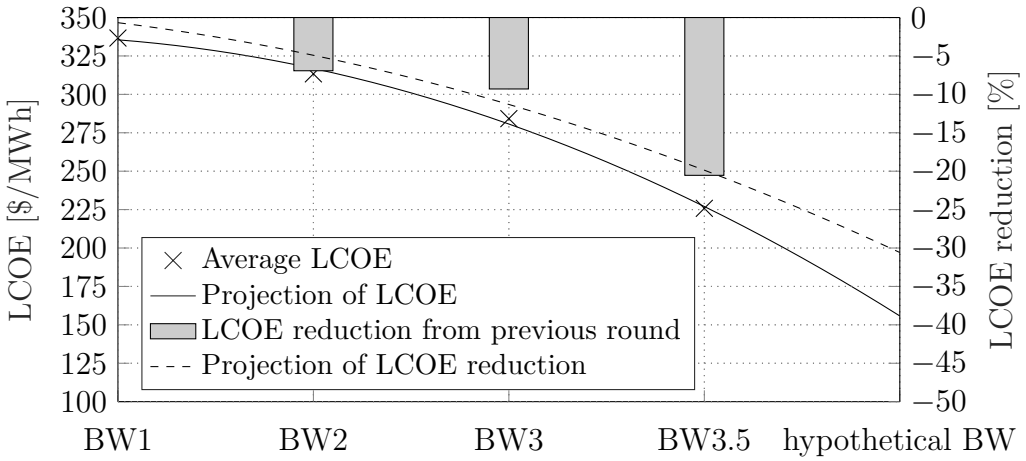

Figure 6.18: Evolution of average LCOE per bid window of the REIPPPP for PTPPs in South Africa with data from Lilliestam *et al.* (2018) and projection of possible LCOE reductions in a hypothetical future bid window.

structure is implemented and relatively large power plant configurations are required. A baseload operation of CSP plants is generally recommended for South Africa to fully make use of the value of CSP with storage in order to facilitate a transition from a carbon-based power generation to a renewable one. Although a significant LCOE reduction is possible under baseload operation in comparison to a two-tier tariff structure, further LCOE reductions are possible through the hybridisation of CSP with PV when a baseload operating strategy

is adopted. This can either be done in the form of using a small PV installation (which is currently still significantly cheaper than CSP) to cover the parasitic consumption during the day or by adding a commercial-scale PV plant that is operated together with the CSP plant in a way where the power production from CSP is shifted to the night-time after the TES has been charged during the day while the PV plant was in operation (see for example Starke *et al.*, 2016; Pan and Dinter, 2017).

6.3.2 Minimum possible PPA tariff

As described in section 3.6.3, Eq. (3.49) can be used to calculate the minimum PPA tariff that is required by a project in order to achieve a NPV of zero at a fixed target IRR, which is assumed to be the project's nominal WACC. A multi-objective optimisation has been carried out to minimise the required PPA tariff under the current financial conditions as discussed in chapter 3 for both South Africa and Namibia. A 20 year PPA has been assumed as this is also the time frame currently offered in South African PPAs. As this approach yields a single levelised tariff in real terms that can only be used under a baseload tariff structure, the power plants were simulated under baseload operation. The results are shown in Figure 6.19. For both countries, PPA tariffs below the current base tariff offered during off-peak times in South Africa under BW3.5 (150.3 \$/MWh) are possible. In fact, the minimum required PPA tariff in South Africa is 119.4 \$/MWh, which is 20 % lower than the current base tariff and 57 % lower than the average awarded baseload tariff under BW2 (277.9 \$/MWh[3]). Since the currently implemented two-tier tariff structure in

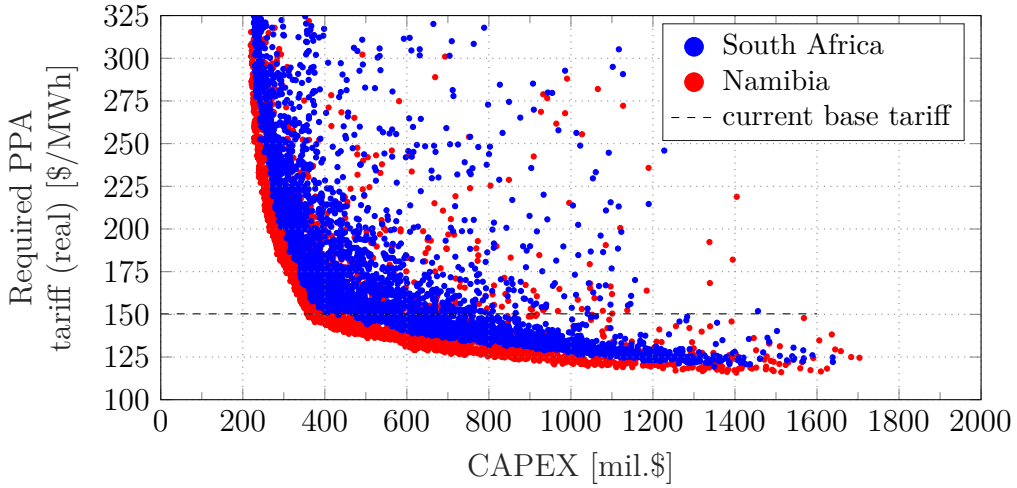

Figure 6.19: Required PPA tariff for baseload power plants in South Africa and Namibia as well as current PPA base tariff in South Africa during off-peak times.

[3] Deflated to $\$_{2018}$.

South Africa rewards power generation with an inflated tariff during peak times, the levelised tariff that is effectively paid out is considerably higher than the base tariff (as discussed in section 6.3.1). Comparing the minimum required PPA tariffs to the levelised PPA prices from Figure 6.16 shows that a significantly lower tariff could be paid out. There, the minimum levelised two-tier tariff that could be achieved was 181.6 $/MWh, which is more than 50 % higher than the minimum required tariff if a baseload operation was adopted. Therefore, it is recommended that policy makers review their current tariff structures and consider a return to a baseload tariff where a significantly reduced PPA tariff is possible for MSPTPPs. However, it should be noted that the indicated minimum PPA tariffs refer to a tariff that would result in a project's NPV to be zero and should therefore be chosen slightly higher in order to allow some profit to be generated.

The minimum required PPA tariff in Namibia is 115.8 $/MWh which is 23 % lower than the current base tariff offered in South Africa. Although Namibia currently does not have any experience with CSP and its tariff requirements, the results from this study can serve as a stepping stone for policy makers to propose a suitable tariff for baseload power generation. Despite the solar irradiance at the two investigated locations being similar, Namibia's minimum PPA tariffs are lower than South Africa's tariffs due to slightly better financial conditions and a higher solar-to-electric efficiency. In fact, Figure 6.20 shows a comparison of the overall power plant efficiency at both locations. The higher efficiencies in Namibia can be attributed to the slightly cooler air conditions in Kokerboom as compared to Upington. During cooler days, the ACC's performance increases and therefore the power cycle's efficiency does as well. Furthermore, the solar field efficiency is also marginally higher in Namibia due to the steeper incidence angles at the location's latitude which is closer to

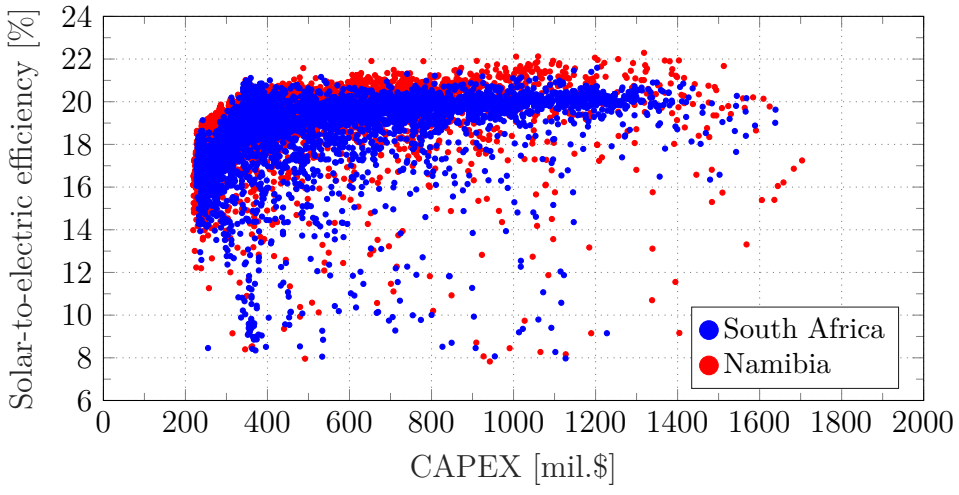

Figure 6.20: Solar-to-electric efficiencies of baseload power plants in South Africa and Namibia.

the equator than Upington. As a result, the overall power plant efficiency in Namibia can be up to 1 percentage point higher than in South Africa.

In 2017, Eskom proposed a renegotiation of the bid tariffs of BW3.5 and 4, including a tariff cap for baseload generation of 770 ZAR/MWh for a 20-year PPA (Engineering News, 2017). Assuming an exchange rate of 13.242 ZAR/$ in 2018 (X-Rates, 2019*c*), this corresponds to a deflated value of 60.9 $/MWh using the CPI from StatsSA (2020). This tariff is considerably lower than the baseload and two-tier tariffs of the previous bid windows and slightly higher than the annual average DAM trading price in 2018 with 49.7 $/MWh. As can be seen in Figure 6.19, a PPA tariff of 60.9 $/MWh over a 20 year period is not financially feasible under current financial conditions. However if the duration of the PPA was increased to 35 years — which is for example the case for the combined tower and trough plant *DEWA IV* in Dubai (Lilliestam and Pitz-Paal, 2018) — and the financing costs were significantly reduced, it would be possible for a baseload power plant to operate under such a scenario with no change to the other financial parameters or assumed investment costs in 2018 as per chapter 3. A debt interest rate of 6 % is possible through a loan from a development bank (REEEI, 2012) and some companies looking for global expansion opportunities are willing to accept a return on equity of 8 % to 10 % in order to diversify risk through developing a project portfolio worldwide (WWF, 2014*b*). A further reduction of project-related risks (such as power market risks, grid integration risks and counterparty risks) through public de-risking instruments can also help in order to reduce the financing costs of renewable energy projects (Wassbein *et al.*, 2013).

Assuming a cost of equity of 9 % and a debt interest of 6 % for a baseload power plant in South Africa, Figure 6.21 shows the required PPA tariffs in order for a project to achieve a NPV of zero. It can be seen that the proposed tariff cap of 60.9 $/MWh can be undercut by a number of projects, with a minimum possible PPA tariff of 50.4 $/MWh (in real terms). For this, the best performing power plant configurations comprise a gross turbine capacity of between 85 MW and 240 MW in combination with a large TES of 14 h to 20 h. Furthermore, the low cost of equity and long PPA term also considerably altered the financing structure of the projects, leading to debt fractions below 36 % for all configurations. Therefore, a developer with a strong balance sheet who can raise working capital at low costs in its home market would be required. Lastly given the high share of equity financing, a bank is more likely to issue a loan at an interest rate of 6 % for the remaining project costs, especially since the developer carries most of the risk. Therefore, it has been shown that PPA tariffs below 60 $/MWh are possible for MSPTPPs in South Africa under the right financial conditions.

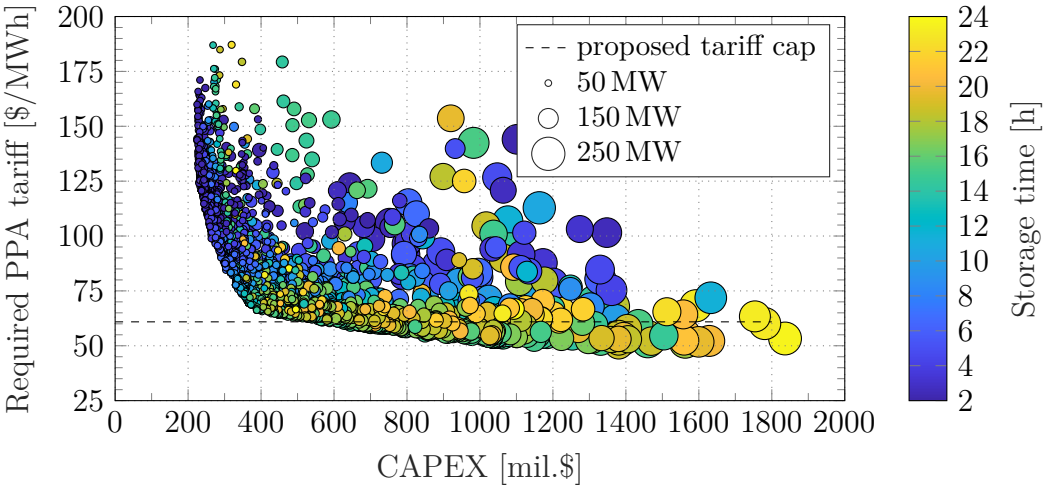

Figure 6.21: Required PPA tariff for baseload power plants in South Africa with reduced financing costs and a PPA duration of 35 years showing the corresponding storage times and gross turbine capacities.

6.3.3 Operation under day-ahead market pool prices

In order to assess the viability of a MSPTPP in Namibia — where there are currently no feed-in-tariffs or PPA agreements in place — one option is the participation in the DAM, a market place where electricity is traded daily for delivery the next day (SAPP, 2020). This open and competitive market provides CSP developers with an opportunity to prove the ability of CSP projects which operate under flexible conditions as well as to provide baseload and peaking power at competitive prices. Assuming the same financing costs as in the section above, i.e. an operational lifetime of 35 years, a debt interest rate of 6 % and a cost of equity of 9 %, a multi-objective optimisation with the hourly DAM trading prices from 2018 (see section 3.5.3) has been performed, minimising the CAPEX and maximising the IRR. For this, the PDS introduced in section 2.5.2 has been used in order to identify the hours of the day with the highest prices during which the plant should be operated.

The results show that, assuming an annual price escalation of 5 %, relatively large plants are needed in order to be financially viable. Figure 6.22 shows the required gross turbine capacities and TES full load hours necessary in order to achieve a NPV greater than zero. An installed turbine capacity between 125 MW and 250 MW in combination with a TES capacity between 14 h and 23 h yield the highest NPV as they are able to bridge periods of lower prices, i.e. typically during night-time and especially on Sundays. However, these plants all have a CAPEX of above 850 mil. $ which requires a high risk-adversity from the developer as the optimal financing structure of these plants determined by the algorithm requires a share of equity of more than 65 %.

Figure 6.23 depicts the LCOE and the corresponding IRR of plants oper-

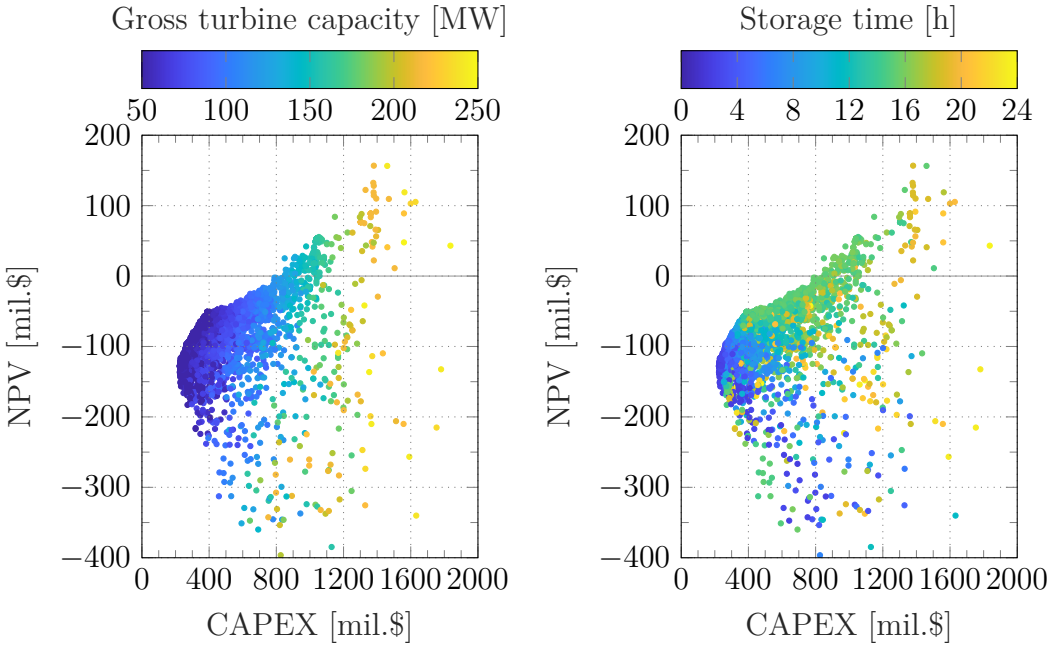

(a) Installed gross turbine capacity. **(b)** TES capacity.

Figure 6.22: NPV of power plants in Namibia operating under DAM pool prices and influence of (a) the gross turbine capacity and (b) the TES capacity.

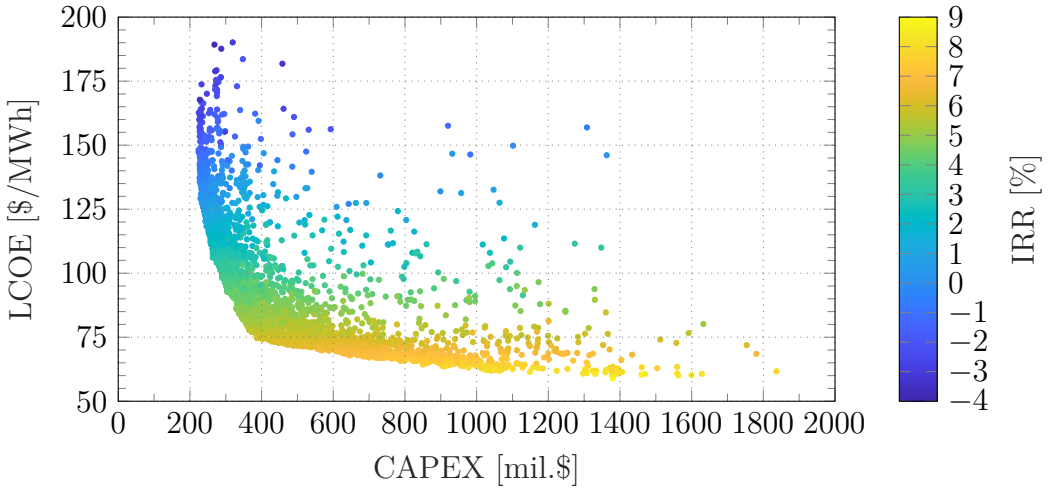

Figure 6.23: LCOE-CAPEX trade-off and corresponding IRR for power plants in Namibia operating under DAM trading prices.

ating under the DAM prices. Financially viable plants can reach an LCOE between 58.9 $/MWh and 65.6 $/MWh which is mainly due to the significantly reduced financing costs and the long project term of 35 years. Compared to the minimum possible LCOE of 108.9 $/MWh under current financial conditions using a baseload tariff (see section 6.3.1), the reduced financing costs

enable a significant LCOE reduction of approximately 46 %. This shows that a project's financing terms are the biggest barrier of potential cost reductions in CSP plants and that public instruments are needed in order to de-risk the current risk environment in South Africa and Namibia to attract developers that will accept lower returns on equity and banks that will issue loans at lower interest rates. Furthermore, the IRR of the financially feasible projects is between 7.4 % and 8.7 %. The resulting WACC of the profitable projects lies between 7.2 % and 7.4 %, which is approximately 35 % less than the nominal WACC of 11.45 % under current financial conditions with a debt/equity ratio of 70/30. Although the IRR is only slightly higher than the WACC and the expected profits for the developer are therefore considerably smaller as compared to a project with a PPA agreement, it has been shown that the participation on the spot market is possible for CSP plants in Southern Africa if the financing costs can be significantly reduced.

6.4 LCOE Projections Until 2050

The following section discusses the results of the LCOE evolution of MSPTPPs until 2050. The method to project the future development of the LCOE has been introduced in section 3.7 and is based on the calculation of the simplified LCOE with Eq. (3.52). This method requires a value for the total installed costs in the base year (2018) in Eq. (3.50). However, there is currently no MSPTPP in operation worldwide that could serve as a starting point for the cost analysis. Therefore to obtain a single value that is representative of the total installed costs of a MSPTPP in South Africa in 2018, the data obtained from the optimisation process in section 6.2 is used. Firstly, it is assumed that all the power plant configurations generated by the algorithm for the baseload tariff case (using FPS2) represent a fictional fleet of CSP plants in South Africa. This fleet consists of numerous differently sized plants designed for a baseload operating strategy with a consequently large variation in technical and economic plant performance. Considering only baseload power plants enables the comparison with conventional power plants currently in operation or under construction in South Africa, i.e. coal-fired power stations that operate as baseload plants. Although the optimisation process initially generates a high number of unprofitable and under-performing plants, it can be assumed that there are inherently more well-performing plants, since the optimiser's task was to maximise the plant's IRR and minimise the investment costs, whereby the algorithm converges towards more financially feasible power plant configurations. Nevertheless, only profitable plants ($NPV > 0$) are considered as no developer or investor would build a plant that is not financially feasible. Lastly, the weighted average of the total installed costs of this fleet can be computed based on this fictional combination of power plants.

Figure 6.24 shows the resulting weighted average, as well as the 5^{th} and

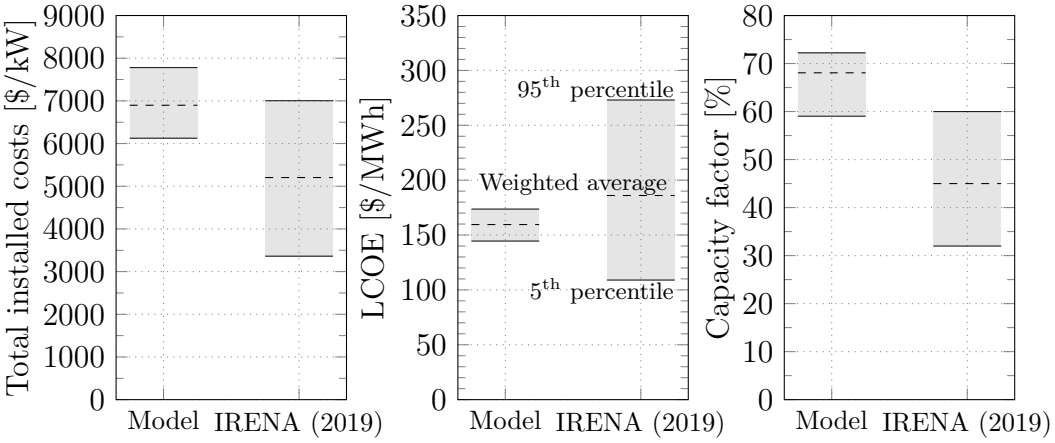

Figure 6.24: Comparison of weighted average installed costs, LCOE and capacity factor of baseload plants (using FPS2) with data for 2018 from IRENA (2019).

95$^{\text{th}}$ percentiles, in comparison to data of global CSP plants built in 2018 from IRENA (2019). It can be seen that the weighted average of the total installed costs obtained from the model are 6898 \$/kW, which is more than 30 % higher than the installed costs of actually built power plants with 5204 \$/kW. This significant difference can mainly be explained through the fact that the optimisation process generated numerous power plants with considerably large solar fields ($SM > 3$) and storage systems ($t_{\text{TES}} > 10$ h), which shifts the range between the 5$^{\text{th}}$ and 95$^{\text{th}}$ percentiles of the total installed costs towards higher costs. To support this, Figure 6.25 shows the correlation between the total installed costs, the solar multiple, the storage time and the installed turbine capacity. It can be seen that the majority of the power plants have large solar fields and storage sizes, whereas there is an even distribution of turbine ca-

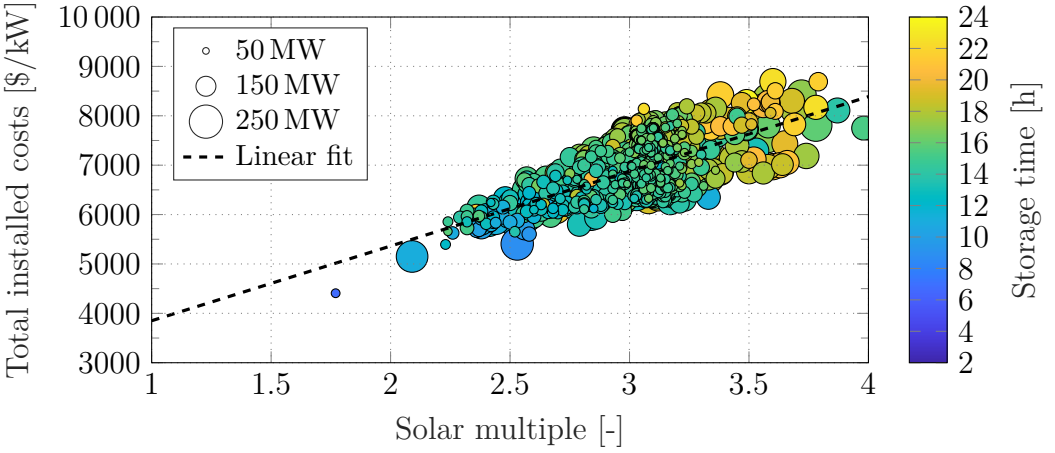

Figure 6.25: Correlation between total installed costs, solar multiple, TES size and turbine capacity of profitable baseload plants using FPS2 in South Africa.

pacities. The installed costs are evidently directly linked to the solar field and storage size, where higher solar multiples and large storage capacities drive the total installed costs up. However, the increased costs of large power plants can be reduced by installing large turbine capacities, resulting in lower specific investment costs as compared to smaller turbines.

In order to enable a comparison of the LCOE, the values reported in Figure 6.24 are based on the simplified LCOE method as presented in section 3.6.1. This method uses the same approach and assumptions as IRENA (2019) (discount rate of $d = 10\,\%$ and economic life of the power plant of $n_{\text{op}} = 25$ years). The weighted average LCOE of the fictional CSP fleet is 159.5 \$/MWh. In comparison, the weighted average LCOE of global CSP plants built in 2018 is 186 \$/MWh (IRENA, 2019) which corresponds to a difference of approximately 14 %. Although the weighted average of the total installed costs is more than 30 % higher in the model, the LCOE is 14 % lower. This can be explained by looking at the weighted average capacity factor in the rightmost chart in Figure 6.24. As a result of the above mentioned large power plants with predominately large storage capacities, the weighted average capacity factor is also significantly higher at 68 %. In comparison, the weighted average capacity factor of CSP plants built in 2018 is 45 % with an average storage capacity of 8.3 h which includes both baseload and peaking power plants. The average storage capacity of the fictional fleet is 15.4 h as they are optimised for baseload operation under a constant tariff. Therefore, the high capacity factors result in an increased electricity generation by implication, which in turn compensates for the higher installed costs when calculating the LCOE.

Figure 6.26 depicts the data distribution of the annual electricity generation and the specific electricity production per installed capacity of the CSP fleet. The weighted average electricity generation per year in year one is 807 GW h. This does not, however, reflect the previous statement of high capacity factors

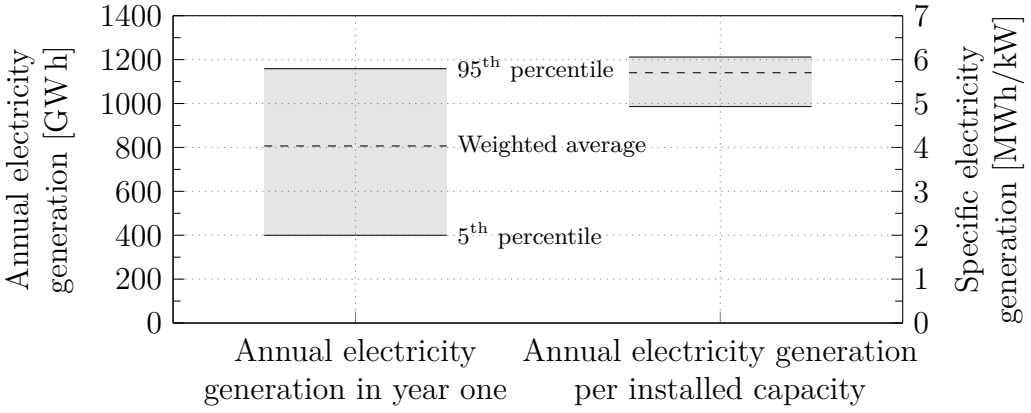

Figure 6.26: Weighted average of annual electricity generation in year one and specific electricity generation per installed capacity in South Africa.

leading to a high electricity generation as, for example, a small plant with a high capacity factor simply generates less electricity than a large plant with a high capacity factor. Therefore by correlating the annual electricity generation with the installed turbine capacity provides a more accurate depiction of the power plants' productivity. In fact, the specific electricity production per installed capacity has a weighted average of 5.7 MWh/kW. This value clearly lies in the upper third of the data range, which means that the majority of the plants have a higher production rate.

Finally, the LCOE evolution until 2050 for MSPTPPs can be calculated with Eq. (3.52) following the method introduced in section 3.7. This forecast is based on the projected globally installed capacity until 2050 from Trieb *et al.* (2009), whereby the investment costs are reduced annually by the expected LR of 20 %. As discussed above, the total installed costs in 2018 ($CAPEX_{2018}$) are assumed to be the weighted average costs of the fictional fleet and are 6898 $/kW. Similarly, the specific electricity generation per installed capacity (e_{net}) is the weighted average specific electricity generation of 5.7 MWh/kW. This value is applied to the LCOE calculation for each year of the forecast but is reduced by the degradation rate throughout the operational lifetime of the power plant. A summary of the parameters for the LCOE evolution until 2050 used in this study is provided in Table 6.1.

Table 6.1: Values used for the calculation of the LCOE projection of MSPTPPs until 2050 for baseload operation and resulting LCOEs for South Africa and Namibia.

Parameter	Variable	Unit	Value	
Globally installed capacity in 2018	$\dot{W}_{2018}$	[GW]	14.9	
Globally installed capacity in year t	$\dot{W}_t$	[GW]	Eq. (3.51)	
Learning rate	LR	[%]	10; 20	
Discount rate	d	[%]	10	
Annual OPEX	f_{OPEX}	[%/a]	1.5	
Annual insurance costs	f_{ins}	[%/a]	0.5	
Degradation factor	r_{deg}	[%/a]	0.1	
Financial lifetime of the plant	n_{op}	[years]	30	
Installed costs and specific electricity generation			South Africa	Namibia
Total installed costs in 2018	c_{2018}	[$/kW]	6898	7067
Specific annual electricity generation	e_{net}	[MWh/kW]	5.7	5.9
Weighted average LCOE			South Africa	Namibia
LCOE in 2018	$LCOE_{2018}$	[$/MWh]	153.8	152.7
LCOE in 2050 ($LR = 20\,\%$)	$LCOE_{2050}$	[$/MWh]	49.6	49.3
LCOE in 2050 ($LR = 10\,\%$)	$LCOE_{2050}$	[$/MWh]	90.1	89.5

Figure 6.27 depicts the results for the LCOE from 2018 to 2050 in South Africa. The weighted average LCOE in 2018 is estimated to be 153.8 \$/MWh and reduces by roughly 68 % by 2050 to 49.6 \$/MWh. To account for uncertainty of the data, the LCOE of the 5$^{\text{th}}$ and 95$^{\text{th}}$ percentiles of the fictional fleet are also depicted. Therefore, the LCOE of the lower cost estimate (5$^{\text{th}}$ percentile) in 2018 is 136.6 \$/MWh and reduces to 44 \$/MWh in 2050. Likewise, the LCOE of the 95$^{\text{th}}$ percentile amounts to 173.4 \$/MWh in 2018 and 56 \$/MWh in 2050. Figure 6.27 also depicts a forecast of electricity costs from new build coal-fired power plants in South Africa. This data is based on the LCOE of Eskom's Kusile power plant, which is currently under construction. According to Eskom, Kusile's LCOE is 1.01 ZAR/kWh, or 76.3 \$/MWh([4]), in 2018 (Department of Energy, 2019*a*). However, recent cost estimates project an LCOE of 1.6 ZAR/kWh (120.1 \$/MWh), considering delays in construction, cost over-runs and increasing operational costs (EE Publishers, 2016; Department of Energy, 2019*a*). Therefore, this comparison considers both costs in order to provide two scenarios for the cost development of coal by 2050:

- *Coal (Eskom)*: scenario based on Kusile's costs estimated by Eskom. A LCOE of 76.3 \$/MWh (in 2018 terms) for Kusile has been reported by Department of Energy (2019*a*) as part of the 2013 Draft IRP Update Report (Department of Energy, 2013).

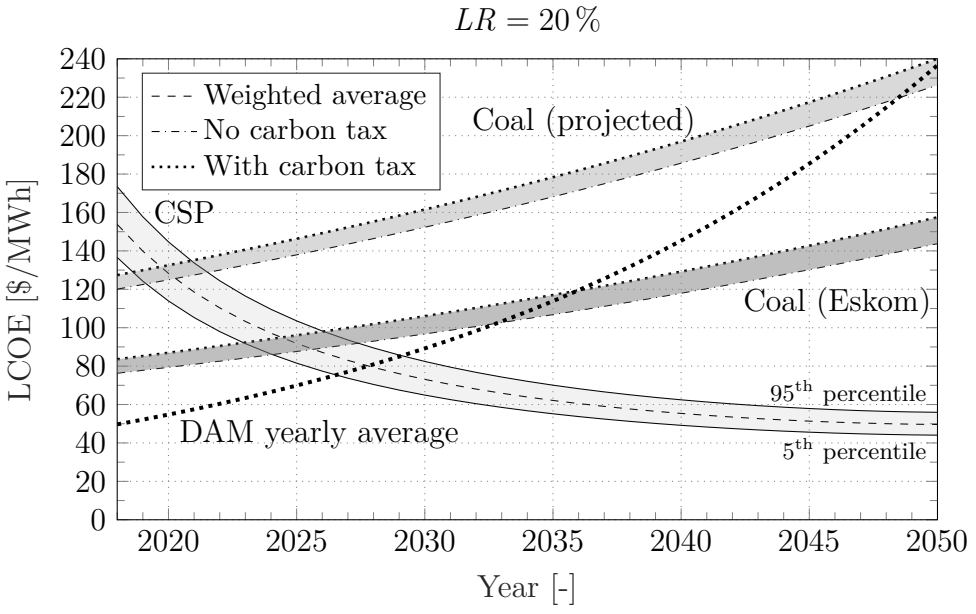

Figure 6.27: LCOE evolution of MSPTPPs in South Africa until 2050 ($LR = 20\,\%$, $d = 10\,\%$, $n_{\text{op}} = 30$ years) in comparison with new build coal-fired power plants with and without carbon tax (EE Publishers, 2016; Department of Energy, 2019*a*).

[4] Yearly average exchange rate of 13.242 ZAR/\$ in 2018 (X-Rates, 2019*c*).

- *Coal (projected)*: scenario based on Kusile's projected costs estimated by industry experts. The estimated LCOE is 120.1 \$/MWh considering a real discount rate of 8 % and an operational lifetime of 30 years (EE Publishers, 2016; Department of Energy, 2019*a*).

The production costs of coal are assumed to increase annually by 2 % without considering inflation due to its high accessibility (Hernández-Moro and Martínez-Duart, 2013). Eskom reported a cost increase of 14.1 % per ton of coal in 2018, which resulted in a primary energy unit cost (ZAR/MWh) increase of 9.71 % between the financial years of 2017/18 and 2018/19 (Eskom, 2019). According to Eskom, this cost increase was mainly due to low coal stockpiles and the resulting conclusion of short-term contracts which amount to more than half of Eskom's coal supply by value. In comparison, the increase in primary energy unit cost of coal in the previous financial year was only 5.46 % (Eskom, 2018). Although a cost increase of the coal supply cannot be directly converted into an increase of the total cost of electricity from a coal power plant, an increase of 2 % per year for the total costs represents a conservative scenario.

Furthermore, the electricity generation from coal in South Africa is penalised with a carbon tax of 120 ZAR/tCO_2 (9.1 \$/tCO_2) since 2019 (SARS, 2020). This carbon tax increases annually by inflation plus 2 % per year until 2022 and by inflation thereafter. The emission factor of coal is assumed to be 0.8 tCO_2/MWh based on Kusile's expected carbon emission factor (Engineering News, 2013). The cost of coal for both scenarios is depicted in Figure 6.27 for both, with and without the carbon tax. Nevertheless, it can be seen that Eskom's cost estimate for Kusile is significantly lower than the latest projections from industry experts. Based on Eskom's data, CSP could reach grid parity with coal between 2023 and 2026 considering the carbon tax stays in place. Without the country's carbon tax, CSP's grid parity with coal would just be delayed by one year (between 2024 and 2027). However when looking at the more realistic cost projections for new built coal, MSPTPPs are already competitive with coal-fired plants, reaching grid parity with coal between 2019 and the end of 2021 (with or without carbon tax). Taking the weighted average LCOE as the representation of the cost evolution of CSP with the highest probability, electricity from CSP plants will be cheaper than from coal-fired power plants as early as 2020.

A third scenario based on the yearly average DAM trading price (denominated as *DAM yearly average* in the graphs) is also included for comparison. As already discussed in section 3.5.3, the yearly average DAM trading price in 2018 was 49.7 \$/MWh. Although the yearly average increased by 16 % per year over the last three years, it is assumed that a tariff escalation of 5 % per year is more likely. Based on these assumptions, the DAM trading price in 2050 is expected to be 236.7 \$/MWh (without inflation). This scenario is included as it is expected that CSP plants are able to operate in the spot market

as soon as the financial conditions in South Africa improve (i.e. low costs of debt and equity) since the financing costs make up a large percentage of the LCOE (as shown in section 3.4). A reduction in the costs of debt and equity can mainly be achieved through increased maturity of CSP plants resulting in a lower technological risk or through favourable long-term perspectives for lenders (Lilliestam and Pitz-Paal, 2018). However, a high foreign exchange risk and "an awareness of local issues" (Eberhard and Naude, 2016) can still pose a significant barrier to attract (especially international) lenders. Nevertheless under current financial conditions, MSPTPPs will only be able to effectively participate on the spot market between 2026 and 2029 due to the steep reduction in investment costs under a LR of 20 %. Although the scenario with a LR of 20 % is highly optimistic in the short-term, this time frame is supported by the continuous cost reductions of CSP in recent years, especially considering that the carbon tax and coal prices will likely increase in the future.

However, in order to also provide a more conservative outlook, Figure 6.28 depicts the LCOE development of MSPTPPs considering a LR of only 10 %. In this scenario, the LCOE of CSP decreases significantly slower and reaches a value between 80 $/MWh and 101.7 $/MWh in 2050 (range between 5th and 95th percentile). The weighted average of this scenario is 90.1 $/MWh. Comparing this range to Eskom's estimated cost of new build coal, CSP will reach grid parity with coal between 2027 and 2037. The more likely projected cost development of Eskom's new build coal power plants, however, will result in seeing higher costs of coal compared to CSP between 2019 and 2025. Consid-

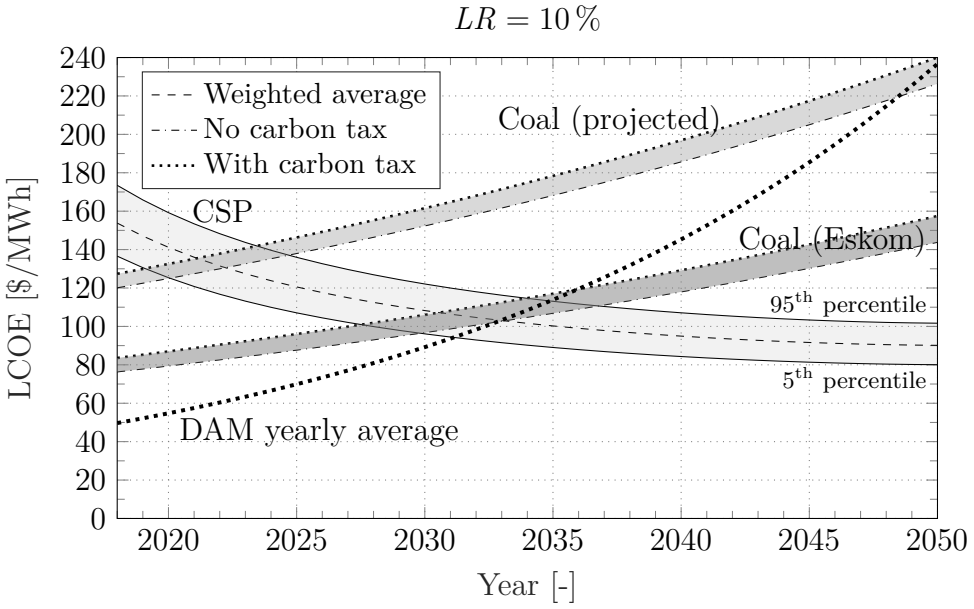

Figure 6.28: LCOE evolution of MSPTPPs in South Africa until 2050 ($LR = 10\,\%$, $d = 10\,\%$, $n_{op} = 30$ years) in comparison with new build coal-fired power plants with and without carbon tax (EE Publishers, 2016; Department of Energy, 2019*a*).

ering the weighted average as the most probable cost development, MSPTPPs will be competitive with new build coal in South Africa as early as 2021 under this conservative scenario with a LR of only 10 %. In terms of spot market participation under the DAM trading prices, it is estimated that CSP can be financially feasible between 2031 and 2035. However, an increased technological maturity level and more favourable loan conditions have the potential to significantly move up this time horizon.

The same approach has also been used for the forecast of the LCOE evolution by 2050 in Namibia. Under a LR of 20 %, the weighted average LCOE in 2050 is 49.3 $/MWh, whereas it is 89.5 $/MWh under a LR of 10 %. The results show that the difference in LCOE between South Africa and Namibia is less than 1 %. Therefore, the same time-frames for grid parity apply to both Namibia and South Africa.

In conclusion, it is evident that, depending on the LR of the global CSP deployment, MSPTPPs operating under baseload conditions will be cheaper than new-build coal-power plants in South Africa between 2020 and 2021. Furthermore, spot market participation is expected to be feasible between 2026 and 2035 but can be achieved earlier if favourable financial conditions allow a lower cost of debt and equity. Furthermore, long PPAs of at least 30 years should be considered by policy makers or off-takers (e.g. utilities like Eskom or NamPower) in order to increase the investor's confidence with long-term perspectives.

Chapter 7

Conclusions

MSPTPPs are a financially and technically suitable alternative to conventional PTPPs in Southern Africa. The main findings and contributions of this study are summarised in the following section. Lastly, an outlook for further work is provided at the end of this chapter.

7.1 Contribution

The first objective of this study was to develop a dynamic model of a MSPTPP, including two different approaches for the freeze protection strategy, i.e. one using a recirculation from the cold tank (FPS1) and one based on the same concept but with the addition of mixing warm fluid from the hot tank (FPS2). In order to reduce the required computational effort of the model, an empirical heat loss equation for the receiver tube was implemented and the governing partial differential equation were simplified by assuming a lumped capacitance model for the HTF and absorber tube. For the solar field model, a validation with measurement data from a molten salt test loop confirmed the viability of these assumptions with a relative error of the loop outlet temperature of between 0.69 % and 0.99 % for decreasing levels of discretisation. Similarly, the RMSE of the collector conversion efficiency was between 2.16 % and 3.05 % and the error of the thermal energy output of the loop varied between 1.54 % and 2.71 % for decreasing spatial resolutions. Thus, it was concluded that the developed model accurately reproduces the thermal behaviour of the solar collector, including the temperature response of the implemented FP model. The reduced computational effort for smaller levels of discretisation is traded in for a higher error but a feasible compromise between model error and simulation time was found to be a division of the SCA into 5 CVs.

To validate the entire power plant model, a validation for three different molten salts was carried out using SAM. The results showed that the model performed well with Solar Salt as HTF with a mean absolute error of 2.51 °C for the outlet temperature of the solar field. Using Hitec or Hitec XL resulted

in larger errors in the model, mainly due to the underestimation of the heat losses in the model as compared to SAM. Although heat losses from expansion bellows and support brackets were neglected in the model, a validation with measurement data showed that this assumption was justifiable. The validation with SAM also confirmed the accuracy of the model in terms of net power output with mean absolute errors between 1.48 MW and 3.68 MW (or 2.7 % and 6.7 % of the installed capacity of 55 MW_e), which was due to different start-up and shut-down approaches as well as the TES fill level. The latter was found to have the largest mismatch between the model and SAM which was a result of the different storage dispatch strategies and FP integrations. Nevertheless, it was concluded that the results obtained from the model were in good agreement with the results from SAM.

In order to also validate the location-tailored economic model, a comparison with data from two real power plants in South Africa was carried out. As these plants use thermal oil as HTF as well as different collectors and receivers, the model was adapted accordingly by implementing an indirect TES, the appropriate collectors and receivers as well as the fluid properties of thermal oil. The results showed that both the technical and financial performance indicators calculated by the model match the data from the real power plants with a maximum error for the LCOE of −5 % in the case of Bokpoort and −3.2 % for Kathu. Considering the LCOE as a reasonable measure for the overall technical and financial performance of a power plant, it was concluded that the model's accuracy is highly acceptable.

A sensitivity analysis was carried out to test the robustness of the model towards uncertainties of the input data and to identify the key technical and financial design parameters that lead to the best potential improvements in terms of the power plant's efficiency and profitability. It was found that using the FP approach that makes use of heat stored in the hot tank offers the largest potential of decreasing the plant's LCOE, where reserving 6 % of the hot tank fill level for FP yielded the best result. Other key parameters were found to be the gross turbine capacity, the solar multiple and the TES full load hours, where larger components offered the highest potential for LCOE reductions. In terms of operational parameter set points, the allowable inlet temperature of the hot tank, the live steam pressure and the FP temperature threshold were found to have the greatest effect on reducing the LCOE. Regarding the financial parameters, it was found that the IRR, the LCOE and the NPV of MSPTPPs are most sensitive to the PPA tariff, the debt interest rate and the economic lifetime of the power plant. Therefore, long PPA terms of up to 35 years in combination with debt interest rates below 12 % were recommended in order to significantly reduce the financing costs.

In order to combine the cost reduction potential of all design parameters from the sensitivity analysis, a multi-objective optimisation was carried out, minimising the CAPEX and maximising the IRR. First, it was shown that using Solar Salt as HTF yielded the lowest LCOEs in comparison to Hitec

and Hitec XL. Therefore, the latter two salt mixtures were disregarded from further analyses as they were outperformed by Solar Salt. Next, the effect of the two proposed freeze protection strategies, i.e. FPS1 and FPS2, on the power plant performance was investigated for baseload and two-tier tariff structures through a multi-objective optimisation. The results showed that FPS2 offered the most advantages in terms of electric energy requirement reduction and an overall increase in financial viability due to an increased efficiency of the power plants under both the baseload and two-tier tariff structure. Nevertheless, it was found that an electric FP system is necessary for both freeze protection strategies as they cannot completely eliminate the need for electric energy in order to keep the HTF temperature above the desired value at all times.

An analysis of the optimal power plant configurations and operational parameter set points for FPS2 showed that a combination of turbine capacities above 100 MW and a TES size of between 14 h and 16 h are recommended in order to minimise the LCOE when a baseload tariff is implemented. Furthermore, a FP temperature threshold between 260 °C and 270 °C and a mass flow rate between 4 kg/s and 6 kg/s are recommended for baseload operation. The required hot tank fill level reserved for FP under FPS2 should be limited to below 5 %. The minimum possible LCOE was found to be 108.9 $/MWh for this scenario. Under a two-tier tariff structure, it was found that the recommended turbine capacity is below 100 MW in combination with a TES capacity of between 13 h and 20 h in order to achieve a minimum LCOE of 125 $/MWh. A FP temperature threshold of 265 °C to 270 °C is recommended for these power plant configurations in combination with a solar field standby mass flow rate of between 4 kg/s and 6 kg/s. Lastly, the hot tank fill level reserved for FP can be lowered to below 1 % due to the large storage capacities.

Furthermore, analysing the results of the multi-objective optimisation of power plants under the baseload and two-tier tariff structure using FPS2 showed that a significant reduction of the LCOE is possible for MSPTPPs in comparison to currently operational CSP plants in South Africa. However, a baseload tariff structure was recommended in order to reduce the levelised PPA tariff payable by the government or the off-taking utility. It was found that the minimum required PPA tariff for an economically feasible power plant under current financial conditions is 119.4 $/MWh in South Africa and 115.8 $/MWh in Namibia for a 20 year PPA term. Assuming reduced financing costs and a longer PPA of 35 years yielded a minimum required PPA tariff of 50.4 $/MWh in South Africa, with the best performing power plant combinations comprising a gross turbine capacity of between 85 MW and 240 MW in combination with a relatively large TES of 14 h to 20 h. This tariff is well below the tariff cap for renewable energy projects of 60.9 $/MWh proposed by Eskom in 2017.

Since Namibia does currently not have any feed-in-tariffs in place, the possibility of a participation in a spot market environment was assessed through a multi-objective optimisation assuming reduced financing costs and an economic lifetime of 35 years. Using the hourly DAM trading prices of 2018, it

was shown that installed turbine capacities between 125 MW and 250 MW in combination with a TES capacity between 14 h and 23 h are required in order to bridge periods of lower prices, i.e. typically during night-time and especially on Sundays. However, these plants all have a CAPEX of above 850 mil. $ which requires a high risk-adversity from the developer as the optimal financing structure of these plants determined by the algorithm required a share of equity of more than 65 %. The LCOE, under these favourable financing conditions, was found to be between 58.9 $/MWh and 65.6 $/MWh for plants with a NPV greater than zero.

Using the results from the multi-objective optimisation for baseload power plants under current financial conditions, LCOE projections until 2050 were made, assuming a LR of 10 % and 20 %. In South Africa, a LCOE of 90.1 $/MWh and 49.6 $/MWh is expected by 2050 for the respective scenarios. The LCOE projections for Namibia forecast an LCOE in 2050 of 89.5 $/MWh and 49.3 $/MWh, respectively. For the more likely scenario with a LR of 20 %, grid parity of MSPTPPs with projected coal-fired power stations was found to be possible between 2019 and the end of 2021 in both countries. Additionally, a potential spot market participation of CSP plants in Southern Africa was found to be possible between 2026 and 2029 assuming an annual escalation of the DAM trading prices by 5 %.

Lastly, the MSPTPP model developed in this study has also been used for the validation of the developed power plant model for Solar Salt, Hitec and Hitec XL as HTF in Pan *et al.* (2018*a*) and for performance assessments and comparisons with conventional PTPPs and solar towers in Pan *et al.* (2018*b*) and Pan *et al.* (2019).

7.2 Further Work

The power plant model presented in this study provides a foundation for further analyses in terms of technical and economic feasibility of MSPTPPs. To further improve the accuracy of the model, an adaptation of the empirical heat loss equation is recommended that also includes the effects of ambient conditions (e.g. air temperature and wind speed) on the receiver heat loss. Likewise, considering heat losses from expansion bellows and support brackets will lead to a more accurate calculation of the receiver heat losses. Although the method of lumping the thermal capacitance of the HTF and the absorber tube together resulted in acceptable results for the scope of this study, using a separate partial differential equation for the absorber tube wall is recommended in order to obtain a more flexible model that can also be used with other receivers. If empirical heat loss equations for other types of receivers are available, these equations can easily be implemented in the receiver model. However since this type of data is typically not readily available for the majority of receivers, an implementation of the iterative calculation of the receiver

heat losses through conduction, convection and radiation heat transfer is recommended, in addition to also including the calculation of the glass envelope surface temperatures. The resulting increase of the computational effort and simulation time during multi-objective optimisations can be off-set by an integration of multi-core parallel processing of multiple simulations at once, either on a local machine or through a high performance computing cluster.

For the proposed freeze protection strategy making use of the thermal energy stored in the hot tank, the implementation of an adaptive control of the hot tank level reserved for FP based on forecasting is recommended. By doing so, the daily fill level reserved for FP can be controlled according to the predicted weather conditions of the following days, freeing up more of the TES's storage capacity during good weather periods for power production and reserving more for FP purposes in the case of prolonged bad weather periods. A possible elimination of the required electric FP system through this fill level control should then be investigated.

A water consumption model considering water usage from the ACC, steam cycle makeup, blowdown quench and mirror washing has also been implemented in this study but was beyond the scope of the analysis. Therefore, a multi-objective optimisation including the minimisation of water consumption in MSPTPPs shall be conducted in a future study. Similarly, an analysis regarding the minimisation of turbine stops is recommended to reduce the need for maintenance. The developed model can also be used for the assessment of different tariff structures and financing conditions as well as their effects on the power plants' technical and economic performance. This can, for example, be used by developers or policy makers alike to determine a plant's required bidding PPA tariff.

Lastly, an analysis of a combined power production of CSP and PV, including technical and economic optimisations through the multi-objective optimisation process, is recommended in order to further drive down costs. This can be in the form of a PV-assisted CSP plant, where PV is used to cover the parasitic consumption of the CSP plant, or in the form of a combined baseload power plant, where a PV plant's day-time generation enables the CSP plant to shift its power generation into the night-time (as for example proposed by Pan and Dinter, 2017).

Appendices

Appendix A

Meteorological Data

The following section describes, in brief, the meteorological data sets for the two locations selected for this study, namely Upington (South Africa) and Kokerboom (Namibia). Both data sets were obtained in the form of a *typical meteorological year* (TMY3).

A.1 Upington (South Africa)

The meteorological data for Upington, located in the Northern Cape Province in the north west of South Africa, was obtained from *Meteonorm* (Meteotest, 2014). This data is based on measurement data from a weather station in Upington. Figure A.1 shows the DNI, air temperature and wind speed for the

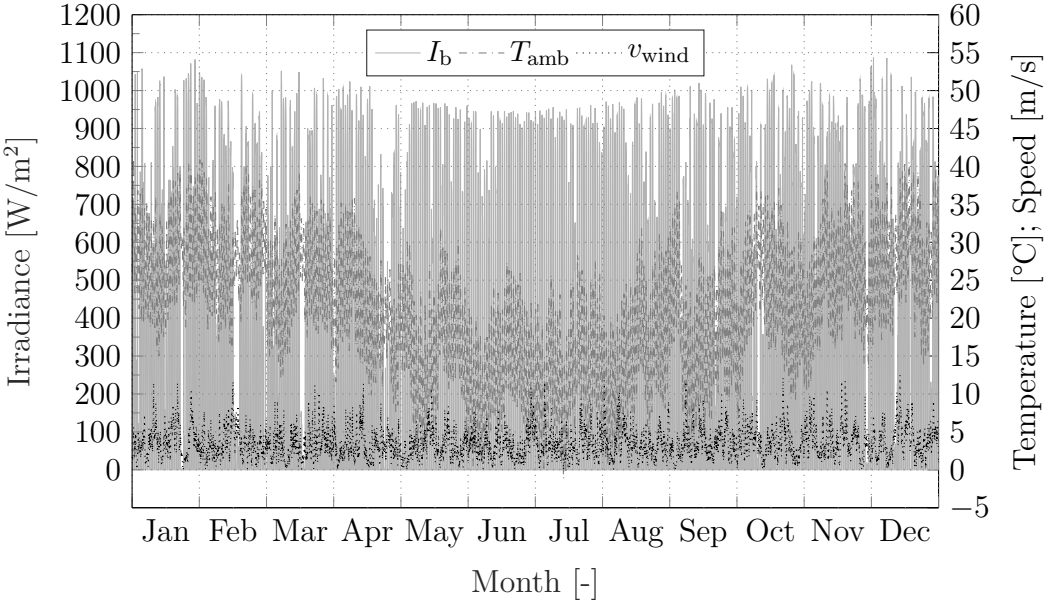

Figure A.1: Meteorological data for Upington, South Africa (TMY3).

site. The average air temperature is 21.4 °C and ranges from a low of −1.2 °C to a maximum of 41 °C. The uncertainty of the air temperature is 0.3 °C. The annual direct normal irradiation is 2863 kW h/m^2 with an uncertainty of 6 %. The peak irradiance is 1087 W/m^2. The wind speed lies in the range of 0.1 m/s to 12.5 m/s with an average wind speed of 3.5 m/s.

A.2 Kokerboom (Namibia)

The meteorological data for Kokerboom, located in the Karas Region near Keetmanshoop in the south east of Namibia, was obtained from *NamPower* (NamPower, 2017), which has been prepared by *CSP Services* as part of a bankable solar resource assessment of six sites in Namibia (CSP Services, 2017). The meteorological data for the chosen site has a probability of 90 % that in any given year the meteorological data will be accurate for the site (P90). Figure A.2 shows the DNI, air temperature and wind speed for the site. The average air temperature is 19.9 °C and ranges from a low of −1.2 °C to a maximum of 39.6 °C. The annual direct normal irradiation is 2905 kW h/m^2. The peak irradiance is 1105 W/m^2. The wind speed lies in the range of 0.1 m/s to 10.8 m/s with an average wind speed of 3.1 m/s.

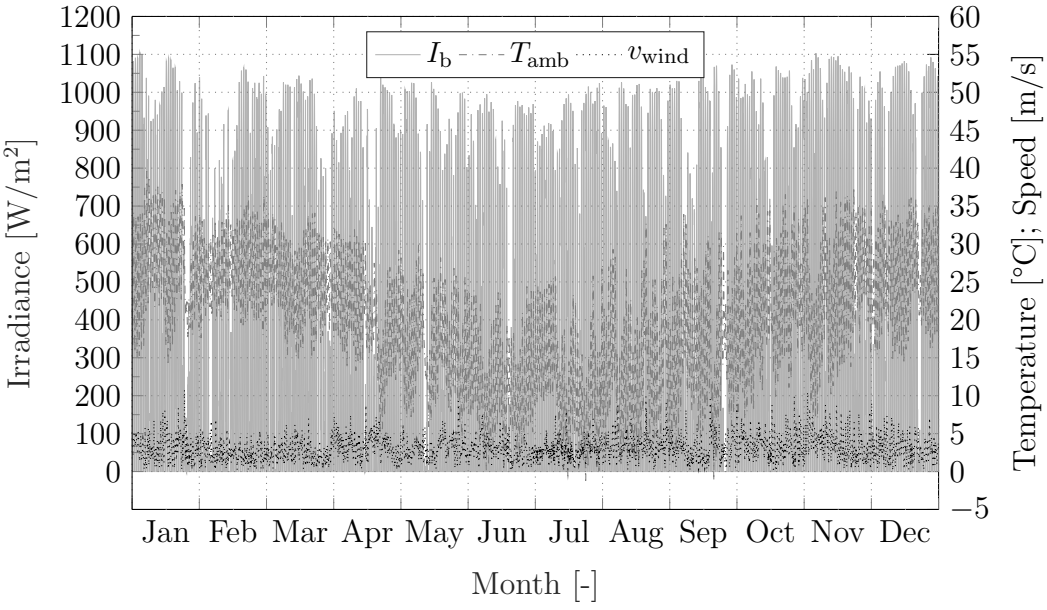

Figure A.2: Meteorological data for Kokerboom, Namibia (TMY3).

Appendix B

Solar Time and Solar Geometry

The following sections describe the methods and computations used to obtain the solar time which is necessary to calculate the solar angles at any given location. The main inputs for these calculations are the location's longitude, latitude and time zone. Based on this information, the solar angles at the location can be calculated for each hour of the year.

B.1 Solar Time

In order to calculate all necessary sun-angles for the estimation of the incident solar radiation on the receivers, it is essential to convert the local time at the investigated location to the solar time. Two correction factors are applied to the local time, i.e. the longitude correction LC and a correction from the equation of time EOT. All equations are based on Duffie and Beckman (2006) (unless otherwise stated) and use degrees.

To correct the difference between the plant's longitude ψ_{loc} and the standard meridian ψ_{st} of the local time zone, Eq. (B.1) gives the longitude correction LC in minutes

$$LC = 4(\psi_{\text{st}} - \psi_{\text{loc}}), \tag{B.1}$$

where ψ_{loc} is the longitude of the location in question in degrees west of the time zone UTC0 (Coordinated Universal Time), with $0° < \psi < 360°$. The standard meridian ψ_{st} is a function of the time zone TZ and can be found with

$$\psi_{\text{st}} = \begin{cases} |TZ| \times 15°, & \text{for } TZ \leq 0 \\ (24 - TZ) \times 15°, & \text{for } TZ > 0, \end{cases} \tag{B.2}$$

where $TZ = 0$ is UTC+0. The second correction accounts for the perturbations in the earth's rotation and is given in minutes by the equation of time

$$\begin{aligned} EOT = 229.2\,[&0.000075 + 0.001868\cos(B) - 0.032077\sin(B) \\ &- 0.0141615\cos(2B) - 0.04089\sin(2B)], \end{aligned} \tag{B.3}$$

where B is given for the n^{th} day of the year by

$$B = (n-1)\frac{360}{365}. \tag{B.4}$$

Finally, the solar time can be calculated by converting the two correction factors from minutes to the decimal time format and adding them to the local time t_{loc} in decimal format:

$$t_{\text{sol}} = t_{\text{loc}} + \frac{EOT}{60} + \frac{LC}{60} + D. \tag{B.5}$$

The parameter D simply accounts for daylight savings. It adjusts the solar time by one hour in case the location in question is currently experiencing daylight saving time or not:

$$D = \begin{cases} 1, & \text{for daylight saving in effect} \\ 0, & \text{for no daylight saving in effect (default).} \end{cases} \tag{B.6}$$

B.2 Solar Angles

The DNI is measured by tracking the sun about two axes whereas a parabolic trough field can only track about one axis. Hence, the angle between the solar beam radiation and the aperture normal of the tracking surface — which forms a plane with the tracking axis as depicted in Figure B.1a — needs to be calculated. The incidence angle θ for a solar field tracking about a north-south oriented axis after Stine and Geyer (2001) is:

$$\theta = \cos^{-1}\sqrt{1-\cos^2(\theta_{\text{e}})\cos^2(\gamma)}. \tag{B.7}$$

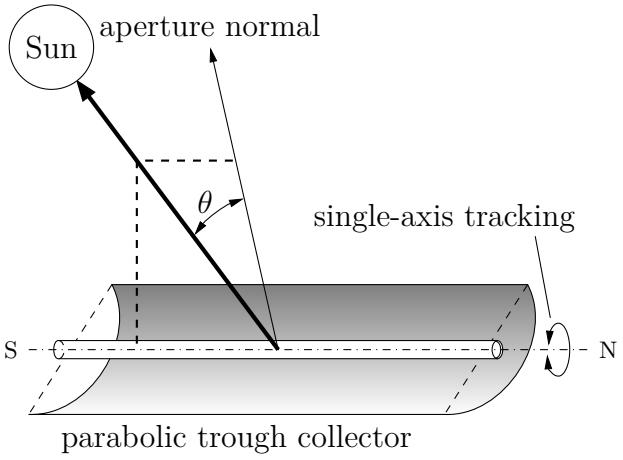

(a) Incidence angle for a single-axis tracking surface.

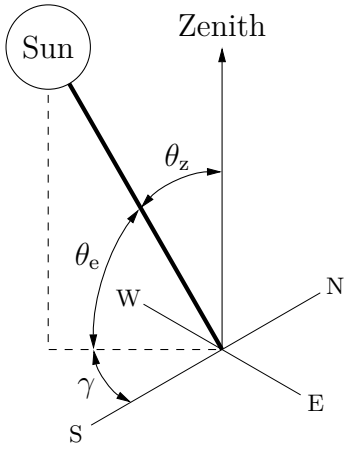

(b) Solar zenith angle, solar elevation angle and solar azimuth angle for a horizontal surface.

Figure B.1: Solar angles for (a) a single-axis tracking surface and (b) a horizontal surface in the northern hemisphere.

To determine this angle, the sun's exact position relative to the location of the solar field needs to be calculated. Eq. (B.7) requires the solar elevation angle θ_e and solar azimuth angle γ, which are indicated in Figure B.1b. To find the solar elevation angle, it is first necessary to calculate the solar zenith angle θ_z which represents the angle between the line to the sun and the line perpendicular to the horizontal surface. The solar zenith angle is

$$\theta_z = \cos^{-1}\left[\cos(\phi)\cos(\delta)\cos(\omega) + \sin(\phi)\sin(\delta)\right], \tag{B.8}$$

where ϕ is the latitude of the location north or south of the equator with north being positive and $-90° \leq \phi \leq 90°$ and ω is the hour angle, which can be converted from the solar time with

$$\omega = 15°\,(t_{sol} - 12)\,. \tag{B.9}$$

The declination angle δ can be calculated for each day n of a year to account for the tilt of the Earth's axis:

$$\delta = 23.45° \sin\left(360\frac{284+n}{365}\right). \tag{B.10}$$

Finally, the solar elevation angle θ_e can simply be determined from

$$\theta_e = 90° - \theta_z. \tag{B.11}$$

The last information needed to calculate the incidence angle θ is the angular displacement of the projection of the solar beam irradiance on the horizontal plane from due south (see Figure B.1b). This is given by the solar azimuth angle γ as:

$$\gamma = \text{sign}(\omega)\left|\cos^{-1}\left(\frac{\cos(\theta_z)\sin(\phi) - \sin(\delta)}{\sin(\theta_z)\cos(\phi)}\right)\right|. \tag{B.12}$$

Appendix C

HTF Properties

The heat transfer fluids considered in this study are three molten salt mixtures, namely *Solar Salt*, *Hitec®* and *Hitec® XL*, as well as the conventional thermal oil *Therminol® VP-1*. All fluid properties are a function of the bulk fluid temperature in [°C], assuming that the fluid is homogeneously mixed. The temperature-dependent correlations for the thermo-physical fluid properties (i.e. density, specific heat capacity, thermal conductivity and viscosity) of each HTF are listed below.

C.1 Solar Salt

Thermo-physical correlations for Solar Salt have been taken from SQM (2017):

$$\rho = 2090 - 0636\,T, \qquad [\mathrm{kg/m^3}] \qquad \text{(C.1)}$$

$$c_p = 1443 + 0.172\,T, \qquad [\mathrm{J/(kg\,K)}] \qquad \text{(C.2)}$$

$$k = 0.443 + 1.9 \times 10^{-4}\,T, \qquad [\mathrm{W/(m\,K)}] \qquad \text{(C.3)}$$

$$\mu = 2.2714 \times 10^{-2} - 1.2 \times 10^{-4}\,T + 2.281 \times 10^{-7}\,T^2 - 1.474 \times 10^{-10}\,T^3. \qquad [\mathrm{Pa\,s}] \qquad \text{(C.4)}$$

C.2 Hitec® Heat Transfer Salt

Thermo-physical correlations for Hitec have been taken from Yang and Garimella (2010) based on measurement data as reported in Coastal Chemical Co. (n.d.):

$$\rho = 1938 - 0.732\,(T - 200)\,, \qquad [\mathrm{kg/m^3}] \qquad \text{(C.5)}$$

$$c_p = 1561.7, \qquad [\mathrm{J/(kg\,K)}] \qquad \text{(C.6)}$$

$$k = 0.421 - 6.5 \times 10^{-4}\,(T - 260)\,, \qquad [\mathrm{W/(m\,K)}] \qquad \text{(C.7)}$$

$$\mu = e^{-4.343 - 2.0143(\ln T - 5.011)}. \qquad [\mathrm{Pa\,s}] \qquad \text{(C.8)}$$

C.3 Hitec® XL

Thermo-physical correlations for Hitec XL have been taken from NREL (2013*b*):

$$\rho = 2240 - 0.8266\,T, \qquad [\mathrm{kg/m^3}] \quad \text{(C.9)}$$

$$c_p = 1536 - 0.2624\,T - 1.139 \times 10^{-4}\,T^2, \qquad [\mathrm{J/(kg\,K)}] \quad \text{(C.10)}$$

$$k = 0.519, \qquad [\mathrm{W/(m\,K)}] \quad \text{(C.11)}$$

$$\mu = 1.3695 \times 10^{6}\,T^{-3.36369}. \qquad [\mathrm{Pa\,s}] \quad \text{(C.12)}$$

C.4 Therminol® VP-1

Thermo-physical correlations for Therminol VP-1 have been taken from Eastman (2019):

$$\rho = 1083.25 - 0.90797\,T + 7.8116 \times 10^{-4}\,T^2 - 2.367 \times 10^{-6}\,T^3, \qquad [\mathrm{kg/m^3}] \quad \text{(C.13)}$$

$$c_p = 1498 + 2.414\,T + 5.9591 \times 10^{-3}\,T^2 - 2.9879 \times 10^{-5}\,T^3 + 4.4172 \times 10^{-8}\,T^4, \qquad [\mathrm{J/(kg\,K)}] \quad \text{(C.14)}$$

$$k = 0.137743 - 8.19477 \times 10^{-5}\,T - 1.92257 \times 10^{-7}\,T^2 + 2.5034 \times 10^{-11}\,T^3 - 7.2974 \times 10^{-15}\,T^4, \qquad [\mathrm{W/(m\,K)}] \quad \text{(C.15)}$$

$$\mu = \rho\, e^{\left(\frac{544.149}{T+114.43} - 2.59578\right)}. \qquad [\mathrm{Pa\,s}] \quad \text{(C.16)}$$

Appendix D

Solar Field Piping Layout and Sizing

For the solar field, an H-layout with four solar field subsections ($N_{\mathrm{SF,sec}} = 4$) is assumed (see Figure 2.9 for an overview of the solar field layout). In order to size the runner and header pipes, an allowable flow velocity range of the fluid is used with which the pipe diameters are calculated. A minimum flow velocity v_{min} of 1 m/s and a maximum flow velocity v_{max} of 3 m/s are assumed. This method requires the nominal mass flow rate $\dot{m}_{\mathrm{nom}}$ of the solar field, which is calculated based on the required thermal power of the power cycle ($\dot{Q}_{\mathrm{PB,th}}$) for a given solar multiple with

$$\dot{m}_{\mathrm{nom}} = \frac{\dot{Q}_{\mathrm{PB,th}} SM}{c_{p,\mathrm{avg}}(T_{\mathrm{SF,out}} - T_{\mathrm{SF,in}})}. \tag{D.1}$$

$T_{\mathrm{SF,in}}$ is the cold tank outlet temperature at the inlet of the cold runner and $T_{\mathrm{SF,out}}$ is the solar field outlet temperature at the hot runner outlet. As the headers and runners have a significant steel mass and contain a considerable amount of HTF, the thermal inertia of the runner and header piping also needs to be accounted for. Hence, in combining the hot headers and runners into one node, the outlet temperature of the solar field ($T_{\mathrm{SF,out}}$) can be calculated with

$$T_{\mathrm{SF,out}} = (T_{\mathrm{SF,out,0}} - T_{\mathrm{loop,out}}) \exp\left(-\frac{\dot{m}_{\mathrm{HTF}}}{\overline{V}_{\mathrm{h}} \rho_{\mathrm{HTF,h}} + m_{\mathrm{run,hdr,h}}} \Delta t\right) + T_{\mathrm{loop,out}}, \tag{D.2}$$

as adapted from Wagner and Gilman (2011). Here, $T_{\mathrm{SF,out,0}}$ is the solar field outlet temperate from the previous time step and $\dot{m}_{\mathrm{HTF}}$ is the mass flow rate in the current time step. The average fluid volume in the hot headers and runners $\overline{V}_{\mathrm{h}}$ is multiplied by the hot fluid density $\rho_{\mathrm{HTF,h}}$ to obtain the mass of the HTF in the pipes. $m_{\mathrm{run,hdr,h}}$ represents the steel mass of the hot header and runner piping and Δt is simply the length of the time step. $T_{\mathrm{loop,out}}$ is the fluid temperature at the outlet of the loop adjusted for heat losses in the cross-over piping and is calculated according to Eq. (2.45) using the outlet

temperature of the last SCA in the loop (T_{out}) with

$$T_{\text{loop,out}} = T_{\text{out}} - \frac{h_{\text{piping}} A_{\text{piping}} \left(T_{\text{out}} - T_{\text{amb}}\right)}{\dot{m}_{\text{HTF}} c_{p,\text{HTF}}}. \tag{D.3}$$

Likewise, the loop inlet temperature (T_{in}) adjusted to account for the thermal inertia of the cold runner and header can be calculated with

$$T_{\text{loop,in}} = \left(T_{\text{loop,in,0}} - T_{\text{SF,in}}\right) \exp\left(-\frac{\dot{m}_{\text{HTF}}}{\overline{V}_{\text{c}} \rho_{\text{HTF,c}} + m_{\text{run,hdr,c}}} \Delta t\right) + T_{\text{SF,in}}. \tag{D.4}$$

Assuming four solar field subsections, the runner and header mass flow rates are

$$\dot{m}_{\text{run}} = \frac{\dot{m}_{\text{nom}}}{2} \tag{D.5}$$

$$\dot{m}_{\text{hdr}} = \frac{\dot{m}_{\text{nom}}}{N_{\text{SF,sec}}} \tag{D.6}$$

and the diameter of the runners can then be calculated with

$$d_{\text{run}} = \sqrt{\frac{4\dot{m}_{\text{run}}}{\rho_{\text{HTF,avg}} v_{\text{max}} \pi}}. \tag{D.7}$$

The calculation of the header diameter follows the same principle but needs to take into account that the header pipe diameter should be continuously reduced after extraction of HTF by the loops in order to obtain a uniform flow velocity in each loop. Furthermore, using smaller piping sizes ultimately also reduces the costs of the pipes. However, in order to avoid scaling down the header after each loop extraction (which would significantly increase the cost of the pipe assembly) the earlier defined flow velocity range is used to only reduce the header diameter whenever the flow velocity falls outside the specified limits. Figure D.1 illustrates this concept, where the header is divided into header sections i of equal diameter as part of each header group j. The total amount of header groups N_{grp} is limited to 10. The number of divisions $N_{\text{div},j}$ with equal diameter in each header group is calculated with

$$N_{\text{div},j} = \left\lfloor \frac{\dot{m}_{\text{sec},j,0} - \dot{m}_{\text{min},j}}{2\dot{m}_{\text{loop}}} \right\rfloor, \quad \text{for } j{=}1{,}\min(N_{\text{grp}}{,}10), \tag{D.8}$$

where $\dot{m}_{\text{sec},j,0}$ is the mass flow rate at the inlet of each header group j and $\dot{m}_{\text{loop}}$ is the maximum loop mass flow rate obtained with

$$\dot{m}_{\text{loop}} = \frac{\dot{m}_{\text{max}}}{N_{\text{loops}}}. \tag{D.9}$$

The total number of header sections in a single header is given by the number of loops N_{loops} divided by the number of solar field subsections $N_{\text{SF,sec}}$ with

$$N_{\text{sec}} = \left\lceil \frac{N_{\text{loops}}}{2N_{\text{SF,sec}}} \right\rceil. \tag{D.10}$$

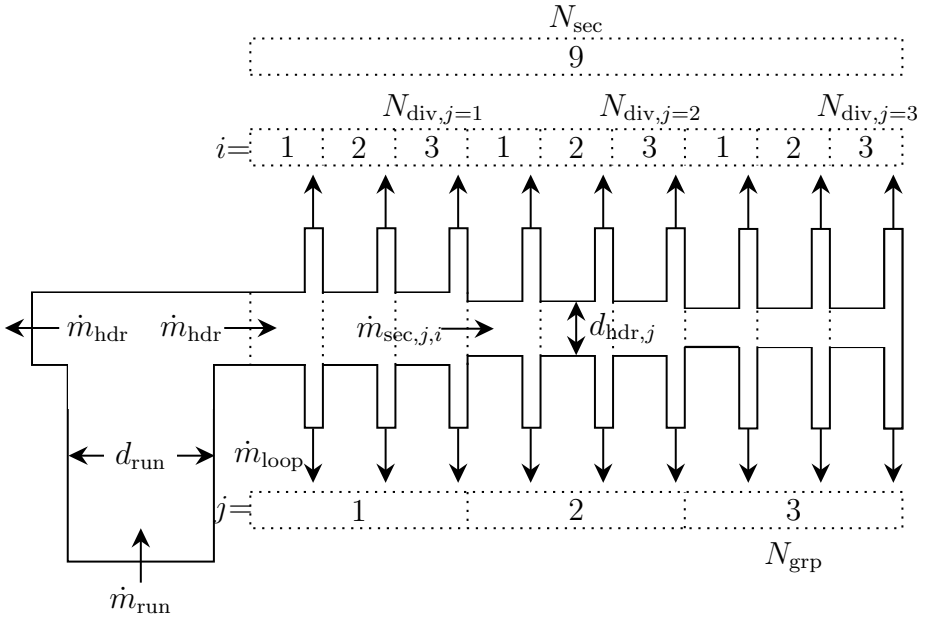

Figure D.1: Schematic header pipe design with decreasing pipe diameters $d_{\text{hdr},j}$ for $N_{\text{div},j}$ header sections per group N_{grp} (adapted from Wagner and Gilman, 2011).

The mass flow rate for each header section ($\dot{m}_{\text{sec},j,i}$) can be calculated by subtracting the mass flow rate of two loops from the mass flow rate of the previous header section as the HTF is diverted into the loops:

$$\dot{m}_{\text{sec},j,i} = \dot{m}_{\text{sec},j,i-1} - 2\dot{m}_{\text{loop}}, \quad \text{for } i{=}1{,}N_{\text{div},j}, \tag{D.11}$$

$\dot{m}_{\text{min},j}$ in Eq.(D.8) is the minimum allowable mass flow rate in each header group j based on the lower flow velocity limit v_{min} and is calculated with

$$\dot{m}_{\text{min},j} = \rho_{\text{HTF,avg}} v_{\text{min}} \pi \frac{d_{\text{hdr},j}^2}{4}. \tag{D.12}$$

Finally, the header diameter $d_{\text{hdr},j}$ of each header group can be calculated based on the header mass flow rate $\dot{m}_{\text{sec},j,0}$ at the inlet of each header group j:

$$d_{\text{hdr},j} = \sqrt{\frac{4\dot{m}_{\text{sec},j,0}}{\rho_{\text{HTF,avg}} v_{\text{max}} \pi}}. \tag{D.13}$$

The diameter of the first header section is simply calculated based on the header inlet mass flow rate $\dot{m}_{\text{sec},1,0}$ coming from the runner, where

$$\dot{m}_{\text{sec},1,0} = \dot{m}_{\text{hdr}}. \tag{D.14}$$

However since pipes are only available in certain diameters and thicknesses, the actual pipe diameter is chosen based on pipe schedules from Wagner and Gilman (2011), who have selected the appropriate wall thickness and schedule to meet a pressure rating of 25 bar. This is done by selecting the smallest diameter that does not violate the flow velocity limits.

Appendix E

Pressure Drop Model

The pressure drop of the solar field is calculated based on the approach presented by Wagner and Gilman (2011) for the three piping subcategories: runners, headers and loops. Moreover, the pressure drop of pipe fittings (i.e. expansions/contractions, elbows, valves, weldolets and flexible hoses) is also taken into account. Figure E.1 shows the momentum balance of a pipe of length L_{pipe} with a mass flow rate of $\dot{m}_{\text{HTF}}$. Considering the variation of the flow velocity along the flow path due to changes of the cross-sectional area or fluid density, the pressure force F_{p} acting on the fluid, the friction force F_{f} and the gravitational force F_{g}, the momentum balance can be written as

$$\frac{\mathrm{d}}{\mathrm{d}t}\left(\dot{m}_{\text{HTF}} L_{\text{pipe}}\right) = v_1^2 \rho_1 A_1 - v_2^2 \rho_2 A_2 - F_{\text{p}} - F_{\text{f}} - F_{\text{g}}. \tag{E.1}$$

However, as the main focus of this study is the thermal performance of the solar field, the consideration of the pressure wave propagations is not of particular interest. Hence, assuming fully developed flow, Eq. (E.1) can be reduced to a steady-state equation. Furthermore, neglecting the flow velocity variations and gravitational force yields

$$F_{\text{p}} = -F_{\text{f}}. \tag{E.2}$$

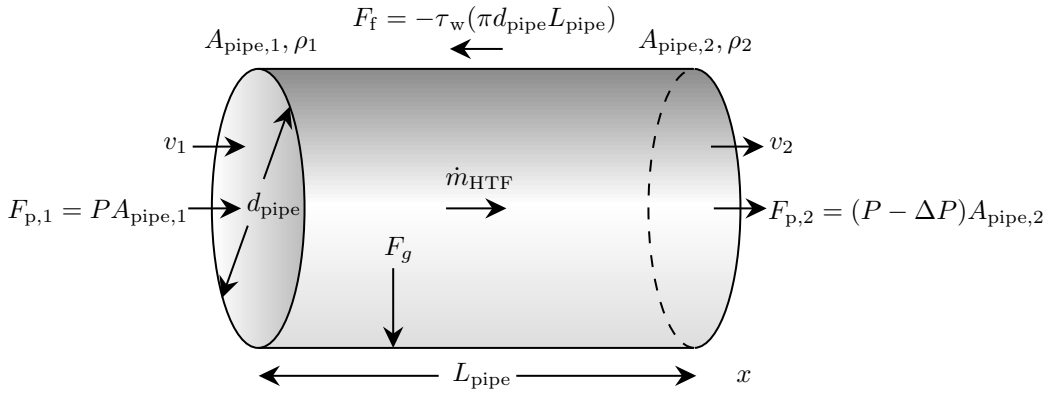

Figure E.1: Momentum balance on a pipe of length L_{pipe}.

Therefore, the difference in pressure force between two neighbouring control volumes equals the friction force. Assuming a constant cross-sectional area A_{pipe} along the entire pipe, the pressure force can be calculated with

$$\begin{aligned} F_{\text{p}} &= F_{\text{p,1}} - F_{\text{p,2}} \\ F_{\text{p}} &= PA_{\text{pipe}} - (P - \Delta P)\, A_{\text{pipe}} \\ F_{\text{p}} &= \Delta P A_{\text{pipe}} \\ F_{\text{p}} &= \Delta P \frac{\pi d_{\text{pipe}}^2}{4}, \end{aligned} \tag{E.3}$$

where ΔP is the pressure drop over the control volume. Likewise, the friction force due to shear stress along the pipe is given by

$$\begin{aligned} F_{\text{f}} &= -\tau_{\text{w}} A_{\text{pipe}} \\ F_{\text{f}} &= -\tau_{\text{w}} \pi d_{\text{pipe}} L_{\text{pipe}}, \end{aligned} \tag{E.4}$$

where τ_{w} is the wall shear stress. Note that the wall shear stress exerts a drag on the fluid and thus works in negative x direction. Substituting Eqs. (E.3) and (E.4) into Eq. (E.2) yields

$$\Delta P \frac{\pi d_{\text{pipe}}^2}{4} = \tau_{\text{w}} \pi d_{\text{pipe}} L_{\text{pipe}}. \tag{E.5}$$

Solving for τ_{w} gives

$$\tau_{\text{w}} = \frac{\Delta P d_{\text{pipe}}}{4 L_{\text{pipe}}}. \tag{E.6}$$

Now, momentum transfer to a wall can be expressed as the dimensionless *skin friction coefficient* C_{f} with

$$C_{\text{f}} = \frac{\tau_{\text{w}}}{\frac{1}{2}\rho v^2}, \tag{E.7}$$

which is simply the ratio between wall shear stress and inertial force of the flow (kinetic energy of the fluid per unit volume of the fluid). Plugging Eq. (E.6) into Eq. (E.7) yields

$$C_{\text{f}} = \frac{\Delta P d_{\text{pipe}}}{2\rho v^2 L_{\text{pipe}}}. \tag{E.8}$$

For hydrodynamically fully developed flow, the skin friction coefficient is related to the *Darcy friction factor* f as

$$f = 4C_{\text{f}}. \tag{E.9}$$

Hence, Eq. (E.8) can be rewritten and solved for the pressure drop as

$$\Delta P_{\text{pipe}} = \frac{f v^2 \rho L_{\text{pipe}}}{2 d_{\text{pipe}}}, \tag{E.10}$$

which is the *Darcy-Weisbach equation* representing the pressure drop across a pipe. The Darcy friction factor for smooth pipes is obtained with (Mills, 1999)

$$f = \begin{cases} \dfrac{64}{Re}, & \text{for } Re < 2300, \quad \text{(E.11)} \\ (0.79 \ln Re - 1.64)^{-2}, & \text{for } 10^4 < Re < 5 \times 10^6, \quad \text{(E.12)} \end{cases}$$

where the Reynolds number is calculated with Eq. (2.54). It has to be noted that large Reynolds numbers are generally more common in PTPPs due to the prevalence of turbulent flow during on-sun operation. As already mentioned in section 2.3.6, only Hitec XL reaches Reynolds numbers below 10^4 at fluid temperatures below 240 °C at its minimum mass flow rate. Since this scenario is rarely the case, Eq. (E.12) is predominately used during the course of a simulation and is also used as an approximation for the transitional flow regime.

Due to the assumption of constant mass flow in each control volume from Eq. (2.28) and temperature-dependent density changes across a loop, the bulk flow velocity v_i in each CV has to be calculated to determine the local Reynolds number with Eq. (2.54). However since the longitudinal temperature distribution across a loop, header or runner can be assumed to be nearly linear, the pressure drop in each piping subsection is evaluated with the average fluid velocity v across the whole pipe instead. Thus,

$$v = \frac{4\dot{m}_{\text{eval}}}{\rho \pi d_{\text{pipe}}^2}, \quad \text{(E.13)}$$

where $\dot{m}_{\text{eval}}$ and d_{pipe} are the evaluation mass flow rate and diameter of the respective piping subsection as per Table E.1. Likewise, the density ρ is a function of the evaluation temperature T_{eval}. In the case of the loop piping, the evaluation temperature is the average loop temperature T_{avg} that is obtained with

$$T_{\text{avg}} = \frac{T_{\text{loop,in}} + T_{\text{loop,out}}}{2}. \quad \text{(E.14)}$$

Table E.1 provides the length and diameter of each piping subsection required for Eq. (E.10) and (E.13) as well as the respective mass flow rate and temperature at which fluid properties are evaluated. The diameters and mass flow rates have been introduced in section D. The length of each piping subsection is obtained with Eqs. (E.15) to (E.19). The length of a loop is obtained by summing up the length of each collector (L_{coll}) and the distance between each collector ($L_{\text{SCA,gap}}$) plus the row spacing L_{spacing} and an additional 40 m for the interconnecting piping:

$$L_{\text{loop}} = 40\,\text{m} + L_{\text{spacing}} + \sum_{i=1}^{N_{\text{SCA}}} \left(L_{\text{coll}} + L_{\text{SCA,gap}} \right). \quad \text{(E.15)}$$

The base length $L_{\text{hdr,base}}$ of the header piping (which represents the direct distance between the runner outlet and the inlet to the last loop) is obtained

Table E.1: Pipe parameters and number of fittings N_{fit} per fitting component $N_{\text{fit,comp}}$ in each piping subsection (loop, header and runner) for the pressure drop calculation. The pressure drop in each piping subcategory is evaluated using the respective pipe length L_{pipe} and diameter d_{pipe} as well as the mass flow rate $\dot{m}_{\text{eval}}$ and temperature T_{eval} in the pipe (adapted from Wagner and Gilman, 2011).

Item	Loop	Header		Runner		K
		Hot	Cold	Hot	Cold	
Pipe parameters						
Pipe length (L_{pipe})	L_{loop}	L_{hdr}	L_{hdr}	L_{run}	L_{run}	-
Pipe diameter (d_{pipe})	d_2	$d_{\text{hdr},j}$	$d_{\text{hdr},j}$	d_{run}	d_{run}	-
Mass flow rate ($\dot{m}_{\text{eval}}$)	$\dot{m}_{\text{loop}}$	$\dot{m}_{\text{hdr}}$	$\dot{m}_{\text{hdr}}$	$\dot{m}_{\text{run}}$	$\dot{m}_{\text{run}}$	-
Temperature (T_{eval})	T_{avg}	$T_{\text{SF,out}}$	$T_{\text{SF,in}}$	$T_{\text{SF,out}}$	$T_{\text{SF,in}}$	-
Header expansions/contractions						
Expansions	0	$N_{\text{grp}}-1$	0	0	0	0.5
Contractions	0	0	$N_{\text{grp}}-1$	0	0	0.5
Fitting components			N_{fit}			
Standard elbows	12	0	0	0	0	0.9
Long elbows	0	$N_{\text{elb,hdr}}$	$N_{\text{elb,hdr}}$	$N_{\text{elb,run}}$	$N_{\text{elb,run}}$	0.6
Gate valves	2	1	1	1	1	0.19
Loop weldolets	2	0	0	0	0	1.8
Loop control valves	1	0	0	0	0	10
Flexible hoses[1]	$2N_{\text{SCA}}$	0	0	0	0	20.6
$N_{\text{fit,comp}}$	5	2	2	2	2	-

with

$$L_{\text{hdr,base}} = \sum_{i=1}^{N_{\text{sec}}} 2L_{\text{spacing}}, \tag{E.16}$$

where the number of header sections N_{sec} is calculated with Eq. (D.10) in Appendix D. Yet as the header piping requires expansion loops to compensate the thermal expansion of the steel, it is assumed that such an expansion loop of 20 m length is positioned every 70 m along the header. Hence, the actual header piping length is

$$L_{\text{hdr}} = L_{\text{hdr,base}} + 20\,\text{m}\left\lfloor \frac{L_{\text{hdr,base}}}{70\,\text{m}} \right\rfloor. \tag{E.17}$$

Likewise, the runner base length $L_{\text{run,base}}$ from the centre of the power island to the inlet of the header is obtained from

$$L_{\text{run,base}} = 2L_{\text{spacing}} + \frac{L_{\text{loop}}}{2}. \tag{E.18}$$

[1] Vasquez Padilla (2011).

Similarly to Eq. (E.17), an expansion loop of 20 m length is placed every 70 m along the loop. An additional 50 m of runner piping are also added, representing the piping distance in and around the power block. Thus, the total runner piping length can be calculated with

$$L_{\text{run}} = 50\,\text{m} + L_{\text{run,base}} + 20\,\text{m}\left\lfloor \frac{L_{\text{run,base}}}{70\,\text{m}} \right\rfloor. \tag{E.19}$$

With the runner and header base length defined, the number of long elbows required in each piping subsection can be calculated with

$$N_{\text{elb,run}} = 2 + \left\lfloor 4\frac{L_{\text{run,base}}}{70\,\text{m}} \right\rfloor, \tag{E.20}$$

$$N_{\text{elb,hdr}} = 1 + \left\lfloor 4\frac{L_{\text{hdr,base}}}{70\,\text{m}} \right\rfloor, \tag{E.21}$$

assuming that each expansion loop requires 4 long elbows. Another 2 elbows are required for the runner piping in and around the power block. Only one additional elbow is required at the header connection to the runner.

As previously mentioned above, the pressure drop calculation of each solar field piping subsection accounts for the pressure drop of the pipe itself as per Eq. (E.10) as well as the pressure drop of additional piping equipment (i.e. fittings and expansion/contraction). The pressure drop of fittings is calculated with

$$\Delta P_{\text{fit},k} = \frac{1}{2} K v^2 \rho N_{\text{fit}}, \qquad \text{for } k{=}1{,}N_{\text{fit,comp}}, \tag{E.22}$$

where N_{fit} is the number of fittings per fitting component $N_{\text{fit,comp}}$ in each piping subsection as per Table E.1. K is the resistance coefficient of the fitting that allows the characterisation of the pressure loss in a fitting based on its function and geometry. The K-values for each type of fitting component are reported in Table E.1. In PTPPs using thermal oil as HTF, ball joint assemblies are generally preferred over flexible hoses due to their increased reliability, lower cost and lower pressure drop (Sargent & Lundy, 2003). The K-value of a ball joint assembly is 8.69 (Wagner and Gilman, 2011) as compared to 20.6 for flexible hoses (Vasquez Padilla, 2011). Hence, the pressure drop in the solar field can be reduced by up to 50 % when using ball joint assemblies instead of flexible hoses (Sargent & Lundy, 2003). However, it is assumed in this study that the SCAs are connected with flexible hoses since no viable ball joint assembly design for high temperature molten salts has been developed yet. According to Abengoa Solar (2013), the main issue with ball joints are the seals of the joints, which are not compatible with molten salts at temperatures of 500 °C due to leaking and oxidation of the graphite seal. The use of flexible hoses is further supported by the fact that Archimede Solar Energy's test loop also uses flexible hoses to connect the collectors. Lastly, the

pressure drop of expansions/contractions in the runner is calculated with

$$\Delta P_{\text{cont/exp},j} = \frac{1}{2} K v^2 \rho, \qquad \text{for } j{=}2{,}N_{\text{grp}}, \tag{E.23}$$

for N_{grp} header groups, where the first header expansion/contraction takes place at the inlet of the second header group ($j = 2$).

The pressure loss of each piping subcategory is simply the sum of the pressure drops of the pipe, fittings and expansions/contractions. For a loop, the pressure drop is then simply the sum of the piping pressure drop across the whole loop and the sum of pressure losses in the fittings with

$$\Delta P_{\text{loop}} = \Delta P_{\text{pipe}} + \sum_{k=1}^{N_{\text{fit,comp}}} \Delta P_{\text{fit},k}. \tag{E.24}$$

Likewise, the pressure drop of the hot and cold runner is calculated with

$$\Delta P_{\text{run,h/c}} = \Delta P_{\text{pipe}} + \sum_{k=1}^{N_{\text{fit,comp}}} \Delta P_{\text{fit},k}. \tag{E.25}$$

Additionally to the pipe and fitting pressure loss, the header pressure drop calculation also takes pipe expansions/contractions for each header group into account. Furthermore, the pressure drop in each header section is averaged with regards to the effective mass flow rate through the respective section as each section feeds two loops, hence continuously reducing the mass flow rate. Therefore, the pressure loss of the header is obtained with

$$\Delta P_{\text{hdr,h/c}} = \sum_{j=1}^{N_{\text{grp}}} \left[\sum_{i=1}^{N_{\text{sec},i}} \left(\Delta P_{\text{pipe},j,i} + \frac{\Delta P_{\text{cont/exp},j} + \Delta P_{\text{fit},j}}{N_{\text{sec},i}} \right) . \frac{2\dot{m}_{\text{sec},j,i}}{\dot{m}_{\text{hdr}}} \right]. \tag{E.26}$$

Finally, the total pressure drop in the solar field can be calculated as the sum of the pressure drops in each piping subcategory with

$$\Delta P_{\text{SF}} = \Delta P_{\text{loop}} + \Delta P_{\text{hdr,h}} + \Delta P_{\text{hdr,c}} + \Delta P_{\text{run,h}} + \Delta P_{\text{run,c}}. \tag{E.27}$$

This pressure drop is used in section 2.7 to calculate the solar field pumping power for the plant's parasitic consumption.

Appendix F

Solar Field and Power Block Validation with SAM[1]

This chapter describes the process of the validation with SAM as presented in section 4.1 in detail. The heat transfer fluids investigated in this validation study are Solar Salt, Hitec and Hitec XL, with their thermo-physical properties as discussed in section 2.3.8. The solar field is formed by the FLABEG Ultimate Trough collector (see Table 2.1) in combination with Archimede Solar Energy's HCEMS-11 receiver tubes (see Table 2.3), specifically developed for the use with molten salts for high temperature applications of up to 550 °C (Archimede Solar Energy, 2017).

F.1 Simulation Setup

As mentioned above, SAM's model differs in a few aspects from the model developed in this study. Therefore, the solar field control, as introduced in section 2.4, was adapted to match SAM's model for the purpose of this comparison. To further warrant comparability of the two models, the following measures were taken to set up the simulations. Firstly, the identical weather data set in form of a typical meteorological year (TMY3) for Upington, South Africa, was used in both models (see Appendix A for details on the weather data). This meteorological data includes, inter alia, the direct normal irradiance, ambient temperature and atmospheric pressure. Secondly, the same geometric, physical and thermal properties were implemented in both models for the main solar field components, i.e. the collectors and receivers. Thirdly, the input parameters for the plant control and any other relevant system variable were set to the same values in both models to ensure comparability. Likewise, parameters relevant for the simulation solver, i.e. simulation time step size and control volume size (nodes per SCA), were set to equal values, which is 1 CV per SCA in the case of SAM. Fourthly, to eliminate the impact of a different

[1] Parts of this chapter have been published in Pan *et al.* (2018*a*).

HTF recirculation strategy within the two models, the inlet temperature for the solar field from SAM was used as an input variable to the new model. Furthermore, SAM does not allow to specify a night time flow rate higher than the minimum flow rate. The effects of the two different recirculation strategies on the solar field operation and the dedicated night time flow rate introduced in section 2.4 are analysed in more detail in section F.3.

The design point parameters of both models for the performance calculations at design are listed in Table F.1. The power plant considered in this validation has a gross turbine capacity of 55 MW, a solar multiple of 1.6 and 6 h of thermal storage capacity. The power cycle is assumed to have a thermal efficiency of 37 % with a boiler pressure of 100 bar. The ambient conditions at design are a DNI of 850 W/m^2 and a dry air temperature of 35 °C. The initial air temperature difference of the ACC is assumed to be 16 °C. Regarding the solar field, the inlet temperature is set to 290 °C fro all three investigated HTFs, whereas the outlet temperature is set to the appropriate upper operating temperature of each molten salt, i.e. 550 °C for Solar Salt and 450 °C for both, Hitec and Hitec XL. Similarly, the freeze protection temperature is 260 °C for Solar Salt, 170 °C for Hitec and 150 °C for Hitec XL.

Table F.1: Design point parameters for the validation.

Parameter	Variable	Unit	Value		
Time step size	Δt	[min]	60		
CV per SCA	Ω	[-]	1		
DNI at design	I_{des}	[W/m^2]	850		
Solar multiple	SM	[-]	1.6		
SF inlet temperature	$T_{\mathrm{SF,in}}$	[°C]	290		
Min. flow rate per loop	$\dot{m}_{\mathrm{min}}$	[kg/s]	2		
TES full-load hours	t_{TES}	[h]	6		
Gross power output	$\dot{W}_{\mathrm{gross,e}}$	[MW]	55		
Cycle thermal efficiency	$\eta_{\mathrm{PB,th}}$	[%]	37		
HPT inlet pressure	$P_{\mathrm{in,HPT}}$	[bar]	100		
ACC ITD at design	T_{ITD}	[°C]	16		
Dry air temperature at design	T_{amb}	[°C]	35		
Heat transfer fluid			Solar Salt	Hitec	Hitec XL
SF outlet temperature	$T_{\mathrm{SF,out}}$	[°C]	550	450	450
FP temperature	T_{fp}	[°C]	260	170	150
Max. flow rate per loop	$\dot{m}_{\mathrm{max}}$	[kg/s]	10.2	18.1	19.8

F.2 Model Error

As already introduced in section 4.1, the model error is quantified in terms of the RMSE with Eq. (4.1) and the MAE with Eq. (4.2). Here, the "measured" outlet temperature corresponds to the temperature obtained from the simulations in SAM and is thus denominated as $T_{\text{out,SAM},j}$.

Table F.2 lists the design point performances for the various HTFs in SAM and the model. The receiver heat losses and solar field thermal power both have a low error of maximal 0.64 %. However, large errors of up to 13.48 % occur for the solar field heat loss because of the different calculation methods within the two models. Hitec and Hitec XL have the same design point heat loss because they have the same design solar field outlet temperature of 450 °C, whereas Solar Salt has higher heat losses due to its higher operating temperature of 550 °C. The solar field conversion efficiency also shows acceptable errors for all HTFs.

For the validation, annual simulations with the various heat transfer fluids were carried out with a time step of 1 h in both models. The results were then compared in terms of the RMSE and the MAE, which are presented in Table F.3 and discussed in more detail hereinafter. The MAE has been chosen

Table F.2: Comparison of the design point performances in SAM and the model for the three investigated HTFs.

Performance at design	Unit	*Solar Salt*		
		SAM	Model	Rel. error
Receiver heat loss	[W/m]	312.3	311.9	−0.13 %
SF thermal power	[MW_{th}]	225.6	224.8	−0.37 %
SF heat loss	[MW_{th}]	16.4	17.1	4.11 %
SF conversion efficiency	[%]	70.2	68.8	−1.97 %
Performance at design	**Unit**	***Hitec***		
		SAM	Model	Rel. error
Receiver heat loss	[W/m]	209.8	210.0	0.10 %
SF thermal power	[MW_{th}]	231.6	230.1	−0.64 %
SF heat loss	[MW_{th}]	10.5	11.9	13.33 %
SF conversion efficiency	[%]	71.48	70.42	−1.48 %
Performance at design	**Unit**	***Hitec XL***		
		SAM	Model	Rel. error
Receiver heat loss	[W/m]	209.8	210	0.10 %
SF thermal power	[MW_{th}]	231.6	230.5	−0.47 %
SF heat loss	[MW_{th}]	10.5	11.4	8.71 %
SF conversion efficiency	[%]	71.48	70.56	−1.29 %

Table F.3: Comparison of the RMSE and MAE of performance indicators between SAM and the model for the three investigated heat transfer fluids.

Heat transfer fluid		Solar Salt		Hitec		Hitec XL	
Parameter	Unit	*RMSE*	*MAE*	*RMSE*	*MAE*	*RMSE*	*MAE*
SF outlet temperature	[°C]	5.47	2.51	6.89	3.64	7.91	4.67
Absorbed thermal power	[MW_{th}]	2.33	1.34	6.57	2.84	6.95	2.91
Heat loss in SF	[MW_{th}]	4.14	2.48	5.46	3.37	5.45	3.43
Loop flow rate	[kg/s]	0.81	0.13	1.54	0.32	1.71	0.31
Net electricity output	[MW_e]	4.43	1.48	6.12	3.54	6.11	3.68
Hot tank fill level	[%]	9.72	5.89	10.31	6.12	10.76	6.54

as a performance indicator additionally to the more commonly used RMSE because it is less sensitive to outliers. Consequently, the MAE is more reliable than the RMSE to assess the average model performance error as suggested by Willmott and Matsuura (2005). Nevertheless, the RMSE is also included in this analysis for coherence.

Figure F.1a shows the DNI of four consecutive days from the annual simulation, whereby the sky during day one is clear in the morning and overcast in the afternoon. Day two and four represent a day with lightly overcast sky and day three outlines the DNI of a typical day with no cloud cover. Figure F.1b depicts the corresponding absorbed thermal power of the HTF and heat losses of the whole solar field in the case of Solar Salt. Although the design heat losses of the model are higher than SAM's, they are underestimated during the simulation which, in return, results in increased absorbed power of the HTF. This can mainly be attributed to the two different calculation approaches and the reliance of the empirical heat loss model on merely the absorber surface temperature. As the heat losses of the receiver tube used in this study were determined empirically (see section 2.3.4), it can be assumed that the model presented here is more accurate for this specific receiver type and that SAM is overestimating the heat losses. However, Figure F.1c shows that the lower heat losses of the model do not significantly affect the solar field outlet temperature compared to SAM in the case of Solar Salt. In fact, with a MAE of 2.51 °C for Solar Salt (Table F.3) the model shows a good agreement with the results from SAM. Likewise, the MAE of the flow rate in the case of Solar Salt is similarly low with 0.13 kg/s.

The highest MAE and RMSE for the outlet temperature can be observed for Hitec XL with 4.67 °C and 7.91 °C, respectively, which can be attributed to the aforementioned overestimation of the heat loss in the solar field with SAM. Although this does not significantly affect the model performance with Solar Salt as HTF, it leads to larger errors when using Hitec or Hitec XL. This is mainly due to the two different approaches of calculating the heat loss, which appears to generate larger errors at lower receiver tube temperatures.

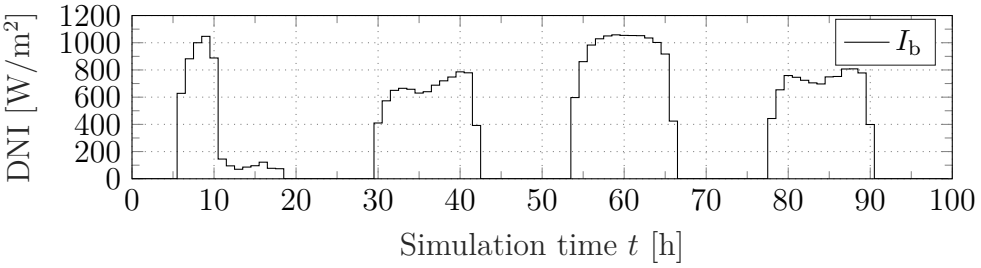

(a) Direct normal irradiance.

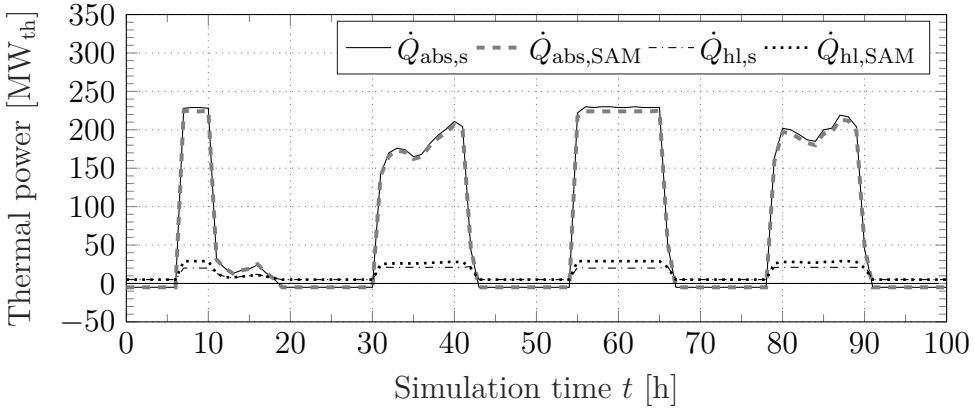

(b) Absorbed thermal power and heat losses in the solar field.

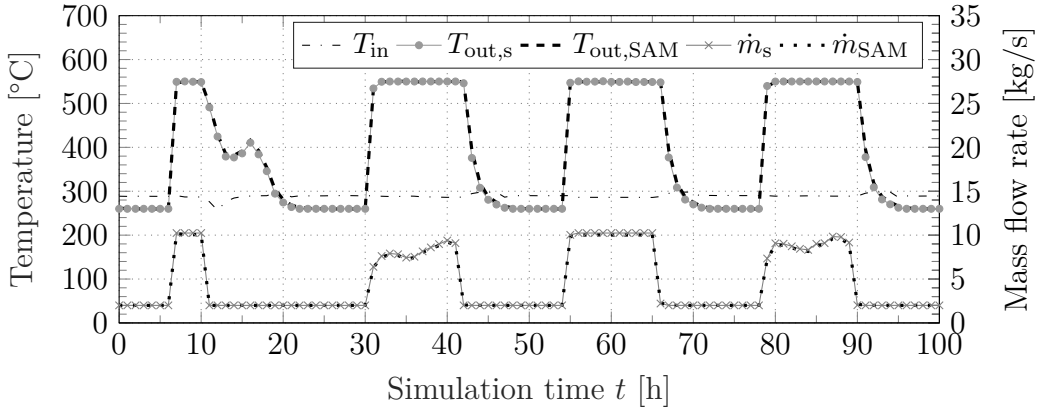

(c) Solar field fluid temperature and mass flow rate.

Figure F.1: Comparison of transient results between SAM and the model for Solar Salt with a time step size of 60 min and 1 CV per SCA.

Furthermore, heat losses from expansion bellows and support brackets are neglected in the model, leading to an overall lower heat loss. However, a validation of the solar field with measurement data in section 4.2 shows that the omission of these heat losses is acceptable since the empirical heat loss model produces highly acceptable results.

Since the upper operating temperature of Solar Salt is 100 °C higher than

the one of Hitec and Hitec XL, the error in the heat loss calculation is lower in the case of Solar Salt. This can also be seen in the relative error of the receiver heat loss at design in Table F.2, where the model underestimates the heat loss by −0.13 % compared to SAM, whereas it overestimates it by 0.10 % for both Hitec and Hitec XL.

Overall, it can be observed that Hitec XL shows the highest MAE and RMSE for for most performance indicators, whereas the errors for Solar Salt are significantly lower. The reason for this discrepancy is the already mentioned difference in calculating the heat losses of the receiver tubes as well as the initial errors at the design point as reported in Table F.2. For example, the solar field heat loss of the model at design is only 4.11 % higher than with SAM in the case of Solar Salt, whereas it is 8.71 % higher when using Hitec XL. This large variation at design clearly propagates through the annual simulation and thus reduces the overall model performance with Hitec and Hitec XL.

The RMSE of the net electricity output is in the range of 4.4 MW to 6.1 MW for the three fluids, whereas the MAE of Solar Salt (1.48 MW) is significantly lower than the MAE of the other two heat transfer fluids (3.54 MW for Hitec and 3.68 MW for Hitec XL). This corresponds to a relative error between 2.7 and 6.7 % compared to the installed capacity of 55 MW_e. The reason for the larger variation between the MAE of Solar Salt and that of the other two fluids is also linked to the aforementioned errors in the calculation of the heat loss of the receiver tubes. A larger error in the solar field outlet temperature and mass flow rate automatically also results in a larger error in the power output. In the case of Solar Salt however, the MAE is relatively small with 1.48 MW. Figure F.2 shows the net power output and the hot tank fill level of the two models. It can be seen that the net power output of the model shows good agreement with the results from SAM. However, some discrepancies can be seen at full-load operation, which is due to the parasitic consumption of the solar field pump and the condenser, as well as during the start-up and shut-down of

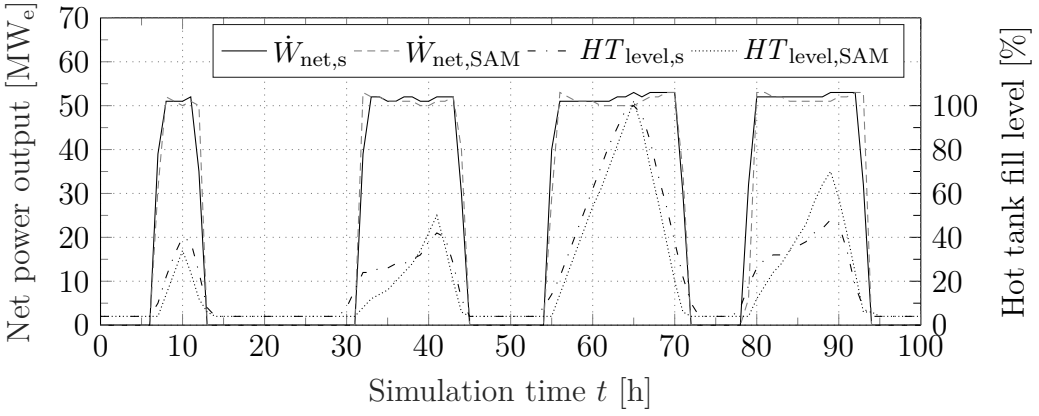

Figure F.2: Comparison of net electric power output and hot tank fill level between SAM and the model.

the turbine, which can be attributed to the start-up curves implemented in the model (see section 2.6.1) as well as the stored energy in the TES. The effect of the latter can be seen when looking at the hot tank fill level in Figure F.2. Although the model shows good agreement with SAM for some days, it can be seen that the model generally starts to fill the hot tank earlier in the morning and stores more energy over the course of the day. The reason for this is that power production in the model only begins once the hot tank has enough energy stored to run the power cycle for at least 1 hour. Hence, while SAM starts operation of the power block as soon as there is thermal energy available from the solar field, the model charges the TES and only starts operation later. Furthermore, the thermal power of the solar field is larger in the model as compared to SAM (see Figure F.1) due to the lower heat losses. Lastly, the two different approaches of night time circulation also have an impact on the hot tank fill level.

The combination of all the above reasons leads to a high RMSE and MAE for all heat transfer fluids. However, there is no significant difference between the three fluids. Because the parabolic trough model in SAM was originally developed for thermal oils as HTF, the operating strategy of the plant is not optimised for the usage of molten salts, resulting in large errors when compared to the model developed in this study. Likewise, SAM does not allow the modification of the model to include strategies that might be relevant for molten salts as for example recirculating fluid from the cold tank through the solar field or adjusting the flow rate during freeze protection. The latter is implemented in the model in the next section and its effect on the model performance as compared to SAM are discussed.

F.3 Dedicated Freeze Protection Mode

As already mentioned in the introduction of section 4.1, SAM was originally developed for the use of thermal oils as HTF. Thus, it is not completely suitable for molten salts due to their special characteristics and requirements. Therefore, the following changes and improvements have been implemented in the model in order to obtain a more accurate representation of a real power plant using molten salt as HTF.

Firstly, it is not possible to provide an empirical value for the thermal inertia for every examined power plant during a multi-objective optimisation with several thousand different power plant configurations. Therefore, the first improvement was to change the terms for the thermal inertia of the solar field piping to their respective estimated steel masses rather than an empirical value as per the implementation in SAM, eliminating the uncertainty of the empirical thermal inertia values.

Secondly, SAM assumes to recirculate the HTF at night from the solar field outlet directly back to the solar field inlet, which accelerates the cool down of

the HTF. This method is not suitable for molten salts due to their high freezing temperature. Thus, a recirculation from the cold tank was implemented. The cooler HTF is pumped from the solar field outlet to the cold tank and warm fluid from the storage is then pumped into the solar field inlet. This allows the usage of the stored energy during night time and reduces the need for electric freeze protection like trace heating (Pan *et al.*, 2018*b*).

Thirdly, a freeze protection flow rate of 4 kg/s has been introduced to guarantee that the salt is not falling below the freezing temperature. Although the heat transfer coefficient increases in that case, the same flow rate is used in Archimede Solar Energy's test loop to avoid freezing of the HTF (Maccari *et al.*, 2015). The solar field control is implemented in the same way as discussed in section 2.4.

The specific flow rates of each operation mode are listed in Table F.4. The effect of these improvements on the performance of the solar field can be seen in Figure F.3. The absorbed thermal power of the HTF in Figure F.3b shows a dip at the end of day three because the hot tank is fully charged. The underlying control strategy then redirects the fluid to the cold tank, which results in an increase of the solar field inlet temperature in Figure F.3c beginning from hour 62. This, in return, increases the heat losses in the solar field and because the fluid is already relatively hot at the loop inlet (approximately 390 °C), the collectors defocus to prevent the HTF from overheating, resulting in a lower absorbed thermal power.

During day one, the sky is clear in the morning and starts to experience cloud cover towards the second half of the day. The solar field control starts from the freeze protection circulation *OM(1)* at night and switches to the design circulation *OM(3)* as soon as the sun rises (the active operation mode is shown in parenthesis on top of Figure F.3c). However, the solar irradiance on the collectors quickly heats the fluid above its maximum operating temperature and the collectors must be defocused. The solar field switches into *OM(4)* where the flow rate is set to its maximum value. At hour 11, the sky is covered by clouds and the solar field control changes from the collector defocusing mode to the standby circulation *OM(2)*. The hot fluid is directed to the cold tank because it is not hot enough for the hot tank. The resulting increase of the cold tank temperature keeps the fluid temperature above the minimum allowable value during the freeze protection circulation *OM(1)* starting at hour 19 and eliminates the need for freeze protection in this case. The effect of the increased

Table F.4: Loop design flow rates for the validation with SAM.

Parameter mode	Variable	Unit	Value
Minimum flow rate	$\dot{m}_{\text{min}}$	[kg/s]	2
Maximum flow rate	$\dot{m}_{\text{max}}$	[kg/s]	12
Freeze protection flow rate	$\dot{m}_{\text{fp}}$	[kg/s]	4

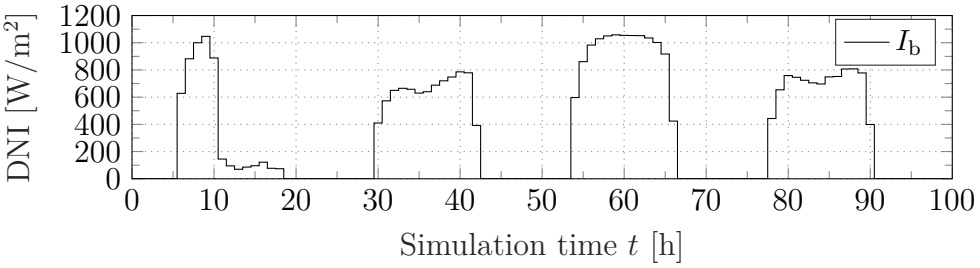

(a) Direct normal irradiance.

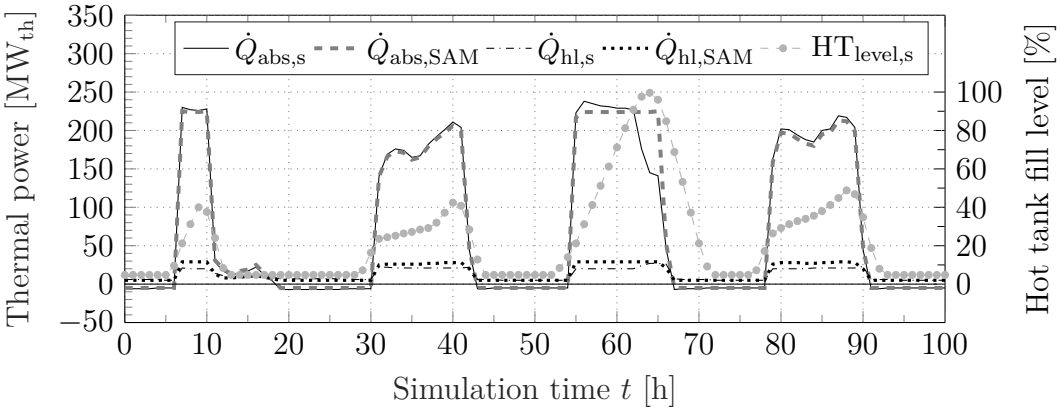

(b) Absorbed thermal power and heat losses in the solar field.

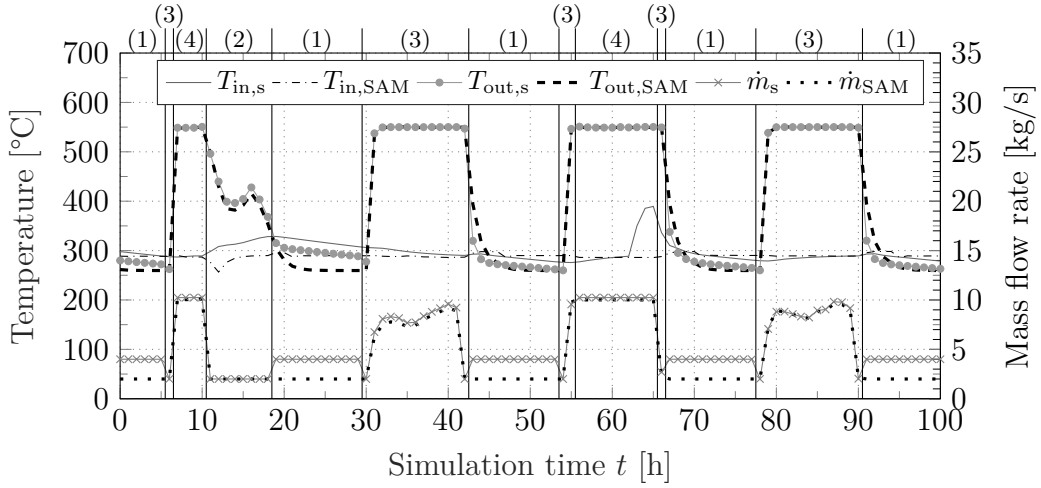

(c) Solar field fluid temperature, mass flow rate and solar field operation modes.

Figure F.3: Comparison of transient results between SAM and the model for Solar Salt with the dedicated freeze protection operation mode.

freeze protection flow rate can be seen at the end of the night at hour 30, where the solar field control is switched to the design circulation mode *OM(3)*, resulting in a drop of the outlet temperature as a result of the lower flow rate.

Appendix G

Sensitivity of Technical and Economic Performance Indicators to Additional Design Variables

The sensitivity of the technical and economic performance indicators to the variation of the temperature threshold for the hot tank inlet are shown in Figure G.1. The solar field and solar-to-electric efficiency decrease with an increasing temperature threshold which also leads to a slightly lower annual net electricity output. This is primarily caused by hot fluid being redirected into the cold tank instead of the hot tank, which results in an increase of the average cold tank temperature. In turn, this leads to higher temperature levels in the solar field and therefore also higher heat losses. As can be seen in Figure G.1b, a lower hot tank inlet temperature threshold results in lower LCOEs, where 415 °C enable a reduction to 127.8 $/MWh.

Figures G.2 and G.3 show the impact of the variation of the freeze protection mass flow rate, collector spacing and nominal ACC air temperature difference at design on the technical and economic performance indicators, respectively. It can be seen that the solar-to-electric efficiency decreases with an increasing freeze protection mass flow rate and a low flow rate of 2 kg/s is favourable due to a resulting reduction of heat losses during night time operation. Nevertheless, higher flow rates of, for example, 4 kg/s might be required in order to keep all piping equipment warm in order to prevent freezing of the HTF in the pipes (as for example in Archimede Solar Energy's demonstration plant).

The variation of the collector row spacing has the largest impact on the solar field efficiency and the resulting net power output. Due to the large size of the UltimateTrough collector, large row spacings are required in order to avoid excessive shadowing of the collectors. A row spacing of 42 m is recommended for the reference plant in order to increase the conversion efficiency and reduce

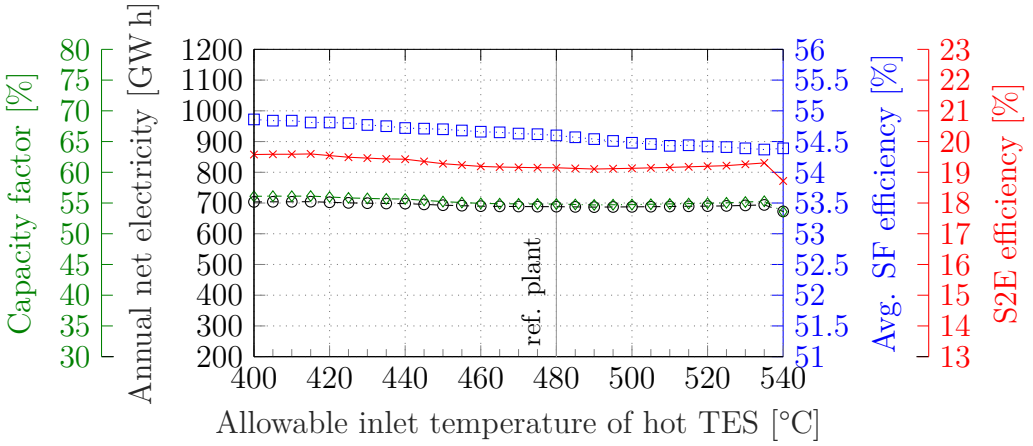

(a) Technical performance indicators.

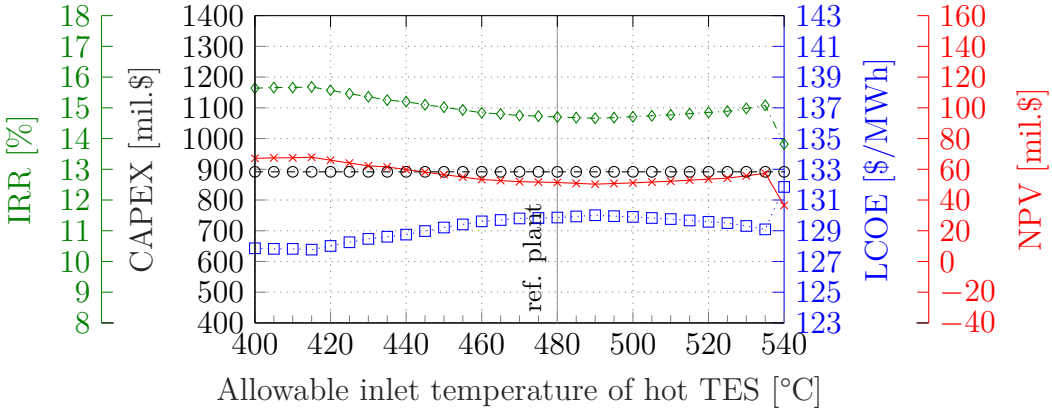

(b) Economic performance indicators.

Figure G.1: Sensitivity of (a) technical performance indicators and (b) economic performance indicators to the variation of the temperature threshold for the hot tank inlet.

the LCOE. However, further increasing the row spacing does not result in a significant reduction of the collector shadowing but rather increases piping distances and therefore also heat losses. Hence, the solar field efficiency reduces with collector row spacings above 42 m.

Lastly, the net electricity output can be increased with a high nominal ACC air temperature difference at design. This leads to a reduction of the condenser fan parasitic consumption which ultimately increases the power output and solar-to-electric efficiency of the power plant. Similarly, the LCOE and IRR increase with a decreasing nominal ACC air temperature difference.

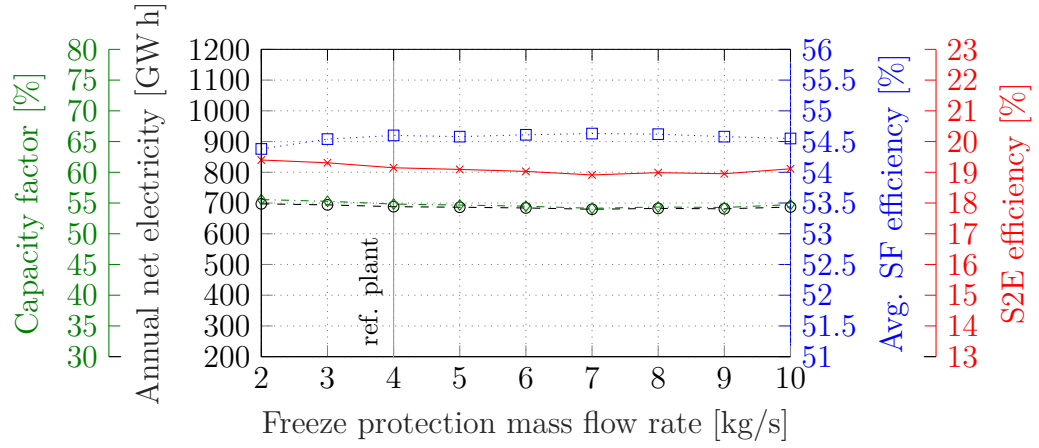

(a) Freeze protection mass flow rate in a loop.

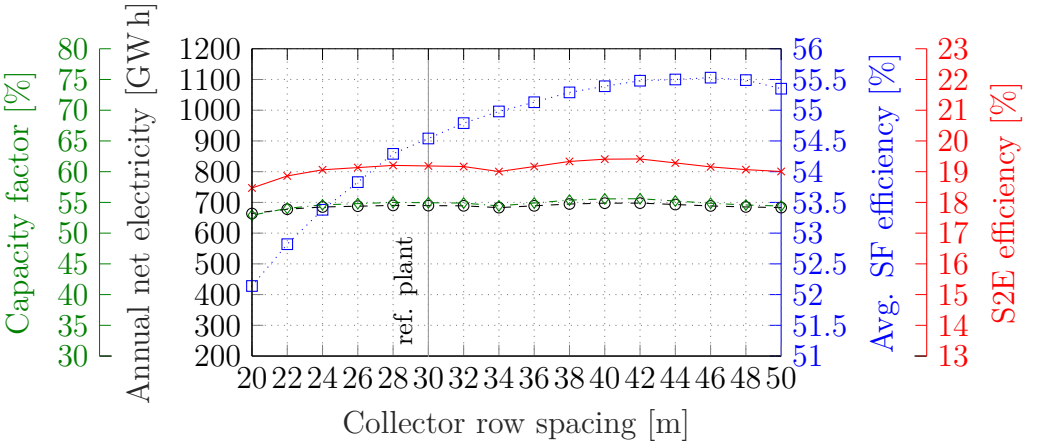

(b) Collector spacing.

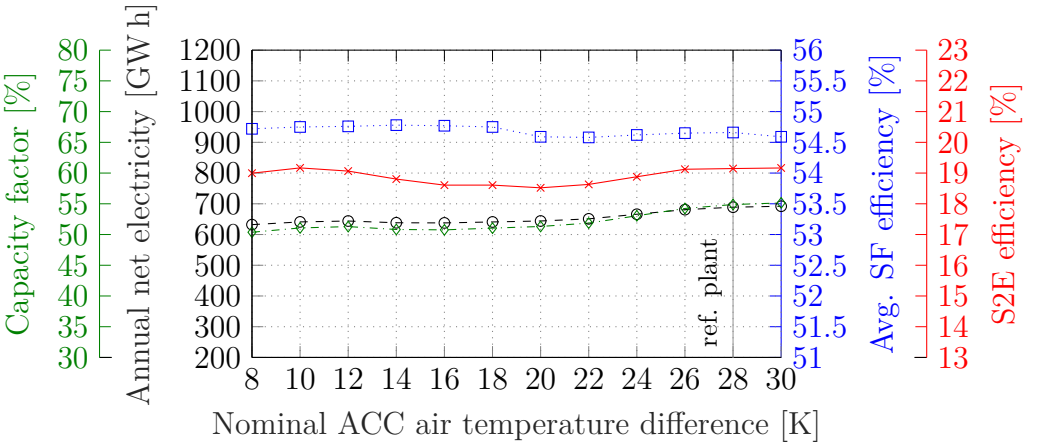

(c) ACC air temperature difference at design.

Figure G.2: Sensitivity of technical performance indicators to the variation of the (a) freeze protection mass flow rate, (b) collector spacing and (c) ACC air temperature difference at design.

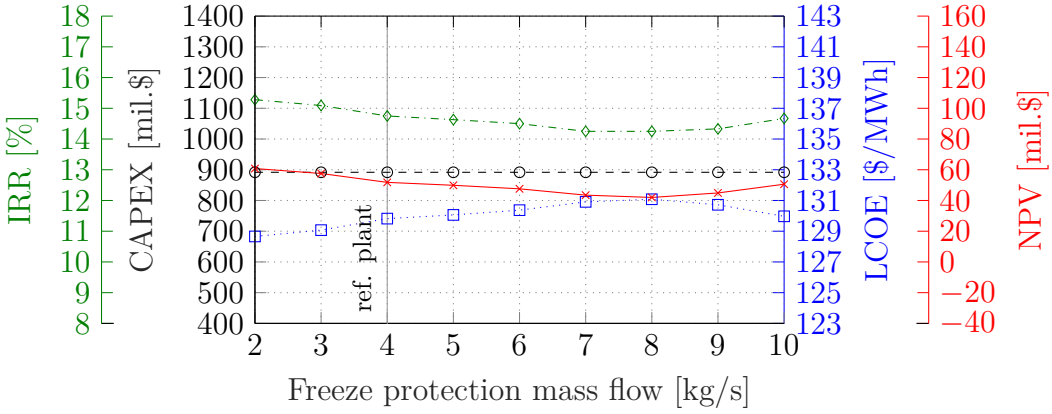

(a) Freeze protection mass flow rate in a loop.

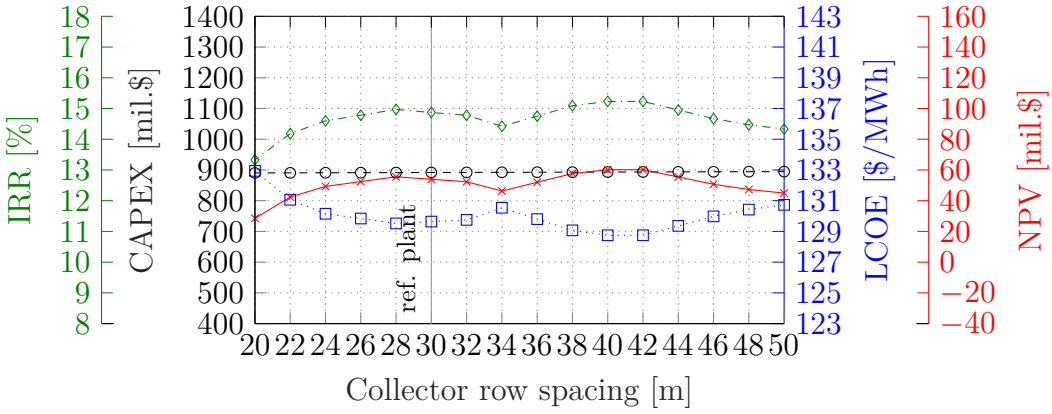

(b) Collector row spacing.

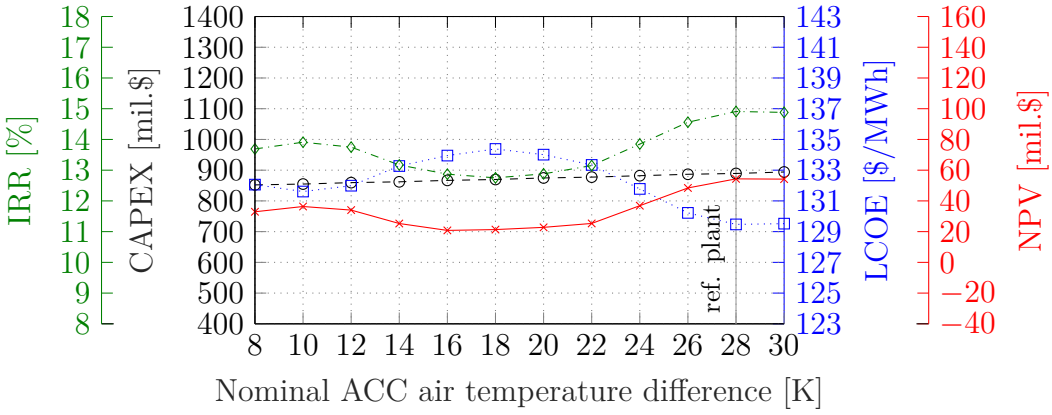

(c) ACC air temperature difference at design.

Figure G.3: Sensitivity of economic performance indicators to the variation of the (a) freeze protection mass flow rate, (b) collector row spacing and (c) ACC air temperature difference at design.

List of References

Abengoa Solar (2013). Development of Molten-Salt Heat Transfer Fluid Technology for Parabolic Trough Solar Power Plants. Lakewood. Available: https://www.osti.gov/scitech/servlets/purl/1090096 [2017-10-12].

Acciona (2019). KATHU. Available: https://www.acciona-industrial.com/projects/thermal-power-generation/planta-termosolar-kathu/ [2019-06-14].

Aerospace Specification Metals Inc. (n.d.). Material Data Sheet. Available: http://asm.matweb.com/search/SpecificMaterial.asp?bassnum=MQ321A [2020-02-06].

Archimede Solar Energy (2017). HCEMS-11 Molten Salts - Product Specification. Available: http://www.archimedesolarenergy.it/en_specifiche-prodotto-hcems-11.htm [2017-07-17].

Augsburger, G. (2013). *Thermo-economic optimisation of large solar tower power plants*, PhD Dissertation. Ecole Polytechnique Fédérale de Lausanne. Lausanne.

Baker, L. (2015). The evolving role of finance in South Africa's renewable energy sector. *Geoforum*, 64:146–156. doi:10.1016/j.geoforum.2015.06.017.

BASF (2020). Solar Chemicals. Available: https://chemicals.basf.com/global/en/Monomers/chemicals-and-servcies-for-solar-industries.html [2020-05-27].

Benoit, H., Spreafico, L., Gauthier, D. and Flamant, G. (2016). Review of heat transfer fluids in tube-receivers used in concentrating solar thermal systems: Properties and heat transfer coefficients. *Renew. Sustain. Energy Rev.*, 55:298–315. doi:10.1016/j.rser.2015.10.059.

Bhula, N. (2017). Bokpoort CSP Plant and Production Overview. Presented at STERG Symposium on 13-14 July 2017. Stellenbosch.

Biencinto, M., Bayón, R., Rojas, E. and González, L. (2014). Simulation and assessment of operation strategies for solar thermal power plants with a thermocline storage tank. *Solar Energy*, 103:456–472. doi:10.1016/j.solener.2014.02.037.

Biencinto, M., González, L. and Valenzuela, L. (2016). A quasi-dynamic simulation model for direct steam generation in parabolic troughs using TRNSYS. *Appl. Energy*, 161:133–142. doi:10.1016/j.apenergy.2015.10.001.

BLS (2019). Producer Price Index (PPI) for Chemical and Allied Products: Aromatics (WPU06140197). Available: `https://www.bls.gov/home.htm` [2019-07-19].

Boukelia, T., Mecibah, M., Kumar, B. and Reddy, K. (2015*a*). Investigation of solar parabolic trough power plants with and without integrated TES (thermal energy storage) and FBS (fuel backup system) using thermic oil and solar salt. *Energy*, 88:292–303. doi:10.1016/j.energy.2015.05.038.

Boukelia, T., Mecibah, M., Kumar, B. and Reddy, K. (2015*b*). Optimization, selection and feasibility study of solar parabolic trough power plants for Algerian conditions. *Energy Convers. Manag.*, 101:450–459. doi:10.1016/j.enconman.2015.05.067.

Boukelia, T., Mecibah, M., Meriche, I. and Belgroun, Z. (2015*c*). Comparative study of parabolic trough power plant with integrated TES and BS using synthetic oil and molten salt. In: *Int. Conf. Control. Eng. Inf. Technol.*, 1–4. IEEE, Tlemcen, Algeria. ISBN 978-1-4799-8212-7. doi:10.1109/CEIT.2015.7232981.

Bradshaw, R.W. and Brosseau, D.A. (2008). Low-Melting Point Inorganic Nitrate Salt Heat Transfer Fluid. In: *SolarPACES 2008*. Sandia, Las Vegas.

Bradshaw, R.W. and Siegel, N.P. (2008). Molten Nitrate Salt Development for Thermal Energy Storage in Parabolic Trough Solar Power Systems. In: *ASME Proc. Energy Sustain.*, 1–7. Jacksonville.

Burkhardt, J.J., Heath, G.A. and Turchi, C.S. (2011). Life Cycle Assessment of a Parabolic Trough Concentrating Solar Power Plant and the Impacts of Key Design Alternatives. *Environ. Sci. Technol.*, 45:2457–2464. doi:10.1021/es1033266.

Burkholder, F. and Kutscher, C. (2009). Heat Loss Testing of Schott's 2008 PTR70 Parabolic Trough Receiver. NREL, Golden. Available: `http://www.nrel.gov/docs/fy09osti/45633.pdf` [2016-10-18].

Camacho, E.F., Berenguel, M. and Rubio, F.R. (1997). *Advanced control of solar plants*. 1st edn. Springer, London, UK. ISBN 3-540-76144-6.

Castañeda, N., Vázquez, J., Domingo, M., Fernández, A. and León, J. (2003). Sener parabolic trough collector design and testing. In: *SolarPACES 2003*. Seville.

Cerni, T. and Price, H. (1997). Solar forecasting for operational support of SEGS plants. In: *Proc. 1997 Am. Sol. Energy Soc. Annu. Conf.*

Chang, C., Sciacovelli, A., Wu, Z., Li, X., Li, Y., Zhao, M., Deng, J., Wang, Z. and Ding, Y. (2018). Enhanced heat transfer in a parabolic trough solar receiver by inserting rods and using molten salt as heat transfer fluid. *Appl. Energy*, 220:337–350. doi:10.1016/j.apenergy.2018.03.091.

Chemical Engineering (2018). Chemical Engineering Plant Cost Index (CEPCI). Available: `http://www.chemengonline.com/pci-home` [2018-04-22].

Cheng, Z., He, Y., Xiao, J., Tao, Y. and Xu, R. (2010). Three-dimensional numerical study of heat transfer characteristics in the receiver tube of parabolic

trough solar collector. *Int. Commun. Heat Mass Transf.*, 37(7):782–787. doi:10.1016/J.ICHEATMASSTRANSFER.2010.05.002.

Coastal Chemical Co. (n.d.). Hitec® Heat Transfer Salt. Houston. Available: `http://stoppingclimatechange.com/MSR-HITECHeatTransferSalt.pdf` [2016-09-26].

Conradie, A.E. and Kröger, D.G. (1996). Performance evaluation of dry-cooling systems for power plant applications. *Appl. Therm. Eng.*, 16(3):219–232. doi:10.1016/1359-4311(95)00068-2.

Consoli, D. (2012). Archimede Solar Thermal Power Plant. ENEL Ingegneria e Innovazione SpA, REM Conference, 01.03.2012. Ravenna. [2016-09-19].

Craig, O.O., Brent, A.C. and Dinter, F. (2017). The current and future energy economics of concentrating solar power (CSP) in South Africa. *South African J. Ind. Eng.*, 28(3):1–14. doi:10.7166/28-3-1835.

CSP Plaza (2016). Chinese Demonstration Project Short List Finally Being Released, All You Want Is Here!! Available: `http://en.cspplaza.com/chinese-demonstration-project-short-list-finally-being-released-all-you-want-is-here.html` [2017-01-12].

CSP Services (2017). Projects. Available: `https://www.cspservices.de/projects/` [2017-05-16].

D'Aguanno, B., Karthik, M., Grace, A.N. and Floris, A. (2018 dec). Thermostatic properties of nitrate molten salts and their solar and eutectic mixtures. *Sci. Rep.*, 8(1):10485. doi:10.1038/s41598-018-28641-1.

De Klerk, B. (2016). STERG Symposium Presentation. STERG Symposium, 14.-15. July 2016. Stellenbosch. Available: `http://sterg.sun.ac.za/wp-content/uploads/2016/04/2_Engie.pdf`

De Meyer, O. (2018). *Optimisation in Plant Operations for a 100 MW Central Receiver CSP Plant with Focus on the Plant Operating Strategies*, PhD Dissertation. Stellenbosch University. Stellenbosch.

De Meyer, O., Dinter, F. and Govender, S. (2017). Value as a parameter to consider in operational strategies for CSP plants. In: *AIP Conf. Proc.*, vol. 1850.

Department of Energy (2013). Integrated Resource Plan for Electricity (IRP) 2010-2030 - Update Report. Pretoria. Available: `http://www.doe-irp.co.za/content/IRP2010_updatea.pdf` [2015-03-10].

Department of Energy (2018). Independent Power Producers Procurement Programme (IPPPP): An Overview as at 30 June 2018. Centurion.

Department of Energy (2019*a*). Independent Power Producers Procurement Programme (IPPPP): An Overview as at 31 December 2018. Centurion.

Department of Energy (2019*b*). Integrated Resource Plan (IRP2019). Pretoria. Available: `http://www.energy.gov.za/IRP/irp-2019.html` [2020-07-27].

Dersch, J., Vogel, T., Polklas, T. and Tümmers, C. (2014). Solar-only Parabolic Trough Plants with High Steam Parameters. *Energy Procedia*, 49:1117–1126. doi:10.1016/j.egypro.2014.03.121.

Dieckmann, S., Dersch, J., Giuliano, S., Puppe, M., Lüpfert, E., Hennecke, K., Pitz-Paal, R., Taylor, M. and Ralon, P. (2017). LCOE reduction potential of parabolic trough and solar tower CSP technology until 2025. *AIP Conf. Proc.*, 1850. doi:10.1063/1.4984538.

Dinter, F. and Möller, L. (2016). A Review of Andasol 3 and Perspective for Parabolic Trough CSP Plants in South Africa. *AIP Conf. Proc.*, 1734. doi:10.1063/1.4949193.

Dinter, F. and Tolksdorf, S. (2018). Design of a molten salt parabolic trough power plant with thermal energy storage and a novel freezing protection. *AIP Conf. Proc.*, 2033:030005–1–030005–8. doi:10.1063/1.5067021.

Donga, R.K. and Kumar, S. (2019). Thermal performance of parabolic trough collector with absorber tube misalignment and slope error. *Solar Energy*, 184:249–259. doi:10.1016/J.SOLENER.2019.04.007.

Dow (2001). DOWTHERM A - Synthetic Organic Heat Transfer Fluid - Liquid and Vapor Phase Data. Available: `http://msdssearch.dow.com/PublishedLiteratureDOWCOM/dh_097a/0901b8038097ad39.pdf?filepath=heattrans/pdfs/noreg/176-01463.pdf&fromPage=GetDoc` [2017-01-12].

Dudley, V.E., Kolb, G.J., Sloan, M. and Kearney, D. (1994). Test results: SEGS LS-2 Solar Collector. SAND94-1884. Sandia National Laboratories. Albuquerque. Available: `https://www.osti.gov/servlets/purl/70756` [2020-07-12].

Duffie, J.A. and Beckman, W.A. (2006). *Solar Engineering of Thermal Processes*. 3rd edn. John Wiley & Sons, Inc., New Jersey.

Duvenhage, F.D. (2019). *Sustainable Future CSP Fleet Deployment in South Africa: a Hydrological Approach to Strategic Manegement*, PhD Dissertation. Stellenbosch University. Stellenbosch.

Eastman (2019). Therminol VP-1 heat transfer fluid. Kingsport. Available: `https://www.therminol.com/products/Therminol-VP1` [2019-08-26].

Eberhard, A. and Naude, R. (2016). The South African Renewable Energy Independent Power Producer Procurement Programme: A Review and Lessons Learned. *J. Energy South Africa*, 27(4):1. doi:10.17159/2413-3051/2016/v27i4a1483.

Edenburn, M.W. (1976). Performance analysis of a cylindrical parabolic focusing collector and comparison with experimental results. *Solar Energy*, 18(5):437–444. doi:10.1016/0038-092X(76)90010-4.

EE Publishers (2016). Understanding the cost of electricity from Medupi, Kusile and IPPs - EE Publishers. Available: `https://www.ee.co.za/article/understanding-cost-electricity-medupi-kusile-ipps.html` [2020-05-18].

Eickhoff, M., Meyer-Grünefeldt, M. and Keller, L. (2016). New operating strategies for molten salt in line focusing solar fields - Daily drainage and solar receiver preheating. In: *AIP Conf. Proc.*, vol. 1734, 070007. AIP Publishing, SolarPACES 2015. doi:10.1063/1.4949154.

Engineering News (2013). Carbon Tax Policy Proposal Aligns with International Trends, but Gaps Remain. Available: `https://www.engineeringnews.co.za/article/carbon-tax-policy-proposal-aligns-with-international-trends-but-gaps-remain-2013-05-09` [2020-05-18].

Engineering News (2015). KaXu Solar One parabolic trough plant and Khi Solar One concentrate solar power projects, South Africa. Available: `https://www.engineeringnews.co.za/print-version/kaxu-solar-one-parabolic-trough-plant-and-khi-solar-one-concentrate-solar-power-projects-south-africa-2015-03-06` [2019-07-21].

Engineering News (2017). Kubayi sets 77c/kWh price cap and October deadline for signing of 26 renewables projects. Available: `https://m.engineeringnews.co.za/article/kubayi-sets-77ckwh-price-cap-and-october-deadline-for-signing-of-26-renewables-projects-2017-09-01` [2019-07-23].

Eskom (2018). Integrated Report 2017. Johannesburg.

Eskom (2019). Integrated Report 2018. Johannesburg.

EY (2019). Worldwide Corporate Tax Guide 2019. London. Available: `https://www.ey.com/Publication/vwLUAssets/ey-worldwide-corporate-tax-guide-2019/$FILE/ey-worldwide-corporate-tax-guide-2019.pdf` [2020-06-25].

Falchetta, M. and Rossi, A. (2014). Dynamic Simulation of the Operation of a Molten Salt Parabolic Trough Plant, Comprising Draining Procedures. *Energy Procedia*, 49:1328–1339. doi:10.1016/j.egypro.2014.03.142.

Ferruzza, D. (2015). *Thermocline Storage for Concentrated Solar Power*, Master thesis, KTH Royal Institute of Technology. Stockholm.

Ferruzza, D., Topel, M., Basaran, I., Laumert, B. and Haglind, F. (2017). Start-up performance of parabolic trough concentrating solar power plants. *AIP Conf. Proc.*, 1850. doi:10.1063/1.4984542.

Ferruzza, D., Topel, M., Laumert, B. and Haglind, F. (2018). Impact of steam generator start-up limitations on the performance of a parabolic trough solar power plant. *Solar Energy*, 169(January):255–263. doi:10.1016/j.solener.2018.05.010.

Fin24 (2016). The R12bn Kathu solar project: Good-bye diesel. Hello molten salt. Available: `https://www.fin24.com/BizNews/the-r12bn-kathu-solar-project-good-bye-diesel-hello-molten-salt-20160817` [2019-06-17].

Forristall, R. (2003). Heat Transfer Analysis and Modeling of a Parabolic Trough Solar Receiver Implemented in Engineering Equation Solver. NREL, Golden.

Available: `http://www.nrel.gov/docs/fy04osti/34169.pdf` [2016-08-30].

Gálvez-Carrillo, M., De Keyser, R. and Ionescu, C. (2009). Nonlinear predictive control with dead-time compensator: Application to a solar power plant. *Solar Energy*, 83(5):743–752. doi:10.1016/J.SOLENER.2008.11.005.

García-Barberena, J. and Erdocia, I. (2016). Simulation and comparison of different operational strategies for storage utilization in concentrated solar power plants. *AIP Conf. Proc.*, 1734:70010. doi:10.1063/1.4949157.

García-Barberena, J., Garcia, P., Sanchez, M., Blanco, M.J., Lasheras, C., Padrós, A. and Arraiza, J. (2012). Analysis of the influence of operational strategies in plant performance using SimulCET, simulation software for parabolic trough power plants. *Solar Energy*, 86(1):53–63. doi:10.1016/j.solener.2011.09.018.

Giostri, A., Binotti, M., Astolfi, M., Silva, P., Macchi, E. and Manzolini, G. (2012). Comparison of different solar plants based on parabolic trough technology. *Solar Energy*, 86(5):1208–1221. doi:10.1016/j.solener.2012.01.014.

GIZ (2013). Assessment of the localisation, industrialisation and job creation potential of CSP infrastructure projects in South Africa-A 2030 vision for CSP. Available: `http://protermosolar.com/helioscsp/wp-content/uploads/2015/05/GIZ-CSPStudy-FinalReportJune2013.pdf` [2019-06-17].

GIZ (2014). CSP Parabolic Trough Technology for Brazil. Available: `https://docplayer.net/15203683-Csp-parabolic-trough-technology-for-brazil-a-comprehensive-documentation-on-the-current-state-of-the-art-of-parabolic-trough-collector-technology.html` [2019-06-14].

Grogan, D. (2013). Development of Molten-Salt Heat Transfer Fluid Technology for Parabolic Trough Solar Power Plants. Sunshot Conference Project Review. Available: `http://energy.gov/eere/sunshot/downloads/development-molten-salt-heat-trasfer-fluid-technology-parabolic-trough-solar` [2016-09-19].

Guédez, R. (2016). *A Techno-Economic Framework for the Analysis of Concentrating Solar Power Plants with Storage*, PhD Dissertation. KTH Royal Institute of Technology. Stockholm.

Guédez, R., Spelling, J. and Laumert, B. (2014*a*). Reducing the Number of Turbine Starts in Concentrating Solar Power Plants Through the Integration of Thermal Energy Storage. *J. Sol. Energy Eng.*, 137(1):011003. doi:10.1115/1.4028004.

Guédez, R., Spelling, J., Laumert, B. and Fransson, T. (2014*b*). Optimization of Thermal Energy Storage Integration Strategies for Peak Power Production by Concentrating Solar Power Plants. *Energy Procedia*, 49:1642–1651. doi:10.1016/j.egypro.2014.03.173.

Guédez, R., Topel, M., Conde, I., Ferragut, F., Callaba, I., Spelling, J., Hassar, Z., Perez-Segarra, C.D. and Laumert, B. (2016). A Methodology for Determining Optimum Solar Tower Plant Configurations and Operating Strategies to Maximize

Profits Based on Hourly Electricity Market Prices and Tariffs. *Sol. Energy Eng.*, 138(2):021006. doi:10.1115/1.4032244.

Guédez, R., Topel, M., Spelling, J. and Laumert, B. (2015). Enhancing the Profitability of Solar Tower Power Plants through Thermoeconomic Analysis Based on Multi-objective Optimization. *Energy Procedia*, 69:1277–1286. doi:10.1016/j.egypro.2015.03.155.

Guillot, S., Faik, A., Rakhmatullin, A., Lambert, J., Veron, E., Echegut, P., Bessada, C., Calvet, N. and Py, X. (2012). Corrosion effects between molten salts and thermal storage material for concentrated solar power plants. *Appl. Energy*, 94:174–181. doi:10.1016/j.apenergy.2011.12.057.

Harnmeijer, J. and Ibikunle, G. (2014). The Potential Role of CSP in South Africa: A Case Study on the Bokpoort CSP Plant.

Heller, L. (2013). Literature Review on Heat Transfer Fluids and Thermal Energy Storage Systems in CSP Plants. Stellenbosch, South Africa.

Hernández-Moro, J. and Martínez-Duart, J. (2012). CSP electricity cost evolution and grid parities based on the IEA roadmaps. *Energy Policy*, 41:184–192. doi:10.1016/j.enpol.2011.10.032.

Hernández-Moro, J. and Martínez-Duart, J. (2013). Analytical model for solar PV and CSP electricity costs: Present LCOE values and their future evolution. *Renew. Sustain. Energy Rev.*, 20:119–132. doi:10.1016/j.rser.2012.11.082.

Hinrichs, M., Wortmann, J., Ladenberger, M. and Federsel, K. (2016). Temperature controlled molten salt recirculation enhances effectiveness of linear concentrating solar fields leading to reduced LCOE. In: *SolarPACES 2016*. Abu Dhabi.

Hirsch, T., Dersch, J., Fluri, T., García-Barberena, J., Giuliano, S., Hustig-Diethelm, F., Meyer, R., Schmidt, N., Seitz, M. and Yildiz, E. (2017). SolarPACES Guideline for Bankable STE Yield Assessment. Available: `http://www.solarpaces.org/wp-content/uploads/SolarPACES_Guideline_for_Bankable_STE_Yield_Assessment_-_Version_2017.pdf` [2018-08-22].

Hirsch, T., Steinmann, W.-D. and Eck, M. (2005). Simulation of transient two-phase flow in parabolic trough collectors using Modelica. In: *Proc. 4th Int. Model. Conf.*, 403–412. 7-8 March 2005, Hamburg, Germany.

IEA (2008). Energy Technology Perspectives. Paris.

IEA (2010). Technology Roadmap: Concentrating Solar Power. Paris.

IEA (2014). Technology Roadmap: Solar Thermal Electricity. Paris.

IFC (2012). Utility Scale Solar Power Plants. New Delhi. Available: `http://www.ifc.org/wps/wcm/connect/04b38b804a178f13b377ffdd29332b51/SOLAR+GUIDE+BOOK.pdf?MOD=AJPERES` [2015-07-22].

Incropera, F.P., DeWitt, D.P., Bergman, T.L. and Lavine, A.S. (2007). *Fundamentals of Heat and Mass Transfer*. 6th edn. John Wiley and Sons, Hoboken, NJ.

ISBN 0-471-76115-x.

Industry Sources (2018). CIF based estimate from industry sources.

IRENA (2018). Renewable Power Generation Costs in 2017. Abu Dhabi, UAE. Available: `https://www.irena.org/-/media/Files/IRENA/Agency/Publication/2018/Jan/IRENA_2017_Power_Costs_2018.pdf` [2019-07-29].

IRENA (2019). Renewable Power Generation Costs in 2018. Abu Dhabi. Available: `https://www.irena.org/-/media/Files/IRENA/Agency/Publication/2019/May/IRENA_Renewable-Power-Generations-Costs-in-2018.pdf` [2020-03-10].

Iverson, B.D., Flueckiger, S.M. and Ehrhart, B.D. (2011). Trough heat collection element deformation and solar intercept impact. In: *SolarPACES 2011*. Granada.

Jeal, C. (2017). *Impacts of a concentrated solar power trough facility on birds and other wildlife in South Africa*, Master thesis, University of Cape Town. Cape Town.

Jones, S.A., Blair, N., Pitz-Paal, R., Schwarzboezl, P. and Cable, R. (2001). Trnsys modeling of the SEGS VI parabolic trough solar electric generating system. In: *Int. Sol. Energy Conf.*, 405–412. Washington, DC. doi:10.1016/0038-092X(79)90164-6.

Kearney, D., Herrmann, U., Nava, P., Kelly, B., Mahoney, R., Pacheco, J., Cable, R., Potrovitza, N., Blake, D. and Price, H. (2003). Assessment of a Molten Salt Heat Transfer Fluid in a Parabolic Trough Solar Field. *J. Sol. Energy Eng.*, 125(2):170. doi:10.1115/1.1565087.

Kistner, R. and Price, H.W. (1999). Financing Solar Thermal Power Plants. In: *ASME Renew. Adv. Energy Syst. 21st Century Conf.* Maui.

Klein, S.A. and al., E. (2017). TRNSYS 17: A Transient System Simulation Program. Madison. Available: `http://sel.me.wisc.edu/trnsys/` [2017-03-01].

Kolb, G.J., Ho, C., Iverson, B., Moss, T. and Siegel, N. (2010). Freeze-Thaw Tests on Trough Receivers Employing a Molten Salt Working Fluid. In: *ASME 4th Int. Conf. Energy Sustain. Vol. 2*, 693–698. ASME. ISBN 978-0-7918-4395-6. doi:10.1115/ES2010-90040.

Kost, C., Mayer, J.N., Thomsen, J., Hartmann, N., Senkpiel, C., Philipps, S., Nold, S., Lude, S., Saad, N. and Schlegl, T. (2013). Levelized Cost of Electricity Renewable Energy Technologies. Tech. Rep., Fraunhofer ISE, Freiburg.

Kost, C., Shammugam, S., Jülch, V., Nguyen, H.-T. and Schlegl, T. (2018). Levelized Cost of Electricity Renewable Energy Technologies. Fraunhofer ISE, Freiburg. [2019-07-29].

Kurup, P. and Turchi, C.S. (2015). Parabolic Trough Collector Cost Update for the System Advisor Model (SAM). NREL, Golden. Available: `http://www.nrel.gov/docs/fy16osti/65228.pdf` [2017-07-26].

Larraín, T., Escobar, R. and Vergara, J. (2010). Performance model to assist solar thermal power plant siting in northern Chile based on backup fuel consumption. *Renew. Energy*, 35(8):1632–1643. doi:10.1016/j.renene.2010.01.008.

Lazard (2017). Lazard's Levelized Cost of Energy Analysis - Version 11.0. Available: `https://www.lazard.com/media/450337/lazard-levelized-cost-of-energy-version-110.pdf` [2019-08-22].

Lenzen, F. (2014). IEA CSP Workshop. Presentation at IEA Solar Electricity Roadmap Workshop, 03.03.2014, Paris. Available: `https://www.iea.org/events/solar-electricity-roadmap-workshop` [2016-08-26].

Leyland, G.B. (2002). *Multi-Objective Optimisation Applied to Industrial Energy Problems*, PhD Dissertation. Ecole Polytechnique Fédérale de Lausanne. Lausanne.

Lilliestam, J., Labordena, M., Ollier, L., Pfenninger, S., Thonig, R. and Tröndle, T. (2018). CSP.guru. Available: `https://zenodo.org/record/3466625` [2019-06-24].

Lilliestam, J., Labordena, M., Patt, A. and Pfenninger, S. (2017). Empirically observed learning rates for concentrating solar power and their responses to regime change. *Nat. Energy*, 2(7):17094. doi:10.1038/nenergy.2017.94.

Lilliestam, J. and Pitz-Paal, R. (2018). Concentrating solar power for less than USD 0.07 per kWh: finally the breakthrough? *Renew. Energy Focus*, 26:17–21. doi:10.1016/J.REF.2018.06.002.

Lippke, F. (1995). Simulation of the Part-Load Behavior of a 30 MWe SEGS Plant. Tech. Rep., SAND95-1293, Sandia National Laboratories, Albuquerque.

Lippke, F. (1997). The Operating Strategy and Its Impact on the Performance of a 30 MWe SEGS Plant. *J. Sol. Energy Eng.*, 119(3):201. doi:10.1115/1.2888019.

Liu, M., Steven Tay, N.H., Bell, S., Belusko, M., Jacob, R., Will, G., Saman, W. and Bruno, F. (2016). Review on concentrating solar power plants and new developments in high temperature thermal energy storage technologies. *Renew. Sustain. Energy Rev.*, 53:1411–1432. doi:10.1016/j.rser.2015.09.026.

Llorente García, I., Álvarez, J.L. and Blanco, D. (2011). Performance model for parabolic trough solar thermal power plants with thermal storage: Comparison to operating plant data. *Solar Energy*, 85(10):2443–2460. doi:10.1016/j.solener.2011.07.002.

Lubkoll, M. (2017). *Performance Characteristics of the Spiky Central Receiver Air Pre-heater (SCRAP)*, PhD Dissertation. Stellenbosch University. Stellenbosch.

Maccari, A., Bissi, D., Casubolo, G., Guerrini, F., Lucatello, L., Luna, G., Rivaben, A., Savoldi, E., Tamano, S. and Zuanella, M. (2015). Archimede Solar Energy Molten Salt Parabolic Trough Demo Plant: A Step Ahead towards the New Frontiers of CSP. *Energy Procedia*, 69:1643–1651. doi:10.1016/j.egypro.2015.03.122.

Maccari, A., Donnola, S., Matino, F. and Tamano, S. (2016). Archimede solar energy molten salt parabolic trough demo plant: Improvements and second year of operation. *AIP Conf. Proc.*, 1734. doi:10.1063/1.4949195.

Manzolini, G., Giostri, A., Saccilotto, C., Silva, P. and Macchi, E. (2011). Development of an innovative code for the design of thermodynamic solar power plants part A: Code description and test case. *Renew. Energy*, 36(7):1993–2003. doi:10.1016/j.renene.2010.12.027.

Matino, F. and Maccari, A. (2015). Molten Salt Receivers Operated on Parabolic Trough Demo Plant and in Laboratory Conditions. *Energy Procedia*, 69:481–486. doi:10.1016/j.egypro.2015.03.056.

Mehos, M., Turchi, C., Vidal, J., Wagner, M., Ma, Z., Ho, C., Kolb, W., Andraka, C. and Kruizenga, A. (2017). Concentrating Solar Power Gen3 Demonstration Roadmap. Tech. Rep., NREL, Golden.

Mendonça, M., Jacobs, D. and Sovacool, B.K. (2009). *Powering the Green Economy: the Feed-in Tariff Handbook*. Earthscan, London. ISBN 1844078574.

Meteotest (2014). Meteonorm V7.1.3.19872 (TMY3). Bern.

Mills, A.F. (1999). *Heat Transfer*. 2nd edn. Prentice Hall. ISBN 9780139476242.

Ministry of Energy (2018). Memorandum from the Parliamentary Office - National Assembly Question: 2962. Cape Town. Available: `https://pmg.org.za/committee-question/10509/` [2019-08-23].

Molyneaux, A. (2002). *A practical evolutionary method for the multi-objective optimisation of complex integrated energy systems including vehicle drivetrains*, PhD Dissertation. Ecole Polytechnique Fédérale de Lausanne. Lausanne.

Morin, G., Karl, M., Mertins, M. and Selig, M. (2015). Molten Salt as a Heat Transfer Fluid in a Linear Fresnel Collector - Commercial Application Backed by Demonstration. *Energy Procedia*, 69:689–698. doi:10.1016/j.egypro.2015.03.079.

NamPower (2017). TMY3 Kokerboom, Namibia. Available: `https://csp.nampower.com.na/` [2017-05-16].

New Energy Update (2017). Abengoa starts final tests on 100 MW South Africa plant; Australia agrees CSP build loan. Available: `http://newenergyupdate.com/csp-today/abengoa-starts-final-tests-100-mw-south-africa-plant-australia-agrees-csp-build-loan` [2019-07-21].

NREL (2009). Solar Advisor Model Reference Manual for CSP Trough Systems - SAM Version 3.0. Golden. Available: `https://www.nrel.gov/analysis/sam/pdfs/sam_csp_reference_manual_3.0.pdf` [2017-07-23].

NREL (2013*a*). SAM 2010 Parabolic Trough Cost Model. Golden. Available: `https://sam.nrel.gov/cost` [2018-07-13].

NREL (2013*b*). SAM HTF Property Tables. Golden. Available: `https://sam.nrel.gov/sites/default/files/content/documents/xls/sam-htf-property-tables.xlsx` [2017-10-19].

NREL (2018). SAM (System Advisor Model), V2018.11.11 (Revision 4). Available: `https://sam.nrel.gov/` [2018-11-22].

NREL (2020). Concentrating Solar Power Projects. Available: `http://www.nrel.gov/csp/solarpaces/index.cfm` [2020-03-06].

Odeh, S.D., Morrison, G.L. and Behnia, M. (1998). Modelling of parabolic trough direct steam generation solar collectors. *Solar Energy*, 62(6):395–406. doi:10.1016/S0038-092X(98)00031-0.

OilPrice.com (2016). Tesla And Other Tech Giants Scramble For Lithium As Prices Double. Available: `http://oilprice.com/Energy/Energy-General/Tesla-And-Other-Tech-Giants-Scramble-For-Lithium-As-Prices-Double.html` [2017-01-16].

Pacheco, J.E. and Kolb, W.J. (1997). Comparison of an Impedance Heating System to Mineral Insulated Heat Trace for Power Tower Applications. In: *Proc. ASME Int. Sol. Energy Conf.*, 1–5. 27-30 April 1997. Washington.

Pan, C.A. and Dinter, F. (2017). Combination of PV and central receiver CSP plants for base load power generation in South Africa. *Solar Energy*, 146:379–388. doi:10.1016/j.solener.2017.02.052.

Pan, C.A., Dinter, F. and Harms, T.M. (2018*a*). Validation of a Molten Salt Parabolic Trough Receiver Model Based on an Empirical Heat Loss Model. In: *SASEC 2018*. Durban, South Africa. ISBN 978-0-7972-1765-2.

Pan, C.A., Dinter, F., Harms, T.M. and Guédez, R. (2021). Development and validation of a dynamic molten salt parabolic trough collector model featuring an empirical heat loss equation. *(submitted for publication)*.

Pan, C.A., Ferruzza, D., Guédez, R., Dinter, F., Laumert, B. and Haglind, F. (2018*b*). Identification of optimum molten salts for use as heat transfer fluids in parabolic trough CSP plants. A techno-economic comparative optimization. In: *AIP Conf. Proc.*, vol. 2033, 30012. doi:10.1063/1.5067028.

Pan, C.A., Guédez, R., Dinter, F. and Harms, T.M. (2019). A techno-economic comparative analysis of thermal oil and molten salt parabolic trough power plants with molten salt solar towers. In: *AIP Conf. Proc.*, vol. 2126, 120014. ISBN 9780735418660. doi:10.1063/1.5117632.

Pareto, V. (1896). *Cours d'Économie Politique - Tome Premier*. Lausanne.

Parrado, C., Marzo, A., Fuentealba, E. and Fernández, A. (2016). 2050 LCOE improvement using new molten salts for thermal energy storage in CSP plants. *Renew. Sustain. Energy Rev.*, 57:505–514. doi:10.1016/j.rser.2015.12.148.

Patnode, A.M. (2006). *Simulation and Performance Evaluation of Parabolic Trough Solar Power Plants*, Master thesis. Univ. of Wisconsin-Madison. Madison.

Pitz-Paal, R. and Jones, S. (1998). A TRNSYS Model Library for Solar Thermal Electric Components (STEC) - A Reference Manual, Release 1.0. IEA-Solar Power and Chemical Energy Systems.

Platzer, W.J. and Dinter, F. (2016). A learning curve for solar thermal power. *AIP*

Conf. Proc., 1734:160013. doi:10.1063/1.4949254.

Poole, I.V. (2017). *Concentrating Solar Power in South Africa - A Comparison between Parabolic Trough and Central Receiver Technologies with Molten Salt as Heat Transfer Fluid*, Master thesis. Stellenbosch University. Stellenbosch.

PV Magazine (2019). Portuguese auction attracts world record bid of 14.8/MWh for solar. Available: `https://www.pv-magazine.com/2019/07/31/portuguese-auction-attracts-world-record-bid-of-e14-8-mwh-for-solar/` [2020-03-10].

Raade, J.W. and Padowitz, D. (2011). Development of Molten Salt Heat Transfer Fluid With Low Melting Point and High Thermal Stability. *J. Sol. Energy Eng.*, 133(3):031013. doi:10.1115/1.4004243.

REEEI (2012). Pre-feasibility study for the establishment of a pre-commercial concentrated solar power plant in Namibia. Windhoek. Available: `http://nei.nust.na/sites/default/files/projects/NA.2012.R.005.2.pdf` [2020-07-25].

Reilly, H.E. and Kolb, G.J. (2001). An Evaluation of Molten-Salt Power Towers Including Results of the Solar Two Project. Sandia National Laboratories, Alberquerque. Available: `http://prod.sandia.gov/techlib/access-control.cgi/2001/013674.pdf` [2016-09-26].

Relloso, S., Calvo, R., Cácamo, S. and Olábarri, B. (2011). Senertrough-1 collector: commercial operation experience, contiunous loop monitoring at Extresol 1 plant and technology deployment. In: *SolarPACES 2011*. Granada.

Republic of South Africa (1962). Income Tax Act 58 of 1962. Pretoria. Available: `http://extwprlegs1.fao.org/docs/pdf/saf93024.pdf` [2020-05-27].

Richert, T., Riffelmann, K. and Nava, P. (2015). The Influence of Solar Field Inlet and Outlet Temperature on the Cost of Electricity in a Molten Salt Parabolic Trough Power Plant. *Energy Procedia*, 69:1143–1151. doi:10.1016/j.egypro.2015.03.184.

Riffelmann, K., Richert, T., Nava, P. and Schweitzer, A. (2014). Ultimate Trough® - A Significant Step towards Cost-competitive CSP. *Energy Procedia*, 49:1831–1839. doi:10.1016/j.egypro.2014.03.194.

Rioglass (2015). Rioglass Solar has signed an agreement with Schott Solar CSP GmbH for the acquisition of its receiver business. Available: `https://www.rioglass.com/rioglass-solar-has-signed-an-agreement-with-schott-solar-csp-gmbh-for-the-acquisition-of-its-receiver-business/` [2020-04-22].

Rioglass (2020). RIOGLASS PTR70-4G. Available: `https://www.rioglass.com/rioglass-ptr704g/` [2020-04-09].

Rodriguez-Sanchez, D. and Rosengarten, G. (2015). Improving the concentration ratio of parabolic troughs using a second-stage flat mirror. *Appl. Energy*, 159:620–632. doi:10.1016/J.APENERGY.2015.08.106.

Ruegamer, T., Kamp, H., Kuckelkorn, T., Schiel, W., Weinrebe, G., Nava, P., Riffelmann, K. and Richert, T. (2014). Molten Salt for Parabolic Trough Applications: System Simulation and Scale Effects. *Energy Procedia*, 49:1523–1532. doi:10.1016/j.egypro.2014.03.161.

SAPP (2020). SAPP Market Trading. Available: `http://www.sappmarket.com/` [2020-05-29].

Sargent & Lundy (2003). Assessment of Parabolic Trough and Power Tower Solar Technology Cost and Performance Forecasts. NREL, Chicago. Available: `http://www.nrel.gov/docs/fy04osti/34440.pdf` [2016-07-27].

SARS (2020). Carbon Tax. Available: `https://www.sars.gov.za/ClientSegments/Customs-Excise/Excise/Environmental-Levy-Products/Pages/Carbon-Tax.aspx` [2020-05-18].

Sau, S., Corsaro, N., Crescenzi, T., D'Ottavi, C., Liberatore, R., Licoccia, S., Russo, V., Tarquini, P. and Tizzoni, A. (2016). Techno-economic comparison between CSP plants presenting two different heat transfer fluids. *Appl. Energy*, 168:96–109. doi:10.1016/j.apenergy.2016.01.066.

Savannah Environmental (2011). Draft Environmental Impact Assessment Report: Proposed Ilanga Solar Thermal Power Plant as Part of the Future Karoshoek Solar Thermal Park, Northern Cape. Sunninghill. Available: `https://sahris.sahra.org.za/sites/default/files/additionaldocs/0.IlangaDEIR-DraftEIAReport.pdf` [2020-04-12].

Schott (2013). SCHOTT PTR®70 Receivers. Technical data sheet. Mainz. Available: `https://www.schott.com/d/csp/2ad9cb93-5b86-4a51-aead-a49b4e869ef8/1.0/schott_ptr70_4th_generation_datasheet.pdf` [2019-06-18].

Schwarzbözl, P. (2006). A TRNSYS Model Library for Solar Thermal Electric Components (STEC). DLR, Köln. Available: `https://sel.me.wisc.edu/trnsys/trnlib/stec/stec_refguide_v3.0.pdf` [2018-07-03].

SENER (2019). Parabolic trough plant Kathu. Available: `https://www.energy.sener/project/parabolic-trough-plant-kathu` [2019-06-14].

Serrano-López, R., Fradera, J. and Cuesta-López, S. (2013). Molten salts database for energy applications. *Chem. Eng. Process. Process Intensif.*, 87–102. doi:10.1016/j.cep.2013.07.008.

Seubert, B.T., Vogel, A.K., Fluri, T.P. and Platzer, W.J. (2015). Freeze Protection Strategies for Molten Salt Parabolic Trough Solar Fields using Residual Heat of Thermocline Storages. In: *SolarPACES 2014*.

Sklar-Chik, M.D., Brent, A.C. and De Kock, I.H. (2016). Critical Review of the Levelised Cost of Energy Metric. *South African J. Ind. Eng.*, 27(4):124–133. doi:10.7166/27-4-1496.

Solargis (2019). Solar resource maps of Africa. Available: `https://solargis.com`

[2020-08-05].

SolarPACES (2018). Redstone CSP Contract Signed After 2-Year Delay. Available: `https://www.solarpaces.org/redstone-csp-contract-signed-after-2-year-delay/` [2019-08-23].

South African Reserve Bank (2020). Selected historical rates - Prime lending rate (predominant rate). Available: `https://www.resbank.co.za/Research/Rates/Pages/SelectedHistoricalExchangeAndInterestRates.aspx` [2020-10-03].

Spelling, J., Jöcker, M. and Martin, A. (2012). Annual performance improvement for solar steam turbines through the use of temperature-maintaining modifications. *Solar Energy*, 86(1):496–504. doi:10.1016/J.SOLENER.2011.10.023.

Spelling, J.D. (2013). *Hybrid Solar Gas-Turbine Power Plants: A Thermoeconomic Analysis*, PhD Dissertation. KTH Royal Institute of Technology. Stockholm.

SQM (2017). SQM's Thermo-solar salts specifications. Available: `http://www.sqm.com/en-us/productos/quimicosindustriales/salestermo-solares/productostermo-solares.aspx#divcompatibilidad` [2017-02-16].

Staine, F. (1995). *Intégration énergétique de procédés industriels par la méthode du pincement étendue aux facteurs exergétiques*, PhD Dissertation. Ecole Polytechnique Fédérale de Lausanne. Lausanne.

Starke, A.R., Cardemil, J.M., Escobar, R.A. and Colle, S. (2016). Assessing the performance of hybrid CSP+PV plants in northern Chile. *Solar Energy*, 138:88–97. doi:10.1016/j.solener.2016.09.006.

StatsSA (2020). CPI History 1960-March 2020. Available: `http://www.statssa.gov.za/publications/P0141/CPIHistory.pdf?` [2020-05-29].

Stine, W.B. and Geyer, M. (2001). Power From The Sun. Online Book, J.T. Lyle Center for Regenerative Studies, California State Polytechnic University, Pomona, CA. Available: `http://www.powerfromthesun.net` [2015-05-04].

Stoddard, M.C., Faas, S.E., Chiang, C.J. and Dirks, J.A. (1987). SOLERGY - A Computer Code for Calculating the Annual Energy from Central Receiver Power Plants. Sandia National Laboratories. Albuquerque. [2020-02-26].

Stolten, D. and Scherer, V. (2013). *Transition to Renewable Energy Systems*. Wiley-VCH Verlag GmbH & Co. KGaA, Weinheim, Germany. ISBN 978-3-527-33239-7.

Stuetzle, T., Blair, N., Mitchell, J.W. and Beckman, W.A. (2004). Automatic control of a 30 MWe SEGS VI parabolic trough plant. *Solar Energy*, 76(1-3):187–193. doi:10.1016/j.solener.2003.01.002.

Stuetzle, T.A. (2002). *Automatic Control of the 30 MWe SEGS VI Parabolic Trough Plant*, Master thesis. Univ. of Wisconsin-Madison, Madison.

Telsnig, T., Eltrop, L., Winkler, H. and Fahl, U. (2013). Efficiency and costs of different concentrated solar power plant configurations for sites in Gauteng and the Northern Cape, South Africa. *J. Energy South Africa*, 24(1):77–89.

The MathWorks Inc. (2017). MATLAB version 9.2.0.538062 (R2017a). Natick.

The World Bank (2007). Environmental Impact Assessment for the Proposed Establishement of a Concentrating Solar Power (CSP) Plant and Related Infrastructure in the Northern Cape Province. Johannesburg. Available: `http://documents.worldbank.org/curated/en/345051468101380430/text/E22790VOL1020BOX0342035B.txt` [2019-07-21].

The World Bank (2019). Project Snapshots - South Africa. Available: `https://ppi.worldbank.org/en/snapshots/country/south-africa` [2019-08-21].

Topel, M. (2014). *Steam Turbine Thermal Modeling for Improved Transient Operation*, Licentiate Thesis. KTH Royal Institute of Technology, Stockholm.

Topel, M. (2017). *Improving Concentrating Solar Power Plant Performance through Steam Turbine Flexibility*, PhD Dissertation. KTH Royal Institute of Technology. Stockholm.

Trading Economics (2019*a*). Namibia - Economic Indicators. Available: `https://tradingeconomics.com/namibia/indicators` [2019-07-23].

Trading Economics (2019*b*). South Africa - Economic Indicators. Available: `https://tradingeconomics.com/south-africa/indicators` [2019-07-22].

Trading Economics (2020). Namibia Prime Lending Rate. Available: `https://tradingeconomics.com/namibia/lending-rate#:$\sim$:text=Inthelong-term%2Cthe,accordingtooureconometricmodels.` [07.10.2020].

Trieb, F. (2004). Das Szenariomodell ATHENE - Ausbau thermischer Solarkraftwerke für eine nachhaltige Energieversorgung. SOKRATES-Projekt. DLR, Stuttgart. Available: `https://www.dlr.de/tt/Portaldata/41/Resources/dokumente/institut/system/projects/AP1_3_ATHENE.pdf` [2020-02-11].

Trieb, F., O'sullivan, M., Pregger, T., Schillings, C. and Krewitt, W. (2009). Characterisation of Solar Electricity Import Corridors from MENA to Europe - Potential, Infrastructure and Cost. DLR, Stuttgart, Germany. Available: `https://elib.dlr.de/59448/1/Solar_import_DLR_2009_07.pdf` [2020-03-27].

Turchi, C.S., Boyd, M., Kesseli, D., Kurup, P., Mehos, M., Neises, T., Sharan, P., Wagner, M. and Wendelin, T. (2019). CSP Systems Analysis - Final Project Report. NREL, Golden. Available: `www.nrel.gov/publications.` [2019-06-17].

UNDP (2014). Human Development Report 2014. New York. Available: `http://hdr.undp.org/sites/default/files/hdr14-report-en-1.pdf` [2015-03-30].

University of Wisconsin-Madison (2014). Trnsys 17 - Mathematical Reference. Solar Energy Laboratory, Univ. of Wisconsin-Madison. Madison.

Vasquez Padilla, R. (2011). *Simplified Methodology for Designing Parabolic Trough Solar Power Plants*, PhD dissertation. University of South Florida. Tampa.

Vignarooban, K., Xu, X., Arvay, A., Hsu, K. and Kannan, A. (2015). Heat transfer fluids for concentrating solar power systems - A review. *Appl. Energy*, 146:383–396.

doi:10.1016/j.apenergy.2015.01.125.

Viljoen, N. (2014). Modeling and Analysis of Stress in High Temperature Molten Salt Trough Receivers. *Energy Procedia*, 49:551–559. doi:10.1016/j.egypro.2014.03.059.

Vogel, A., Reiling, H., Fluri, T. and Platzer, W. (2015). High Temperatures in Line Focusing Systems: Dual Loop Cycle Efficiency and Heat Losses. *Energy Procedia*, 69:1461–1470. doi:10.1016/j.egypro.2015.03.095.

Wagner, M.J. and Gilman, P. (2011). Technical Manual for the SAM Physical Trough Model. NREL. Golden. Available: `http://www.nrel.gov/docs/fy11osti/51825.pdf` [2017-11-25].

Wagner, P. (2012). *Thermodynamic simulation of solar thermal power stations with liquid salt as heat transfer fluid*, Master thesis. Technical University of Munich. Munich.

Wagner, P. and Wittmann, M. (2014). Influence of Different Operation Strategies on Transient Solar Thermal Power Plant Simulation Models with Molten Salt as Heat Transfer Fluid. *Energy Procedia*, 49:1652–1663. doi:10.1016/j.egypro.2014.03.174.

Wassbein, O., Glemarec, Y., Bayraktar, H. and Schmidt, T. (2013). Derisking Renewable Energy Investment. UN Development Programme. New York. Available: `https://seors.unfccc.int/applications/seors/attachments/get_attachment?code=AK0L8IMC1D0P9WHF9ZGV750GGANPKB5N` [2019-08-22].

Willmott, C.J. and Matsuura, K. (2005). Advantages of the mean absolute error (MAE) over the root mean square error (RMSE) in assessing average model performance. *Clim. Res.*, 30:79–82.

Wittmann, M., Breitkreuz, H., Schroedter-Homscheidt, M. and Eck, M. (2008). Case Studies on the Use of Solar Irradiance Forecast for Optimized Operation Strategies of Solar Thermal Power Plants. *IEEE J. Sel. Top. Appl. Earth Obs. Remote Sens.*, 1(1):18–27. doi:10.1109/JSTARS.2008.2001152.

Wittmann, M., Eck, M. and Müller-Steinhagen, H. (2011). Methodology for optimized operation strategies of solar thermal power plants with integrated heat storage. *Solar Energy*, 85(4):653–659. doi:10.1016/j.solener.2010.11.024.

Wu, Y.-T., Chen, C., Liu, B. and Ma, C.-F. (2012). Investigation on forced convective heat transfer of molten salts in circular tubes. *Int. Commun. Heat Mass Transf.*, 39(10):1550–1555. doi:10.1016/j.icheatmasstransfer.2012.09.002.

Wu, Z., Li, S., Yuan, G., Lei, D. and Wang, Z. (2014). Three-dimensional numerical study of heat transfer characteristics of parabolic trough receiver. *Appl. Energy*, 113:902–911. doi:10.1016/J.APENERGY.2013.07.050.

WWF (2014*a*). Enabling Renewable Energy in South Africa: Assessing the Renewable Energy Independent Power Producer Procurement Programme. Available: `http://awsassets.wwf.org.za/downloads/enabling_re_in_sa.pdf` [2015-08-06].

WWF (2014*b*). Renewable Energy Vision 2030 - South Africa. Available: `http://awsassets.wwf.org.za/downloads/a16369_wwf_reip_report_online.pdf` [2019-08-22].

X-Rates (2019*a*). Monthly average exchange rates 2017 (South African Rand per US Dollar). Available: `https://www.x-rates.com/average/?from=USD&to=ZAR&amount=1&year=2017` [2019-08-21].

X-Rates (2019*b*). Monthly average exchange rates 2018 (Chinese Yuan Renminbi per US Dollar). Available: `https://www.x-rates.com/average/?from=USD&to=CNY&amount=1&year=2018` [2019-08-21].

X-Rates (2019*c*). Monthly average exchange rates 2018 (South African Rand per US Dollar). Available: `https://www.x-rates.com/average/?from=USD&to=ZAR&amount=1&year=2018` [2019-08-21].

Xu, H., Li, Y., Sun, J. and Li, L. (2019). Transient model and characteristics of parabolic-trough solar collectors: Molten salt vs. synthetic oil. *Solar Energy*, 182:182–193. doi:10.1016/j.solener.2019.02.047.

Xu, X., Vignarooban, K., Xu, B., Hsu, K. and Kannan, A. (2016). Prospects and problems of concentrating solar power technologies for power generation in the desert regions. *Renew. Sustain. Energy Rev.*, 53:1106–1131. doi:10.1016/j.rser.2015.09.015.

Yang, H., Wang, Q., Huang, Y., Gao, G., Feng, J., Li, J. and Pei, G. (2019). Novel parabolic trough power system integrating direct steam generation and molten salt systems: Preliminary thermodynamic study. *Energy Convers. Manag.*, 195:909–926. doi:10.1016/j.enconman.2019.05.072.

Yang, Z. and Garimella, S.V. (2010). Thermal analysis of solar thermal energy storage in a molten-salt thermocline. *Solar Energy*, 84(6):974–985. doi:10.1016/j.solener.2010.03.007.

Yebra, L.J., Berenguel, M., Bonilla, J., Roca, L., Dormido, S. and Zarza, E. (2010). Object-oriented modelling and simulation of ACUREX solar thermal power plant. *Math. Comput. Model. Dyn. Syst.*, 16(3):211–224. doi:10.1080/13873954.2010.507420.

Yebra, L.J., Berenguel, M., Dormido, S. and Zarza, E. (2008). Object oriented modelling and simulation of parabolic trough collectors with Modelica. *Math. Comput. Model. Dyn. Syst.*, 14(4):361–375. doi:10.1080/13873950701847199.

Zaversky, F., Medina, R., García-Barberena, J., Sánchez, M. and Astrain, D. (2013). Object-oriented modeling for the transient performance simulation of parabolic trough collectors using molten salt as heat transfer fluid. *Solar Energy*, 95:192–215. doi:10.1016/j.solener.2013.05.015.